TRANSIENT MODELING AND SIMULATION OF PISTON DEVICES MOVING THROUGH SINGLE-PHASE AND TWO-PHASE FLOWS IN PIPES APPLIED TO PIGS AND PLUNGERS

Raphael Viggiano Neves de Freitas

Tese de Doutorado apresentada ao Programa de Pós-graduação em Engenharia Mecânica, COPPE, da Universidade Federal do Rio de Janeiro, como parte dos requisitos necessários à obtenção do título de Doutor em Engenharia Mecânica.

Orientadores: Gustavo Cesar Rachid Bodstein
Felipe Bastos de Freitas Rachid

Rio de Janeiro
Julho de 2022

TRANSIENT MODELING AND SIMULATION OF PISTON DEVICES MOVING THROUGH SINGLE-PHASE AND TWO-PHASE FLOWS IN PIPES APPLIED TO PIGS AND PLUNGERS

Raphael Viggiano Neves de Freitas

TESE SUBMETIDA AO CORPO DOCENTE DO INSTITUTO ALBERTO LUIZ COIMBRA DE PÓS-GRADUAÇÃO E PESQUISA DE ENGENHARIA DA UNIVERSIDADE FEDERAL DO RIO DE JANEIRO COMO PARTE DOS REQUISITOS NECESSÁRIOS PARA A OBTENÇÃO DO GRAU DE DOUTOR EM CIÊNCIAS EM ENGENHARIA MECÂNICA.

Orientadores: Gustavo Cesar Rachid Bodstein
Felipe Bastos de Freitas Rachid

Aprovada por: Prof. Gustavo Cesar Rachid Bodstein
Prof. Felipe Bastos de Freitas Rachid
Prof. Roney Leon Thompson
Prof. Gabriel Lisbôa Verissimo
Prof. Leonardo Santos de Brito Alves
Prof. Eduardo Pereyra

RIO DE JANEIRO, RJ - BRASIL
JULHO DE 2022

Freitas, Raphael Viggiano Neves de

Transient modeling and simulation of piston devices moving through single-phase and two-phase flows in pipes applied to pigs and plungers/ Raphael Viggiano Neves de Freitas. – Rio de Janeiro: UFRJ/COPPE, 2022.

XVI, 227 p.: il.; 29,7 cm.

Orientadores: Gustavo Cesar Rachid Bodstein

Felipe Bastos de Freitas Rachid

Tese (doutorado) – UFRJ/ COPPE/ Programa de Engenharia Mecânica, 2022.

Referências Bibliográficas: p. 211-221.

1. Piston Devices. 2. Numerical Simulation. 3. Single and Two-Phase Flows. I. Bodstein, Gustavo Cesar Rachid *et al.* II. Universidade Federal do Rio de Janeiro, COPPE, Programa de Engenharia Mecânica. III. Título.

Acknowledgments

I would like to acknowledge all the people that were part of the journey that led to the conclusion of this work.

First, I would like to immensely thank my wife Carina Sondermann for being my partner and an integral part of my entire academic life. You are responsible for all the motivation that led me to my achievements. Without you by my side, this work would not be possible, you always believed in my potential. We shared all the emotions, good and bad, through the thought period this thesis was elaborated.

I am grateful to my advisors Dr. Gustavo Bodstein and Dr. Felipe Rachid. I thank you for all your shared experience, knowledge, and guidance. You are an essential part that led to the conclusion of this work.

I would also like to acknowledge Dr. Cem Sarica and Dr. Eduardo Pereyra for the opportunity they gave me, and for the experience and knowledge shared, not only during my time as visiting scholar at The University of Tulsa, but also afterward. I also thank the staff, technicians, and students from TUFFP and TUHWALP for receiving and treating me as one of their own.

I am grateful for the staff and students at LabMFA: Jaciara Roberta, Aline, Rodrigo, Matheus, Antônia and Lionel. You provided a great and light working atmosphere during our day-to-day routines.

I would also like to thank CAPES and Petrobras for the financial and academic support that led to this work.

Finally, I would like to thank all my family. My brother Victor, my sister Nathalia, and, especially, my parents Elizabeth and José. Your support, care, guidance, and example brought me here. You always believed that education was fundamental in my life, and I will be always grateful for that.

Resumo da Tese apresentada à COPPE/UFRJ como parte dos requisitos necessários para a obtenção do grau de Doutor em Ciências (D.Sc.)

MODELAGEM E SIMULAÇÃO TRANSIENTE DE DISPOSITIVOS TIPO PISTÃO LANÇADOS EM ESCOAMENTOS MONOFÁSICOS E BIFÁSICOS EM DUTOS, APLICADO A PIGS E PLUNGERS

Raphael Viggiano Neves de Freitas

Julho/2022

Orientadores: Gustavo Cesar Rachid Bodstein
Felipe Bastos de Freitas Rachid

Programa: Engenharia Mecânica

A passagem de um pistão ao longo de tubulações é comumente utilizada na indústria de óleo e gás para atender diversos objetivos: limpeza, monitoramento e aumento da eficiência na produção. Este tipo de dispositivo necessita da interação com o escoamento para se mover ao longo da tubulação, ou seja, é a diferença de pressão através do pistão que permite sua movimentação. Para garantir correta operação deste dispositivo, é essencial prever a dinâmica do pistão e os seus efeitos no escoamento. No presente trabalho duas modelagens de *pig* são estudadas e um modelo de *plunger* em estágio de ascensão é posposto. O modelo de *pig* é aplicado a escoamento monofásico e bifásico incluindo a vazão de *bypass* através do corpo do pistão. O modelo do *plunger* em ascensão inclui os efeitos de retorno de líquido e deslizamento de gás através do dispositivo. Além disso, é proposta uma nova metodologia de acoplamento entre os modelos de pistão com os de escoamento transiente. Para o caso em que escoamento bifásico é analisado, dois modelos de dois fluidos são testados em associação com diversos métodos numéricos e validados através da solução de problemas *benchmarks*. Os resultados obtidos com para *pig* são comparados com resultados presentes na literatura para escoamentos monofásicos e bifásico no padrão estratificado. Já os resultados para *plunger* são validados com dados da literatura e, também, com dados experimentais adquiridos neste trabalho.

Abstract of Thesis presented to COPPE/UFRJ as a partial fulfillment of the requirements for the degree of Doctor of Science (D.Sc.)

TRANSIENT MODELING AND SIMULATION OF PISTON DEVICES MOVING THROUGH SINGLE-PHASE AND TWO-PHASE FLOWS IN PIPES APPLIED TO PIGS AND PLUNGERS

Raphael Viggiano Neves de Freitas

July/2022

Advisors: Gustavo Cesar Rachid Bodstein
Felipe Bastos de Freitas Rachid

Department: Mechanical Engineering

The passage of piston devices through pipes is commonly used in the oil and gas industries for the purposes of cleaning, monitoring, and increasing production efficiency. These devices are not self-driven and require their interaction with the flow entailing a pressure discontinuity across the piston body that drives it along the pipe. To ensure the proper operation of such devices it is crucial to predict the dynamics of the piston and its effects on the flowline. In this work, two modeling approaches are studied for pigs, and one model is proposed for a plunger upstroke. The pig model is applied to single-phase flow, and two-phase flow, including the bypass flow through the piston body. The plunger upstroke model includes the effects of liquid fallback and the gas slippage through the plunger body. In addition, a new methodology is proposed for the coupling of the piston models with the transient one-dimensional flow models. For the two-phase flow models, two two-fluid models are tested with different numerical methods, with the combinations of model-method being validated through benchmarking. The results obtained with the pig model are compared with results from the literature under single-phase and two-phase stratified flow. The results obtained with the plunger upstroke model are also validated with data from the literature, and with experimental data acquired during this work.

Contents

List of Figures x
List of Tables xv
1 Introduction 1
1.1 Motivation 1
1.1.1 Pigging 1
1.1.2 Plunger Lift 2
1.2 Objectives 3
1.3 Present Contribution 5
1.4 Structure of the Work 6
2 Literature Review 8
2.1 Two-Phase Flow Patterns 8
2.2 Two-Phase Flow Mathematical Models 9
2.2.1 Two-Fluid Model 10
2.3 Piston Models 12
2.3.1 Pig Modeling 13
2.3.2 Plunger Modeling 16
3 Single Phase Flow Model 18
3.1 Set of Governing Equations 18
3.2 Hyperbolicity Analysis 20
4 Two-Fluid Models 23
4.1 4E1P Model 23
4.1.1 Hyperbolicity Analysis (4E1P) 26
4.2 5E2P Model 30
4.2.1 Relaxation Procedure 32
4.2.2 Instantaneous Pressure Relaxation 34
4.2.3 Hyperbolicity Analysis (5E2P) 35
4.3 Source Terms 38
5 Numerical Methods for Hyperbolic Equations 42
5.1 General Discretization 42
5.2 CFL Stability Condition 44
5.3 Lax-Friedrichs and Richtmyer Methods 44

5.3.1 Lax-Friedrich Method 45
5.3.2 Richtmyer Method 45
5.4 FORCE Methods 46
5.5 FCT Method 46
5.6 AUSM-Type Method 49
5.7 Roe-Type scheme 52
5.7.1 Roe Linearization 52
5.7.2 Numerical Scheme 53
5.1 Discretization of the Non-Conservative Term 55
5.2 Imposition of Boundary Conditions 56
6 Numerical Benchmarking and Validation 57
6.1 Water Faucet 57
6.2 Two-Fluid Shock-Tube Problem 74
6.3 Pipeline Stratified Flow 80
6.3.1 Case 1: Relative Low Holdup 82
6.3.2 Case 2: Relative High Holdup 87
6.3.3 Accuracy Analysis 90
7 Piston Models 96
7.1 Pig Model 96
7.1.1 Pig Model Under Single-Phase Flow 100
7.1.2 Pig Model Under Two-Phase Flow 104
7.2 Plunger Upstroke Model 107
7.2.1 Liquid Discharge 112
7.2.2 A Plunger Gap Model 114
7.3 Coupled Piston and Flow Motion Problem 123
7.3.1 Piston Model Solution 123
7.3.2 Mesh Reconstruction 126
8 Experimental Facility 131
8.1 Experimental Facility Description 131
8.2 Experimental Procedure 134
8.3 Experimental Matrix 135
8.4 Experimental Data Treatment 135
9 Pigging Results and Discussion 138
9.1 Single Phase Ideal Pig 138

9.2 Pigging in Single-Phase Liquid Flow 143
9.2.1 Influence of Bypass Holes 148
9.3 Pigging in Single-Phase Gas Flow 150
9.3.1 Influence of Bypass Holes 154
9.4 Two-Phase Pigging 156
9.4.1 4E1P Results 157
9.4.2 5E2P Results 169
9.4.3 Comparison with References 180
10 Plunger Upstroke Results and Discussion 185
10.1 Comparison Against Experimental Data 185
10.1.1 Titanium Plunger Case 186
10.1.2 Logging Plunger Case 193
10.1.3 Adjusted Bottom Hole Pressure 197
11 Final Considerations 205
11.1 Conclusions 205
11.2 Recommendations for Future Work 209
References 211
Appendix A – Matrices for AUSM-type Methods 222
Appendix B –Averaged States for Roe Linearization 225
Appendix C – Uncertainty Analysis 226

List of Figures

Figure 3.1: Structure of the Riemann problem for the one-dimensional isothermal set of Euler fluid flow equations. 22
Figure 5.1: One-dimensional discrete mesh by means of the Godunov scheme. 43
Figure 6.1: Water faucet problem schematic. (a) Initial uniform condition. (b) Flow snapshot sometime between initial and steady-state condition. (c) Steady-state condition. 58
Figure 6.2:Water faucet problem, void fraction results using 4E1P model with multiple methods. 61
Figure 6.3:Water faucet problem, liquid velocity results using 4E1P model with multiple methods. 62
Figure 6.4:Water faucet problem, gas velocity results using 4E1P model with multiple methods. 63
Figure 6.5:Water faucet problem, pressure results using 4E1P model with multiple methods. 64
Figure 6.6:Water faucet problem, void fraction results using 5E2P model with multiple methods. 67
Figure 6.7:Water faucet problem, liquid velocity results using 5E2P model with multiple methods. 68
Figure 6.8:Water faucet problem, gas velocity results using 5E2P model with multiple methods. 69
Figure 6.9:Water faucet problem, pressure results using 5E2P model with multiple methods. 70
Figure 6.10:Shock tube problem, void fraction results with multiple methods. 76
Figure 6.11: Shock tube problem, liquid velocity results with multiple methods. 77
Figure 6.12:Shock tube problem, gas velocity results with multiple methods. 78
Figure 6.13: Shock tube problem, pressure results with multiple methods. 79
Figure 6.14: Pressure distribution, stratified flow case 1. 84
Figure 6.15: Holdup distribution, stratified flow case 1. 85
Figure 6.16: Gas velocity distribution, stratified flow case 1. 85
Figure 6.17: Liquid velocity distribution, stratified flow case 1. 86
Figure 6.18: Pressure distribution, stratified flow case 2. 88
Figure 6.19: Holdup distribution, stratified flow case 2. 89

Figure 6.20: Gas velocity distribution, stratified flow case 2. 89
Figure 6.21: Liquid velocity distribution, stratified flow case 2. 90
Figure 6.22: Accuracy analysis, 4E1P AUSMDV. 92
Figure 6.23: Accuracy analysis, 4E1P AUSMV. 92
Figure 6.24: Accuracy analysis, 4E1P ModFORCE. 93
Figure 6.25: Accuracy analysis, 4E1P Roe scheme. 93
Figure 6.26: Accuracy analysis, 5E2P ModFORCE method. 94
Figure 6.27: Accuracy analysis, 5E2P Roe scheme. 95
Figure 7.1: Schematic drawing of the fitting of a pig inside a pipeline (Patricio *et al.*, 2020). 97
Figure 7.2: Velocity profile through the gap from the pig frame of reference. 100
Figure 7.3: Schematic of the pig control volume. 102
Figure 7.4: Cup pig with holes (Patricio, 2016). 103
Figure 7.5: Sketch for a Two-phase flow bypass pig. 105
Figure 7.6: Plunger upstroke schematic. (a) Simplified version with no gas slippage or liquid fallback. (b) Extended version considering gas slippage, liquid fallback, and the onset of a Taylor bubble region. 110
Figure 7.7: Fluid path through the wellhead. 112
Figure 7.8: Schematic for plunger-tubing gap problem. 115
Figure 7.9: Example of a phase fraction solution for the plunger gap problem (1). 119
Figure 7.10: Example of a phase fraction solution for the plunger gap problem (2). .. 119
Figure 7.11: Example of a gas velocity solution for the plunger gap problem. 120
Figure 7.12 Example of a liquid velocity solution for the plunger gap problem. 120
Figure 7.13: Example of interfacial velocity solution for the plunger gap problem. ... 121
Figure 7.14: Example of gas mass flow rate solution for the plunger gap problem..... 122
Figure 7.15: Example of liquid mass flow rate solution for the plunger gap problem. 122
Figure 7.16: Sketch of upstream and downstream meshes with the piston control volume. 126
Figure 7.17: Mesh composition after mesh reconstruction procedure, note that the piston position is highlighted in red. 129
Figure 7.18: Mesh composition after readjusting the last cell of the upstream mesh, and the first cell of the downstream mesh. 130
Figure 8.1: Experimental facility schematic (Akiiartdinov et al., 2020). 133
Figure 9.1: Pressure at pig front and tail during the first seconds of the simulation. ... 141

Figure 9.2: Pig velocity during the first seconds of the simulation. 141
Figure 9.3: Pig velocity through time for the single-phase ideal pig case..... 142
Figure 9.4: Pig position through time for the single-phase ideal pig case..... 142
Figure 9.5: Pressure along the line for the single-phase ideal pig case. 143
Figure 9.6: Pressure along the line for the pigging in liquid flow case. 145
Figure 9.7: Liquid velocity along the line for the pigging in liquid flow case. 146
Figure 9.8: Pressure profile comparison for the pigging in liquid flow case. 147
Figure 9.9: Liquid velocity comparison for the pigging in liquid flow case. 147
Figure 9.10: Influence of bypass holes for the pigging in liquid flow case. 149
Figure 9.11: Pressure along the line for the pigging in gas flow case. 151
Figure 9.12: Pressure profile comparison for the pigging in gas flow case. 152
Figure 9.13: Gas velocity comparison for the pigging in gas flow case (1). 152
Figure 9.14: Gas velocity comparison for the pigging in gas flow case (2). 153
Figure 9.15: Pig velocity comparison for the single-phase gas flow case. 154
Figure 9.16: Single-phase pig gas pressure along the line. 155
Figure 9.17: Pressure profile with Roe scheme and 4E1P, two-phase pigging. 158
Figure 9.18: Pressure profile with AUSMV method and 4E1P, two-phase pigging. ... 158
Figure 9.19: Pressure profile with ModFORCE method and 4E1P, two-phase pigging. 159
Figure 9.20: Pressure profile with FCT method and 4E1P, two-phase pigging. 159
Figure 9.21: Holdup profile with Roe scheme and 4E1P, two-phase pigging. 161
Figure 9.22: Holdup profile with AUSMV method and 4E1P, two-phase pigging. 161
Figure 9.23: Holdup profile with ModFORCE method and 4E1P, two-phase pigging. 162
Figure 9.24: Holdup profile with FCT method and 4E1P, two-phase pigging. 162
Figure 9.25: Gas velocity profile with Roe scheme and 4E1P, two-phase pigging..... 164
Figure 9.26: Gas velocity profile with AUSMV method and 4E1P, two-phase pigging. 164
Figure 9.27: Gas velocity profile with ModFORCE method and 4E1P, two-phase pigging. 165
Figure 9.28: Gas velocity profile with FCT method and 4E1P, two-phase pigging. 165
Figure 9.29: Liquid velocity profile with Roe scheme and 4E1P, two-phase pigging. 166
Figure 9.30: Liquid velocity profile with AUSMV method and 4E1P, two-phase pigging. 166

Figure 9.31: Liquid velocity profile with ModFORCE method and 4E1P, two-phase pigging. 167
Figure 9.32: Liquid velocity profile with FCT method and 4E1P, two-phase pigging. 167
Figure 9.33: Pig velocities with time for the 4E1P model, two-phase pigging case. ... 168
Figure 9.34: Pressure profile with Roe scheme and 5E2P, two-phase pigging. 170
Figure 9.35: Pressure profile with AUSMV method and 5E2P, two-phase pigging. ... 170
Figure 9.36: Pressure profile with ModFORCE method and 5E2P, two-phase pigging. 171
Figure 9.37: Pressure profile with FCT method and 5E2P, two-phase pigging. 171
Figure 9.38: Holdup profile with Roe scheme and 5E2P, two-phase pigging. 172
Figure 9.39: Holdup profile with AUSMV method and 5E2P, two-phase pigging. 173
Figure 9.40: Holdup profile with ModFORCE method and 5E2P, two-phase pigging. 173
Figure 9.41: Holdup profile with FCT method and 5E2P, two-phase pigging. 174
Figure 9.42: Gas velocity profile with Roe scheme and 5E2P, two-phase pigging..... 175
Figure 9.43: Gas velocity profile with AUSMV method and 5E2P, two-phase pigging. 175
Figure 9.44: Gas velocity profile with ModFORCE method and 5E2P, two-phase pigging. 176
Figure 9.45: Gas velocity profile with FCT method and 5E2P, two-phase pigging. 176
Figure 9.46: Liquid velocity profile with Roe scheme and 5E2P, two-phase pigging. 177
Figure 9.47: Liquid velocity profile with AUSMV method and 5E2P, two-phase pigging. 177
Figure 9.48: Liquid velocity profile with ModFORCE method and 5E2P, two-phase pigging. 178
Figure 9.49: Liquid velocity profile with FCT method and 5E2P, two-phase pigging. 178
Figure 9.50: Pig velocities with time for the 5E2P model, two-phase pigging case. ... 179
Figure 9.51: Pressure profile 4E1P, two-phase pigging, comparison with references. 180
Figure 9.52: Holdup profile 4E1P, two-phase pigging, comparison with references... 181
Figure 9.53: Gas velocity profile 4E1P, two-phase pigging, comparison with references. 181
Figure 9.54: Liquid velocity profile 4E1P, two-phase pigging, comparison with references. 182
Figure 9.55: Pig velocities with time for the 4E1P model, comparison with references. 183

Figure 10.1: Rarefaction wave entering the tubbing. 188
Figure 10.2: Plunger position against time, titanium plunger case. 189
Figure 10.3: Plunger velocities against time, titanium plunger case. 190
Figure 10.4: Pressure against time (12psig), titanium plunger case. 191
Figure 10.5: Pressure against time (14psig), titanium plunger case. 191
Figure 10.6: Pressure against time (16psig), titanium plunger case. 192
Figure 10.7: Pressure against time (18psig), titanium plunger case. 192
Figure 10.8: Plunger position against time, logging plunger case. 195
Figure 10.9: Plunger velocity against time, logging plunger case. 195
Figure 10.10: Pressure against time (14psig), logging plunger case. 196
Figure 10.11: Pressure against time (16psig), logging plunger case. 196
Figure 10.12: Pressure against time (18psig), logging plunger case. 197
Figure 10.13: Plunger position against time, logging plunger case, after pressure adjustment. 199
Figure 10.14: Plunger velocity against time, logging plunger case, after pressure adjustment. 199
Figure 10.15: Pressure against time (14psig), logging plunger case, after pressure adjustment. 200
Figure 10.16: Pressure against time (16psig), logging plunger case, after pressure adjustment. 200
Figure 10.17: Pressure against time (18psig), logging plunger case, after pressure adjustment. 201
Figure 10.18: Plunger acceleration against time, logging plunger case, after pressure adjustment. 202
Figure 10.19: Pressure difference across the plunger against time, logging plunger case, after pressure adjustment. 203
Figure 10.20: Liquid slug front velocity against time, logging plunger case, after pressure adjustment. 204

List of Tables

Table 6-1: Simulation set up for the water faucet problem. 60
Table 6-2: Inlet and outlet boundary conditions for the water faucet benchmark..... 60
Table 6-3: Remaining area between curves for the water faucet problem using the 4E1P model with 2500 cells..... 66
Table 6-4: Remaining area between curves for the water faucet problem using the 5E2P model with 2500 cells..... 72
Table 6-5: Computational time for the water faucet problem under various configurations. 73
Table 6-6: Left and right states of the large relative velocity shock tube problem. 74
Table 6-7: Simulation set up for the large relative velocity shock tube benchmark. 75
Table 6-8: Pipe properties for the stratified flow cases. 81
Table 6-9: Fluid Properties for the stratified flow case 1. 82
Table 6-10: Inlet and outlet boundary conditions for the stratified flow case 1..... 83
Table 6-11: Relative difference 4E1P with Roe against references for stratified case 1. 83
Table 6-12: Relative difference 5E2P with Roe against references for stratified case 1. 84
Table 6-13: Fluid Properties for the stratified flow case 2. 87
Table 6-14: Inlet and outlet boundary conditions for the stratified flow case 2..... 87
Table 6-15: Relative difference 4E1P with Roe against references for stratified case 2. 88
Table 6-16: Relative difference 5E2P with Roe against references for stratified case 2. 88
Table 7-1: Fluid Properties, IsoparL, and air for the gap problem example. 118
Table 8-1: Instrument position in the tubbing, from the base of the bumper spring. ... 132
Table 8-2: IsoparL properties. 135
Table 8-3: Titanium alloy Plunger properties..... 135
Table 8-4: High-speed pressure sensors calibration coefficients. 137
Table 9-1: Pipe properties, single-phase pigging cases. 139
Table 9-2: Inlet and outlet boundary conditions for the ideal pig case. 139
Table 9-3: Gas properties for the ideal pig case. 139
Table 9-4: Pig properties for the single-phase pigging cases. 140

Table 9-5: Liquid properties for the pigging in liquid flow case..... 144
Table 9-6: Inlet and outlet boundary conditions for the pigging in liquid flow case. .. 144
Table 9-7: Pig velocities comparison for the pigging in liquid flow case..... 148
Table 9-8: Influence of holes on traveling time and bypass flow rate for the single-phase liquid case..... 149
Table 9-9: Gas properties for the pigging in gas flow case..... 150
Table 9-10: Inlet and outlet boundary conditions for the pigging in gas flow case. 150
Table 9-11: Influence of holes on traveling time and bypass flow rate for the single-phase gas case..... 155
Table 9-12: Pipe properties for the two-phase pigging case. 156
Table 9-13: Fluid Properties for the two-phase pigging case..... 156
Table 9-14: Inlet and outlet boundary conditions for the two-phase pigging case..... 157
Table 9-15: Pig properties for the two-phase pigging case. 157
Table 10-1: Fluid properties, experimental plunger cases..... 186
Table 10-2: Titanium Alloy plunger properties..... 187
Table 10-3: Logging Plunger properties..... 194
Table 10-4: Polynomial parameters for bottom hole pressure adjustment..... 198
Table C. 1: Systematic uncertainty of instruments for the plunger lift facility……..….226

1 Introduction

1.1 Motivation

Multiphase flows are predominant in a variety of engineering processes in the many branches of the industry. Particularly in the oil and gas industry, a mixture of oil and gas is typically transported inside pipelines from the production sites to the processing plants. Due to oil and its byproducts being critical to generating the required energy and maintaining the necessary infrastructure for modern society, it is of alarming importance its continuous production. Over time, different obstacles may rise during the production and transport of oil and gas through wells and pipelines, thus, devices in the form of pistons, such as pigs and plungers, are utilized to deal with some of these obstacles and keep a continuous production.

This work is primarily motivated by the necessity of robust numerical tools that are able to reproduce the physics of piston devices used by the oil and gas industries and predict their interaction with the flow. During the operation of the pipes, it is essential to predict single and two-phase flows, especially when high costs and efficiency of the production are affected. Since this challenging problem is intrinsically unsteady, a transient numerical approach gives a more detailed and complete description of its behavior. The operation and importance of these devices for the oil and gas industries are described in the following sections.

1.1.1 Pigging

During the lifetime of an oil and gas pipeline, hydrates, paraffin, and asphaltenes may deposit on the pipe walls, decreasing the flow rate of the fluids and, eventually, leading to an unaccounted clogging of the line. To assure the flow, tools, known as pigs, were engineered with the intention to clean the pipe from these deposits. Pigs are pistons made of many shapes and materials and passively are driven by their interaction with the fluid dynamics in the pipe. The etymology of the term pig originally comes from the noise that these tools make while they pass through the pipeline, resembling the squealing of pigs. Modern pigs, however, are not only limited to just cleaning devices, they can also be used as inspection tools that may log temperature, pressure, altimetry of the pipeline,

and the state of the pipe walls that may be affected by corrosion or metal loss. Ascribable to this modern function, in some recent works, pigs are referred to as the acronym pipe-inspection-gauge.

As stated previously, pigs are driven passively by their interaction with the flow dynamics. As the piston is launched in the pipeline, it creates a physical restriction that is followed by the rise of a pressure jump across the pig body, the resulting force accelerates the piston making it scrape the fluids, deposits, and debris left in the pipeline. The employment of pig devices was originally based on rule of thumbs rather than the employment of physical models based on the dynamics of the pig and the fluid. Later models were developed based on the physical phenomena of the pig conceptual problem. An effective way to model these devices is essential to guarantee their effective deployment, since an improper pig launch may cause the equipment to get stuck in the line or not properly scrape the deposits, generating the opposite effect by compromising flow assurance.

1.1.2 Plunger Lift

Historically, the most common type of oil and gas producing wells are drilled vertically into a conventional reservoir, where the hydrocarbon source is kept sealed by a cap rock. With the advent of modern technologies for horizontal drilling and hydraulic fracturing, there is an increase in the installation of unconventional wells, where the source of hydrocarbons is entrained in the rock itself, typically shale. These wells have a sharp decline rate of production, and, usually, a high gas-liquid ratio, GLR. At a certain point in the well's life, the gas will have insufficient momentum to carry the liquid to the production flowline. This will result in a liquid loading at the bottom hole, and with the increase of the liquid column in the bottom hole, the pressure increases reducing the production gradually. Eventually, if this effect is not considered, the rise in the liquid column and bottom-hole pressure may kill the well, stopping the production entirely. Therefore, to maximize production, the removal of the liquid column is desired. To achieve that, several artificial lift techniques can be employed such as foam lift, gas lift, and plunger lift.

In the case of plunger lift, a piston is utilized to create a solid mechanical seal between the liquid and gas phases lifting the liquid column from the bottom hole to the production line, and, consequently, reducing the bottom-hole pressure and increasing

production. In addition, not because of their primary design, but as a consequence of their operation, plungers can clean the tubing by removing deposits similarly to pigs. Moreover, to improve efficiency, plunger lift operations can also be combined with gas lift, as means of gas-assisted plunger lift (GAPL). Plunger operations can be performed with many different plunger types that can be classified into two main categories.

- Conventional plungers: a simple piston with no mechanical device built into it is dropped from the well-head to the bottom hole with the well closed. When the piston is resting at the bottom, the system is left stationary to build pressure. At an optimized set pressure, the well is opened creating a large pressure difference between the liquid column front and the plunger tail, raising the liquid column to the production line.
- Continuous-flow plungers: a piston with a mechanism that enables it to be dropped from the well-head without necessarily closing the well. This type of plunger has two different configurations, the low drag configuration or hollow piston configuration that enables the piston to fall through the tubing while production takes place. When it reaches the bottom, through a built-in mechanism, a high drag configuration takes place creating the mechanical seal and elevating the liquid column with the plunger.

1.2 Objectives

The general objective of this work is to develop a transient one-dimensional numerical model that can simulate a piston traveling inside a flowline where the piston is driven by its interaction with the flow. The model is divided into three sections: the upstream flow; the downstream flow, which can be both solved for single or two-phase flow; and the section for the piston control volume. The methodology must be able to capture the disturbances caused by the piston as well as the transient physical phenomena of the flow while the piston is passing through the pipe.

The first specific objective of this work is to evaluate two one-dimensional two-fluid models together with five different numerical methods that comprise a combination of ten model-method methodologies, which are herein called numerical models. This evaluation is necessary since a fully comprehensive study applied to two-fluid models and numerical methods for solving system of hyperbolic partial differential equations was

not found in the literature, and some of the numerical models analyzed in this work have not yet been tested to the same extent as intended here. The two mathematical models are: the single-pressure four equation model, referred to as 4E1P for short; and the two-pressure five equation model, 5E2P These models are isothermal, which means that the energy equation is neglected. The numerical methods selected are: two variations of the Advection Upstream Splitting Method, AUSMV and AUSMDV; the Flux Corrected Transport Method (FCT); a modification of the First Order Center Scheme named ModFORCE; and a method based on the Roe linearization scheme. The numerical models are tested against two benchmark problems and their behavior is reported from a physical and numerical perspective.

An additional objective of this work is to propose and test a new methodology for coupling the piston models with the fluid flow models. This new methodology separates the models into three regions that are connected through their boundary conditions. The piston model was conceived in a Lagrangian perspective that is developed using the basic principles of conservation of mass and momentum through the Reynolds transport theorem, whereas the fluid flow models are solved within an Eulerian description using numerical schemes for hyperbolic partial differential equations.

Finally, this work also aims to develop a specific model for a plunger upstroke that is extended from previous models present in the literature encompassing some of the numerical phenomena observed through the experiments published by Akhiiardinov *et al.* (2020) that are reiterated by the experimental results carried out in this work. During a plunger upstroke, there is not only a presence of liquid fallback and gas slippage but also the onset of a Taylor bubble that the plunger and the liquid slug on its top to have different dynamics.

To evaluate and validate the model, experimental data was also acquired for the plunger upstroke stage in the testing facilities of the University of Tulsa Horizontal Wells and Artificial Lift Projects (TUHWALP) and Fluid Flow Projects (TUFFP), Oklahoma, USA. For that, the plunger-well facility was used to acquire data on both the plunger dynamics and the flow.

1.3 Present Contribution

The passage of pistons through pipelines in the context of pigging operations or plunger lift constitutes a problem that is intrinsically transient and requires the solution of two coupled problems. One is the problem for the fluid flow inside the pipeline, and the other for the piston. Solving the problem is of extreme importance to better understand the phenomena present in these operations, as well as to predict the outcome of the real case scenarios in the search for optimizing the processes. The general contribution of this work lies in the development of numerical models that can tackle these relevant problems. The first problem is a pigging operation run in single-phase flow with either gas or liquid lines. The second is the pigging operation carried out in two-phase gas-liquid flow lines. The third is the plunger upstroke.

To solve the fluid flow that interacts with the piston a system of non-linear hyperbolic partial differential equations that represent the governing principles of continuity and momentum conservation are used in an averaged one-dimensional approach. To solve the more complex two-phase flow equations a pair of two-fluid models, the 4E1P and the 5E2P, are presented and detailed from their physical and mathematical perspectives. A detailed hyperbolicity analysis of the models is performed to ensure proper boundary conditions prescriptions. Also, the necessary closures to make the models physically representative are detailed, for the case of a segregated flow with a well-defined interface. The 5E2P two-fluid model to simulate the piston motion within a pipeline is also a contribution of this work.

From the perspective of the solution of the hyperbolic non-linear partial differential equations, a handful of numerical methods are selected and detailed. The chosen methods are the ModFORCE, FCT, AUSMV, AUSMDV, and the approximate Riemann solver of Roe. One of the main contributions of the present work is the extensive evaluation of multiple model-method combinations for solving two-phase flow in pipes. To carry out this analysis, benchmark cases were selected as well as a stratified flow case with real-scale pipeline dimensions. Also, the evaluation of the models from the perspective of spatial accuracy is performed. The results indicate that the Roe scheme presented with the 4E1P model provides promising results for simulating two-phase flow in pipes. However, the 5E2P model provides an advantage in terms of the extensive range in which

its equations remain hyperbolic. This study, as well as its conclusions, are also a contribution of this work.

A new methodology for coupling the piston models and the fluid flow models is proposed here. In this methodology, the piston control volume is considered to have real dimensions within the pipe domain. The fluid domain is divided into two sections, the upstream and downstream sections, which interface with the piston model through their boundary conditions. The grids at the downstream and upstream sections are updated at each time step by means of linear interpolation. This is also a contribution of this work, since regridding the pipe has not yet been applied to two-phase flow as the piston moves inside the pipe. This methodology is tested for both the single-phase and two-phase pigging cases as well as the plunger upstroke case.

Finally, an unprecedented model for a plunger upstroke is proposed. The model is based on the perspective that the liquid slug at top of the plunger and the plunger can have a separate motion as reported by Akhiiardinov *et al.* (2020). The separate motion of the bodies gives rise to a Taylor bubble in between the bodies. The Taylor bubble, liquid slug, and plunger are lumped into a one-dimensional control volume model. The modeling encompasses two momentum equations, one for the plunger, and one for the liquid slug, along with the kinematic relations between the bodies. To respect the principles of continuity a closure model is also proposed. In this closure, the flow within the gap between the plunge and the pipe wall is approximated by a two-phase flow version of the Couette flow. The flow parameters through the gap are then averaged to a one-dimensional perspective to give closure to the overall plunger upstroke model. This model is tested against experimental data for a conventional plunger upstroke showing promising results.

1.4 Structure of the Work

In chapter 2, a literature review is presented, showing publications that were relevant to the development of this work.

Chapter 3 is dedicated to describing the mathematical model that is used in the single-phase flow simulations of this study.

Chapter 4 is dedicated to describing the mathematical models that are used in the two-phase flow simulations of this study.

In chapter 5, the numerical methods selected are presented in detail, as well as the discretization techniques.

Chapter 6 is devoted to benchmarking and validating the numerical models, that encompass a combination of the two-fluid mathematical models and numerical methods. In addition, an accuracy check of the selected numerical method is performed.

Chapter 7 introduces the piston models for simulating pigs and plungers and the methodology proposed to couple the piston models with the fluid flow models.

Chapter 8 is dedicated to describing the facility used to gather the experimental data presented in this work.

Chapter 9 presents the pigging simulation results for both single and two-phase flow cases.

Chapter 10 presents the plunger upstroke experimental and numerical results, comparing both data sets. Also, a comparison of the model with literature experimental data is performed.

Chapter 11 provides the conclusions of the work.

Appendix A presents the linearized parameters to construct the Roe matrix for the single-phase model and the pair of two-phase models.

Appendix B presents the AUSMV and AUSMDV convective and pressure fluxes.

2 Literature Review

2.1 Two-Phase Flow Patterns

Two-phase flows present more complexity in their modeling than single-phase flows. The tridimensional interaction between both phases as well as the interaction between the fluids and the conduit walls can induce different flow configurations. In a gas-liquid flow, the shapes of the interface between phases together with the interface dynamics define the flow pattern. The interface between the fluids is a moving region that changes constantly with the flow evolution. Besides, it is a region where flow discontinuities exist, presenting extra difficulties in mathematical modeling.

Ishii and Hibiki (2006) classify two-phase flows by the structure of the interface according to the following category: separated, transitory, and disperse flows. Taitel and Dukler (1976) described a map of regimes that may occur in horizontal and nearly horizontal pipes with the dependence on the pipe's geometry, fluid properties, and the velocities of both phases. Some of these regimes can be classified as stratified, bubble, annular and intermittent, as shown in Figure 2.1 and as described below. A more detailed description of each flow pattern can be found in Shoham (2006).

- Stratified: in a horizontal or slightly inclined pipe, the flow presents a stratified pattern where the superficial velocities of gas and liquid displays low values. The liquid stays in the bottom of the pipe with a smooth or wavy interface.
- Bubble: the flow presents dispersed bubbles of gas on the liquid portion. Generally, this flow pattern occurs in horizontal pipes for high liquid flow rates.
- Annular: the flow presents an annular film of liquid surrounding the tube walls and an internal gas core. Generally, in horizontal pipes, it occurs at high gas flow rates.
- Intermittent (slug or elongated bubble): the difference between the superficial velocities of the gas and liquid in a two-phase flow can create waves on the interface of a stratified flow. When these waves get higher amplitudes and reach the top of the pipe, the flow regime is characterized as slug flow. In addition, when the bubbles of a bubbly flow concentrate in a long bubble, the flow is characterized as elongated bubble flow. Elongated bubble flow is the limiting case of slug flow when the liquid slugs are free of entrained bubbles. As the name

suggests, the slugs and elongated bubbles present an intermittent behavior. In some cases, high amplitude waves can be formed rather than slugs. These pseudo-slugs carry similar characteristics to slug flow, making them fall under the intermittent category.

Other flow patterns, that represent a combination of those previously presented, may occur for different pipeline inclinations. Moreover, the regimes present in vertical pipes have similar topologies.

2.2 Two-Phase Flow Mathematical Models

Mathematical models of two-phase flow involve a system of non-linear partial differential equations that represent the physical principles of conservation of mass, momentum, and energy. The full mathematical analysis of two-phase flows is a complex task due to the interactions between the phases with each other, through the common interface, and with the boundaries of the domain, which leads to a transient model that covers the three dimensions of space. This type of problem is hard to be dealt with when one uses the complete set of Navier-Stokes equations. However, in two-phase flows that occur in long pipes, with a low ratio of hydraulic diameter to pipe length, the tridimensional governing equations may be averaged to yield a simpler one-dimensional model. The works of Ishiii and Mishima (1984), Ishii and Hibiki (2003), and Drew and Passman (1999) derive, from the tridimensional single-phase conservation equations, a set of one-dimensional multicomponent governing equations, through procedures of time, volume, and ensemble averaging. Many approaches can be used in order to model two-phase flows, such as pointed out by Stewart and Wendroff (1984) in which two-phase flow models can be classified as:

- Homogeneous Equilibrium Model - HEM: this model treats the two-phase flow as a homogeneous mixture, assuming that the flow parameters, such as pressure, velocity, and temperature, are the same for both phases. This is the simplest approach for two-phase flow Eulerian models. It utilizes only one continuity equation, one equation for momentum conservation as well as one equation for energy conservation.
- Drift-Flux Model - DFM: this type of model takes into account separate velocities for each phase, but considers pressure and temperature as common parameters

shared by the fluids. This type of model considers one or two continuity equations, one equation of momentum conservation and one of energy conservation. However, it differs from the HEM by the addition of a slip velocity relation to accounting for the separate motion of each phase.

- Two-Fluid Model - TFM: two-fluid models are the most complete and robust of the class of one-dimensional two-phase flow models. These models consider separate governing equations for each phase. TFM can tackle the phenomena seen in two-phase flow with more detail by considering different velocities, and, in some cases, different pressures and/or temperatures between each phase. In contrast, these models are more complex, requiring more robust numerical methodologies for their solution. The TFM is the approach utilized in the present work.

2.2.1 Two-Fluid Model

The more classic formulations of this type of model are the ones proposed by Stewart and Wendroff (1984) and Ishii and Mishima (1984), which serve as references for other TFM formulations in the literature. In this model, each phase is considered a separate fluid with its own governing equations, composing a system expressed by two sets of conservation equations of mass, momentum, and energy, one of each corresponding to a specific phase. Then, in the one-dimensional formulation, the model is composed of a set of six non-linear hyperbolic partial differential equations. Not only the number of equations but also the necessity of more constitutive closure relations makes this model more complete than the HEM and DFM. This means that the physics of the flow is better represented by the TFM models. Constitutive relations related to the interaction between fluids are crucial for the two-fluid formulation since these relations create a connection between the phases. Examples of types of constitutive relations are the interfacial interactions and the relation between volume fractions of each phase. A general TFM formulation can consider different pressures between phases locally, however, as pointed out by Essama (2004) and Ishii (1975), introducing non-equilibrium pressure modeling into the TFM highly increases its complexity, since the pressure difference between the phases is bound to the effects of the interface curvature, mass transfer, and dynamic effects. Then, when it comes to subcritical flows the single-pressure assumption that estimates that both phases share a common pressure is commonly used for the sake of

simplicity. This formulation is named in this work as 6E1P, in allusion to a six equations model with single pressure.

In addition, another simplifying hypothesis typically made in previous works in the literature is considered an isothermal two-phase flow. Using this approach, the temperature is considered constant throughout the domain, simplifying the model by neglecting the energy equations. The system of equations is, then, reduced to two equations of mass and two of momentum, composing a four-equation one-pressure model, 4E1P. Some examples of works that use this model are Issa and Kempf (2003), Essama (2004), Ansari and Shokri (2011), and Figueiredo *et al.* (2017).

Instead of considering an isothermal flow, the hypothesis of thermal equilibrium between both phases can be used as a simplification of the 6E1P, in cases where heat transfer is significant but not extreme. The 5E1P, five equations one pressure model, used by Sondermann (2016), considers the internal convection, thermal conduction at the pipe wall, and convection with the environment. With this model, all heat transfer phenomena are treated for the mixture as a whole but still treats the continuity and momentum equations separately for each fluid, resulting in a single-pressure and single-temperature two-fluid model. The same hypothesis is utilized in the two-fluid model used by the well-reputed commercial software OLGA (Schlumberger), described in the work of Bendiksen *et al.* (1991). The model utilized by OLGA considers a different approach for the flow governing equations, since it deals with three phases (water, oil, and gas) and also considers the presence of dispersed liquid droplets in the gas phase. The OLGA model encompasses three continuity equations, one for the gas phase, one for the liquid phase, which incorporates the oil and water fluids, and the last one for the droplets. Regarding the momentum equations, the model has a total of three, one for the water fluid, one for the oil, and one for the combination of gas and liquid droplets. For the energy equation, the model used by the software considers the effects of all phases within one equation.

It is intuitive to presume that other combinations of hypotheses and equations may lead to different two-fluid models that can be more adequate for specific cases of multiphase flow. Even though many configurations are possible for composing a two-fluid model, there are only a few that are unconditionally hyperbolic. The one-dimensional Euler equations for single-phase flow are composed of a set of PDEs that constitutes an unconditionally hyperbolic model. Differently, the one-dimensional two-fluid models, that physically describe multiphase flows in conduits, are mostly conditionally hyperbolic. Hyperbolicity is an important feature that a model should retain

in order to generate valid results. If a model loses hyperbolicity at a given flow configuration, it will make the two-fluid model ill-posed, presenting more than one solution or no solution at all. Contrasting the models presented until this point, the two-fluid model proposed by Baer and Nunziato (1986) is unconditionally hyperbolic. Similarly, to the 6E1P, this model is composed of a set of separate conservation equations for each phase, which are the continuity, momentum, and energy equations, but also includes an additional equation for the compaction of granular material. In this work, the authors are interested in the modeling of the phenomenon of deflagration-to-detonation of granular material. The phases in question are gas and granular solid explosives.

Making use of the Baer and Nunziato (1986) model as a reference, Saurel and Abgrall (1999) proposed an unconditionally hyperbolic two-fluid model directed to gas-liquid flows. This model involves the same conservation equations of the 6E1P, and includes an equation for the transport of the volume fraction, where the volume fraction is advected with an interfacial velocity. With the inclusion of this new equation, one more variable is introduced and both phases are considered to have different pressures. The inclusion of the liquid pressure as a variable makes the hypothesis of liquid compressibility necessary. The pressures are related also to the pressure relaxation phenomena between the phases along the time. Non-equilibrium pressure between the phases is a complex phenomenon to model that takes into consideration various effects and, because of that reason, it is usually simplified. There are works that deal with this model and tackle multiple numerical approaches to solve several test cases, such as Furfaro and Saurel (2015), and Munkejord (2007). This model will be referenced in this work as 7E2P, seven equations two-pressure model.

The hypothesis of isothermal flow is also common in the literature in order to simplify the 7E2P by neglecting the energy equations, and generating a model of five equations and two pressures, the herein called 5E2P. This model is quite similar to the 4E1P model, especially when instantaneous pressure relaxation is considered. The works of Munkejord (2007, 2010), and Freitas (2017) compare both models and show that they produce similar outputs, but with the advantage that the 5E2P is unconditionally hyperbolic.

2.3 Piston Models

The passage of a free-piston in ducts has been used for different applications from cleaning in pigging operations to artificial lift with the usage of plungers. Even though

used for different purposes, pigs and plungers have many similarities in the phenomena that govern their operations. Both of them are pistons that serve as a mechanical seal, are driven passively by the pressure difference across their body, and their operations are intrinsically transient. Several models were developed throughout the years to predict the behavior of such devices.

2.3.1 Pig Modeling

Azevedo *et al*. (1996) derived analytical equations for flow rates through the effective gap, bypass ports, and the bypass through foam pigs in single-phase flow. The authors also derived an equation for the shear force produced by the fluid flowing through the pig gap. Later, Campo (1998) also contributed with the modeling of the acting forces on pigs, considering the friction forces and bypass in his description of the pig dynamics.

In the work of Nieckele *et al.* (2001), the authors developed a model for pigging in single-phase gas or liquid flow separating the solution of the flow and the pig. In the flow, a staggered adaptative mesh is used to solve the principles of continuity and momentum, the time integration is semi-implicit, and the space derivative is based on a central difference method. The mesh is updated based on the pig's position and gets more refined close to the pig. For obtaining the pig dynamics, the momentum and mass balance across the pig body are considered. They have a tailor-made model for the contact forces between the pig and the pipe walls for cup-type pigs, that was developed using the Finite Element Method (FEM). In addition, the authors tested how friction effects affect the piston driving pressure with different configurations of conical cups and disk cups. Another numerical test includes other applications such as dewatering a riser, pigging through a gas pipeline with inward protruding flanges, and reverse motion of bypass pigs.

Nguyen *et al.* (2001) (a) simulate pig dynamics in a gas flowline with a one-dimensional model. The principles of continuity, momentum, and energy conservations are considered in their equations and are solved using the Method of Characteristics (MOC). The pig model is simple, with no bypass, and considers only the force balance at the pig body, which is solved with the Runge-Kutta scheme. The pig interfaces with the flow model through boundary conditions that set the flow velocity equal to the fluid velocity at the pig interface position in both upstream and downstream sections of the pipe. Later, in the same year, Nguyen *et al.* (2001) (b) published a similar approach but considered the bypass flow through the pig. The bypass flow is estimated through a local

pressure loss equation with a combined discharge coefficient, that interfaces with the pig momentum equation through the pressure difference across the pig. With the bypass, the fluid velocities at the pig boundaries are no longer equal to the pig velocity and are derived separately through mass conservation across the pig body.

Esmaeilzadeh *et al.* (2006, 2009) reported a model very similar to Nguyen *et al.* (2001) for solving the pig dynamics in natural gas and liquid pipelines. Their approach for the flow equations is like the one of Nguyen *et al.* (2001) for the gas, whereas for the liquid the energy equation is neglected, and both the gas and liquid flow models are solved using the MOC. The pig model also has no bypass, and its momentum equation is also solved with a Runge-Kuta scheme. They set either mass or pressure as a boundary condition at the inlet and at the outlet pressure, whereas at the pig the fluid velocity is set to be equal to the fluid velocity.

Hosseinalipor *et al.* (2007) (a) proposed a model similar to Nieckele *et al.* (2001) with continuity and momentum equations for the flow, and the bypass flow for the pig. They also used a moving grid but in a different fashion as Nieckele *et al.* (2001), by interpolating the obtained values at each time step in a grid that it is not refined as it gets closer to the pig. They also studied the cases with protruding flanges, and other cases such as the passage of a pig in a line with a branch and comparison of their model using real and ideal gas closures.

Tolamasquim and Nieckele (2008) proposed a PID controller method to assist and control pigging operations maintaining pig velocity and pipeline pressures under a desirable operational range. This work uses pigging simulations in the fashion of Nieckele *et al.* (2001) to test their proposed PID controller.

Patricio *et al.* (2016) (a) and (b) proposed a model for single-phase pigging where the pig is a singular surface moving through a fixed mesh. Their work uses continuity and momentum conservation principles for the flow, and the continuity in the bypass flow and momentum for the pig control volume. To solve the flow, the authors use a full explicit approach to solving the system of hyperbolic partial differential equations of the flow model with the Flux Corrected Transport method (FCT). The coupling between the pig and fluid flow is done similarly to Nieckele *et al.* (2001) using moving boundary conditions that are found through the solution of the pig model at each time step. Later, Patricio *et al.* (2020) tested their modeling for different situations under the gas or liquid flow, where the influence of bypass holes is considered, and the simulation of closure of valves in the pipe bringing the pig into a complete stop is tested. The model seems to be

the most up-to-date one, being able to estimate mechanical and hydrodynamical friction terms as well as a bypass between the pig and the pipe wall, through bypass holes in the pig body and through a porous material.

Li *et al.* (2021) presented a Lagrangian-Eulerian approach for solving the single-phase flow, coupled with a pig model with the force balance equation and a bypass flow estimated through a local pressure loss equation with a combined discharge coefficient. Their numerical results presented good agreement when compared to experimental data.

In the work of Minami and Shoham (1995), the authors proposed a pigging model for two-phase flow. The model considers a mixed Eulerian-Lagrangian approach by dividing the pipe into three regions. The downstream and upstream regions are treated with an Eulerian pseudo-steady-state approach, whereas the liquid slug control volume is treated with a Lagrangian approach. The models are solved numerically and compared with experimental results for cases where a single pig is passing through the pipe as well as cases where multiple pigs are in operation. In a similar fashion, Housseinalipour *et al.* (2007) (b) proposed a model for two-phase pigging as well, extending it to different flow patterns such as annular, bubbly, and slug flow. In both works, the numerical results obtained have small divergences from the experimental results. This can be related to the fact that the gas slippage through the pig is not considered.

Lima and Yeung (1999) proposed a model where the two-phase flow equations are treated differently for each approach, the continuity equations are treated in a transient way, whereas the momentum equations are treated as in equilibrium, composing a pseudo-steady-state model. In addition, the flow governing equations are treated separately depending on the flow pattern. The flow models are solved using semi-implicitly through Newton's method, and the pigging model is very similar to Minami and Shoham (1995). The authors stress their model for different flow patterns and pipe inclinations showing good agreement against experimental data.

Xiao-Xuan Xu and Gong (2005) proposed an approach very similar to Minami and Shoham (1995) for two-phase pigging and compared their results with the commercial software OLGA (Dynamic Multiphase Flow Simulator from Schlumberger). Also, Jamshidi and Sarkari (2016) tested a similar model in different application scenarios. The results are compared the results with OLGA presenting good agreement.

Patricio *et al.* (2018) proposed a more complete model using a full transient two-fluid model to solve the two-phase flow, coupled with a two-phase version of their pig model.

In this work, the authors tested how the pig affects a two-phase flow under a specific local leakage in the pipeline.

Other works solve the pig motion using two or three-dimensional approaches. These approaches differ from the one-dimensional in terms of the capability of simulating real cases with long pipelines. However, the results are interesting and serve as a reference to visualize the dynamics between the pigs and the fluid flow. For single-phase cases, Mirshamsi and Rafeeyan (2015) can be cited, and for two-phase cases Chen *et al.* (2020), Hu and Tao (2022), and Shengtao *et al.* (2022).

2.3.2 Plunger Modeling

Foss and Gaul (1965) provided through a Lagrangian approach, a model for estimating the casing pressure required to lift a conventional plunger with a constant velocity as it drags the liquid column with it during an upstroke. Through Newton's second law, they estimate the casing pressure required to keep the plunger traveling at a constant velocity of 5.08 m/s. This approach is highly simplified as the plunger velocity is expected to change during an upstroke and the acceleration effect is neglected.

Lea (1982) modeled the dynamics of a plunger upstroke through the force balance on a control volume that encapsulates both the plunger and the liquid slug that stands on top of it. The model extends from Foss and Gaul (1965) by being able to capture the velocity variation during an upstroke. Also, the methodology models the gas expansion behind the plunger through the real gas hypothesis and considers the friction effects of the gas moving ahead of the liquid body. Later, Marcano and Chacin (1994) extended Lea's (1982) model by adding liquid loss during the plunger upstroke. The liquid loss rate is introduced via an empirical formulation obtained from Mower's *et al*. (1985) data that correlates the liquid fallback from the plunger as linearly proportional to the plunger velocity.

In later work, Gasbarri and Wiggins (2001) improved Lea's (1982) model with the addition of a transient gas section above the control volume and gas quasi-steady-state conditions behind it. They also improved on the modeling by considering the inflow of gas and liquid from the casing to the tubing affecting the bottom-hole pressure. However, their models do not consider the effects of gas slippage and liquid falling back through the plunger.

In all previously referenced modeling works, the velocity of both the plunger and the liquid column being carried are assumed to be equal or nearly equal. Through experimental observations, Akhiiardinov *et al.* (2020) verified that for conventional operations the liquid slug and the plunger travel with different velocities during an upstroke. This happens because, with the gas slippage, there is an onset of a Taylor bubble between the plunger and the liquid slug, rather than all the gas entraining through the liquid column. The authors, then, provided separate equations for the motion of the liquid slug body and the plunger, that are validated by their experimental data. In their experiments, a logging plunger with a built-in accelerometer and pressure sensor is used. Moreover, they have proximity sensors along with pressure transducers along with their experimental facility, enabling them to use their experimental data as input in the model while validating the results through the logging piston data.

All models reported here are general and do not consider different types of plungers. It is expected that for different plunger types, different dynamics will occur. Akhiiardinov (2020) performed an extensive experimental campaign using different types of plungers under different types of conditions and verified that changing a plunger can affect the liquid fallback and gas slippage through the plunger, affecting the overall dynamics. The author also provided closure relations for the liquid fallback for different plungers on a 2-in diameter tubbing.

All the modeling work mentioned here would be more robust with closures for liquid fallback and gas slippage, however, there is a lack of closures in the literature for that. To design better closures, a modeling of the flow under the gap between the plunger and the pipe is desired. Also, a cohesive model for the flow under the gap was not found in the literature.

3 Single Phase Flow Model

This chapter presents the set of equations used to simulate single-phase flow in pipelines. From the perspective of a low hydraulic diameter to pipe length ratio, numerically solving the full set of three-dimensional Navier-Stokes equations becomes unfeasible. Averaging the flow governing equations to obtain a set of one-dimensional equations gives a more practicable system to solve numerically. The hypotheses considered for the formulation presented in this chapter are:

- Axial molecular and turbulent diffusive viscous effects are neglected;
- Constant viscosity;
- Compressible flow;
- Isothermal Flow;
- Constant cross-sectional area.

As stated above, the flow is considered isothermal, which means that the energy equation is neglected. In the formulation used, the flow is compressible, nevertheless, an approximation to compressible flow can be obtained with the following equation of state,

$$p = c^2(\rho - \rho_0), \tag{3.1}$$

where p and ρ are respectively the pressure and density of the fluid, c is the speed of sound in the medium, and ρ_0 is the reference density of the fluid. The ideal gas equation can be returned from the equation of state, Eq. (3.1), by doing $\rho_0 = 0$ and $c = \sqrt{RT}$, where R is the universal gas constant and T is the fluid temperature.

3.1 Set of Governing Equations

Averaging the set of three-dimensional Navier-Stokes equations with the previously stated hypotheses returns the one-dimensional Euler equations for compressible flow. To model the frictional losses, a source term is included in the momentum equation. The governing equations of mass and momentum conservations are given in a conservative form as follows

$$\frac{\partial(\rho)}{\partial t} + \frac{\partial(\rho u)}{\partial x} = 0, \tag{3.2}$$

$$\frac{\partial(\rho u)}{\partial t} + \frac{\partial(\rho u^2 + p)}{\partial x} = B_f + T_w, \tag{3.3}$$

where x is the space coordinate along the pipe, t is the time, and u is the velocity of the fluid. The source terms B_f and T_w represent the body force and the friction force between the fluid and the pipe wall, respectively. These terms can be written as

$$B_f = -\rho g \sin\theta, \tag{3.4}$$

$$T_w = -\frac{1}{2}\frac{S}{A} f \rho u |u|, \tag{3.5}$$

where g is the local gravitational acceleration, θ is the pipe inclination angle with the horizontal plane, S is the pipe internal perimeter, and A is the pipe internal cross-sectional area. The friction factor f is given by Moody (1947)

$$f = \max\left(\frac{16}{Re}; 0.001375\left[1 + \left[2\text{x}10^4 \frac{\varepsilon}{d} + \frac{10^6}{Re}\right]^{\frac{1}{3}}\right]\right), \tag{3.6}$$

$$Re = \frac{\rho |u| d}{\mu}. \tag{3.7}$$

In the previous equations, Re is the dimensionless Reynolds number, μ the fluid dynamic viscosity, ε the pipe wall roughness, and d the pipe diameter. The correlation given by Eq.(3.6) automatically returns the friction factor for the regime the flow is under. The first argument of the maximum function returns the friction factor for laminar flow, while the second argument returns the value of f for turbulent flow.

The set of governing equations, Eqs. (3.2) and (3.3), can be written in the following conservative canonical form,

$$\frac{\partial \mathbf{q}}{\partial t} + \frac{\partial \mathbf{f}(\mathbf{q})}{\partial x} = \mathbf{s}(\mathbf{q}), \tag{3.8}$$

where the conservative vector $\mathbf{q}$, flux vector $\mathbf{f}$, and source vector $\mathbf{s}$ are respectively given by,

$$\mathbf{q} = \begin{bmatrix} q_1 \\ q_2 \end{bmatrix} = \begin{bmatrix} \rho \\ \rho u \end{bmatrix}, \tag{3.9}$$

$$\mathbf{f}(\mathbf{q}) = \begin{bmatrix} f_1 \\ f_2 \end{bmatrix} = \begin{bmatrix} \rho u \\ \rho u^2 + p \end{bmatrix} = \begin{bmatrix} q_2 \\ \frac{q_2^2}{q_1} + c^2(q_1 - \rho_0) \end{bmatrix}, \tag{3.10}$$

$$\mathbf{s}(\mathbf{q}) = \begin{bmatrix} s_1 \\ s_2 \end{bmatrix} = \begin{bmatrix} 0 \\ B_f + T_w \end{bmatrix}. \tag{3.11}$$

3.2 Hyperbolicity Analysis

The hyperbolicity analysis of the mathematical flow models is of great importance since these models are in general composed of non-linear hyperbolic partial differential equations. A combination of parameters may lead the system to lose hyperbolicity making it ill-posed. The undesired ill-posedness of the model may render unstable numerical outputs that can lead to convergence failure. Moreover, the model may present multiple solutions or no solutions at all, losing its physical meaning, and, thus, invalidating a possible numerical solution. Even though the Euler equations for compressible flow are well known for being unconditionally hyperbolic, the hyperbolicity analysis is made necessary here, since some of the resulting entities of the analysis are of paramount importance to many of the numerical methods used to solve the system.

First, the system is written in a quasi-linear form,

$$\frac{\partial \mathbf{q}}{\partial t} + \mathbf{A}(\mathbf{q}) \frac{\partial \mathbf{q}}{\partial x} = \mathbf{s}(\mathbf{q}), \tag{3.12}$$

where the coefficient matrix $\mathbf{A}$ is the Jacobian obtained by,

$$\mathbf{A} = \frac{d\mathbf{f}}{d\mathbf{q}} = \begin{bmatrix} \frac{df_1}{dq_1} & \frac{df_1}{dq_2} \\ \frac{df_2}{dq_1} & \frac{df_2}{dq_2} \end{bmatrix}. \tag{3.13}$$

Therefore,

$$\mathbf{A} = \begin{bmatrix} 0 & 1 \\ -\left(\frac{q_2}{q_1}\right)^2 + c^2 & 2\frac{q_2}{q_1} \end{bmatrix} = \begin{bmatrix} 0 & 1 \\ c^2 - u^2 & 2u \end{bmatrix}. \tag{3.14}$$

The vector $\boldsymbol{\lambda}$ composed of the eigenvalues of the system is verified by performing the solution of the characteristic polynomial obtained by, $\det(\mathbf{A} - \lambda\mathbf{I}) = 0$. Therefore,

$$\boldsymbol{\lambda} = \begin{bmatrix} \lambda_1 \\ \lambda_2 \end{bmatrix} = \begin{bmatrix} u - c \\ u + c \end{bmatrix}. \tag{3.15}$$

The respective right eigenvectors $\mathbf{r}$ are,

$$\mathbf{r_1} = \begin{bmatrix} 1 \\ \lambda_1 \end{bmatrix} = \begin{bmatrix} 1 \\ u - c \end{bmatrix}, \qquad \mathbf{r_2} = \begin{bmatrix} 1 \\ \lambda_2 \end{bmatrix} = \begin{bmatrix} 1 \\ u + c \end{bmatrix}, \tag{3.16}$$

hence the matrix $\mathbf{R}$ composed by the right eigenvectors as columns,

$$\mathbf{R} = \begin{bmatrix} 1 & 1 \\ \lambda_1 & \lambda_2 \end{bmatrix} = \begin{bmatrix} 1 & 1 \\ u - c & u + c \end{bmatrix}. \tag{3.17}$$

For the given system to be hyperbolic the Jacobian matrix $\mathbf{A}$ must be diagonalizable and have real eigenvalues, hence the eigenvectors must be linearly independent. Since the eigenvalues of the system are real and the eigenvectors are linearly independent, the Euler equations for isothermal compressible flow are hyperbolic.

The physical meaning behind the eigenvalues and eigenvectors is that they provide information about the elementary waves of the associate problem, formally known as the Riemann problem. The eigenvalues are the characteristic wave velocities, while the eigenvectors are the characteristic fields. Each set of eigenvalues and its respective eigenvector correlate to a particular elementary wave, such as contact, shock, and rarefaction waves. For the one-dimensional isothermal set of Euler fluid flow equations, the eigenvalue λ_1 and its eigenvector $\mathbf{r_1}$ are the characteristic velocity and field associated with the rarefaction wave, whereas the λ_2, and $\mathbf{r_2}$ with the shock wave. To give a visual perspective, the schematic in Fig. 3.1 is the structure of the Riemann problem in the (x, t) plane for the one-dimensional isothermal set of Euler fluid flow equations, where initially

there is a discontinuity between the left state $\mathbf{q}_{Left}$ and the right state $\mathbf{q}_{Right}$. The characteristic waves will propagate with time giving rise to an intermediary state $\mathbf{q}^*$, that is the solution in the domain between the two waves.

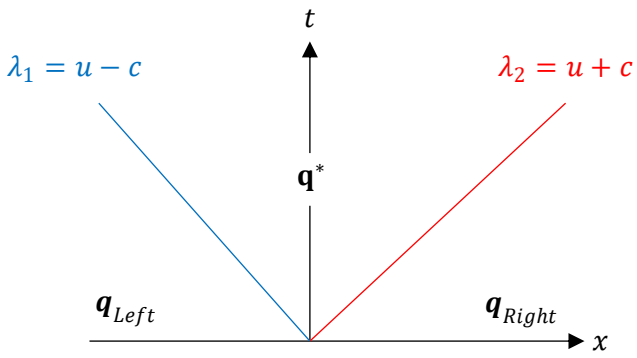

Figure 3.1: Structure of the Riemann problem for the one-dimensional isothermal set of Euler fluid flow equations.

4 Two-Fluid Models

This chapter will present two transient two-fluid models selected to represent the physics of two-phase flow in pipes. Both mathematical models are one-dimensional two-fluid models having separate governing equations for each phase. This means that for a gas-liquid flow, two continuity equations, two momentum equations, and two energy equations. This configuration composes a system of six non-linear partial differential equations and it is conditionally hyperbolic. Unconditionally hyperbolicity is a wanted characteristic for the mathematical model in question knowing that if the model loses hyperbolicity it will render in an ill-posed problem.

The models used in this work are the conditionally hyperbolic single-pressure four-equation model, 4E1P, and the unconditionally hyperbolic two-pressure five-equation model, 5E2P. They are derived from the averaging the Navier-Stokes equations, Ishii and Hibiki (2003), Drew and Passman (1999) for both fluids separately, with the following assumptions:

- Axial Molecular and turbulent diffusive viscous effects are neglected;
- No mass transfer between phases;
- No chemical reaction between phases;
- Constant viscosities;
- Isothermal Flow;
- Constant cross-sectional area.

4.1 4E1P Model

The 4E1P model is the isothermal version of the 6E1P model, with the energy equations being neglected. This version of the two-fluid model is widely used in the literature for solving gas-liquid two-phase flow in pipes. The gas phase is considered compressible, whereas the liquid phase is incompressible. The 4E1P is composed of the following governing equations representing the principles of mass conservation, Eq. (4.1-4.2), and momentum conservation, Eq. (4.3 - 4.4), where the subscript k is utilized to denote the phase to which the physical quantity belongs, $k \in (G, L)$ where G stands for the gas phase and L for the liquid phase.

$$\frac{\partial}{\partial t}(\alpha_G \rho_G) + \frac{\partial}{\partial x}(\alpha_G \rho_G u_G) = 0, \tag{4.1}$$

$$\frac{\partial}{\partial t}(\alpha_L \rho_L) + \frac{\partial}{\partial x}(\alpha_L \rho_L u_L) = 0, \tag{4.2}$$

$$\frac{\partial(\alpha_G \rho_G u_G)}{\partial t} + \frac{\partial(\alpha_G \rho_G u_G^2)}{\partial x} + \alpha_G \frac{\partial p}{\partial x} + \Delta p_{I,G} \frac{\partial \alpha_G}{\partial x} = B_{fG} + T_I + T_{wG}, \tag{4.3}$$

$$\frac{\partial(\alpha_L \rho_L u_L)}{\partial t} + \frac{\partial(\alpha_L \rho_L u_L^2)}{\partial x} + \alpha_L \frac{\partial p}{\partial x} + \Delta p_{I,L} \frac{\partial \alpha_L}{\partial x} = B_{fL} - T_I + T_{wL}. \tag{4.4}$$

As the model name suggests, both phases share the same pressure, p. The symbol α_k represents the phase volume fraction, and the term $\Delta p_{I,k}$ is called the pressure correction term, which represents the difference between the fluids pressure p, and the phase interfacial pressure $p_{I,k}$. The source terms are denoted by B_{fk}, T_I and T_{kw} that represent the body forces, the interfacial friction, and the wall friction respectively. The source terms as well as the interfacial terms, described in the next sections, are a function of the flow parameters, the pipe geometry, and constants relative to the fluids and pipe material. This model of four PDEs has then a set of eight dependent variables α_G, α_L, u_G, u_L, ρ_G, p, $p_{I,G}$, and $p_{I,L}$, making the need for four additional closure equations for the model. The closures are the relationship between the volume fractions,

$$\alpha_G + \alpha_L = 1, \tag{4.5}$$

the equations of state for the and gas phase,

$$p_k = c_k^2(\rho_k - \rho_{k,0}), \tag{4.6}$$

where the reference density, $\rho_{k,0}$, and the speed of sound, c_k, are specific constants of each fluid for a given thermodynamic state with a constant temperature. For the 4E1P model, Eq. (4.6) is only implemented for the gas phase, whereas the liquid phase has a density ρ_k constant. However, it is made necessary that this equation is written in its

complete form, in terms of the non-determined phase k, due to its applicability to the liquid phase in other models of the current work.

The last two closures required are for the interfacial pressures, the chosen model is the one developed by Bestion (1990). The author writes the pressure correction term according to the following relation

$$\Delta p_{I,k} \equiv p_k - p_{I,k} = \varphi \frac{\alpha_G \alpha_L \rho_G \rho_L}{\alpha_G \rho_L + \alpha_L \rho_G} (u_G - u_L)^2, \tag{4.7}$$

where φ is a dimensionless parameter. Evje and Flätten (2003) suggest using the value of $\varphi = 1.2$. This model is widely used in the literature because of its mathematical feature of producing a wide range of primitive variables that grants the 4E1P hyperbolicity. In contrast, the model is not explained from the physical point of view since it was proposed only with this mathematical focus. It is quite remarkable though that the inclusion of this term does not seem to impact negatively the representativeness of the simulations of stratified, slug, and large amplitude waves flow patterns in nearly horizontal two-phase flow in pipes, based on results from Munkejord (2010), Freitas (2017), Ansari and Daramizadeh (2012), and Ferrari *et al.* (2017).

Unfortunately, the system of governing equations, Eqs. (4.1 - 4.4) cannot be rewritten in the conservative canonical form given by Eq. (3.8). Trying to rearrange the equations to a conservative form will give rise to a non-conservative term. Then, the set of governing equations can be rewritten in the following canonical form,

$$\frac{\partial \mathbf{q}}{\partial t} + \frac{\partial \mathbf{f}(\mathbf{q})}{\partial x} = \mathbf{H}(\mathbf{q}) \frac{\partial \mathbf{n}(\mathbf{q})}{\partial x} + \mathbf{s}(\mathbf{q}), \tag{4.8}$$

with the conservative vector **q**, flux vector **f**, the non-conservative matrix **H**, non-conservative vector **n**, and source vector **s**, given respectively by,

$$\mathbf{q} = \begin{bmatrix} q_1 \\ q_2 \\ q_3 \\ q_4 \end{bmatrix} = \begin{bmatrix} \alpha_G \rho_G \\ \alpha_L \rho_L \\ \alpha_G \rho_G u_G \\ \alpha_L \rho_L u_L \end{bmatrix}, \tag{4.9}$$

$$\mathbf{f}(\mathbf{q}) = \begin{bmatrix} \alpha_G \rho_G u_G \\ \alpha_L \rho_L u_L \\ \alpha_G \rho_G u_G^2 + \alpha_G \Delta p_{I,G} \\ \alpha_L \rho_L u_L^2 + \alpha_L \Delta p_{I,L} \end{bmatrix}, \tag{4.10}$$

$$\mathbf{H}(\mathbf{q}) = \begin{bmatrix} 0 & 0 & 0 & 0 \\ 0 & 0 & 0 & 0 \\ 0 & 0 & \alpha_G & 0 \\ 0 & 0 & 0 & \alpha_L \end{bmatrix}, \mathbf{n}(\mathbf{q}) = \begin{bmatrix} 0 \\ 0 \\ (\Delta p_{I,G} - p) \\ (\Delta p_{I,L} - p) \end{bmatrix}, \tag{4.11}$$

$$\mathbf{s}(\mathbf{q}) = \begin{bmatrix} 0 \\ 0 \\ B_{fG} + T_I + T_{Gw} \\ B_{fL} - T_I + T_{Lw} \end{bmatrix}. \tag{4.12}$$

It is important to mention that a wide range of numerical schemes for solving hyperbolic systems of PDEs is written to solve the system equations in the conservative form. Since writing in this form for the 4E1P, and the following 5E2P is not possible, a separate scheme is necessary to discretize the non-conservative terms of the models.

4.1.1 Hyperbolicity Analysis (4E1P)

To evaluate the characteristic waves of the system, the system is first written in quasi-linear form,

$$\frac{\partial \mathbf{q}}{\partial t} + \mathbf{A}(\mathbf{q}) \frac{\partial \mathbf{q}}{\partial x} = \mathbf{s}(\mathbf{q}). \tag{4.13}$$

Since the canonical form, Eq. (4.8), for the 4E1P has a non-conservative term, the coefficient matrix **A** can not only be defined by the Jacobian $d\mathbf{f}/d\mathbf{q}$. It is inefficient to derive the coefficient matrix from the canonical form expressed by Eq. (4.8). However, if the system is rewritten in terms of the primitive variables, it becomes straightforward. Defining the primitive variables vector as

$$\mathbf{w}(\mathbf{q}) = [\alpha_G, p, u_G, u_L]^T, \tag{4.14}$$

the system is then rewritten as,

$$\mathbf{C}(\mathbf{w})\frac{\partial \mathbf{w}}{\partial t} + \mathbf{D}(\mathbf{w})\frac{\partial \mathbf{w}}{\partial x} = \mathbf{s}_{\mathbf{w}}^{*}(\mathbf{w}). \tag{4.15}$$

For sake of generality, the continuity and momentum equations are rearranged, in terms of the primitive variables, using separate pressures. Using the state equation, Eq. (4.6), it can be defined that,

$$\frac{\partial \rho_k}{\partial p_k} = \frac{1}{c_k^2}, \tag{4.16}$$

Then the continuity equation in terms of the primitive variables is given by,

$$\rho_k \frac{\partial \alpha_k}{\partial t} + \alpha_k \frac{1}{c_k^2}\frac{\partial p_k}{\partial t} + \rho_k u_k \frac{\partial \alpha_k}{\partial x} + \alpha_k u_k \frac{1}{c_k^2}\frac{\partial p_k}{\partial x} + \alpha_k \rho_k \frac{\partial u_k}{\partial x} = 0, \tag{4.17}$$

while the momentum equation is,

$$\alpha_k \rho_k \frac{\partial u_k}{\partial t} + \Delta p_{I,k} \frac{\partial \alpha_k}{\partial x} + \alpha_k \frac{\partial p_k}{\partial x} + \alpha_k \rho_k u_k \frac{\partial u_k}{\partial x} = B_{fk} \pm T_I + T_{wk}. \tag{4.18}$$

Since the single-pressure model assumes constant liquid density, $\partial \rho_L / \partial p_L = 0$, and that $p = p_G = p_L$. The matrices $\mathbf{C}$ and $\mathbf{D}$ are obtained as follows,

$$\mathbf{C} = \begin{bmatrix} \rho_G & \alpha_G/c_G^2 & 0 & 0 \\ -\rho_L & 0 & 0 & 0 \\ 0 & 0 & \alpha_G \rho_G & 0 \\ 0 & 0 & 0 & \alpha_L \rho_L \end{bmatrix}, \tag{4.19}$$

$$\mathbf{D} = \begin{bmatrix} \rho_G u_G & \alpha_G u_G/c_G^2 & \alpha_G \rho_G & 0 \\ -\rho_L u_L & 0 & 0 & \alpha_L \rho_L \\ \Delta p_{I,G} & \alpha_G & \alpha_G \rho_G u_G & 0 \\ -\Delta p_{I,\mathrm{L}} & \alpha_L & 0 & \alpha_L \rho_L u_L \end{bmatrix}, \tag{4.20}$$

Then the quasi-linear system in terms of primitive variables,

$$\frac{\partial \mathbf{w}}{\partial t} + \mathbf{B}(\mathbf{w})\frac{\partial \mathbf{w}}{\partial x} = \mathbf{s_w}(\mathbf{w}), \tag{4.21}$$

can be obtained by calculating,

$$\mathbf{B} = \mathbf{C^{-1}D}, \tag{4.22}$$

and,

$$\mathbf{s_w} = \mathbf{C^{-1}s_w^*}. \tag{4.23}$$

Therefore,

$$\mathbf{B} = \begin{bmatrix} u_L & 0 & 0 & -\alpha_L \\ \frac{\rho_G}{\alpha_G} c_G^2 (u_G - u_L) & u_G & c_G^2 \rho_G & \frac{\alpha_L}{\alpha_G}\rho_G c_G^2 \\ \frac{\Delta p_{I,G}}{\alpha_G \rho_G} & \frac{1}{\rho_G} & u_G & 0 \\ \frac{-\Delta p_{I,\mathrm{L}}}{\alpha_L \rho_L} & \frac{1}{\rho_L} & 0 & u_L \end{bmatrix}. \tag{4.24}$$

To return the system from primitive variables back to conservative variables first the transformation matrix **J** is defined as,

$$\mathbf{J} \equiv \frac{\partial \mathbf{q}}{\partial \mathbf{w}}, \qquad and \qquad \mathbf{J^{-1}} \equiv \frac{\partial \mathbf{w}}{\partial \mathbf{q}}. \tag{4.25}$$

That computes,

$$\mathbf{J} = \begin{bmatrix} \rho_g & 0 & 0 & -\alpha_L \\ -\rho_L & u_G & \rho_G c_G^2 & \frac{\alpha_L}{\alpha_G}\rho_G c_G^2 \\ \rho_G \alpha_G & \frac{1}{\rho_G} & u_G & 0 \\ \frac{-\Delta p_{I,\mathrm{L}}}{\alpha_L \rho_L} & \frac{1}{\rho_L} & 0 & u_L \end{bmatrix}. \tag{4.26}$$

One can then use the chain rule on Eq.(4.21) and get,

$$\frac{\partial \mathbf{w}}{\partial \mathbf{q}}\frac{\partial \mathbf{q}}{\partial t} + \mathbf{B}(\mathbf{w})\frac{\partial \mathbf{w}}{\partial \mathbf{q}}\frac{\partial \mathbf{q}}{\partial x} = \mathbf{s}_{\mathbf{w}}(\mathbf{w}), \tag{4.27}$$

thus,

$$\mathbf{J}^{-1}\frac{\partial \mathbf{q}}{\partial t} + \mathbf{B}(\mathbf{w})\,\mathbf{J}^{-1}\frac{\partial \mathbf{q}}{\partial x} = \mathbf{s}_{\mathbf{w}}(\mathbf{w}). \tag{4.28}$$

Finally, it can be inferred that,

$$\mathbf{A} = \mathbf{J}\mathbf{B}\mathbf{J}^{-1}, \tag{4.29}$$

and the original source vector, written in terms of conservative variables is returned,

$$\mathbf{s} = \mathbf{J}\mathbf{s}_{\mathbf{w}}. \tag{4.30}$$

Returning the coefficient matrix,

$$\mathbf{A} = \begin{bmatrix} 0 & 0 & 1 & 0 \\ 0 & 0 & 0 & 1 \\ c_G^2 - u_G^2 & \dfrac{\rho_G c_G^2 - \Delta p_{I,\mathrm{G}}}{\rho_L} & 2u_G & 0 \\ \dfrac{\alpha_L}{\alpha_G}c_G^2 & \dfrac{\alpha_G \Delta p_{I,\mathrm{L}} + \alpha_L \rho_G c_G^2}{\alpha_G \rho_L} & 0 & 2u_L \end{bmatrix}. \tag{4.31}$$

With the coefficient matrix, the following characteristic polynomial is obtained by computing $\det(\mathbf{A} - \lambda\mathbf{I})$,

$$\begin{aligned} P_{4E1P} = \frac{1}{\alpha_G \rho_L}\big[&\alpha_L c_G^2\big(\Delta p_{I,G} - \rho_G(u_G - \lambda)^2\big) \\ &+ \alpha_G(c_G^2 - (u_G - \lambda)^2)\big(\Delta p_{I,L} - \rho_L(u_L - \lambda)^2\big)\big], \end{aligned} \tag{4.32}$$

Even though it is desirable to obtain an analytical solution for the roots of the polynomial in Eq. (4.32), it is unfeasible. Then, the characteristic velocities and the subsequent eigenvectors are obtained numerically. Even with the interfacial pressure, Eq.

(4.7), proposed by Bestion (1990) being formulated to expand the intervals where the 4E1P model is hyperbolic, it does not guarantee that real eigenvalues or linearly independent eigenvectors are obtained, thus the model is conditionally hyperbolic.

It is important to note that at the limit where the gas volume fraction vanishes, $\alpha_G \rightarrow 0$, a singularity appears in the characteristic polynomial turning the solution for its roots inviable.

At the limit when the liquid volume fraction vanishes, $\alpha_L \rightarrow 0$, then the four characteristic velocities can be obtained analytically, $\lambda_1 = \lambda_2 \rightarrow u_L$, $\lambda_3 \rightarrow (u_G - c_G)$, $\lambda_4 \rightarrow (u_G + c_G)$. In that condition there are two equal eigenvalues, that will render the same eigenvectors that evidently are linearly dependent, thus the hyperbolicity of the model cannot be guaranteed.

Another parameter linked to the hyperbolicity of the 4E1P model is the interfacial pressure differences $\Delta p_{I,G}$ and $\Delta p_{I,L}$. If these values are null, the system will lose hyperbolicity, even when they are small enough, the system may lose hyperbolicity. (Ramshaw and Trapp, 1978; Munkejord, 2006). Hence, the importance of the Bestion (1990) correlation that in an overwhelming number of cases gives higher enough values for these parameters to keep the hyperbolicity without hurting the physical representation of the model.

4.2 5E2P Model

The 7E2P two-fluid model presented by Saurel and Abgrall (1999), which is a variant of the one introduced by Baer and Nunziato (1986), achieves unconditionally hyperbolicity by adding an extra equation for the evolution of the volume fraction, composing a system of seven non-linear PDEs. For the present work, the assumption of isothermal flow is utilized along with the model of Saurel and Abgrall (1999), reducing the model to five PDEs, Eqs. (4.33) to (4.37), denominated here as a five-equation two-pressure model, 5E2P. It is important to point out that this simplification does not impact the unconditionally hyperbolic characteristic of the model, as can be seen in the following sections.

The equations for the 5E2P model are given by,

$$\frac{\partial}{\partial t}(\alpha_G) + u_I \frac{\partial}{\partial x}(\alpha_G) = r_P(p_G - p_L), \tag{4.33}$$

$$\frac{\partial}{\partial t}(\rho_G \alpha_G) + \frac{\partial}{\partial x}(\rho_G \alpha_G u_G) = 0, \tag{4.34}$$

$$\frac{\partial}{\partial t}(\rho_L \alpha_L) + \frac{\partial}{\partial x}(\rho_L \alpha_L u_L) = 0, \tag{4.35}$$

$$\frac{\partial(\rho_G \alpha_G u_G)}{\partial t} + \frac{\partial(\rho_G \alpha_G u_G^2)}{\partial x} - \alpha_G \frac{\partial p_G}{\partial x} + \Delta p_{I,G} \frac{\partial \alpha_G}{\partial x} = B_{fG} + T_I + T_{Gw}, \tag{4.36}$$

$$\frac{\partial(\rho_L \alpha_L u_L)}{\partial t} + \frac{\partial(\rho_L \alpha_L u_L^2)}{\partial x} - \alpha_L \frac{\partial p_L}{\partial x} + \Delta p_{I,L} \frac{\partial \alpha_L}{\partial x} = B_{fL} - T_I + T_{Lw}. \tag{4.37}$$

Similar to the 4E1P model, Eqs. (4.34) and (4.35) are the continuity equations and Eqs. (4.36) and (4.37) are the momentum conservation equations, rewritten with separate pressures p_k for each phase. Equation (4.33) represents a transport equation for the volume fraction, where the volume fraction is advected with the interfacial velocity u_I. The term r_p is the pressure relaxation coefficient, which is typically a constant value. This model of five PDEs has then a set of eleven dependent variables u_I, α_G, α_L, u_G, u_L, ρ_G, ρ_L, p_G, p_L, $p_{I,G}$, and $p_{I,L}$, making the need for six additional closure equations for the model. The closures are the same used for the 4E1P, Eqs. (4.5), (4.6), and (4.7), with the addition of an equation for the interfacial velocity.

The model for the interfacial velocity chosen in this work is the one presented by Saurel and Abgrall (1999). This model was chosen for having a physical interpretation that encompasses all flow patterns in two-phase flow inside a duct. This model predicts the interfacial velocity by estimating the local center of a mass composed of both phases. According to the authors, this model corresponds to the speed where all systems that are not in equilibrium will relax. The mass-weighted interfacial velocity is given by,

$$u_I = \frac{\Sigma \alpha_k \rho_k u_k}{\Sigma \alpha_k \rho_k}. \tag{4.38}$$

The set of governing can then be rewritten in the canonical form given by Eq. (4.8) with,

$$\mathbf{q} = \begin{bmatrix} \alpha_G \\ \alpha_G \rho_G \\ \alpha_L \rho_L \\ \alpha_G \rho_G u_G \\ \alpha_L \rho_L u_L \end{bmatrix}, \tag{4.39}$$

$$\mathbf{f}(\mathbf{q}) = \begin{bmatrix} 0 \\ \alpha_G \rho_G u_G \\ \alpha_L \rho_L u_L \\ \alpha_G \rho_G u_G^2 + \alpha_G \Delta p_{IG} \\ \alpha_L \rho_L \alpha_L + \alpha_L \Delta p_{IL} \end{bmatrix}, \tag{4.40}$$

$$\mathbf{H}(\mathbf{q}) = \begin{bmatrix} u_I & 0 & 0 & 0 & 0 \\ 0 & 0 & 0 & 0 & 0 \\ 0 & 0 & 0 & 0 & 0 \\ 0 & 0 & 0 & \alpha_G & 0 \\ 0 & 0 & 0 & 0 & \alpha_L \end{bmatrix}, \mathbf{n}(\mathbf{q}) = \begin{bmatrix} -\alpha_G \\ 0 \\ 0 \\ (\Delta p_{IG} - p_G) \\ (\Delta p_{IL} - p_L) \end{bmatrix}, \tag{4.41}$$

$$\mathbf{s}(\mathbf{q}) = \begin{bmatrix} r_p(p_G - p_L) \\ 0 \\ 0 \\ B_{fG} + T_I + T_{Gw} \\ B_{fL} - T_I + T_{Lw} \end{bmatrix}. \tag{4.42}$$

4.2.1 Relaxation Procedure

When the phases have different pressures and velocities, due to the interaction on the interface, both fluids cannot retain this difference for long periods of time. The pressures are typically more sensitive to this relaxation effect and both pressures converge into an equilibrium pressure in a short period of time. That is the reason why single pressure is a common hypothesis in two-fluid models. As for the velocities, they relax with interfacial friction. For the solution of the 5E2P model, it is necessary to tackle the pressure relaxation and velocity relaxation source terms separately from the other source terms. That is, the source term related to the interfacial friction is modeled as a velocity relaxation term, such as

$$T_I = r_u(u_L - u_G), \tag{4.43}$$

where r_u is a velocity relaxation coefficient. The correct approach is to treat the relaxation effects separately using a fractional-step technique. Dividing the solution where, a priori,

the fractional step related to the hyperbolic system of equations is solved and then the pressure and velocity relaxation effects are treated next in the next fractional step. The relaxation terms r_u and r_p require some care in their determination. For the interfacial drag, there are some consolidated correlations in the literature, that may vary depending on the flow pattern. The higher the value of r_u, the faster the velocities relax, and if $r_u = 0$ both velocities will evolve independently, that is with no interfacial friction. Estimating the pressure relaxation coefficient is a more complex task since the time scale of the pressure relaxation effect is too small. The most common approach is to consider the pressure relaxation coefficient tending to infinity, $r_p \to 0$, thus making the pressure relaxation effect instantaneous. By using that hypothesis both pressures will converge to a common pressure instantly.

The procedure to solve the 5E2P model by the fractional-step technique is done by first solving the hyperbolic system of equations, that is, Eqs. (4.33) to (4.37), considering the relaxation source terms null, $r_u = 0$ and $r_p = 0$, with a proper numerical method. The solution obtained in the previous hyperbolic step is then utilized as an initial value to solve the following system of ordinary differential equations that comprises the relaxation step, Eqs. (4.44) to (4.48).

$$\frac{\partial}{\partial t}(\alpha_G) = r_p(p_G - p_L), \tag{4.44}$$

$$\frac{\partial}{\partial t}(\alpha_G \rho_G) = 0, \tag{4.45}$$

$$\frac{\partial}{\partial t}(\alpha_L \rho_L) = 0, \tag{4.46}$$

$$\frac{\partial}{\partial t}(\alpha_G \rho_G u_G) = r_u(u_L - u_G), \tag{4.47}$$

$$\frac{\partial}{\partial t}(\alpha_L \rho_L u_L) = -r_u(u_L - u_G). \tag{4.48}$$

This system of ODE can be solved by a numerical scheme, such as Runge-Kutta schemes or Backward differentiation Formulas (BDFs), when the values of r_u and r_p are known. When instantaneous pressure or velocity relaxation is utilized, an analytical approach can be utilized to solve the ODE System as described in the next sections.

4.2.2 Instantaneous Pressure Relaxation

As stated before, estimating a value for the pressure relaxation coefficient is not a simple task. A complete model of non-equilibrium pressures between the phases should consider the effects of interfacial curvature and tension, dynamic effects as well as mass transfer between phases (Essama, 2004). The value for the pressure relaxation coefficient is usually unknown and, given the fact that the time scale for the pressures to converge to an equilibrium pressure is too small in subsonic flows, the value for the pressure relaxation coefficient must be relatively high. This fact makes the hypothesis of instantaneous pressure relaxation the most used in the literature. Another important fact is that this hypothesis simplifies the general numerical solution by handling the pressure relaxation step analytically. Saurel and Abgrall (1999) described a direct solution to the instantaneous pressure relaxation step for their seven-equation model that utilizes the primitive variables obtained in the hyperbolic step as an initial condition. Munkejord (2007), utilizing the same methodology, presented a similar solution for the 5E2P model, solving a second-degree equation for the volume fraction to make the pressures equal and maintain the products $\alpha_k\rho_k$ and $\alpha_k\rho_k u_k$ constants at the relaxation step. Later, Munkejord (2010) realized that it would be more robust to solve a second-degree equation for the pressure instead, again maintaining the products $\alpha_k\rho_k$ and $\alpha_k\rho_k u_k$ constants at the relaxation step. To obtain the second-degree equation the pressures must be equalized by using the equations of state, Eq. (4.6), as follows:

$$p = c_G^2\left(\rho_G - \rho_{G,0}\right) \equiv c_L^2\left(\rho_L - \rho_{L,0}\right). \tag{4.49}$$

The previous relation is squared and using the volume fraction relation described by Eq. (4.5) a simple mathematical manipulation gives rise to,

$$p^2 = c_G^2 c_L^2\left(\rho_G - \rho_{G,0}\right)\left(\rho_L - \rho_{L,0}\right)(\alpha_G + \alpha_L). \tag{4.50}$$

After more mathematical manipulations the following second-degree equation is obtained,

$$\psi_1 p^2 + \psi_2 p + \psi_3 = 0, \tag{4.51}$$

Where, $\psi_1 = 1, \quad \psi_2 = c_G^2(\rho_{G,0} - \alpha_G\rho_G) + c_L^2(\rho_{L,0} - \alpha_L\rho_L), \quad \psi_3 = c_G^2 c_L^2(\rho_{G,0}\rho_{L,0} - \alpha_G\rho_G\rho_{L,0} - \alpha_L\rho_L\rho_{L,0})$, in which the following positive solution is used,

$$p = \frac{-\psi_2 + \sqrt{\psi_2^2 - 4\psi_1\psi_3}}{2\psi_1}. \tag{4.52}$$

After obtaining the relaxed pressure the densities are corrected using the equation of state Eq. (4.6). The volume fractions are also corrected by making both products $\alpha_k\rho_k$ and $\alpha_k\rho_k u_k$ constant through time in relation to the hyperbolic step as to respect the principles of conservation.

4.2.3 Hyperbolicity Analysis (5E2P)

Following the same steps of section 4.1.1, it is obtained first the primitive variables vector, defined as,

$$\mathbf{w}(\mathbf{q}) = [\alpha_G, p_G, p_L, u_G, u_L]^T, \tag{4.53}$$

Using the continuity and momentum equations written in terms of primitive variables respectively Eq. (4.34) and Eq. (4.37), and the transport equation for the volume fraction, Eq. (4.33), the system is written in the form of Eq. (4.15), with

$$\mathbf{C} = \begin{bmatrix} 1 & 0 & 0 & 0 & 0 \\ \rho_G & \alpha_G/c_G^2 & 0 & 0 & 0 \\ -\rho_L & 0 & \alpha_L/c_L^2 & 0 & 0 \\ 0 & 0 & 0 & \alpha_G\rho_G & 0 \\ 0 & 0 & 0 & 0 & \alpha_L\rho_L \end{bmatrix}, \tag{4.54}$$

and,

$$\mathbf{D} = \begin{bmatrix} u_I & 0 & 0 & 0 & 0 \\ u_G\rho_G & \alpha_G u_G/c_G^2 & 0 & \alpha_G\rho_G & 0 \\ -u_L\rho_L & 0 & \alpha_L u_L/c_L^2 & 0 & \alpha_L\rho_L \\ \Delta p_{IG} & \alpha_G & 0 & \alpha_G\rho_G u_G & 0 \\ -\Delta p_{IL} & 0 & \alpha_L & 0 & \alpha_L\rho_L u_L \end{bmatrix}. \tag{4.55}$$

From Eq. (4.22) the matrix **B** for the quasi-linear form of Eq. (4.21) is obtained,

$$\mathbf{B} = \begin{bmatrix} u_I & 0 & 0 & 0 & 0 \\ \frac{\rho_G}{\alpha_G} c_G^2 (u_G - u_I) & u_G & 0 & \rho_G c_G^2 & 0 \\ -\frac{\rho_L}{\alpha_L} c_L^2 (u_L - u_I) & 0 & u_L & 0 & \rho_L c_L^2 \\ \frac{\Delta p_{I,G}}{\alpha_G \rho_G} & \frac{1}{\rho_G} & 0 & u_G & 0 \\ -\frac{\Delta p_{I,L}}{\alpha_L \rho_L} & 0 & \frac{1}{\rho_L} & 0 & u_L \end{bmatrix}. \tag{4.56}$$

While the transformation matrix **J** obtained by Eq. (4.25),

$$\mathbf{J} = \begin{bmatrix} 1 & 0 & 0 & 0 & 0 \\ \rho_G & \alpha_G / c_G^2 & 0 & 0 & 0 \\ -\rho_L & 0 & \alpha_L / c_L^2 & 0 & 0 \\ \rho_G u_G & \alpha_G u_G / c_G^2 & 0 & \alpha_G \rho_G & 0 \\ -\rho_L u_L & 0 & \alpha_L u_L / c_L^2 & 0 & \alpha_L \rho_L \end{bmatrix}. \tag{4.57}$$

Through Eq. (4.29) the coefficient matrix **A** is obtained,

$$\mathbf{A} = \begin{bmatrix} u_I & 0 & 0 & 0 & 0 \\ 0 & 0 & 0 & 1 & 0 \\ 0 & 0 & 0 & 0 & 1 \\ \Delta p_{I,G} - \rho_G c_G^2 & c_G^2 - u_G^2 & 0 & 2u_G & 0 \\ -\Delta p_{I,L} + \rho_L c_L^2 & 0 & c_L^2 - u_L^2 & 0 & 2u_L \end{bmatrix}. \tag{4.58}$$

Then, the system can be rewritten in terms of the conservative variables by the quasi-linear form given by Eq. (4.13). Through computing the roots of the characteristic polynomial by, $\det(\mathbf{A} - \lambda \mathbf{I}) = 0$, the following vector composed of the eigenvalues is obtained,

$$\boldsymbol{\lambda} = \begin{bmatrix} \lambda_1 \\ \lambda_2 \\ \lambda_3 \\ \lambda_4 \\ \lambda_5 \end{bmatrix} = \begin{bmatrix} u_I \\ u_G - c_G \\ u_G + c_G \\ u_L - c_L \\ u_L + c_L \end{bmatrix}, \tag{4.59}$$

and the following matrix **R** composed by the right eigenvectors **r** as columns,

$$\mathbf{R} = \begin{bmatrix} 1 & 0 & 0 & 0 & 0 \\ -\dfrac{\phi_G}{\chi_G} & 1 & 1 & 0 & 0 \\ \dfrac{\phi_L}{\chi_L} & 0 & 0 & 1 & 1 \\ -\lambda_1 \dfrac{\phi_G}{\chi_G} & \lambda_2 & \lambda_3 & 0 & 0 \\ \lambda_1 \dfrac{\phi_L}{\chi_L} & 0 & 0 & \lambda_4 & \lambda_5 \end{bmatrix}, \tag{4.60}$$

where the quantities χ_k and ϕ_k are respectively defined by,

$$\chi_k = c_k^2 - (u_I - u_k)^2, \tag{4.61}$$

$$\phi_k = \Delta p_{I,k} - \rho_k c_k^2. \tag{4.62}$$

The eigenvalues of the 5E2P system are always real and well defined, as for the eigenvectors a more detailed analysis is required. A detailed analysis for an analogous formulation was made by Ranson and Ricks (1984) and later presented by Munkejord (2007) for the current 5E2P formulation. It is straightforward to verify that $\mathbf{r}_2$, $\mathbf{r}_3$, $\mathbf{r}_4$ and $\mathbf{r}_5$ are linearly independent, whereas eigenvector $\mathbf{r}_1$ linear independence from the other eigenvectors will be conditional on the quantities χ_k and ϕ_k.

1) If $\chi_G \neq 0$ and $\chi_L \neq 0$ then the eigenvector $\mathbf{r}_1$ is linearly independent of the other eigenvectors.
2) If $\chi_G = 0$ and $\chi_L \neq 0$ then exists a linearly independent eigenvector $\mathbf{r}_1$ if and only if $\phi_G = 0$, where $\mathbf{r}_1$ will be given by,

$$\mathbf{r}_1 = [1, 0, \phi_L/\chi_L, 0, \lambda_1 \phi_L/\chi_L]^T, \tag{4.63}$$

3) If $\chi_G \neq 0$ and $\chi_L = 0$ then exists a linearly independent eigenvector $\mathbf{r}_1$ if and only if $\phi_L = 0$, where $\mathbf{r}_1$ will be given by,

$$\mathbf{r}_1 = [1, -\phi_G/\chi_G, 0, -\lambda_1\phi_G/\chi_G, 0]^T, \quad (4.64)$$

4) If $\chi_G = 0$ and $\chi_L = 0$ then exists a linearly independent eigenvector $\mathbf{r}_1$ if and only if $\chi_G = 0$ and $\phi_L = 0$, where $\mathbf{r}_1$ will be given by,

$$\mathbf{r}_1 = [1,0,0,0,0]^T. \quad (4.65)$$

The hyperbolicity of the 5E2P model then depends on the previously enumerated conditions, and when the eigenvectors are linearly independent the model is hyperbolic. To lose hyperbolicity the interfacial velocity needs to be under the specific condition of $u_I = u_k \pm c_k$. Since the model is proposed here to be used for simulating applicable cases of oil and gas pipelines, where the velocities are relatively low, supersonic flow conditions are not much of a concern. For the purposes of the applications intended here, the 5E2P is then considered unconditionally hyperbolic.

Notice that, differently from the 4E1P model, there is not a great dependency on the hyperbolicity with the interfacial pressure differences $\Delta p_{I,k}$, major problems will only occur when $\Delta p_{I,k} = \rho_k c_k^2$. With this model, the interfacial pressure differences may have relatively low values and even be equal to zero, without compromising hyperbolicity. As to keep the models relatable, here the same correlation will be used for the interfacial pressure across all models.

4.3 Source Terms

To characterize the one-dimensional models and make the model relevant for stratified, slug, and large amplitude wave patterns, the right-hand side terms of the governing equations must be defined and some geometric relations are needed to be established. The wetted perimeters S_k of each phase are expressed as

$$S_L = d\left[\pi - \cos^{-1}\left(2\frac{h_L}{d} - 1\right)\right], \quad (4.66)$$

$$S_G = \pi d - S_L. \quad (4.67)$$

where d is the pipe diameter and h_L is the liquid height, while the interfacial perimeter S_I is obtained by,

$$S_I = d\sqrt{1-\left(2\frac{h_L}{d}-1\right)^2}. \tag{4.68}$$

The hydraulic diameter, d_{hk} , corresponding to each phase is given by

$$d_{hG} = 4\frac{A_G}{S_G + S_I}, \tag{4.69}$$

$$d_{hL} = 4\frac{A_L}{S_L}. \tag{4.70}$$

where the superficial areas of each phase A_k are obtained by

$$A_G = \alpha_G A, \tag{4.71}$$

$$A_L = \alpha_L A. \tag{4.72}$$

The last geometrical relation that should be determined is the relation between the liquid volume fraction and the liquid height. It can be written as

$$\frac{dh_L}{d\alpha_L} = \frac{\pi d}{4}\frac{\sqrt{1-\varsigma^2}}{1-\varsigma^2}, \tag{4.73}$$

and

$$\alpha_L = \frac{1}{\pi}\left\{\pi - \cos^{-1}[\varsigma] + \varsigma\sqrt{(1-\varsigma^2)}\right\}, \tag{4.74}$$

where ς is defined as

$$\varsigma \equiv \frac{2h_L}{d} - 1. \tag{4.75}$$

With these established geometrical relations, the source terms on the right rand side of the 4E1P Eq. (4.3) to Eq. (4.4), and 5E2P models Eq. (4.36) to Eq. (4.37), can be estimated. First, the body forces accounting for the gravitational acceleration acting on the fluids can be expressed as,

$$B_{fk} = -\rho_k \alpha_k g \sin\theta, \tag{4.76}$$

where g is the gravity acceleration and θ is the inclination angle between the horizontal plane and the pipe center line.

The friction source terms for the wall and interfacial drag are given respectively by,

$$T_{kw} = -\frac{\tau_k S_k}{A}, \qquad \text{where, } \tau_k = \frac{1}{2} f_k \rho_k u_k |u_k|, \tag{4.77}$$

$$T_I = \frac{\tau_I S_I}{A}, \qquad \text{where, } \tau_I = \frac{1}{2} f_I \rho_G (u_G - u_L)|u_G - u_L|, \tag{4.78}$$

where f_k is the friction factor for each phase and f_I is the friction factor for the gas-liquid interface. Also, τ_k is the wall tension for each phase and τ_I is the interfacial tension.

For the liquid and gas friction factors at the wall, the Moody (1947) correlation is used as follows:

$$f_k = \max\left(\frac{16}{Re_k}; 0.001375\left[1 + \left[2\text{x}10^4 \frac{\varepsilon}{d_{hk}} + \frac{10^6}{Re_k}\right]^{\frac{1}{3}}\right]\right), \tag{4.79}$$

where Re_k is the Reynolds number for each phase, k, defined as a function of the density, dynamic viscosity μ_k, velocity and hydraulic diameter d_{hk} according to,

$$\text{Re}_k = \frac{\rho_k d_{hk} |u_k|}{\mu_k}, \tag{4.80}$$

For the interfacial friction factor f_I, Andreussi and Persen (1987) proposed the following equation for stratified flow

$$f_I = \begin{cases} f_G \ , & \text{if } \mathrm{F} \leq 0.36 \\ f_G + 29.7 f_g (\mathrm{F} - 0.36)^{0.67} \left(\frac{h_L}{d}\right)^{0.2} , & \text{otherwise} \end{cases}, \tag{4.81}$$

where, f_G is the friction factor of the gas phase with the wall, and F is the Froude number calculated as

$$\mathrm{F} = u_G \left(\frac{\rho_G}{\rho_L - \rho_G} \frac{dA_L}{dh_L} \frac{1}{A_G g cos\theta}\right). \tag{4.82}$$

5 Numerical Methods for Hyperbolic Equations

This chapter presents the numerical methodologies chosen to solve the system of hyperbolic partial differential equations composing the transient mathematical models previously presented. All the models use an Eulerian approach in a finite volume framework with an explicit scheme for obtaining the local solution of the flow variables at each given time step. The numerical methods selected are: the Flux Corrected Transport method (FCT); a modified version of the First Order Centered Scheme (ModFORCE); two variations of the Advection Upstream Splitting Method (AUSM); and an approximate Riemann solver based on the Roe linearization.

5.1 General Discretization

The pipe domain is discretized in a finite volume framework with a mesh of N_x computational cells. The mesh is uniform with each cell size of Δx,

$$\Delta x \equiv x_{i+\frac{1}{2}} - x_{i-\frac{1}{2}} = \frac{L}{N_x}, \tag{5.1}$$

where L is the total length of the domain. The increment i is utilized to numerate the domain with $i = 1, \ldots, N_x$. The distance from each cell center to the inlet of the domain is given by $x_i = (i - 1/2)\Delta x$ and from each cell boundary, or inter-cell, to the inlet by $x_{i-1/2} = (i-1)\Delta x$, downstream from the cell center, and $x_{i+1/2} = i\Delta x$, upstream from the cell center.

The system of hyperbolic equations in conservative canonical form, Eq. (3.8), can be discretized in a finite volume framework by the Godunov scheme,

$$\mathbf{q}_i^{n+1} = \mathbf{q}_i^n - \frac{\Delta t}{\Delta x}\left[\mathbf{f}_{\mathrm{i}+\frac{1}{2}}^n - \mathbf{f}_{\mathrm{i}-\frac{1}{2}}^n\right] + \Delta t \mathbf{s}_i^n. \tag{5.2}$$

The Godunov scheme is an explicit scheme that is first-order accurate in time, derived through a forward Euler method, and first-order accurate in space. The term $\mathbf{q}_i^{n+1}$ represents the local approximation of $\mathbf{q}$ in the position i at the time step $t^{n+1} = t^n + \Delta t$, with Δt being the time step. Note that $\mathbf{f}_{\mathrm{i}+1/2}^n$ and $\mathbf{f}_{\mathrm{i}-1/2}^n$ are the flux terms approximated

at the respective inter-cell positions $x_{i+1/2}$ and $x_{i-1/2}$. The fluxes at the inter-cells can be written as functions of the flow configuration of its upstream and downstream cells,

$$\mathbf{f}_{i-\frac{1}{2}}^{n+1} = \mathbf{f}_{i-\frac{1}{2}}^{n+1}(\mathbf{q}_{i-1}^{n}, \mathbf{q}_{i}^{n}), \qquad \mathbf{f}_{i+\frac{1}{2}}^{n+1} = \mathbf{f}_{i-\frac{1}{2}}^{n+1}(\mathbf{q}_{i}^{n}, \mathbf{q}_{i+1}^{n}), \tag{5.3}$$

which can be obtained by the solution of the associate Riemann problem or by the means of an adequate numerical approximation. The overall numerical scheme can, then, be extended to greater orders of accuracy. The following figure, Fig. 5.1, shows the schematic of the discretized domain as it was described. In the figure, the dashed cells $\mathbf{q}_0^n$ and $\mathbf{q}_{N_x+1}^n$ are the cells for the boundary conditions required by an initial value boundary problem, that will be described in the following sections.

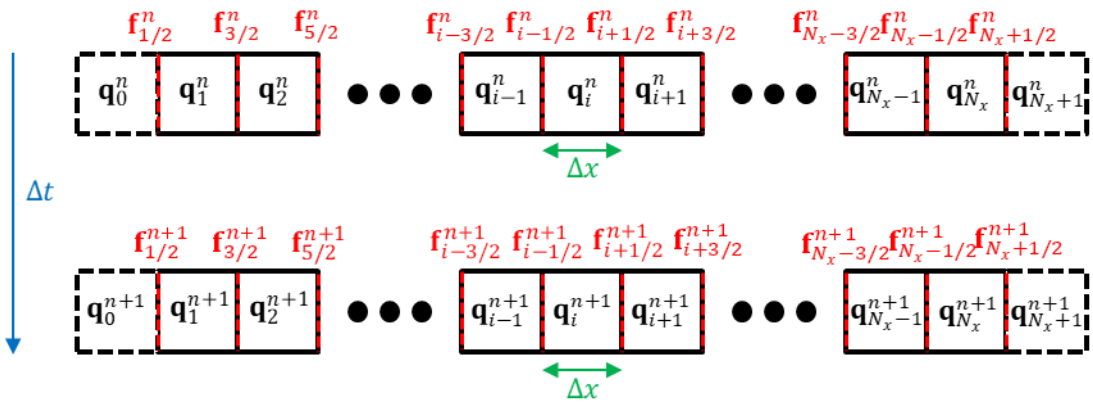

Figure 5.1: One-dimensional discrete mesh by means of the Godunov scheme.

Unfortunately, some systems of hyperbolic equations cannot be written in full conservative form, such as the 4E1P and 5E2P previously described. An alternative canonical form, given by Eq. (4.8), renders an extra term for the non-conservative term. This term can be discretized separately, and the discrete system will have the following form,

$$\mathbf{q}_i^{n+1} = \mathbf{q}_i^n - \frac{\Delta t}{\Delta x}\left[\mathbf{f}_{i+\frac{1}{2}}^n - \mathbf{f}_{i-\frac{1}{2}}^n\right] + \Delta t\left(\mathbf{H}\frac{\partial \mathbf{N}}{\partial x}\right)_j^n + \Delta t\mathbf{s}_i^n. \tag{5.4}$$

5.2 CFL Stability Condition

Since the stepping in time used in Eq. (5.4) to evolve the flow quantities is explicit, the time step Δt is chosen based on the CFL (Courant-Friedrichs-Lewy) condition, which is given by,

$$\Delta t \leq CFL \frac{\Delta x}{\lambda_{max}}, \tag{5.5}$$

where CFL is a positive number that is, usually, less than or equal to one, depending mainly on the chosen numerical scheme. The closer to unity, if the numerical method keeps stable, the more efficient the numerical scheme. The parameter λ_{max} is the largest eigenvalue in absolute value in the flow domain for the given time step, and expresses, physically, the largest speed at which characteristic waves propagate in the flow.

$$\lambda_{max} = \max_i \left[\max_{N_{eq}} \left| \lambda_i^{N_{eq}} \right| \right], \qquad i = 1, \dots, N_x \,, \tag{5.6}$$

where N_{eq} is the number of equations for a given hyperbolic system. As seen in previous chapters for flow equations, this eigenvalue is typically close to the speed of sound in the media, making it easy to establish upper-bound values for λ_{max} and make computational times faster by avoiding the calculation of all eigenvalues at every position and time step.

This condition establishes that for explicit schemes during a time step of the simulation no information is allowed to propagate further to a single numerical cell, otherwise numerical stability is not guaranteed.

5.3 Lax-Friedrichs and Richtmyer Methods

The Lax-Friedrichs and Richtmyer methods are both introductory methods for the solution of a hyperbolic system of PDEs. The Lax-Friedrich scheme is known for being diffusive, damping discontinuities and sharp gradients, while the Richtmyer scheme for being dispersive, inducing numerical spurious oscillations. These features make these numerical schemes mostly inapplicable in their pure form for simulating two-phase flows,

especially when sharp gradients are present. On the other hand, these methods serve as a basis for other methods such as the ones described in the following sections, FORCE, and FCT.

5.3.1 Lax-Friedrich Method

The Lax-Friedrich is a central method that is first-order accurate in space and time. It is a simple scheme to implement, and it estimates the inter-cell flux by the following relation

$$\mathbf{f}_{i+1/2}^{n} = \mathbf{f}_{i+1/2}^{LF} \equiv \frac{1}{2}(\mathbf{f}_{i+1}^{n} + \mathbf{f}_{i}^{n}) - \frac{\Delta x}{2\Delta t}(\mathbf{q}_{i+1}^{n} - \mathbf{q}_{i}^{n}), \tag{5.7}$$

where the cell flux is a function of the local conservative variables vector, $\mathbf{f}_i^n = \mathbf{f}_i^n(\mathbf{q}_i^n)$.

5.3.2 Richtmyer Method

The Richtmyer is a two-step counterpart of the Lax-Wendroff central scheme. The one-step version of this scheme is second-order accurate in space and time but requires the computation of the flux vector Jacobian to estimate the intercell flux, whereas the two-step versions are Jacobian free methodologies. There are two versions of a two-step Lax-Wendroff scheme, which are the Richtmyer and the MacCormack scheme. As pointed out by Essama (2004), both methodologies lead to near-identical solutions, but the Richtmyer version is chosen because it is simpler in its implementation, the reason why it is the one implemented in this work. The Richtmyer scheme is also second-order accurate in space and time and is implemented in the following steps. First, the intermediary inter-cell conservative variables vector is estimated by

$$\widetilde{\mathbf{q}}_{i+1/2}^{n+1/2} = \frac{1}{2}(\mathbf{q}_{i+1}^{n} + \mathbf{q}_{i}^{n}) - \frac{1}{2}\frac{\Delta t}{\Delta x}[\mathbf{f}(\mathbf{q}_{i+1}^{n}) - \mathbf{f}(\mathbf{q}_{i}^{n})]. \tag{5.8}$$

In the next step, the Richtmyer intercell flux vector approximation according to,

$$\mathbf{f}_{i+1/2}^{n} = \hat{\mathbf{f}}_{i+1/2}^{\mathrm{RI}} \equiv \mathbf{f}\left(\widetilde{\mathbf{q}}_{i+\frac{1}{2}}^{n+\frac{1}{2}}\right). \tag{5.9}$$

5.4 FORCE Methods

In order to avoid the diffusive solutions of the Lax-Friedrich method and the oscillatory solutions of the Richtmyer method, the First-Order-Centered method, known as FORCE (Toro, 1997), estimates the numerical flux at the inter-cell based on the average of the Lax-Friedrich and Richtmyer intercell fluxes,

$$\mathbf{f}_{i+1/2}^{n} = \mathbf{f}_{i+\frac{1}{2}}^{FORCE} \equiv \frac{1}{2}\left(\mathbf{f}_{i+\frac{1}{2}}^{LF} + \hat{\mathbf{f}}_{i+\frac{1}{2}}^{\mathrm{RI}}\right). \tag{5.10}$$

In general, the force method leads to better results than the Lax-Friedrichs method for two-phase flows using a two-fluid model, but it still retains some of the numerical diffusive errors from the Lax-Friedrich method. To counterbalance that, a GFORCE flux, as described in Toro and Titarev (2006) and Romenski *et al.* (2010) can be implemented,

$$\mathbf{f}_{i+1/2}^{n} = \mathbf{f}_{i+\frac{1}{2}}^{FORCE} \equiv (1-\omega)\mathbf{f}_{i+1/2}^{LF} + \omega\hat{\mathbf{f}}_{i+1/2}^{\mathrm{RI}}, \tag{5.11}$$

where the weight ω is obtained as a function of the local CFL number by

$$\omega = \frac{1}{1+CFL}, \tag{5.12}$$

To further evaluate the capacity of the FORCE and GFORCE approach for evaluating the inter-cell flux, Sondermann *et. al* (2021) also test other modified values for the weight ω for both 4E1P and 5E2P models. This study concluded that fixed values of ω =0.87 for the 4E1P model and ω =0.98 for the 5E2P model were optimal for their simulations, addressing the code as a Modified FORCE scheme, ModFORCE.

5.5 FCT Method

The Flux-Corrected Transport (FCT) method proposed originally by Boris and Book (1973), was further developed by Book *et. al* (1975) and Boris and Book (1976), and later generalized by Zalesak (1979). The FCT technique was the first high-resolution method to introduce the concept of limiters in the literature. It may be interpreted as a

"predictor/corrector" scheme in which diffusion is introduced in the predictor stage and anti-diffusion is introduced in the corrector stage. Further details about the well-known classical FCT method may be found in Fletcher (1988) and Hirsch (1990).

In the context of transient two-phase flows in pipes, Figueiredo *et al.* (2012) investigated the time and space accuracy using the FCT method and concluded that it is first-order in time and second-order in space accurate. The FCT method was also utilized to solve distinct two-phase flow models on different flow scenarios by Bueno (2013), Bueno *et al.* (2012), Sondermann (2016), Figueiredo (2010), Patricio (2016), Freitas (2017) and Sondermann *et al.* (2021).

If $\mathbf{q}_i^n$ is the conservative variables in the previous time step and $\widetilde{\mathbf{q}}_i^{n+1}$ is the newly updated solution generated by the Ritchmyer method, μ^{FCT} and ν^{FCT} and are diffusion and anti-diffusion coefficients, respectively, the fluxes and state vectors are given as follows:

1) A first approximation of the conservative variables vector, $\widetilde{\mathbf{q}}_i^{n+1}$ by the Richmeyer method,

$$\widetilde{\mathbf{q}}_i^{n+1} = \mathbf{q}_i^n - \frac{\Delta t}{\Delta x}\left[\hat{\mathbf{f}}_{i+1/2}^{\mathrm{RI}} - \hat{\mathbf{f}}_{i-1/2}^{\mathrm{RI}}\right], \tag{5.13}$$

where the scheme to obtain the approximate Richtmyer flux vector at the intercell is detailed in the previous subsection.

2) Generation of the diffusive fluxes:

$$\mathbf{f}_{i+1/2}^{d} = \nu_{i+1/2}^{FCT}(\mathbf{q}_{i+1}^n - \mathbf{q}_i^n). \tag{5.14}$$

3) Calculation of the diffusion of the solution:

$$\overline{\mathbf{q}}_{i+1/2}^{n+1} = \widetilde{\mathbf{q}}_i^{n+1} + \left(\mathbf{f}_{i+1/2}^{d} - \mathbf{f}_{i-1/2}^{d}\right). \tag{5.15}$$

4) Calculation of the anti-diffusive fluxes:

$$\mathbf{f}_{i+1/2}^{\mathrm{ad}} = \mu_{i+1/2}^{FCT}(\widetilde{\mathbf{q}}_{i+1}^{n+1} - \widetilde{\mathbf{q}}_i^{n+1}). \tag{5.16}$$

5) Limitation of the anti-diffusive fluxes:

$$\mathbf{f}_{i+1/2}^{\text{cad}} = S\max\{0,\quad \min\{S(\bar{\mathbf{q}}_i^{n+1} - \bar{\mathbf{q}}_{i-1}^{n+1}),\quad |\mathbf{f}_{i+1/2}^{\text{ad}}|,\quad S(\bar{\mathbf{q}}_{i+2}^{n+1} - \bar{\mathbf{q}}_{i+1}^{n+1})\}\}. \tag{5.17}$$

where,

$$S = \text{sign}(\mathbf{f}_{i+1/2}^{\text{ad}}), \tag{5.18}$$

in which the calculations involving S in Eqs. (5.17) and (5.18) are to be interpreted component-wise.

6) Finally, the inter-cell flux can be computed, as

$$\mathbf{f}_{i+1/2}^{n} = \hat{\mathbf{f}}_{i+1/2}^{\text{FCT}} \equiv \hat{\mathbf{f}}_{i+1/2}^{\text{RI}} + \frac{\Delta x}{\Delta t}\left(\mathbf{f}_{i+1/2}^{\text{cad}} - \mathbf{f}_{i+1/2}^{d}\right). \tag{5.19}$$

The values for the diffusive and anti-diffusive coefficients are estimated differently in the literature. The recommendation is to balance the coefficients in order to minimize the errors resulting from numerical diffusion and dispersion as pointed out by Boris and Book (1976). Lezeau and Thompson (1998) and Xiao and Shoham (1991) estimated the values of $\mu_{i+1/2}^{FCT}$= 0.125 and $\nu_{i+1/2}^{FCT}$= 0.125. Essama (2004), Freitas (2017) and Sondermann *et al.* (2021) explore other values for the coefficients in various simulations and show that for different models and flow scenarios the balance between the coefficients can vary for optimized results. Fletcher (1988) presented a general rule to calculate the coefficients, by the relations

$$\mu_{i+1/2}^{FCT} = \eta_0 + \eta_1\left(\frac{\Delta t}{\Delta x}\lambda_{max,i+\frac{1}{2}}\right)^2 \tag{5.20}$$

$$\nu_{i+1/2}^{FCT} = \eta_0 + \eta_2\left(\frac{\Delta t}{\Delta x}\lambda_{max,i+\frac{1}{2}}\right)^2 \tag{5.21}$$

where η_0, η_1 and η_2 are constants that can be estimated to minimize the errors of numerical diffusion and dispersion. The values for the constants as pointed out by Fletcher

(1988), are $\eta_0 = 1/3$, $\eta_1 = -1/6$ and $\eta_2 = 1/6$. The value $\lambda_{max,i+1/2}$ is obtained by the arithmetic mean of the upstream and downstream eigenvalues, $\lambda_{max,i+1/2} = 0.5(\lambda_{max,i} + \lambda_{max,i+1})$. Freitas (2017) and tested this relation for various flow cases with the 4E1P and 5E2P models and concluded it does not produce optimal results, but it can be a general rule of thumb for stable simulations.

5.6 AUSM-Type Method

The Advection Upstream Splitting Method (AUSM) was initially implemented by Liou and Steffen (1993) to calculate the inter-cell flux under single-phase conditions. This method was proved to require low computational cost if compared to approximate Riemann solvers that need to obtain the Jacobian or coefficient matrix in its solution, complicating the solution. On top of that, AUSM methods are robust and present very good accuracy when tested against other methods. The AUSM method has hybrid flux-splitting, as verified by Evje and Flätten (2003), presenting characteristics related to FVS, flux vector splitting, and FDS, flux difference splitting numerical schemes. On the one hand, FVS methods have a simpler implementation that is compensated with a more diffusive solution. On the other hand, FDS methods are more computationally demanding due to matrix calculations, but present less diffusive behavior, and consequently, more accuracy.

The inter-cell flux is calculated by separating the convective and the pressure flux terms, as follows

$$\mathbf{f}^{\mathrm{AUSM}}_{\mathrm{i}+\frac{1}{2}} = \mathbf{f}^{c}_{\mathrm{i}+\frac{1}{2}} + \mathbf{f}^{p}_{\mathrm{i}+\frac{1}{2}}. \tag{5.22}$$

For the 4E1P model:

$$\mathbf{f}^{c} = \begin{bmatrix} \rho_G \alpha_G u_G \\ \rho_L \alpha_L u_L \\ \rho_G \alpha_G u_G^2 \\ \rho_L \alpha_L u_L^2 \end{bmatrix}, \mathbf{f}^{p} = \begin{bmatrix} 0 \\ 0 \\ \alpha_G \Delta p_{IG} \\ \alpha_L \Delta p_{IL} \end{bmatrix}, \tag{5.23}$$

and for the 5E2P model:

$$\mathbf{f}^c = \begin{bmatrix} 0 \\ \rho_G \alpha_G u_G \\ \rho_L \alpha_L u_L \\ \rho_G \alpha_G u_G^2 \\ \rho_L \alpha_L u_L^2 \end{bmatrix}, \mathbf{f}^p = \begin{bmatrix} 0 \\ 0 \\ 0 \\ \alpha_G \Delta p_{IG} \\ \alpha_L \Delta p_{IL} \end{bmatrix}. \tag{5.24}$$

In the work of Evje and Flätten (2003), the authors applied some modifications to the method described in Wada and Liou (1997). Two AUSM methods were considered: AUSMV, similar to FVS methods, and AUSMD, tending to FDS. The convective flux term, $\mathbf{f}^c$, for the mass equation is calculated as follows,

$$\begin{aligned} &(\rho_k \alpha_k u_k)_{i+1/2} \\ &\quad = (\rho_k \alpha_k)_i \tilde{V}^+(u_k, c, \chi^L)_i + (\rho_k \alpha_k)_{i+1} \tilde{V}^-(u_k, c, \chi^R)_{i+1} \end{aligned} \tag{5.25}$$

The convective flux term, $\mathbf{f}^c$, for the momentum equation is calculated as follows for the AUSMV method

$$\begin{aligned} &(\rho_k \alpha_k {u_k}^2)_{i+1/2} \\ &\quad = (\rho_k \alpha_k u_k)_i \tilde{V}^+(u_k, c, \chi^L)_i \\ &\quad + (\rho_k \alpha_k u_k)_{i+1} \tilde{V}^-(u_k, c, \chi^R)_{i+1} \end{aligned} \tag{5.26}$$

For the AUSMD method,

$$\begin{aligned} &(\rho_k \alpha_k {u_k}^2)_{i+1/2} \\ &\quad = \frac{1}{2}(\rho_k \alpha_k u_k)_{i+1/2} [\tilde{V}^+(u_k, c, \chi^L)_i + \tilde{V}^-(u_k, c, \chi^R)_{i+1}] \\ &\quad - \frac{1}{2}\left|(\rho_k \alpha_k u_k)_{i+\frac{1}{2}}\right| [\tilde{V}^-(u_k, c, \chi^R)_{i+1} - \tilde{V}^+(u_k, c, \chi^L)_i], \end{aligned} \tag{5.27}$$

where:

$$\begin{aligned} &\tilde{V}^{\pm}(u_k, c, \chi^{L,R}) \\ &= \begin{cases} \chi^{L,R}\left[\pm\frac{1}{4c}(u_k \pm c)^2\right] + (1 - \chi^{L,R})\frac{u_k \pm |u_k|}{2}, if |u_k| \le c \\ \qquad\qquad \frac{u_k \pm |u_k|}{2}, otherwise, \end{cases} \end{aligned} \tag{5.28}$$

and

$$\chi^L = \frac{2(\rho/\alpha)^L}{(\rho/\alpha)^L + (\rho/\alpha)^R}, \qquad \chi^R = \frac{2(\rho/\alpha)^R}{(\rho/\alpha)^L + (\rho/\alpha)^R}. \tag{5.29}$$

The superscripts *L* or *R* designate left and right cells and the subscript *k* stands for the respective phase, gas or liquid. The variable u_k is the fluid velocity in phase *k.* The parameter *c* in the above equations is the speed of sound for the mixture, and this term might be modeled, for instance, as an average between the gas and liquid speed of sounds, such as suggested by Kitamura and Lior (2012) and used in Sondermann (2021).

The pressure flux term for both methods, AUSMV and AUSMD, are calculated according to the following expression

$$(\alpha_k \Delta p_{Ik})_{i+1/2} = P^+(u_k, c)_i (\alpha_k \Delta p_{Ik})_i + P^-(u_k, c)_{i+1} (\alpha_k \Delta p_{Ik})_{i+1} \tag{5.30}$$

where:

$$P^{\pm}(u_k, c) = \begin{cases} \left[\pm\frac{1}{4c}(u_k \pm c)^2\right]\frac{1}{c}\left(\pm 2 - \frac{u_k}{c}\right), if\ |u_k| \le c \\ \frac{u_k \pm |u_k|}{2u_k}, \text{otherwise.} \end{cases} \tag{5.31}$$

The entire flux term written for the two models that are evaluated in this work, 4E1P and 5E2P, are presented in Appendix A with more details.

Based on the AUSMV and AUSMD methods, the AUSMDV was described by Evje and Flätten (2003), and the convective flux is calculated as

$$\mathbf{f}^{\text{AUSMDV},c}_{\text{i}+\frac{1}{2}} = ss\,\mathbf{f}^{\text{AUSMV},c}_{\text{i}+\frac{1}{2}} + (1 - ss)\mathbf{f}^{\text{AUSMD},c}_{\text{i}+\frac{1}{2}}. \tag{5.32}$$

The AUSMDV method is a balance between the AUSMV and AUSMD, and the pressure flux is the same as presented in Eq. (5.30). The parameter *ss* is a weighting parameter and can be defined in several ways. For the present work, this parameter was estimated based on previous studies by Sondermann (2021), being equal to 0.8.

5.7 Roe-Type scheme

The previously presented methods estimate the flux at the inter-cell as a function of the conservative variables at the adjacent cells, $\mathbf{f}_{i+1/2}^{n+1} = \mathbf{f}_{i-1/2}^{n+1}(\mathbf{q}_i^n, \mathbf{q}_{i+1}^n)$. The Roe-type scheme presented in Evje and Flaten (2003), Munkejord (2005), Santim and Rosa (2015), and LeVeque (2004), takes the Godunov scheme, Eq. (5.2), into a different perspective, where the solution of the associate Riemann problem can be expressed as a set of waves propagating form the cell boundaries into the cell. Then, Eq. (5.2) is rewritten as,

$$\mathbf{q}_i^{n+1} = \mathbf{q}_i^n - \frac{\Delta t}{\Delta x}\left[\mathcal{A}^-\Delta\mathbf{q}^n_{i+\frac{1}{2}} + \mathcal{A}^+\Delta\mathbf{q}^n_{i-\frac{1}{2}}\right], \tag{5.33}$$

where in the perspective of the Riemann problem $\mathcal{A}^-\Delta\mathbf{q}^n_{i+1/2}$ encompass the net effect of the left-going waves emanating from the intercell $x_{i+1/2}$ and $\mathcal{A}^+\Delta\mathbf{q}^n_{i-1/2}$ the net effect of the right-going waves emanating from $x_{i-1/2}$. This approach is attractive in the context of the 4E1P and 5E2P systems because they cannot be written in a full conservative form and the quasi-linear form Eq. (4.13) is used instead, thus, a separate discretization of the non-conservative terms is not required.

5.7.1 Roe Linearization

The Roe linearization (Roe, 1984), defines the approximate Riemann solution of the hyperbolic system of equations by replacing its quasi-linear form with a linearized problem at each inter-cell.

$$\frac{\partial\hat{\mathbf{q}}}{\partial t} + \widehat{\mathbf{A}}_{i+1/2}\frac{\partial\hat{\mathbf{q}}}{\partial x} = 0. \tag{5.34}$$

In this equation, the Roe matrix, $\widehat{\mathbf{A}}_{i+1/2}$**,** is an approximation of the coefficient matrix **A** at the cell interface, through the neighboring cells**,**

$$\widehat{\mathbf{A}}_{i+1/2}\left(\hat{\mathbf{q}}_{i+1/2}\right) = \widehat{\mathbf{A}}_{i+1/2}(\mathbf{q}_i, \mathbf{q}_{i+1}), \tag{5.35}$$

where $\widehat{\mathbf{q}}_{i+1/2}$ is an average state between the neighboring cells $\mathbf{q}_i$ and $\mathbf{q}_{i+1}$, defined such that the resulting Roe matrix must satisfy the following conditions,

- $\widehat{\mathbf{A}}_{i+1/2}$ must be diagonalizable with real eigenvalues to guarantee hyperbolicity;
- $\widehat{\mathbf{A}}_{i+1/2}(\mathbf{q}_i, \mathbf{q}_{i+1}) \rightarrow \mathbf{A}(\overline{\mathbf{q}})$ as $\mathbf{q}_i, \mathbf{q}_{i+1} \rightarrow \overline{\mathbf{q}}$ to make the method consistent with the original conservation law, Eq. (4.13),
- $\widehat{\mathbf{A}}_{i+1/2}(\mathbf{q}_i, \mathbf{q}_{i+1}) = \mathbf{f}(\mathbf{q}_{i+1}) - \mathbf{f}(\mathbf{q}_i)$ to ensure that the method is conservative.

The definition for the averaged primitive variables $\widehat{\mathbf{w}}_{i+1/2}$ for each of the models is presented in Appendix B. With the averaged values for the primitive variables the averaged state $\widehat{\mathbf{q}}_{i+1/2}$ analogously to the definition of $\mathbf{q}$, and the same is done to the Roe matrix $\widehat{\mathbf{A}}_{i+1/2}$ that is analogous to the definition of the coefficient matrix $\mathbf{A}$. Through the same operations done in the hyperbolicity analysis of the models, the linearized versions of the vector of eigen values $\boldsymbol{\lambda}_{i+1/2}$ and the matrix composed of the right eigenvectors $\mathbf{R}_{i+1/2}$ are obtained through the Roe matrix. Note that the 4E1P does not have an analytical formulation for these entities, then, in its numerical code, the eigenstructure is obtained straight through the linear algebra operations.

5.7.2 Numerical Scheme

After obtaining the Roe matrix, the linearized waves and wave speeds, eigenvalues, at the inter-cells are used to define the entities from Eq. (5.36). For a detailed description of their derivation, refer to LeVeque (2004).

$$\mathcal{A}^{-}\Delta\mathbf{q}^{n}_{i+1/2} = \sum_{p=1}^{n_{eq}} (\lambda^{p}_{i+1/2})^{-}\mathbf{w}^{\mathrm{p}}_{\mathrm{i+1/2}}, \tag{5.36}$$

$$\mathcal{A}^{+}\Delta\mathbf{q}^{n}_{i-1/2} = \sum_{p=1}^{n_{eq}} (\lambda^{p}_{i-1/2})^{+}\mathbf{w}^{p}_{i-1/2}. \tag{5.37}$$

The positive indexes indicate that the waves are right-going waves, with positive speed, the negative indexes denote the left-going waves, with negative speed. The index

p numerates a specific eigenvalue of the system with $1 \leq p \leq n_{eq}$, which for a system of hyperbolic equations n_{eq} is the total number of equations, thus the number of eigenvalues of the system. The vector $\mathbf{w}^p_{i\pm1/2}$ represents the waves crossing the cell's interface and $\lambda^p_{i\pm1/2}$ are the characteristic velocities, eigenvalue, of the wave of number p. To filter the left-going or right-going waves the following operation is done,

$$(\lambda^p_{j-1/2})^{\pm} = \frac{1}{2}\left(\lambda^p_{j-1/2} \pm \left|(\lambda^p_{j-1/2})\right|\right). \tag{5.38}$$

The waves crossing the cell's interface are obtained through,

$$\mathbf{w}^p_{i\pm1/2} = \beta^p_{i\pm1/2}\mathbf{r}^p_{i\pm1/2}, \tag{5.39}$$

with $\mathbf{r}^p_{i\pm1/2}$ being the right eigenvector correspondent to the eigenvalue $\lambda^p_{i\pm1/2}$. The term $\beta^p_{j-1/2}$ are proportionally coefficients, that according to Toro (1999) can be interpreted as wave amplitudes,

$$\beta^p_{i+1/2} = \mathbf{R}^{-\mathbf{1}}_{i+1/2}(\mathbf{q}_{i+1} - \mathbf{q}_i), \qquad \beta^p_{i-1/2} = \mathbf{R}^{-\mathbf{1}}_{i-1/2}(\mathbf{q}_i - \mathbf{q}_{i-1}). \tag{5.40}$$

To expand the current scheme into second-order a Lax-Wendroff method can be used as,

$$\mathbf{q}^{n+1}_i = \mathbf{q}^n_i - \frac{\Delta t}{\Delta x}\left[\sum_{p=1}^{m}\left(\lambda^p_{i+\frac{1}{2}}\right)^{-}\mathbf{w}^p_{i+\frac{1}{2}} + \sum_{p=1}^{m}\left(\lambda^p_{i-\frac{1}{2}}\right)^{+}\mathbf{w}^p_{i-\frac{1}{2}}\right] - \frac{\Delta t}{\Delta x}\left[\tilde{\mathbf{f}}^n_{i+\frac{1}{2}} - \tilde{\mathbf{f}}^n_{i-\frac{1}{2}}\right], \tag{5.41}$$

where the terms $\tilde{\mathbf{f}}^n_{i\pm1/2}$ are high-resolution flux correction terms, as defined by LeVeque (2004), and it is a function of the eigenstructure of Roe matrix,

$$\tilde{\mathbf{f}}^{n}_{\mathrm{i}\pm1/2} = \frac{1}{2}\sum_{p=1}^{m}\left|(\lambda^{p}_{\mathrm{i}\pm1/2})\right|\left(1-\frac{\Delta t}{\Delta x}\left|(\lambda^{p}_{\mathrm{i}\pm1/2})\right|\right)\phi(\Psi^{p}_{\mathrm{i}\pm1/2})\mathbf{w}^{p}_{i\pm1/2}. \tag{5.42}$$

With $\phi(\Psi^{p}_{j-1/2})$ being a flux limiter function to avoid numerical oscillations that may be induced by the accuracy extension. The Flux limiter function used here is the van Leer (1974) slope limiter function that is expressed by,

$$\phi(\Psi) = \frac{\Psi + |\Psi|}{1 + |\Psi|}. \tag{5.43}$$

The entity Ψ is a smoothness parameter defined as,

$$\Psi^{p}_{i+1/2} = \frac{\beta^{p}_{\mathrm{I}+1/2}}{\beta^{p}_{\mathrm{I}+1/2}}\text{ , with }\mathrm{I} = \begin{cases} i-1 \text{ if } \lambda^{p}_{i+1/2} > 0 \\ i+1 \text{ if } \lambda^{p}_{i+1/2} < 0 \end{cases}. \tag{5.44}$$

5.1 Discretization of the Non-Conservative Term

For the methods previously presented, apart from the Roe scheme, the discretization of the non-conservative term present in Eq. (5.4) is required. The monotonized central slope, MC slope Van Leer (1974), is used to discretize the non-conservative term of Eq. (5.4). This scheme was already tested by Essama (2004), Figueiredo *et al.* (2017), Sondermann *et al.* (2019), Patricio *et al.* (2020), and Sondermann *et al.* (2021) in the context of two-fluid models. It is also called the second-order Minmod slope limiter and is described as follows,

$$\left(\mathbf{H}\frac{\partial \mathbf{n}}{\partial x}\right)^{n}_{j} = \frac{\mathbf{H}^{n}_{j}}{\Delta x}\mathbf{m}(\mathbf{x},\mathbf{y},\mathbf{z}), \tag{5.45}$$

where $\mathbf{H}^{n}_{j} = \mathbf{H}(\mathbf{q}^{n}_{j})$ and the $\mathbf{m}(\mathbf{x},\mathbf{y},\mathbf{z})$ is the Minmod function defined as

$$m(\mathbf{x},\mathbf{y},\mathbf{z}) \equiv \begin{cases} s\min\{|\mathbf{x}|,|\mathbf{y}|,|\mathbf{z}|\}, & \text{if } \operatorname{sgn}(\mathbf{x}) = \operatorname{sgn}(\mathbf{y}) = \operatorname{sgn}(\mathbf{z}) = s \\ 0, & \text{otherwise,} \end{cases} \tag{5.46}$$

The value of m is obtained component-wise for the vector $\mathbf{m}$ with,

$$\mathbf{x} \equiv 2(\mathbf{n}_{i+1}^{n} - \mathbf{n}_{i}^{n}), \mathbf{y} \equiv \frac{1}{2}(\mathbf{n}_{i+1}^{n} - \mathbf{n}_{i-1}^{n}), \mathbf{z} \equiv 2(\mathbf{n}_{i}^{n} - \mathbf{n}_{i-1}^{n}). \tag{5.47}$$

5.2 Imposition of Boundary Conditions

The imposition of the boundary conditions is done through the implementation of ghost cells outside the discretized domain, $\mathbf{q}_0^n$ and $\mathbf{q}_{N_x+1}^n$, where boundary values can be prescribed. The hyperbolicity analysis of the model that is being used in a simulation is crucial in the determination of the number of imposed boundary conditions and their location, Jeffrey (1976). Locally, the number of positive eigenvalues, for instance, will determine the number of boundary conditions imposed at the inlet, since they define the number of right-going waves emanating from the boundary to the domain at the inlet. Analogously, the number of negative eigenvalues defines the number of boundary conditions set at the outlet.

In the simulations of the herein work, the Dirichlet type boundary conditions will be used, where the value for the entity imposed at the boundary is either constant or done through a transient manner, in which the boundaries conditions are a function of time.

Since we are limited to subcritical flow conditions, the single-phase model will always have a positive and a negative eigenvalue at all locations. Typically at the inlet, a mass flow rate or a velocity is imposed, whereas the pressure is imposed at the outlet. Similarly, for the two-fluid models, the mass flow rate, superficial velocities or velocities, and volume fractions are prescribed at the inlet and the pressures at the outlet.

6 Numerical Benchmarking and Validation

This section is dedicated to presenting the results for benchmark problems commonly used in two-phase flow simulations. For the one-dimensional transient single-phase formulation, a wide range of problems with exact analytical solutions can be formulated. In addition, all methods selected here are well known for being up to par in simulating transient one-dimensional single-phase flow, even in the presence of sharp discontinuities. Hence, benchmarking single-phase cases was not made necessary.

For the two-phase-flow models, however, the formulation of benchmarks is a challenge since there is no analytical solution to the transient formulation of the one-dimensional two-fluid models. Some efforts in the literature were made to evaluate each method selected separately, including Ansari and Daramizadeh (2012), Munkejord (2007), Freitas (2017), and others. As far as the author is concerned, there are no works in literature that compare a wide variety of numerical methods combined with the previously reported two-fluid models. A selection of a model-method combination, knowns as a numerical model, that is optimal in representing the physics of a two-phase flow in pipes is desired.

The results herein presented for the water faucet problem and the large relative velocity shock tube are an extension of the results published in the literature, Sondermann *et al.* (2021).

6.1 Water Faucet

The water faucet also called gravity-dominated flow, is an initial-boundary value problem that was first described by Ransom (1987), and is widely used as a benchmark for two-fluid models. It consists of a one-dimensional problem, in which a gas-liquid two-phase flow is set up in a vertical pipe of length L. The boundary conditions are set as constants, with velocities and volume fractions at the inlet and pressure at the outlet. In this problem, the interfacial friction forces are neglected, and the flow is treated as isothermal.

In the initial configuration, represented by Fig. 6.1(a), all flow variables are constant through all the fluid domain and equal to the boundary conditions. The liquid moves with

a uniform initial velocity, whereas the gas is stationary in the outer annulus region. Uniform distributions of the volume fractions are also established across the domain.

When the gravity is felt by the flow for $t > 0$, the liquid phase accelerates, and a discontinuity is formed at the inlet due to the constant boundary conditions, which propagates along the pipe. After some time has passed, the region filled by the liquid becomes thinner along the pipe, showing a discontinuity in the volume fractions at some intermediate position. This discontinuity moves along the pipe towards the outlet as time progresses. Therefore, for an intermediate time instant, Fig. 6.1(b), the liquid holdup decreases along the pipe up to the point where the discontinuity is located and jumps up across the discontinuity to return to its initial value, whereas the void fraction experiences the opposite effect. Since the liquid phase is assumed to be incompressible and the pressure variation along the tube is assumed to be small, both liquid and gas densities are essentially constant. Because the liquid velocity increases, the holdup decreases from the pipe inlet to the position where the jump is located to conserve mass and stay constant from that point on towards the outlet. On the other hand, the gas remains stagnant in the region from the pipe inlet to the location of the void fraction jump, but gas must enter the pipe from the outlet at a constant speed to occupy the increased volume that was created due to the thinning of the liquid film. Fig. 6.1(c) is a representation of the flow in a steady-state situation, after the volume fraction discontinuity leaves the domain.

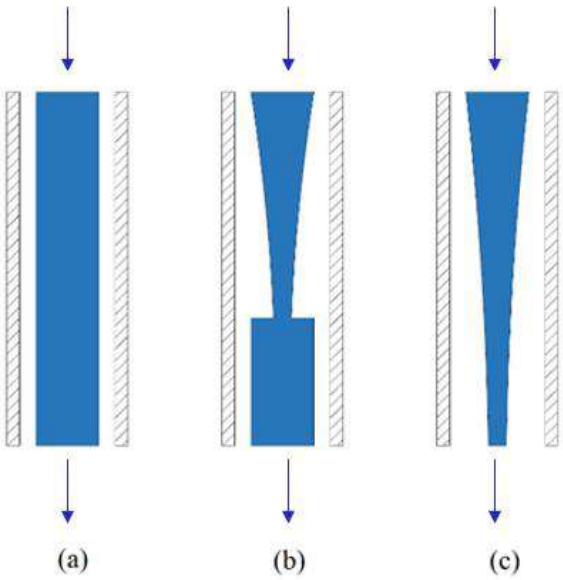

Figure 6.1: Water faucet problem schematic. (a) Initial uniform condition. (b) Flow snapshot sometime between initial and steady-state condition. (c) Steady-state condition.

An interesting aspect of the water faucet benchmark is that under the hypothesis of constant pressure it has an analytical solution, making the problem useful to verify the performance of numerical models with respect to their capability to reproduce the physics of the two-phase flow as well as their accuracy in capturing and transporting discontinuities in the flow. According to Ransom (1987) and Coquel *et al.* (1997), the analytical solutions for the void fraction and liquid velocity are given by

$$\alpha_G(x,t) = \begin{cases} 1 - \dfrac{(\alpha_L u_L)_{x=0}}{\sqrt{2gx + (u_L^2)_{x=0}}}, & \text{if } x \le x_d \\ 1 - (\alpha_L)_{x=0}, & \text{otherwise.} \end{cases} \tag{6.1}$$

$$u_L(x,t) = \begin{cases} \sqrt{(u_L^2)_{x=0} + 2gx}, & \text{if } x \le x_d \\ (u_L)_{x=0} + gt, & \text{otherwise.} \end{cases} \tag{6.2}$$

where the discontinuity location, x_d, is given by $x_d \equiv (u_L)_{x=0}t + \frac{1}{2}gt^2$.

In contrast to the analytical solution proposed by Ransom (1987), where the pressure is constant, the numerical simulation produces a non-zero pressure variation over the fluid domain. However, as this expected variation is minimal, the analytical solution serves as a good reference for the graphical comparison with the numerical solution. Later, Zou *et al*. (2016), complementing the work carried out by Ransom (1987), deduced the analytical solution for the remaining variables, pressure, and gas velocity, which are written as

$$u_G(x,t) = \begin{cases} 0 & \text{, if } x \le x_d \\ -\dfrac{1 - (\alpha_G)_{x=0}}{(\alpha_G)_{x=0}} gt, & \text{otherwise.} \end{cases} \tag{6.3}$$

$$p = \begin{cases} (p)_{x=L} - \dfrac{\rho_G g(L - x_d)}{(\alpha_G)_{x=0}} + \dfrac{1}{2}\rho_G \left(\dfrac{1 - (\alpha_G)_{x=0}}{(\alpha_G)_{x=0}} gt \right)^2 + \\ \rho_G \dfrac{1 - (\alpha_G)_{x=0}}{(\alpha_G)_{x=0}} gt((u_L)_{x=0} + gt) - \rho_G g(x_d - x), \text{ if } x \le x_d \\ (p)_{x=L} - \dfrac{\rho_G g(L - x)}{(\alpha_G)_{x=0}}, & \text{otherwise.} \end{cases} \tag{6.4}$$

In the solution presented in Eqs. (6.3) and (6.4), the interfacial pressure is neglected, and the pressure profile is derived from the gas phase perspective since the liquid phase

is in free-fall motion. In the numerical simulations herein performed, on the other hand, the term corresponding to the interfacial pressure is non-zero for both mathematical models with the interfacial pressure term being represented by Bestion's (1990) correlation given in Eq.(4.7).

The following Table 6.1, details the setup for all constant parameters necessary to set up the simulated faucet flow, whereas Table 6.2 details the boundary conditions and their respective positions.

Table 6-1: Simulation set up for the water faucet problem.

Parameter	Value
Gravity	9.81 m/s²
Speed of sound in the liquid	1000 m/s
Speed of sound in the gas	316.2 m/s
Reference gas density	0 kg/m³
Reference liquid density	1000 kg/m³
Pipe length	12 m
Time (snapshot)	0.6 s

Table 6-2: Inlet and outlet boundary conditions for the water faucet benchmark.

Flow Variable	Value
p at outlet ($x=L$)	10^5 Pa
u_G at inlet ($x=0$)	0 m/s
u_L at inlet ($x=0$)	10 m/s
α_G at inlet ($x=0$)	0.2 (-)

The following results report the simulations for each one of the methods coded using the 4E1P model for various mesh sizes, 100, 500, 1000, 2500, 5000, and 10000 cells. The CFL number was set to 0.45 for all methods, to respect their stability criteria, whereas the Roe scheme is run with both 0.45 and 0.9 values for comparison. All presented results account for a snapshot of the transient simulation, at a time equal to 0.6s. In Fig. 6.2, the results for the void fraction can be found, Fig.6.3 shows the results for liquid velocity, Fig. 6.4 presents the gas velocity, and Fig. 6.5 the pressure results are plotted.

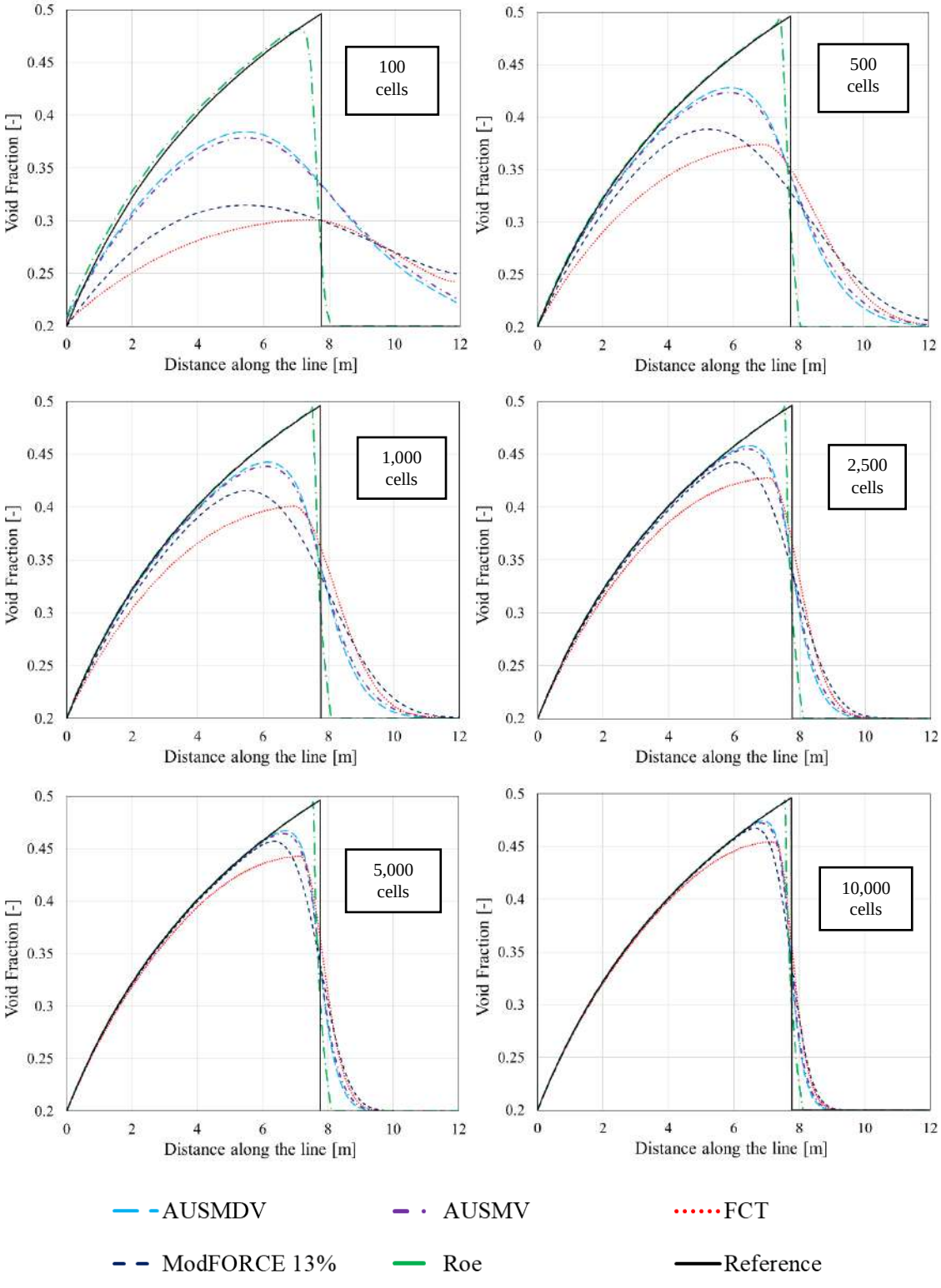

Figure 6.2:Water faucet problem, void fraction results using 4E1P model with multiple methods.

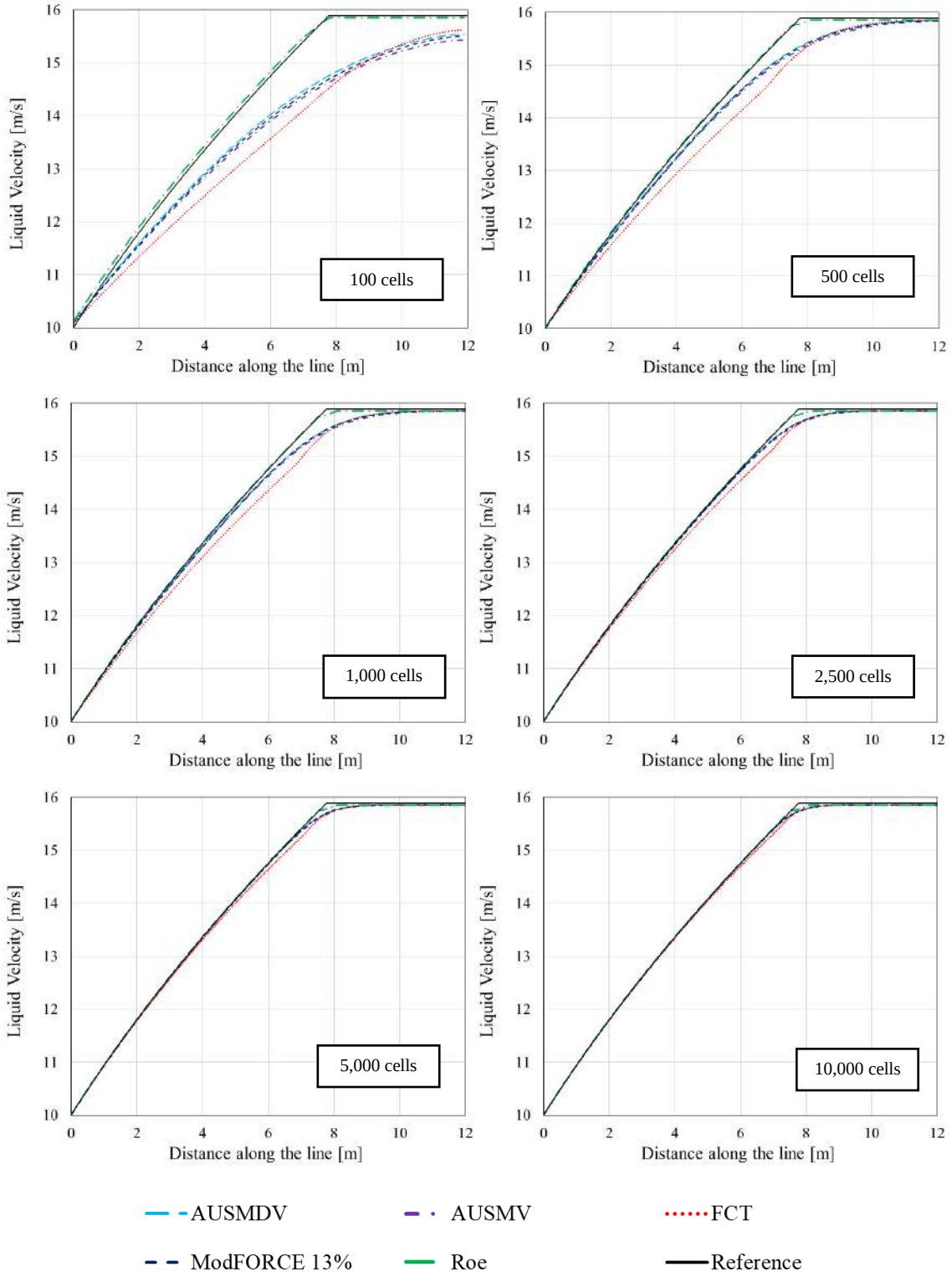

Figure 6.3:Water faucet problem, liquid velocity results using 4E1P model with multiple methods.

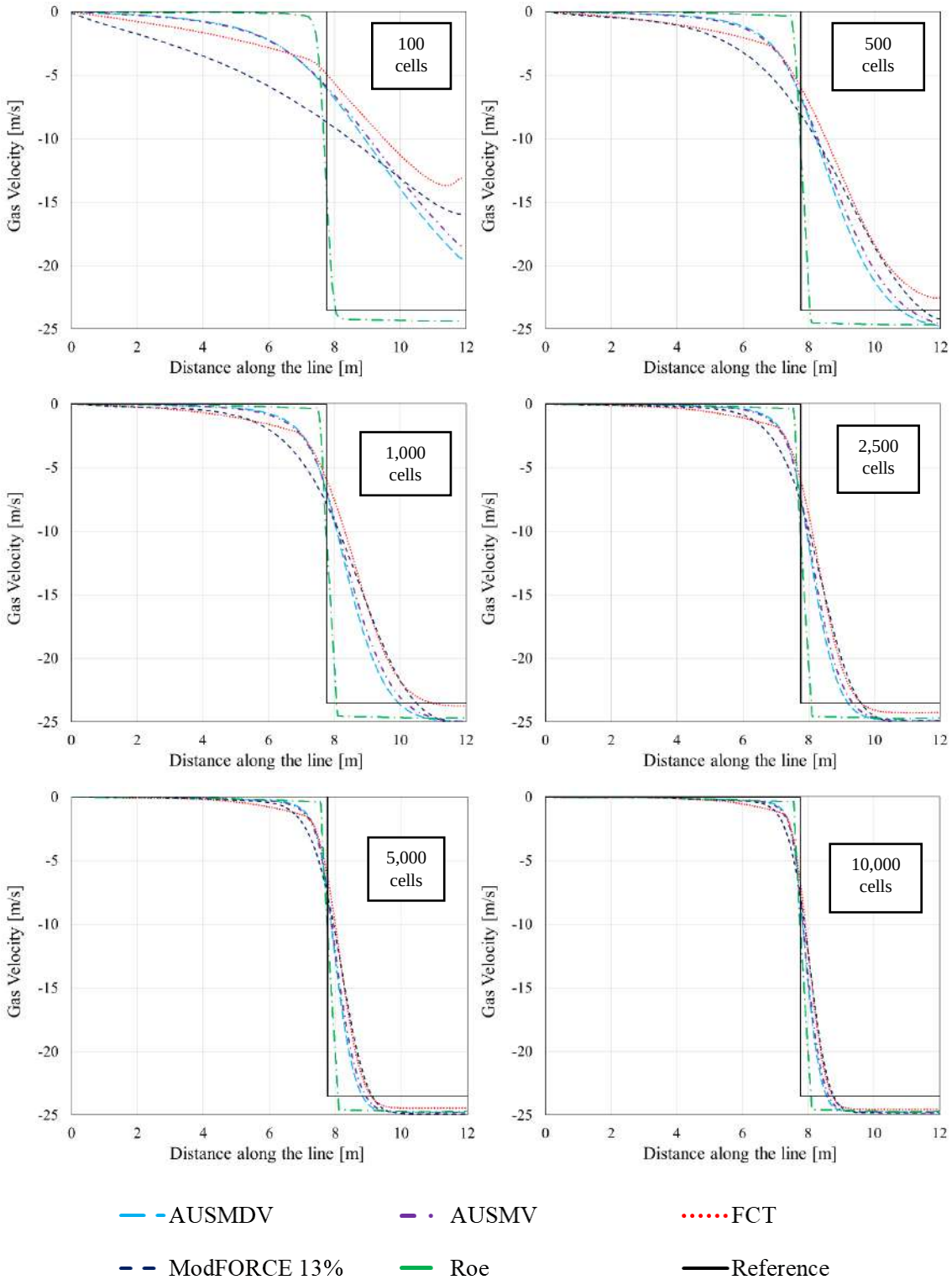

Figure 6.4:Water faucet problem, gas velocity results using 4E1P model with multiple methods.

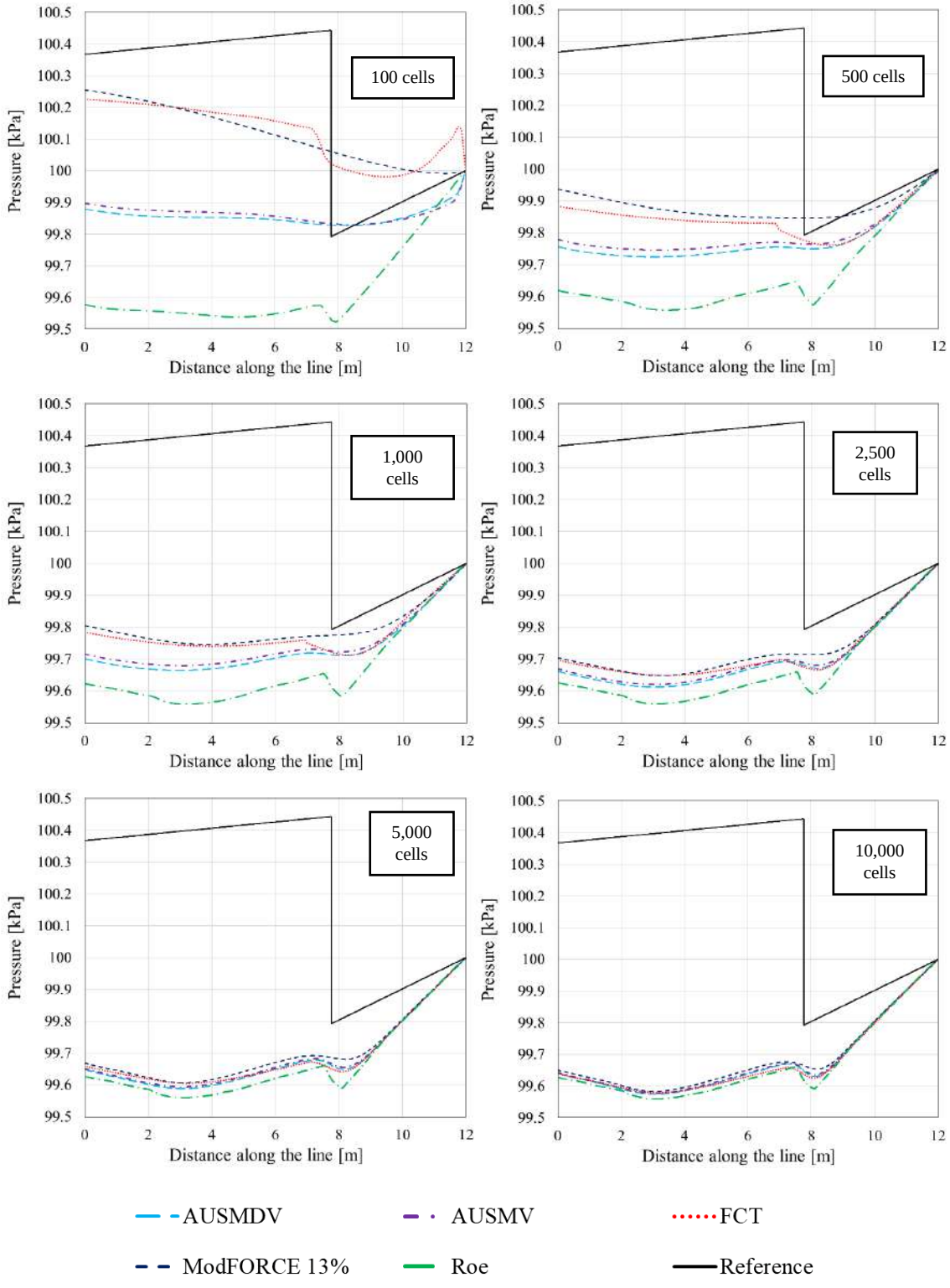

Figure 6.5:Water faucet problem, pressure results using 4E1P model with multiple methods.

It is worth mentioning that for all plots presented, the results for the Roe scheme with CFL=0.45 are omitted because for both CFL=0.45 and 0.90 the Roe scheme does not show any noticeable difference between the different CFL results. To optimize the determination of the inter-cell fluxes by balancing the diffusive and dispersive effects, the FORCE method was modified to the weight of ω =0.87, as suggested by Sondermann *et al.* (2021), and the FCT, for the same reasons, use $\mu_{i+1/2}^{FCT}$= 0.125 and $\nu_{i+1/2}^{FCT}$= 0.165, according to Freitas (2017).

In the void fraction results, it is evident that the Roe scheme better represents the analytical solution than any other method. It is remarkable that this scheme shows results with 100 cells that are comparable to the results of the other methods with 10000 cells in terms of the void fraction crest values and the sharpness of the discontinuity. In general, for all grid sizes, the AUSM-type methods follow as the next better results, with the ASUMDV showing a slightly better representation of the analytical solution than the AUSMV, followed by the ModFORCE and the FCT methods, where the FCT has a slightly sharper discontinuity, and the ModFORCE results showing a better representation of the crest top. As the grid gets refined, every method gets closer to the analytical solution, and, except for the Roe scheme, every method seems to have the same behavior in terms of order of accuracy in space. The Roe scheme seems to have less benefit in grid refinement in this study, however, as already mentioned, the method has smaller errors even with the smallest grid used if comparable to the other methods on the largest grid.

For the liquid and gas velocities, the same conclusions can be taken when comparing the simulated results with the analytical solution. In the liquid velocity profile, the numerical results correlate well with the analytical solution, this is evident as the finer the grid gets, the more accordance between the solutions is verified. However, in the gas velocity solutions, there are some differences from the numerical results with the analytical solution of Zou *et al.* (2016). In the discontinuity position, the solution has a good match, whereas the outlet velocity plateau has lower values in the numerical results.

The pressure numerical results have even more differences from the analytical solution in terms of behavior, but the low-pressure variations of the given problem must be considered. The differences between numerical results and the analytical solution provided by Zou *et al.* (2016) can be related to the hypothesis of zero interfacial pressure the authors consider to obtain their solution. For the 4E1P model, a zero interfacial

pressure would render the model to become non-hyperbolic, and Bestion (1990) is used to model the interfacial pressure. Thus, the results are not a one-to-one comparison, however, they are kept here as they are the only analytical reference provided in the literature for the pressure and gas velocity. It is important to mention that some authors that study the water faucet problem omit results for both gas velocity and pressure due to the lack of an analytical solution. When these results are provided, such as in Munkejord (2005) and Sondermann *et al.* (2021), the ones obtained by the herein work show excellent agreement. Then, the results obtained with the Roe scheme with 10000 cells can be used as a reference for the other ones.

To quantify a type of error between each method with the 4E1P model, the area between the curves of the numerical and analytical solution can be used, and is presented in Table 6.3, where the lower the results the better the solution. Note that the results expressed in the table corroborate with the previous discussions.

Table 6-3: Remaining area between curves for the water faucet problem using the 4E1P model with 2500 cells.

Method	Flow Variable	Remaining area
AUSMDV	Void Fraction -α_G	0.157165 $[-]_x[m]$
ASUMV	Void Fraction -α_G	0.173291 $[-]_x[m]$
FCT	Void Fraction -α_G	0.294920 $[-]_x[m]$
ModFORCE 13%	Void Fraction -α_G	0.252893 $[-]_x[m]$
Roe (*CFL=0.45*)	Void Fraction -α_G	0.039286 $[-]_x[m]$
Roe (*CFL=0.90*)	Void Fraction -α_G	0.039262 $[-]_x[m]$
AUSMDV	Liq. velocity -v_L	0.519644 $[m/s]_x[m]$
ASUMV	Liq. velocity -v_L	0.612666 $[m/s]_x[m]$
FCT	Liq. velocity -v_L	0.294920 $[m/s]_x[m]$
ModFORCE 13%	Liq. velocity -v_L	0.252893 $[m/s]_x[m]$
Roe (*CFL=0.45*)	Liq. velocity -v_L	0.186876 $[m/s]_x[m]$
Roe (*CFL=0.90*)	Liq. velocity -v_L	0.186858 $[m/s]_x[m]$

Following the same fashion, the next simulation results are presented in Figs. 6.6 to 6.9, and report the simulations for each one of the models coded using the 5E2P model.

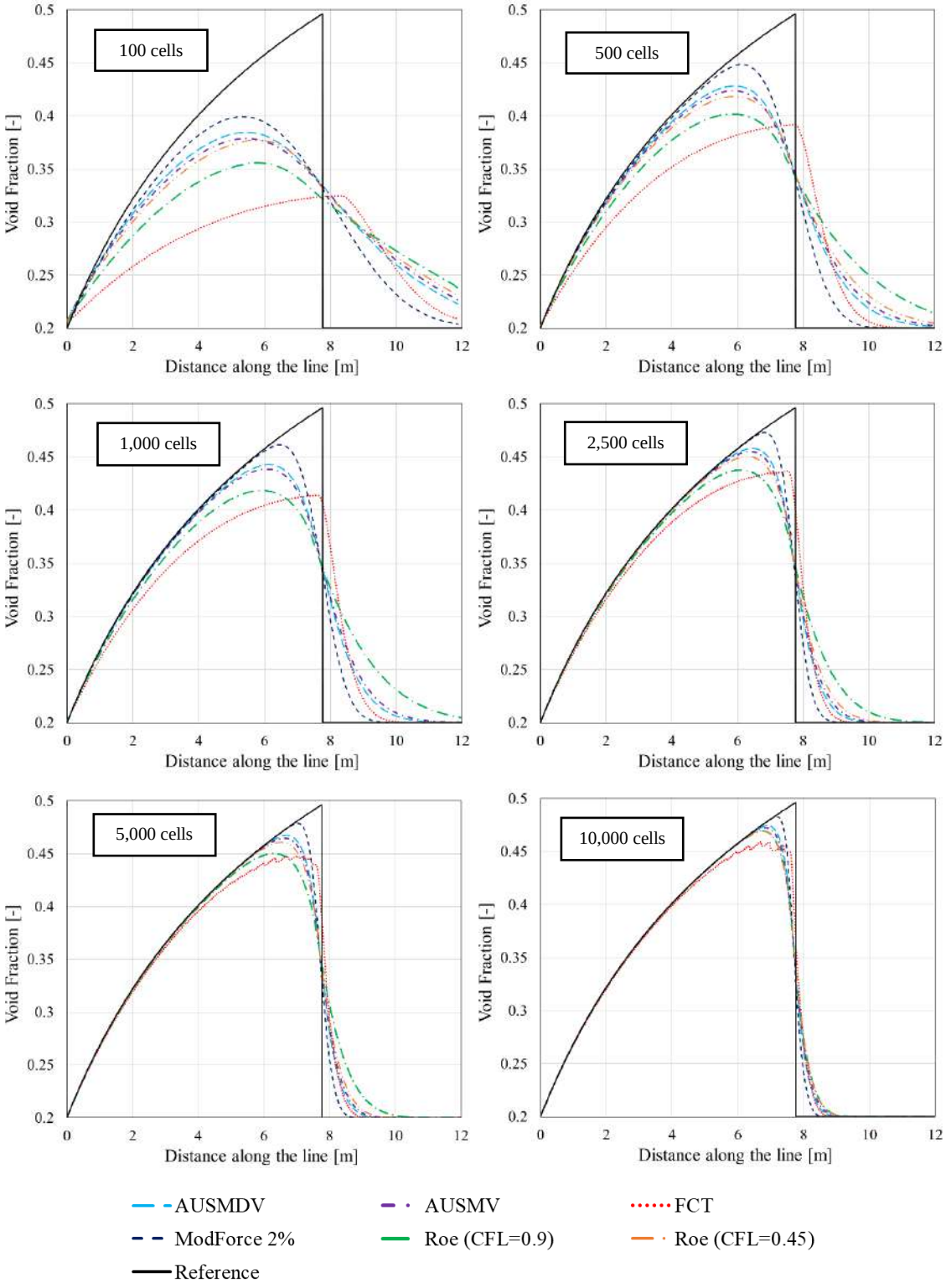

Figure 6.6:Water faucet problem, void fraction results using 5E2P model with multiple methods.

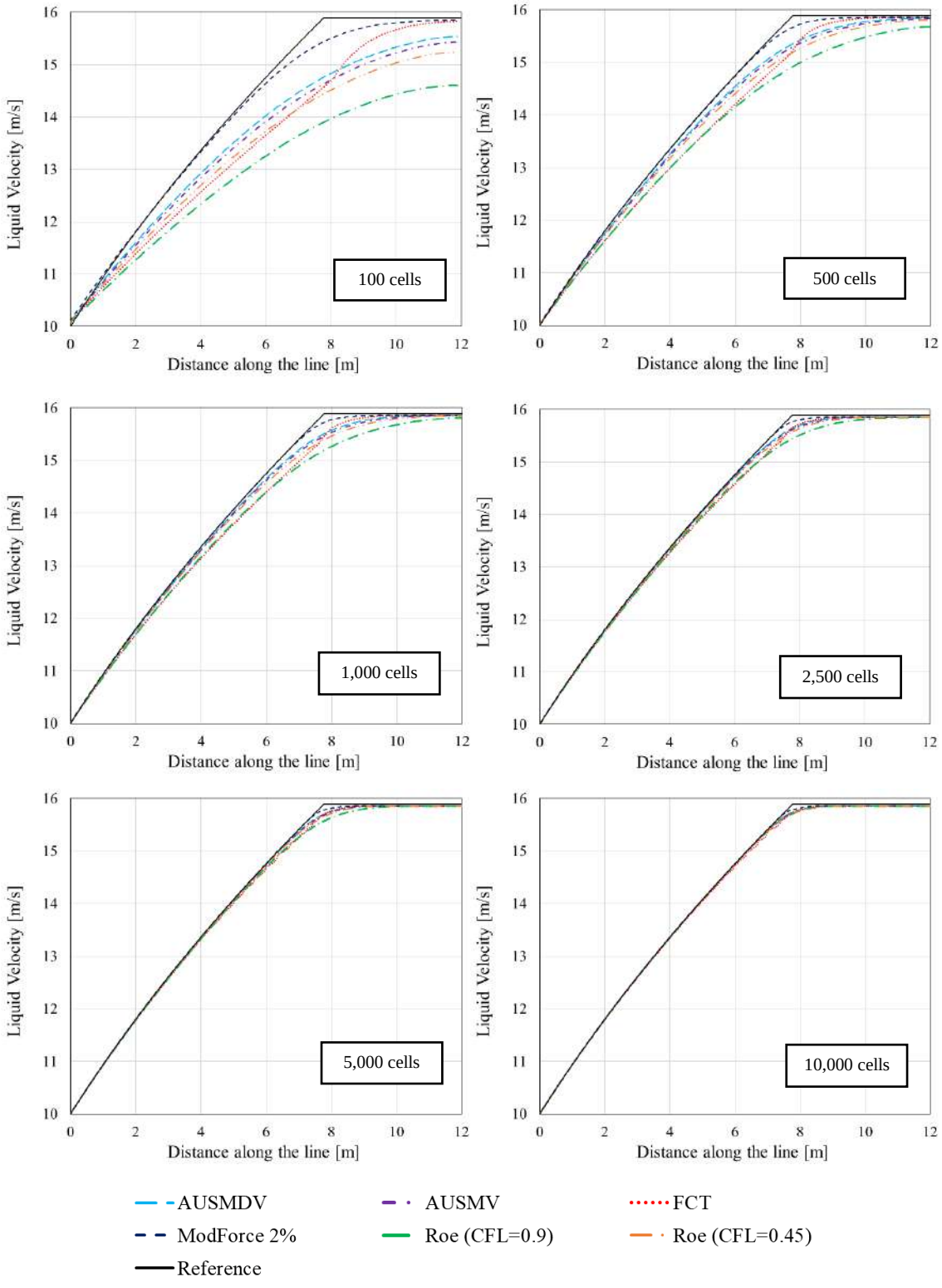

Figure 6.7:Water faucet problem, liquid velocity results using 5E2P model with multiple methods.

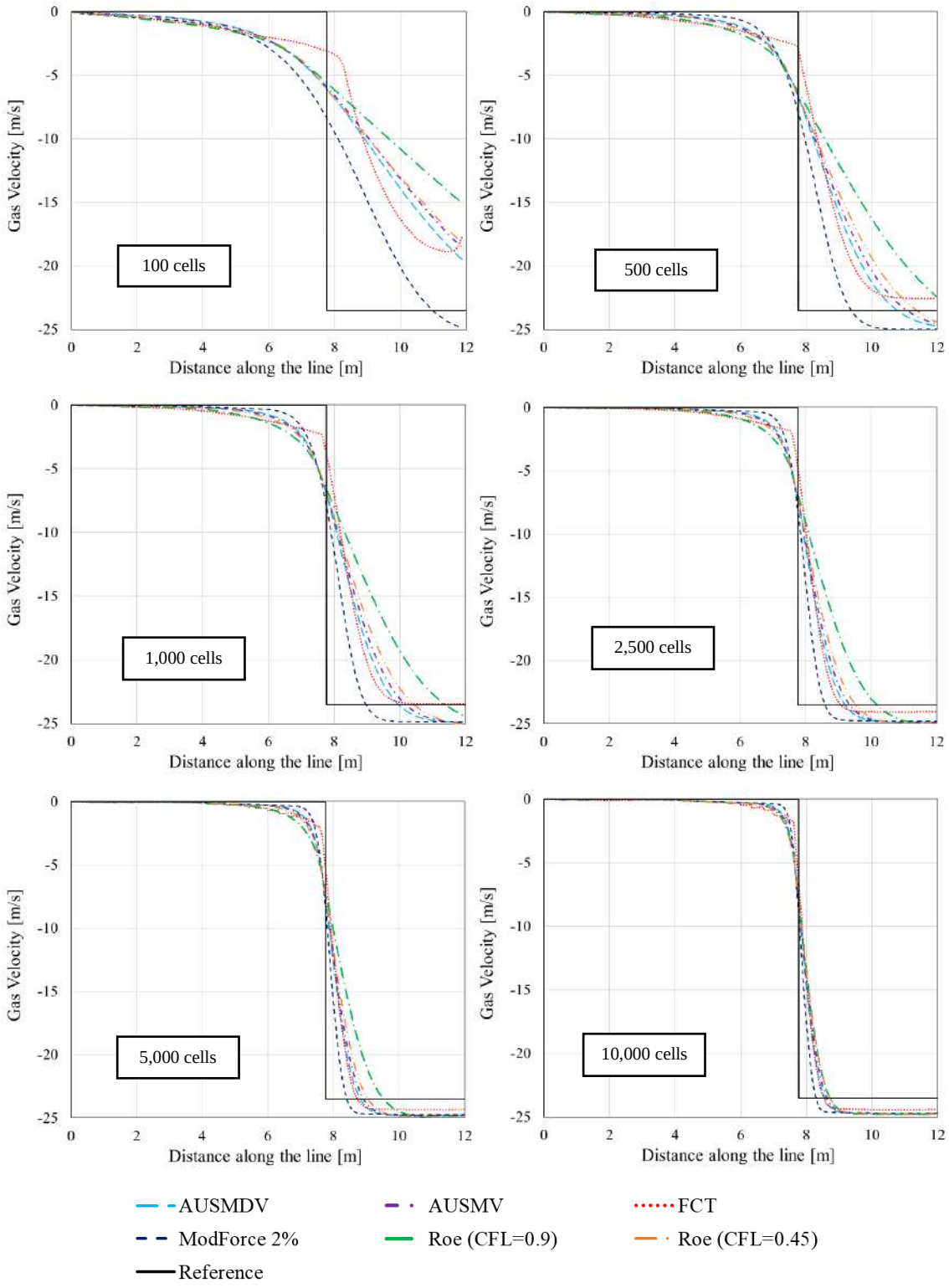

Figure 6.8:Water faucet problem, gas velocity results using 5E2P model with multiple methods.

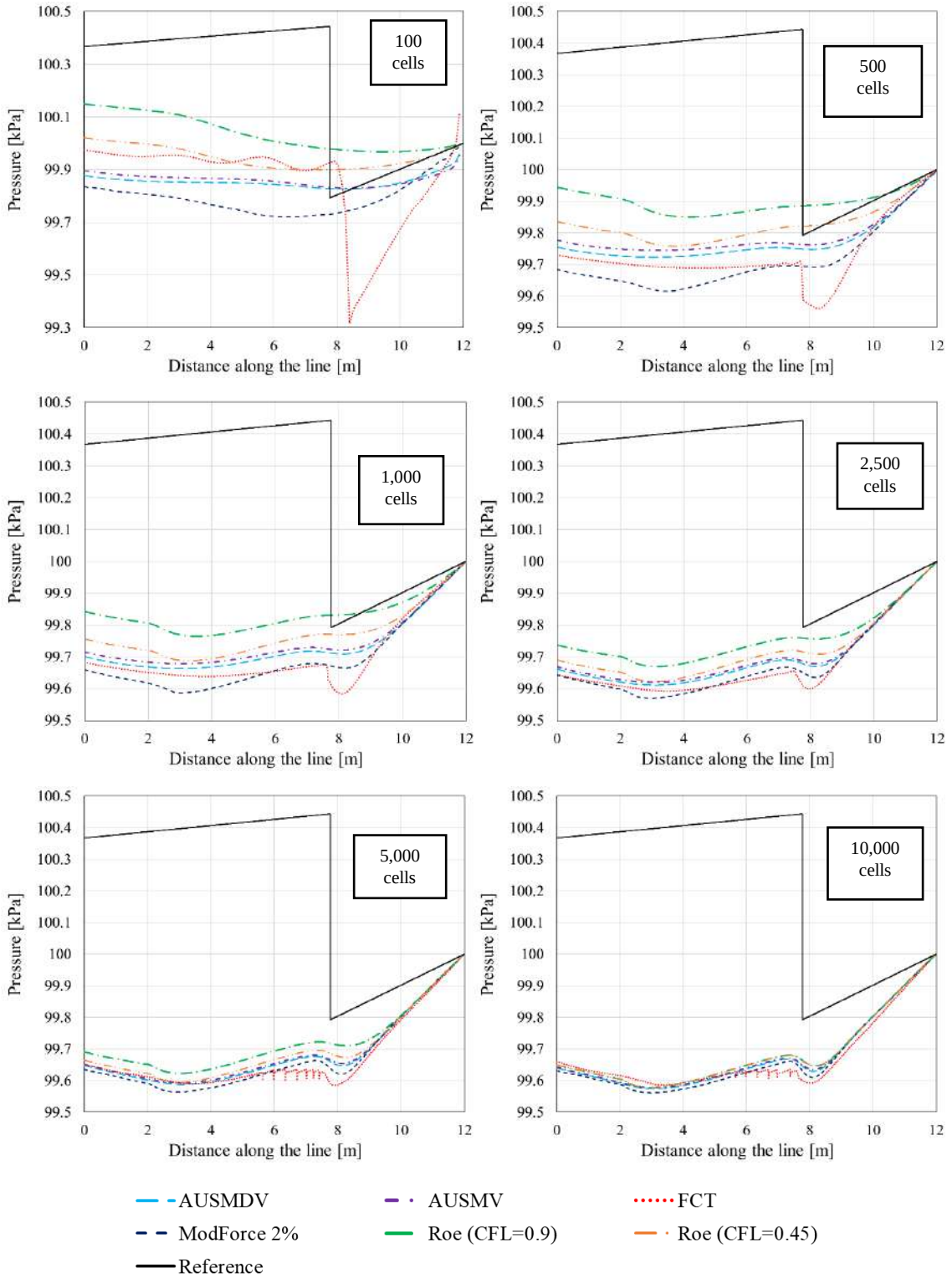

Figure 6.9:Water faucet problem, pressure results using 5E2P model with multiple methods.

Once more, to optimize the determination of the inter-cell fluxes by balancing the diffusive and dispersive effects, the FORCE method was modified to the weight of ω =0.98, as suggested by Sondermann *et al.* (2021), and the FCT method, for the same reasons, use $\mu_{i+1/2}^{FCT}$= 0.125 and $\nu_{i+1/2}^{FCT}$= 0.135, according to Freitas (2017). Note that the coefficients are different from the 5E2P showing that the models adjust differently under the influence of numerical diffusion and dispersion. Differently from the 4E1P, the results with the 5E2P model with the Roe scheme show differences with CFL=0.45 and 0.9, so both solutions are included in the plot.

Contrasting with the results obtained with the 4E1P model, the Roe scheme with the 5E2P model did not result in the most accurate for any of the grid sizes. Also, the Roe scheme benefits more with both grid refinement and the lower CFL number. In the void fraction results, for all mesh sizes, the ModFORCE method shows the more accurate results for all grid sizes explored, in representing the sharpness of the discontinuity, the void fraction crest peak, and discontinuity position. This can be explained since this method-model combination is able to handle 98% of the Richtmyer method balance under the FOCE method without any spurious oscillations, and the Richtmyer method is known for being second-order accurate in space and time, higher than the other methods. This also repeats for the liquid velocity results. If the 4E1P model is used with the Roe scheme and 10000 cells as reference for gas velocity and pressure, the same can be stated for the gas velocity and pressure results.

To quantify the error of each method with the 5E2P the area between curves is used again, see Table 6.4. The area between curves corroborates with the visual inspection of the plots where the ModFORCE has lower errors followed by the AUMSDV, AUSMV, Roe scheme, and FCT. The table shows the results for 2500 cells again, and for simplicity, other mesh sizes are omitted, since the same conclusions are found.

Table 6-4: Remaining area between curves for the water faucet problem using the 5E2P model with 2500 cells.

Method	Flow Variable	Remaining area
AUSMDV	Void Fraction -α_G	0.157156 $[-]_x$[m]
ASUMV	Void Fraction -α_G	0.173291 $[-]_x$[m]
FCT	Void Fraction -α_G	0.230663 $[-]_x$[m]
ModFORCE 2%	Void Fraction -α_G	0.099182 $[-]_x$[m]
Roe (*CFL=0.45*)	Void Fraction -α_G	0.195822 $[-]_x$[m]
Roe (*CFL=0.90*)	Void Fraction -α_G	0.274311 $[-]_x$[m]
AUSMDV	Liq. velocity -v_L	0.519565 $[m/s]_x$[m]
ASUMV	Liq. velocity -v_L	0.612587 $[m/s]_x$[m]
FCT	Liq. Velocity -v_L	0.230663 $[m/s]_x$[m]
ModFORCE 2%	Liq. velocity -v_L	0.099182 $[m/s]_x$[m]
Roe (*CFL=0.45*)	Liq. velocity -v_L	0.195822 $[m/s]_x$[m]
Roe (*CFL=0.90*)	Liq. velocity -v_L	0.274311 $[m/s]_x$[m]

It is important to recognize that all the model-method combinations were able to represent the expected physics of the problem with reasonable magnitudes for all flow parameters. When comparing all combinations, the Roe scheme with the 4E1P model clearly represents better the problem, however, the option of using the 5E2P model must not be disregarded, since it is more wide range of hyperbolicity with unconditional hyperbolicity under subcritical velocities.

To give an idea of the computational work spent by each of the model-method combinations, Table 6.5 shows an example of the computational time demanded by all the results obtained with a mesh of 10000 cells. The results were obtained using Fortran language compiled on Intel® Fortran Compiler (Visual Studio 2020) on a Microsoft Windows 11 operational system. The machine CPU has an Intel® Core™ i7-12700K (25M Cache, up to 5.0GHz) with 32Gb DDR4 3600 MHz RAM.

Table 6-5: Computational time for the water faucet problem under various configurations.

Model	Grid size	Method	CFL	CPU time
4E1P	10,000	AUSMDV	0.45	01h:00m:30.156s
4E1P	10,000	AUSMV	0.45	00h:56m:39.031s
4E1P	10,000	FCT	0.45	01h:12m:04.172s
4E1P	10,000	ModFORCE 13%	0.45	00h:45m:43.109s
4E1P	10,000	Roe	0.45	07h:18m:56.718s
4E1P	10,000	Roe	0.90	04h:08m:44.781s
5E2P	10,000	AUSMDV	0.45	01h:30m:15.344s
5E2P	10,000	AUSMV	0.45	01h:25m:17.422s
5E2P	10,000	FCT	0.45	01h:47m:59.187s
5E2P	10,000	ModFORCE 2%	0.45	01h:19m:49.672s
5E2P	10,000	Roe	0.45	04h:14m:14.391s
5E2P	10,000	Roe	0.90	01h:39m:51.172s

Note that the evaluated CPU time and real-time may change every different run, with different temperature, power output, and other factors, however, they give an excellent estimation of the computational demands of each model-method combination. For every method, except the Roe scheme, the 4E1P model renders results slightly faster than the 5E2P model, that is obviously because more equations are required to be solved, but also because of the additional computation of the instantaneous pressure relaxation procedure. Note that the 4E1P here is faster because an upper bound value for λ_{max} is used for the 4E1P model with $\lambda_{max} = c_L$, as reported in Table 6.5. This is done to get the same time step with the same grid size with both models. Establishing an upper bound helps the 4E1P methods by not requiring the calculation of the eigenvalues at every cell location at all time steps, since the root-finding procedure for the characteristic polynomial, Eq.(4.32,) is computationally demanding. Note also that using an upper bound does not negatively affect the results since the time steps are smaller than by using the real values of λ_{max}, thus CFL condition is also guaranteed. With the Roe scheme, the opposite takes place with the 5E2P model rendering faster results, the scheme requires the computation of the eigenstructure of the system with the 5E2P model the eigenvalues and eigenvectors

are obtained analytically, whereas the 4E1P requires their computation by solving the eigenstructure numerically. For the herein codes, the numerical computation of the eigenvalues and eigenvectors of the 4E1P is more computationally demanding than the extra equations and relaxation procedure of the 5E2P code.

6.2 Two-Fluid Shock-Tube Problem

The shock tube problem selected as a benchmark is an initial value problem named large relative velocity previously investigated in the works of Cortes *et al.* (1998), Evje and Flätten (2003), Munkejord (2006), Ferrari *et al*. (2017), Sondermann *et al.* (2021) and Sondermann (2021). It is another problem that evaluates the model-method combination in dealing with discontinuities and sharp gradients. This conceptual problem can be interpreted as a duct where two established states exist in the fluid domain. The discontinuity is set at the middle of the pipe separating the left and right states, as detailed in Table 6.6.

Table 6-6: Left and right states of the large relative velocity shock tube problem.

Flow variable	Left side	Right side
Gas velocity-u_G	65m/s	50m/s
liquid velocity-u_L	1m/s	1m/s
Void Fraction-α_G	0.29(-)	0.3(-)
Pressure-p	265000Pa	265000Pa

The problem establishes a discontinuity in the gas velocity and a slight discontinuity in the liquid velocity. Note that the velocities between fluids are quite large, given the problem its name. Note that no friction is considered in this benchmark, so the fluids do not interact via interfacial friction, however, the phases are linked through their volume fractions, common pressure, and the interfacial pressure for the required constant parameters to set up the simulation see Table 6.7.

Table 6-7: Simulation set up for the large relative velocity shock tube benchmark.

Constant	Value
Pipe length	100 m
Sound speed in the liquid	1000 m/s
Sound speed in the gas	316.2 m/s
Reference gas density	0 kg/m³
Reference liquid density	1000 kg/m³
Discontinuity initial location	50 m
Pipe inclination	0 º
Time (snapshot)	0.1 s
Mesh size	2000 cells

Unfortunately, like many other benchmarks for two-phase flow, this shock tube problem does not have an analytical solution, hence the results presented here are compared against the well-established numerical results of Evje and Flätten (2003).

In the following plot, Fig. 6.10, the results for void fraction are presented for both 4E1P and 5E2P models in several grid sizes, followed by the liquid velocity in Fig. 6.11, gas velocity in Fig. 6.12, and pressure in Fig. 6.13.

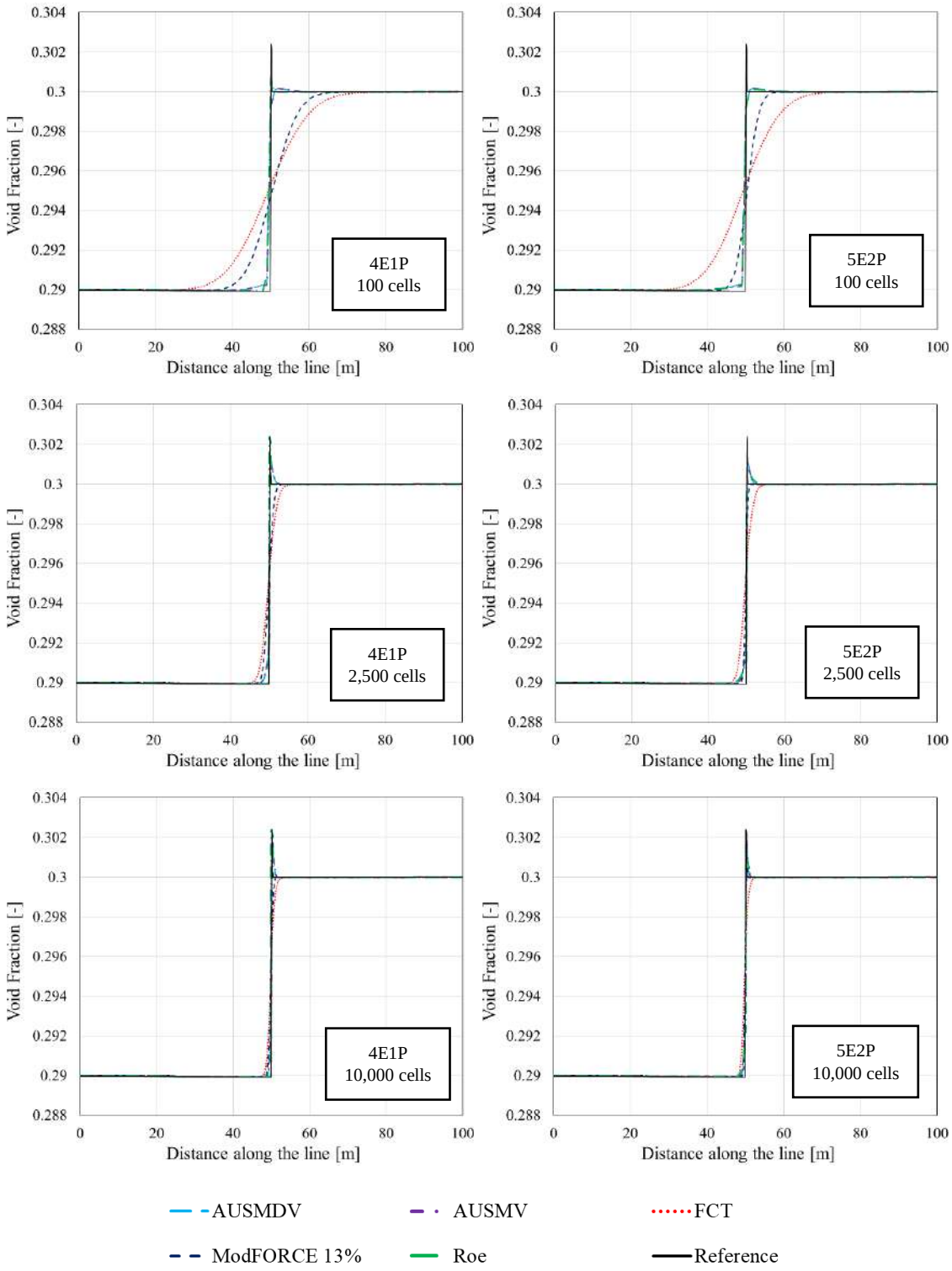

Figure 6.10:Shock tube problem, void fraction results with multiple methods.

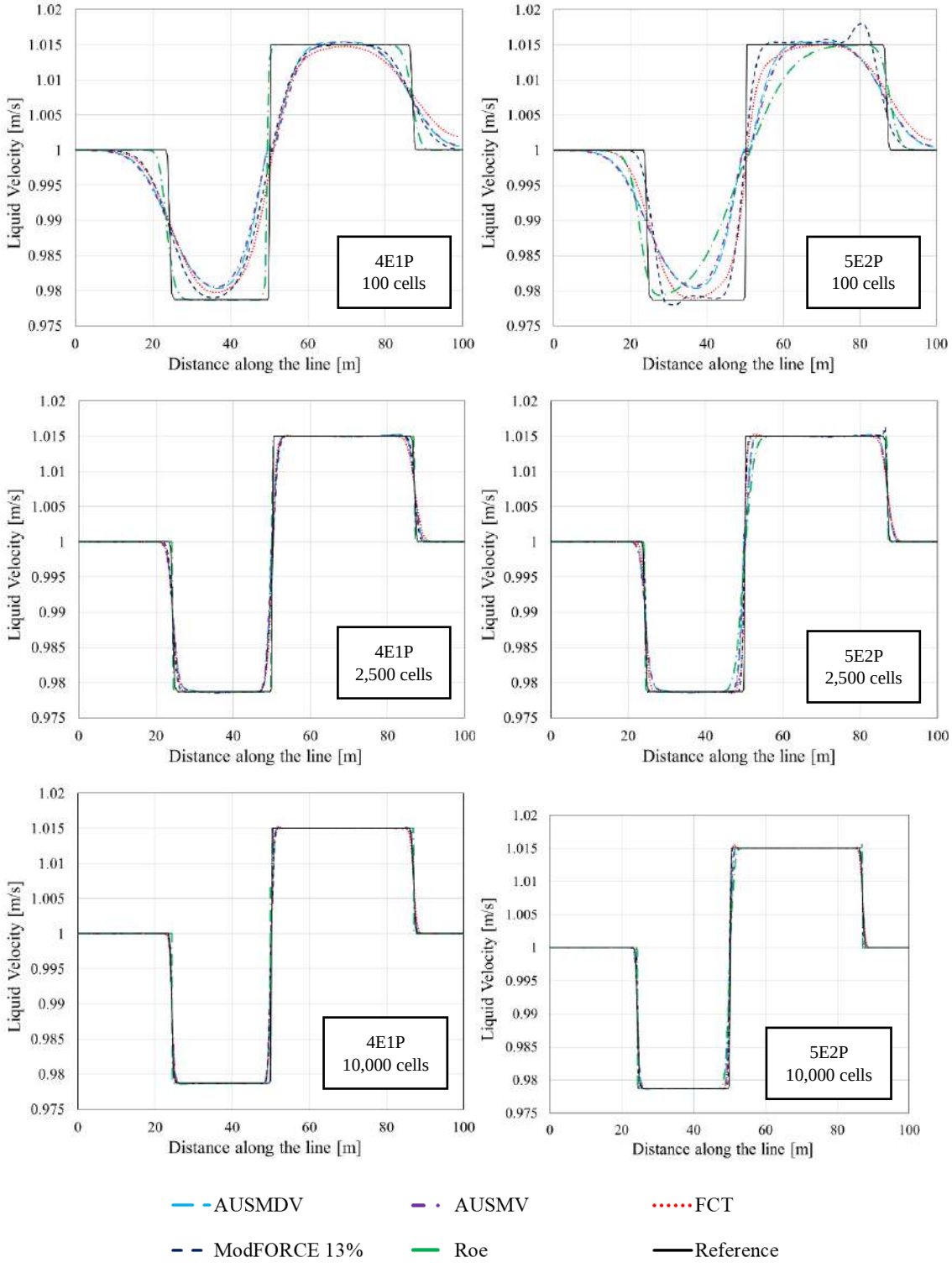

Figure 6.11: Shock tube problem, liquid velocity results with multiple methods.

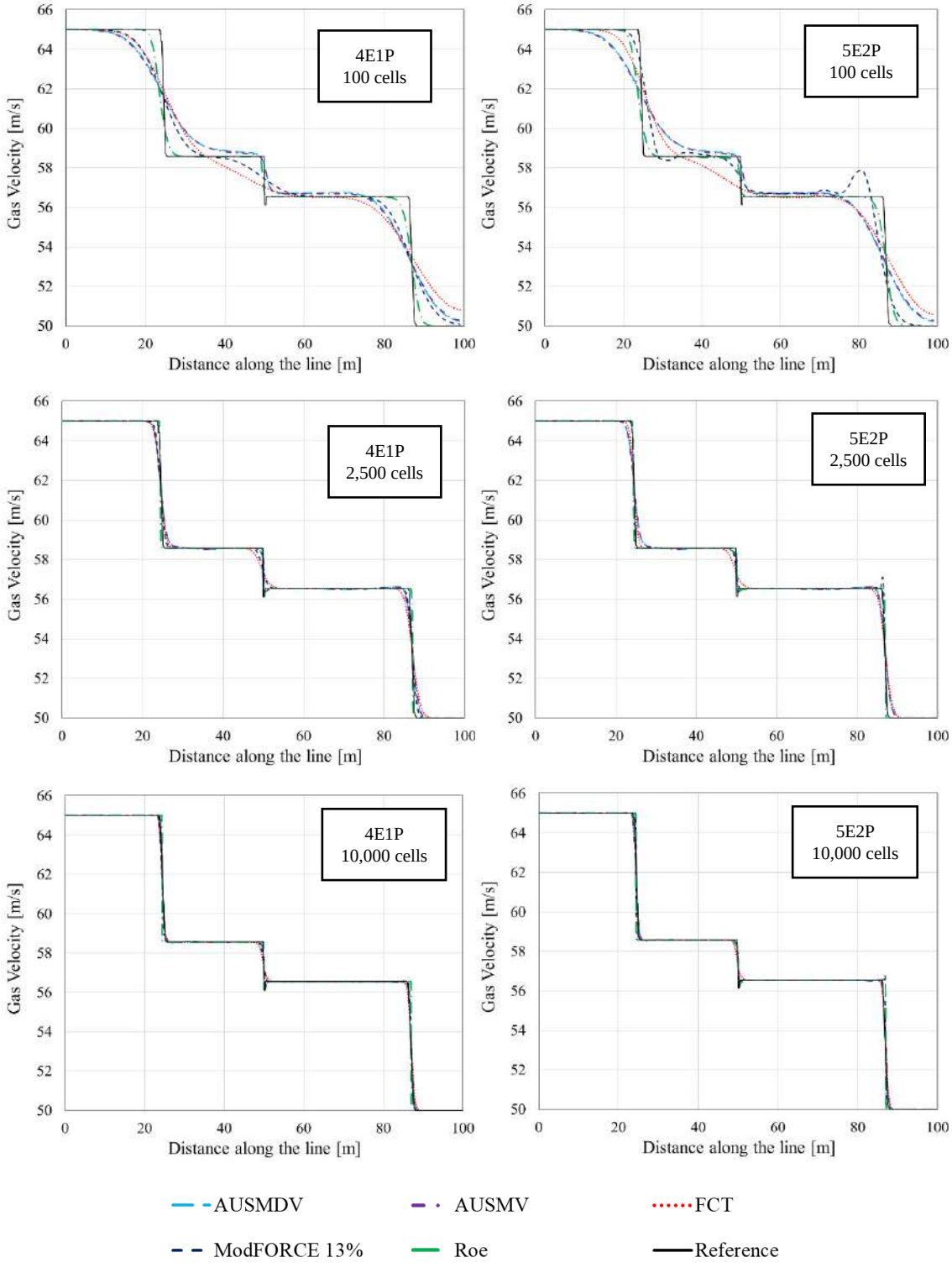

Figure 6.12:Shock tube problem, gas velocity results with multiple methods.

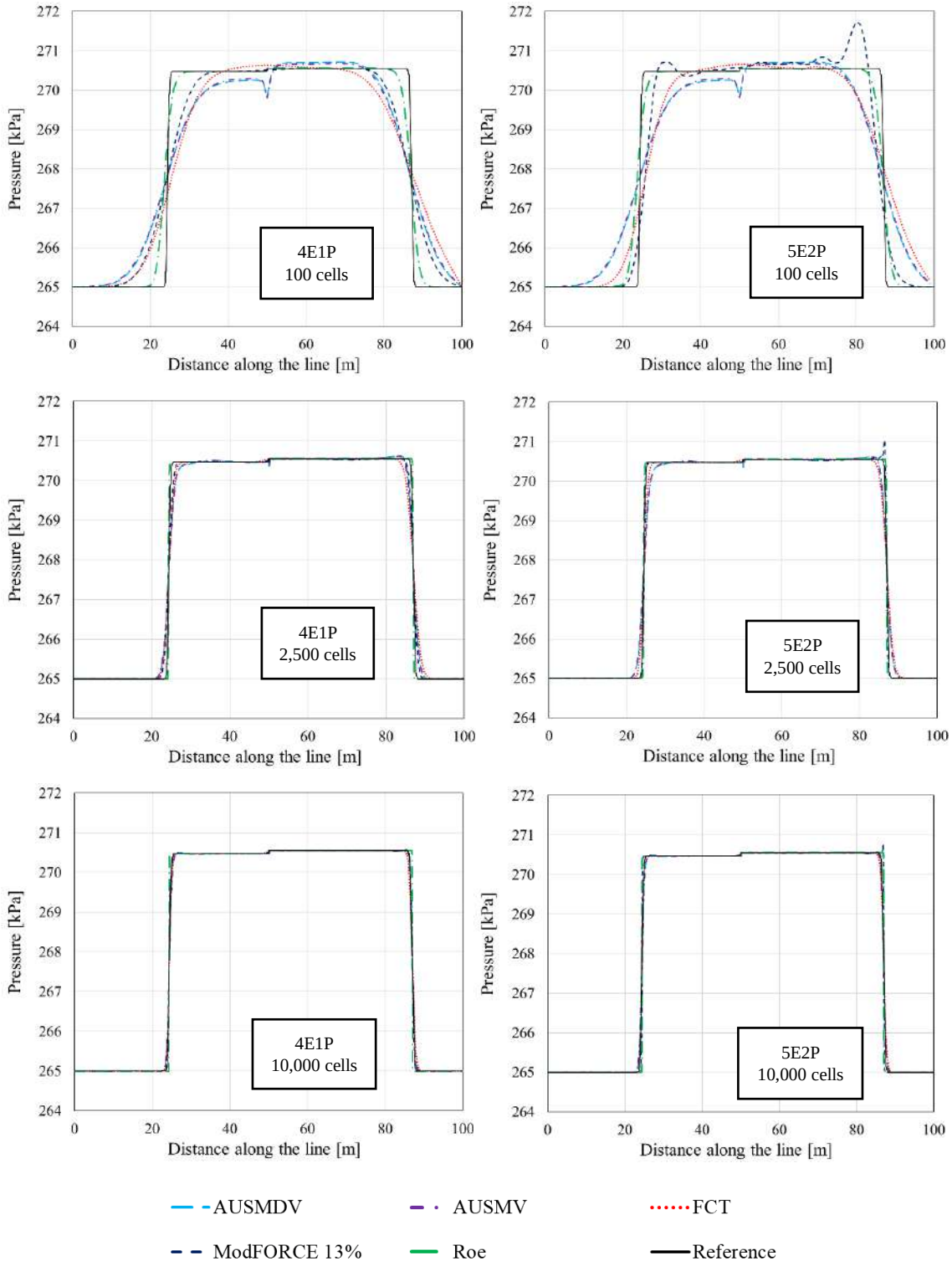

Figure 6.13: Shock tube problem, pressure results with multiple methods.

From these results, similar conclusions from the water faucet benchmark can be inferred. First, all model-method combinations can predict the expected physics from the reference solution, with the sharp discontinuities being well tracked and represented in the transient solution. Again, the 4E1P model with the Roe scheme seems quite remarkable as it represents the solution better than the others, even on coarser grids. For the 5E2P model, the ModFORCE scheme seems better as well, however, there is not much difference between the different methods, especially on finer grids.

6.3 Pipeline Stratified Flow

As for final validation, stratified flow two cases for a full-scale pipeline flow under stratified conditions were selected. Since there is a lack of field data openly available, the two cases studied by Figueiredo *et al.* (2017) are selected. The results obtained are compared with Figueiredo *et al.* (2017) and with the commercial software OLGA.

Figueiredo *et al.* (2017) use one of the model-method combinations that is used in the present work, which is the 4E1P model with the FCT method, and the same closures. However, there is a difference in the treatment of the non-conservative term resulting from the momentum equations, Eq. (4.3) and Eq. (4.4). There are two ways of writing this term, by including both interfacial pressure and fluid pressure on the conservative and non-conservative sides, as considered here, or as the authors did by separating the fluid pressure on the conservative side and the interfacial pressure on the non-conservative. Freitas (2017) did a study on this matter and verified that some minor differences exist between the two choices. The choice of the treatment of the non-conservative terms here is done based on the Roe scheme results given in the previous benchmarks, since the Roe scheme is based on the mathematical model written in a quasi-linear form it is not biased by this choice, also the conditions for the linearized flow matrix are robust towards the method being conservative. Then, the non-conservative term that converges to the Roe scheme solution was selected for both 4E1P and 5E2P.

The OLGA Dynamic Multiphase Flow is used here as a comparison as well since it is widely used by the oil and gas industry. OLGA was initially developed in 1980, but constant development was applied to it since then. The software models the flow in three phases, gas, liquid (oil-water mixture), and a water-oil droplet dispersed in the gas phase through three continuity equations, three momentum equations, and an energy equation. For its numerical method, OLGA uses a first-order implicit upwind scheme for both space

and time integration, and the option to solve the continuity equations in space through a second-order accurate TVD scheme (Total Variation Diminishing). For thermodynamic state closure, OLGA relies on PVT (Pressure Volume Temperature) table files containing the equilibrium thermodynamic properties of the fluids as a function of pressure, temperature, and composition.

For the following simulations, the horizontal pipeline given in Table 6.8 will be considered. The simulation starts by assuming a uniform flow field where the flow parameters are constant from the inlet to the outlet and given by the values of each respective boundary condition. From the initial condition, the simulation is left to run until it reaches a steady-state. As criteria for time convergence towards obtaining steady-state flow conditions the following can be employed, evaluating both the conservative and primitive variables,

$$\xi_{\mathbf{q},i}^{n+1}(\mathbf{q}) = \max\left[\frac{\left|\left(q_j\right)_i^{n+1} - \left(q_j\right)_i^{n}\right|}{\max\left(1, \left(q_j\right)_i^{n}\right)}\right], \tag{4.5}$$

$$\xi_{\mathbf{w},i}^{n+1}(\mathbf{w}) = \max\left[\frac{\left|\left(w_j\right)_i^{n+1} - \left(w_j\right)_i^{n}\right|}{\max\left(1, \left(w_j\right)_i^{n}\right)}\right], \tag{4.6}$$

$$\max\left[\xi_{\mathbf{q}}^{n+1}(\mathbf{q}), \xi_{\mathbf{w}}^{n+1}(\mathbf{w})\right] \leq 10^{-6}, \tag{4.7}$$

where $i \in \{1, N_x\}$, and $j \in \left\{1, n_{eq}\right\}$.

Table 6-8: Pipe properties for the stratified flow cases.

Parameter	Symbol	Value
Pipe length	L	45 km
Pipe diameter	d	0.45 m
Inclination Angle	θ	0
Roughness	ε	4.572_x10^{-5} m

In the next subsections, the results of two flow scenarios will be given, evaluated against the expected physics of the problem, and compared with the references. Followed

by the presentation of the results, an accuracy analysis of each numerical scheme will be presented. Note that for the herein studied methods, no significant difference is seen, with the main difference being between the models Then, for simplicity of visualization in the following primitive variables plots, only the results with the Roe scheme are presented. For direct comparison with the reference, a grid of 2500 cells is used for both cases, where Figueiredo *et al.* (2017) conclude the FCT method is second order in space accurate.

6.3.1 Case 1: Relative Low Holdup

The first case, named by Figueiredo *et al.* (2017) as a low holdup case, addresses a lower limit of the void fraction where the flow in the pipeline is stratified. The fluid properties are given in Table 6.9, and the boundary conditions are given in Table 6.10.

Table 6-9: Fluid Properties for the stratified flow case 1.

Parameter	Symbol	Value
Temperature	T	273 K²
Ideal gas constant	R	419.6 J/kg.K
Sound speed in gas	$c_G = \sqrt{RT}$	338.45 m/s
Sound speed in liquid	c_L	900 m/s
Reference gas density	$\rho_{0,G}$	0 kg/m^3
Reference liquid density	$\rho_{0,L}$	719.7 kg/m^3
Dynamic viscosity gas	μ_G	1.2847_x10^{-5} Pa.s
Dynamic viscosity liq.	μ_L	0.4207_x10^{-3} Pa.s

Table 6-10: Inlet and outlet boundary conditions for the stratified flow case 1.

Flow Variable	Value
α_L at inlet ($x=0$)	0.008
u_G at inlet ($x=0$)	5.25 m/s
u_L at inlet ($x=0$)	0.98 m/s
p at outlet ($x=L$)	6 MPa

The pressure distribution along the line, given in Fig. 6.14, shows excellent agreement between the methodology herein used and the references. Also, the pressure distribution shows the negative pressure gradient generated by the friction losses of the fluids against the pipe walls and the interactions between the phases. In the steady-state, the mass flow rate of each phase is constant since the continuity equations are separate for each fluid. The pressure drops as the gas expands and accelerates along the pipeline, which is presented in Fig. 6.15. The liquid, on the other hand, does not have considerable compressibility in the 5E2P model or is considered incompressible in the 4E1P, then, its increase in velocity comes mainly from the momentum exchange between phases that occur through the interfacial friction, as can be noticed in Fig. 6.16. As the liquid accelerates along the line, to keep the mass flow rate constant, there is a decrease in the holdup (Fig. 6.17).

As shown in the following figures, all the expected behaviors match the obtained results and show also great accordance with the references. The following Tables 6.11 and 6.12 show the obtained maximum relative differences between the current results and the references.

Table 6-11: Relative difference 4E1P with Roe against references for stratified case 1.

Flow variable	Relative difference OLGA	Relative difference Figueiredo *et al.* (2017)
Holdup -α_L	19.57%	20.89%
Gas velocity-u_G	1.86%	0.40%
Liq. velocity -u_L	41.52%	5.01%
Pressure -p	0.06%	0.13%

Table 6-12: Relative difference 5E2P with Roe against references for stratified case 1.

Flow variable	Relative difference OLGA	Relative difference Figueiredo *et al.* (2017)
Holdup -α_L	18.77%	20.11%
Gas velocity-u_G	2.34%	0.09%
Liq. velocity -u_L	39.72%	6.22%
Pressure -p	0.014%	0.27%

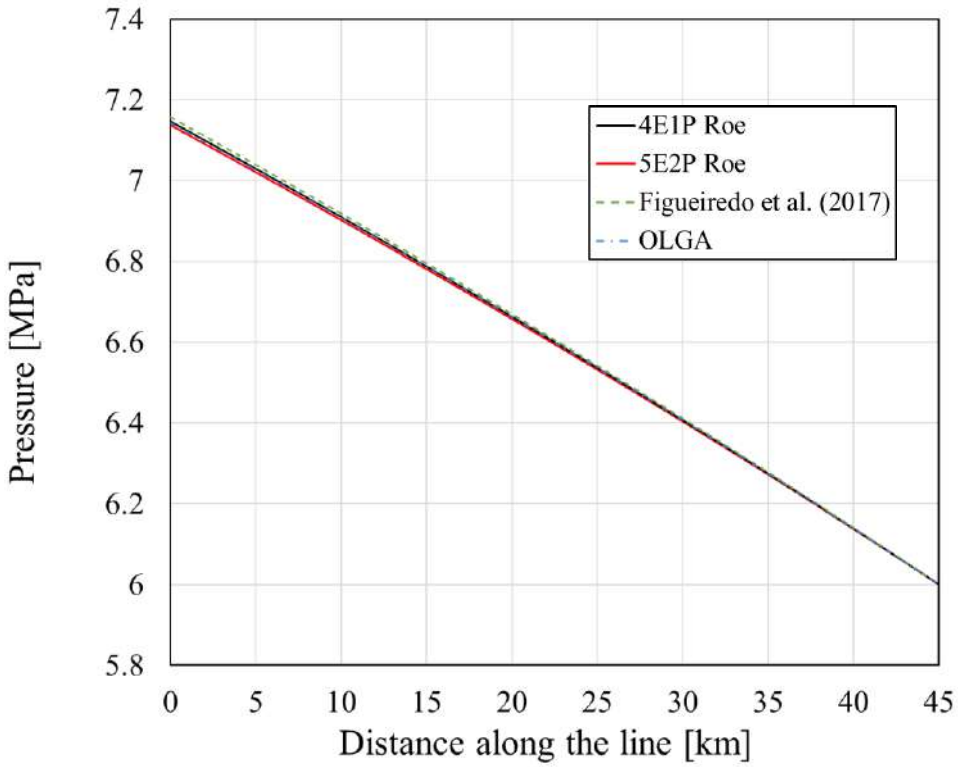

Figure 6.14: Pressure distribution, stratified flow case 1.

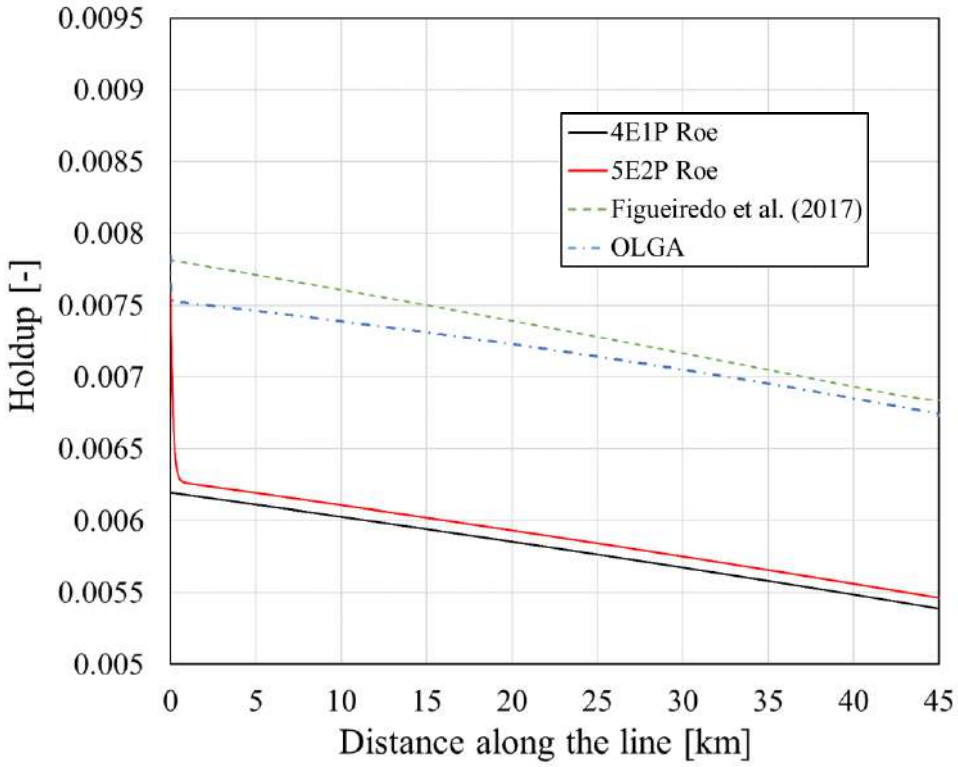

Figure 6.15: Holdup distribution, stratified flow case 1.

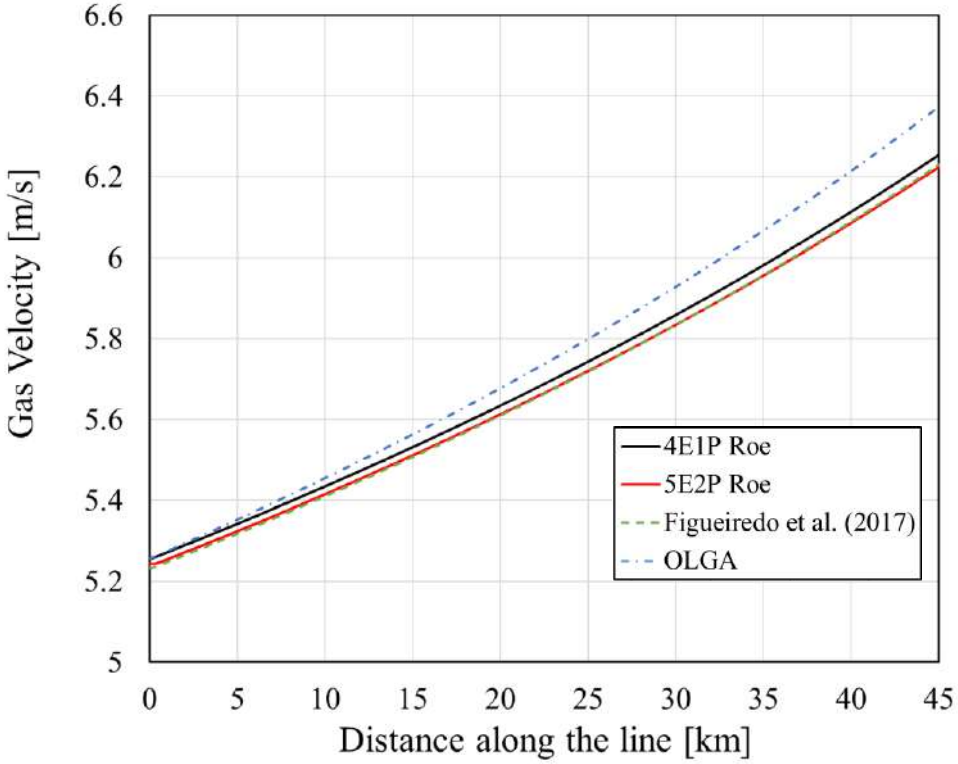

Figure 6.16: Gas velocity distribution, stratified flow case 1.

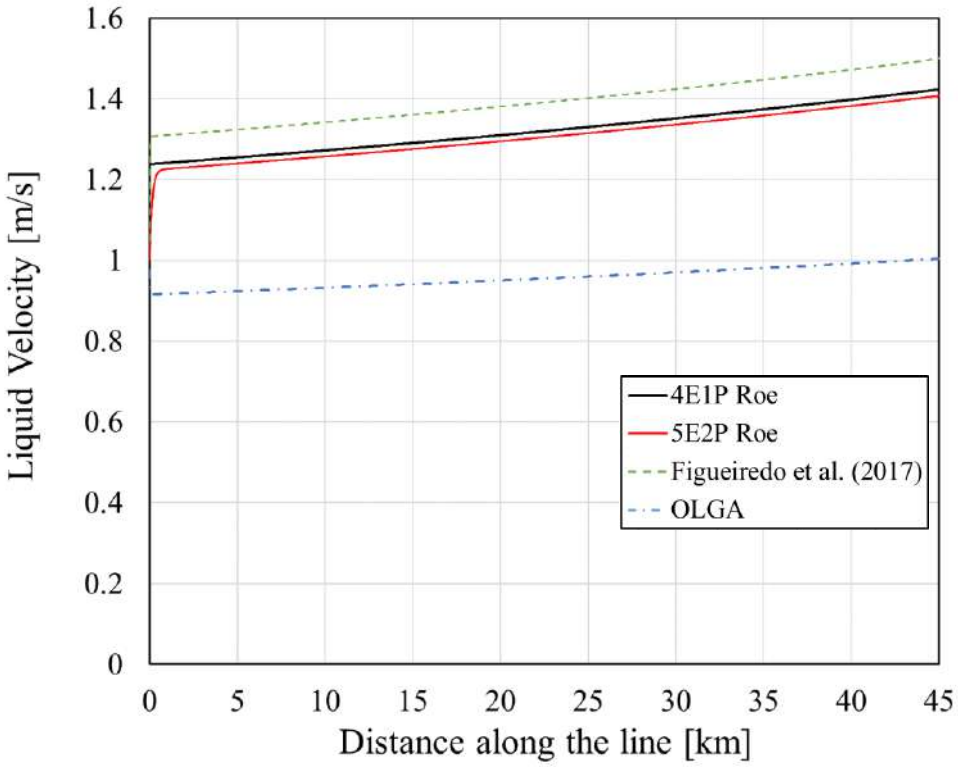

Figure 6.17: Liquid velocity distribution, stratified flow case 1.

The obtained results are in accordance with the expected physics as well as the reference results. The pressure drop obtained matched the references with an excellent agreement, and so did the gas velocity. For the holdup and the liquid velocity greater differences are shown, however, the references do not show excellent agreement with each other. The differences may be attributed to the different approaches of the non-conservative term between Figueiredo *et al.* (2017) and the herein results, and OLGA due to the different modeling. Even with considerable values of relative differences between the results, it is important to note that the current results were able to represent all variables in the expected order of magnitude and trend. Also, the liquid level in the line is low, creating some challenges for the models, all the models present jumps near the inlet boundary for both liquid velocity and holdup. It is possible to reduce the jumps using, for example, a local equilibrium condition in the inlet such as Taitel and Dukler's (1976) equilibrium correlation for stratified flow, as in Sondermann (2021). In the present work, this is opted out for a consistent comparison with the references.

6.3.2 Case 2: Relative High Holdup

The second case, named by Figueiredo *et al.* (2017) as a high holdup case, addresses a higher limit of the void fraction where the flow in the pipeline is stratified. The fluid properties are given in Table 6.13, and the boundary conditions are given in Table 6.14.

Table 6-13: Fluid Properties for the stratified flow case 2.

Parameter	Symbol	Value
Temperature	T	273 K²
Ideal gas constant	R	379.2 J/kg.K
Sound speed in gas	$c_G = \sqrt{RT}$	321.74 m/s
Sound speed in liquid	c_L	900 m/s
Reference gas density	$\rho_{0,G}$	0 kg/m^3
Reference liquid density	$\rho_{0,L}$	699.0 kg/m^3
Dynamic viscosity gas	μ_G	1.2847_x10^{-5} Pa.s
Dynamic viscosity liq.	μ_L	0.4207_x10^{-3} Pa.s

Table 6-14: Inlet and outlet boundary conditions for the stratified flow case 2.

Flow Variable	Value
α_L at inlet ($x=0$)	0.088
u_G at inlet ($x=0$)	4.08 m/s
u_L at inlet ($x=0$)	1.24 m/s
p at outlet ($x=L$)	6.0 MPa

Figure 6.18 presents the pressure profile along the line, followed by the holdup profile in Fig. 6.19, the gas velocity in Fig. 6.20, and the liquid velocity in Fig. 6.21. The relative errors are given in the following Tables 6.15 and 6.16 in the same fashion as in the previous study.

Table 6-15: Relative difference 4E1P with Roe against references for stratified case 2.

Flow variable	Relative difference OLGA	Relative difference Figueiredo *et al.* (2017)
Holdup -α_L	7.37%	12.54%
Gas velocity-u_G	3.68%	0.10%
Liq. velocity -u_L	15.74%	2.57%
Pressure -p	0.58%	0.30%

Table 6-16: Relative difference 5E2P with Roe against references for stratified case 2.

Flow variable	Relative difference OLGA	Relative difference Figueiredo *et al.* (2017)
Holdup -α_L	9.17%	14.23%
Gas velocity-u_G	4.08%	3.19%
Liq. velocity -u_L	13.86%	4.09%
Pressure -p	0.73%	0.46%

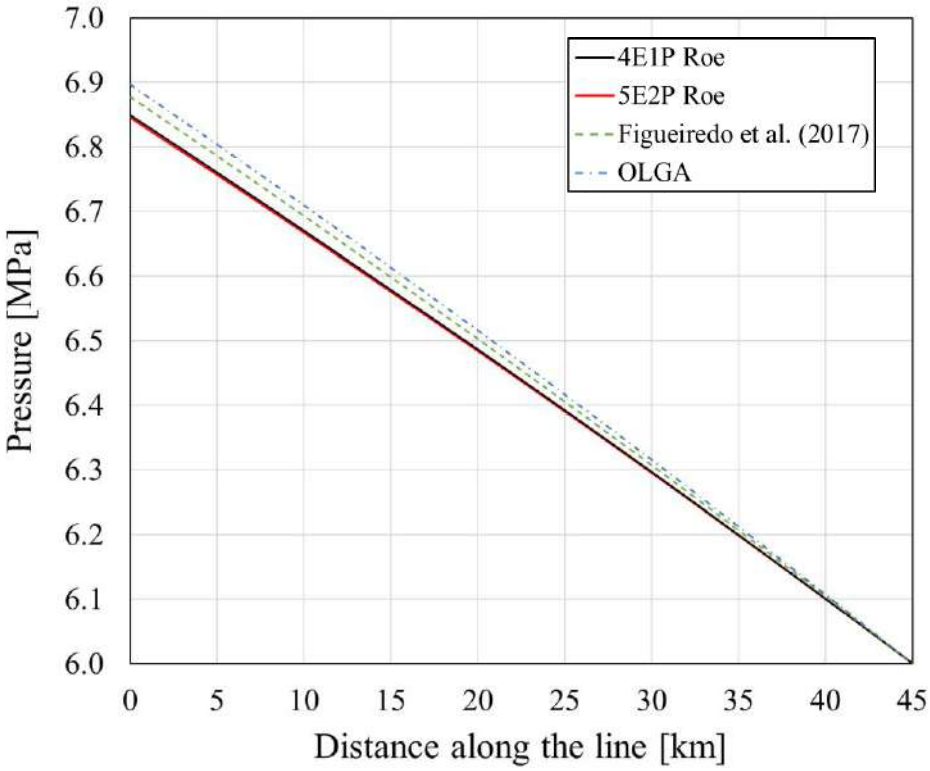

Figure 6.18: Pressure distribution, stratified flow case 2.

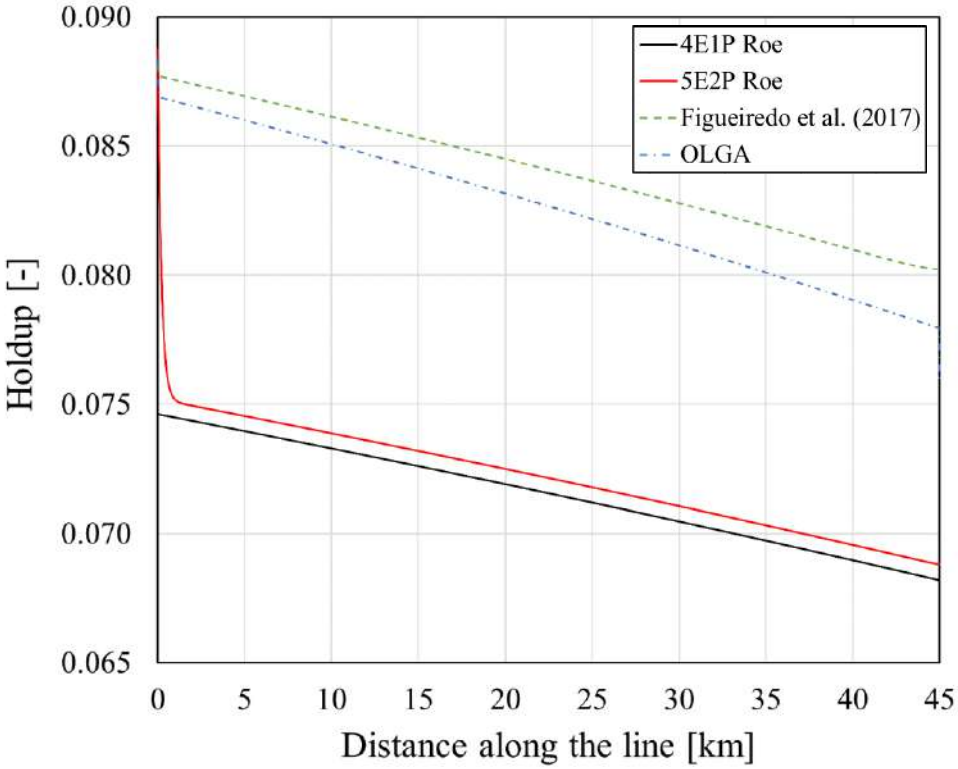

Figure 6.19: Holdup distribution, stratified flow case 2.

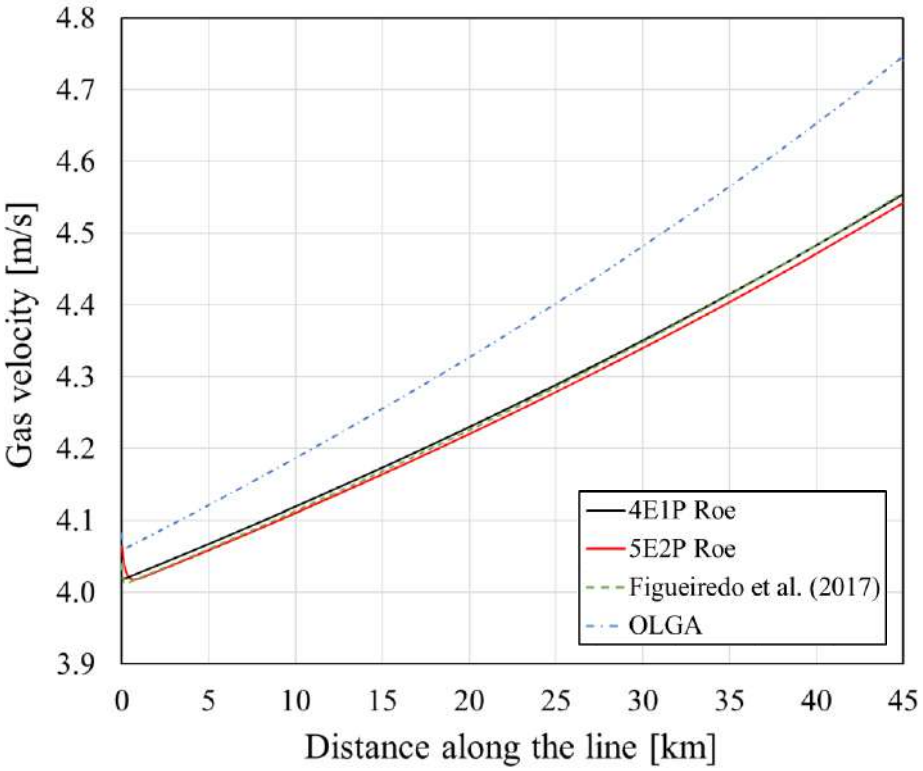

Figure 6.20: Gas velocity distribution, stratified flow case 2.

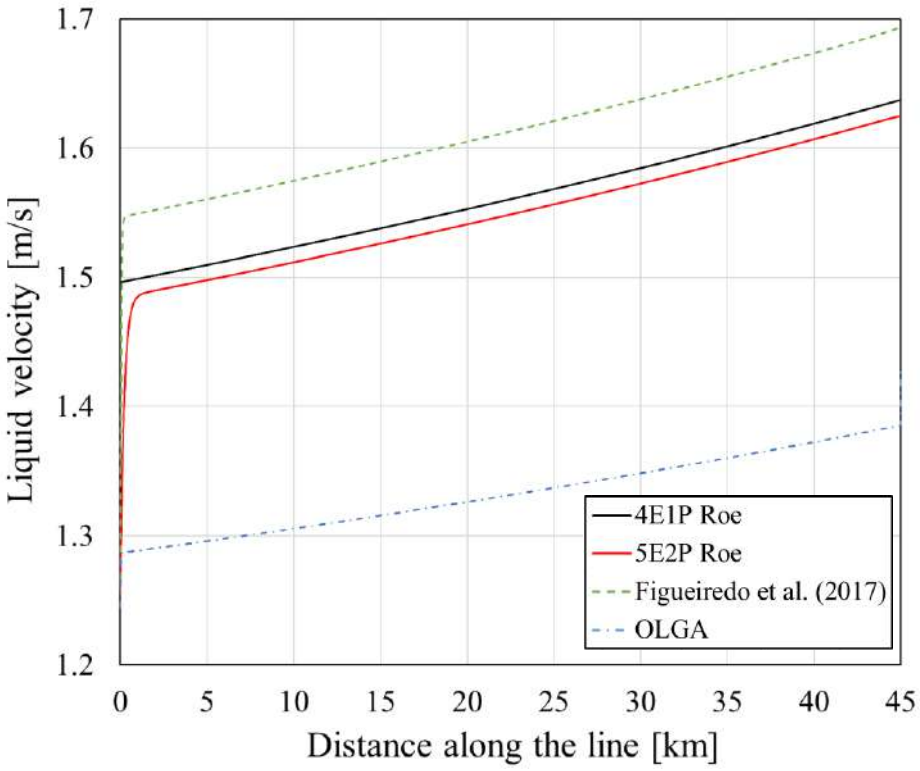

Figure 6.21: Liquid velocity distribution, stratified flow case 2.

The relative high holdup case results are also in accordance with the expected physics as well as the reference results. With the higher holdup, the relative difference between each flow variable decreased in relation to the relative low holdup case. The differences can be attributed again more to the difference in modeling than the numerical approach itself.

6.3.3 Accuracy Analysis

With the given benchmark results, all the numerical models are considered validated. To conclude this evaluation of the model-method combination, a mesh study is performed to determine the accuracy in space of each approach.

The objective is to correlate how the error decays with the refinement of the mesh and to estimate a base grid size for the scale of the simulations that will be carried out. A reference solution in steady-state flow is required for this study to isolate the transient effects and evaluate the space accuracy only. Unfortunately, there is no known full analytical solution of the models with all source terms effects. To deal with that, the previous stratified flow cases can be selected and simulated over the finer selected grid

size of 10000 cells, which is used as a reference solution for the model-method combination. From that grid size using the CFL=0.45 for the AUSM-type methods and the FORCE method, a time step of Δt=2.1315ms is obtained. Analogously, for the Roe scheme with a CFL=0.9, a time step of Δt=4.2621ms is obtained. The simulations with the respective time step kept constant for each method are carried out with mesh sizes of 100, 500, 1000, 2500, and 5000 cells, and compared with the reference grid results of 10000 cells. A global variable is selected to evaluate the error relative to the reference under each grid size. For that, the total momentum integrated along the domain is selected as a global variable that incorporates all the primitive variables and source terms in one single term. Also, for reference, pressure is used as a primitive variable. The relative error can be determined by,

$$\xi = \frac{\left|P - P_{ref}\right|}{P_{ref}}, \tag{6.8}$$

where P_{ref} is the variable selected, either momentum or pressure, in the reference mesh size solution.

The following plots give the results of the analysis. In Fig. 6.22 and Fig. 6.23, the analysis for the AUSM-type methods with the 4E1P method, in Fig. 6.24 the result for the ModFORCE, and Fig. 6.25 the Roe scheme for the same model. The analysis with the 5E2P model is given in Fig. 6.26 and Fig. 6.27 for the ModFORCE and the Roe scheme, respectively. The analysis for the FCT method was deemed unnecessary here since this study has already been carried out by the works of Figueiredo *et al.* (2017) and Sondermann *et al.* (2019), with both concluding that the FCT method with a two-fluid model starts presenting second-order accuracy behavior for meshes higher than 2500 cells. Also, a study for the AUSM-type methods with the 5E2P model was provided by Sondermann (2021) showing that this methodology behaves as first-order accurate.

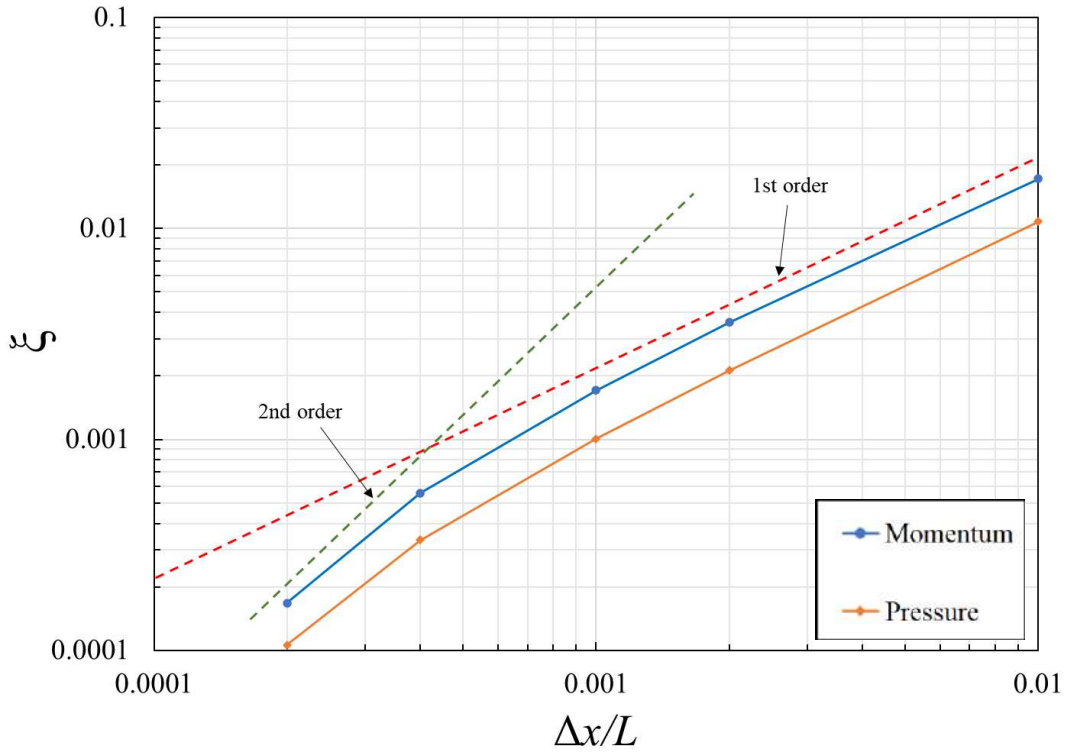

Figure 6.22: Accuracy analysis, 4E1P AUSMDV.

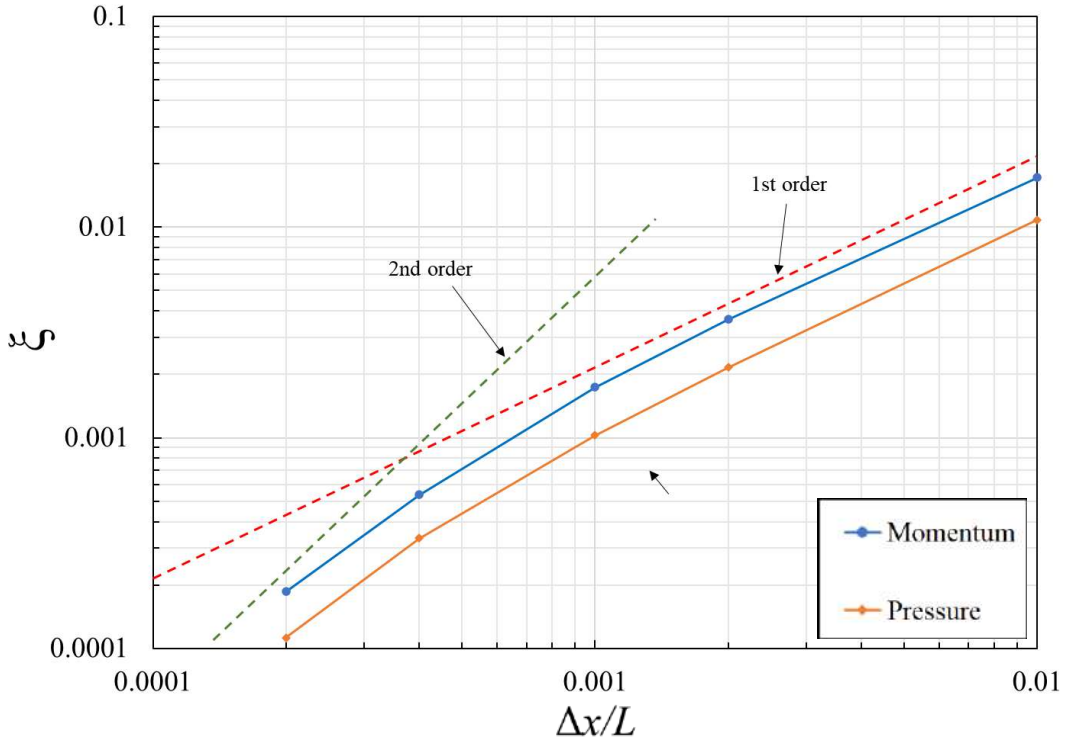

Figure 6.23: Accuracy analysis, 4E1P AUSMV.

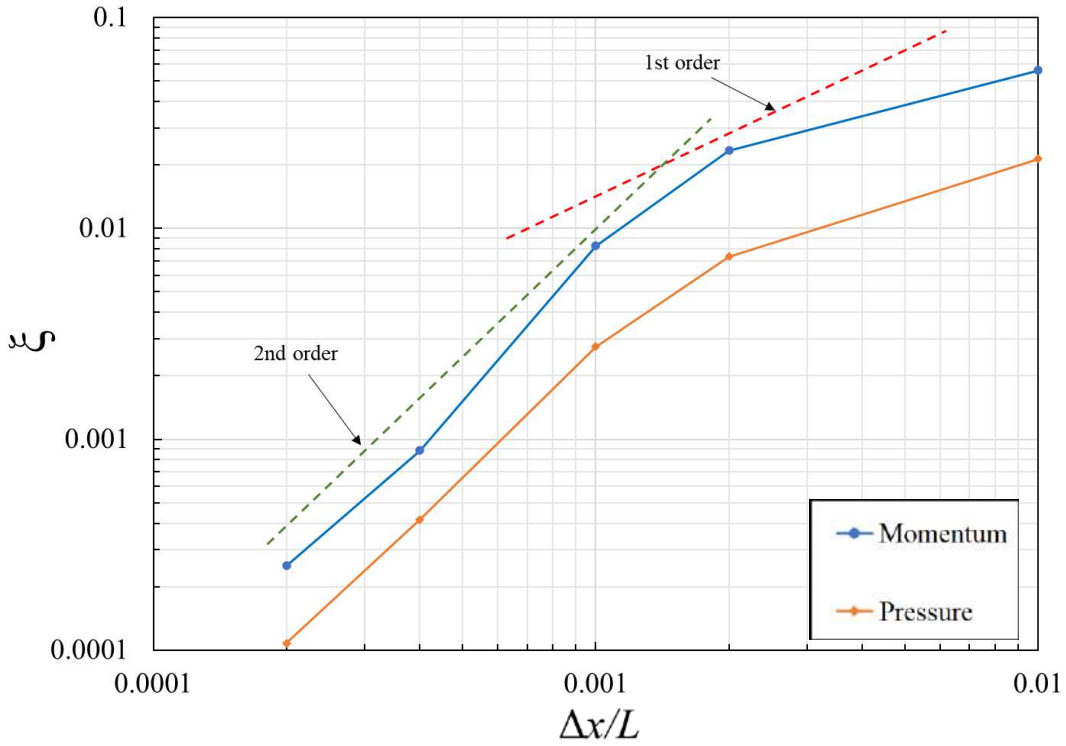

Figure 6.24: Accuracy analysis, 4E1P ModFORCE.

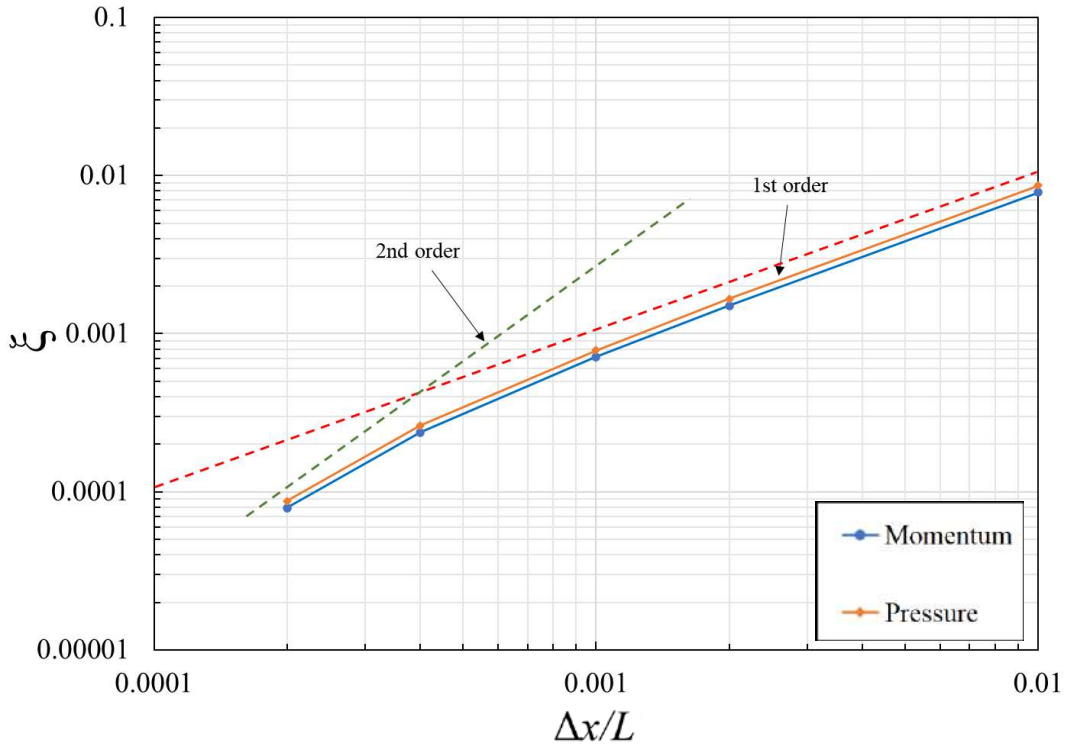

Figure 6.25: Accuracy analysis, 4E1P Roe scheme.

With the carried out study, the AUSM-type methods behave as first-order accurate in space, and the same can be said for the Roe scheme. The ModFORCE scheme, on the

other hand, has second-order accurate behavior. The second-order accuracy of the ModFORCE can be attributed to the Richtmyer method built into it that is only dumped by a fixed percentage of the solution. Even though the Roe scheme here is constructed to be second-order accurate, the expansion to second-order used the Van Leer (1974) slope limiter function to dump unwanted numerical spurious oscillations, which may be in this case dumping second-order behavior in favor of numerical stability. It is also worth noting that even with first-order behavior under the selected mesh sizes, the Roe scheme errors are lower than the other methods with a relative error of the order of 1% for a mesh of 100cells, whereas for example, the ModFORCE would give an error of the order of 10%.

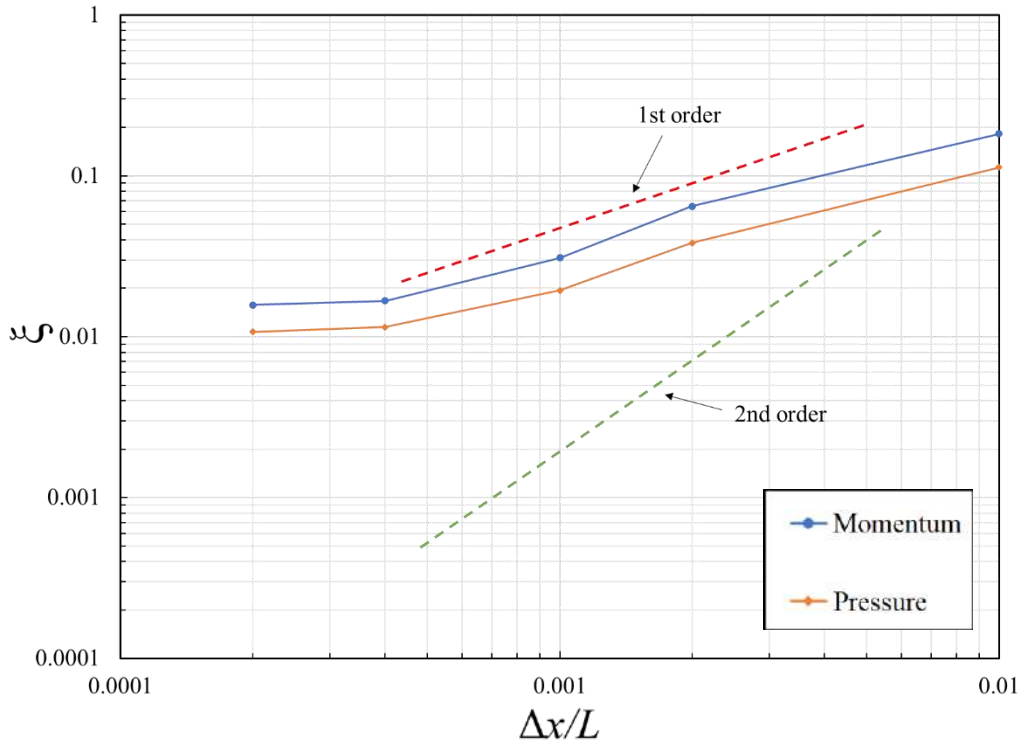

Figure 6.26: Accuracy analysis, 5E2P ModFORCE method.

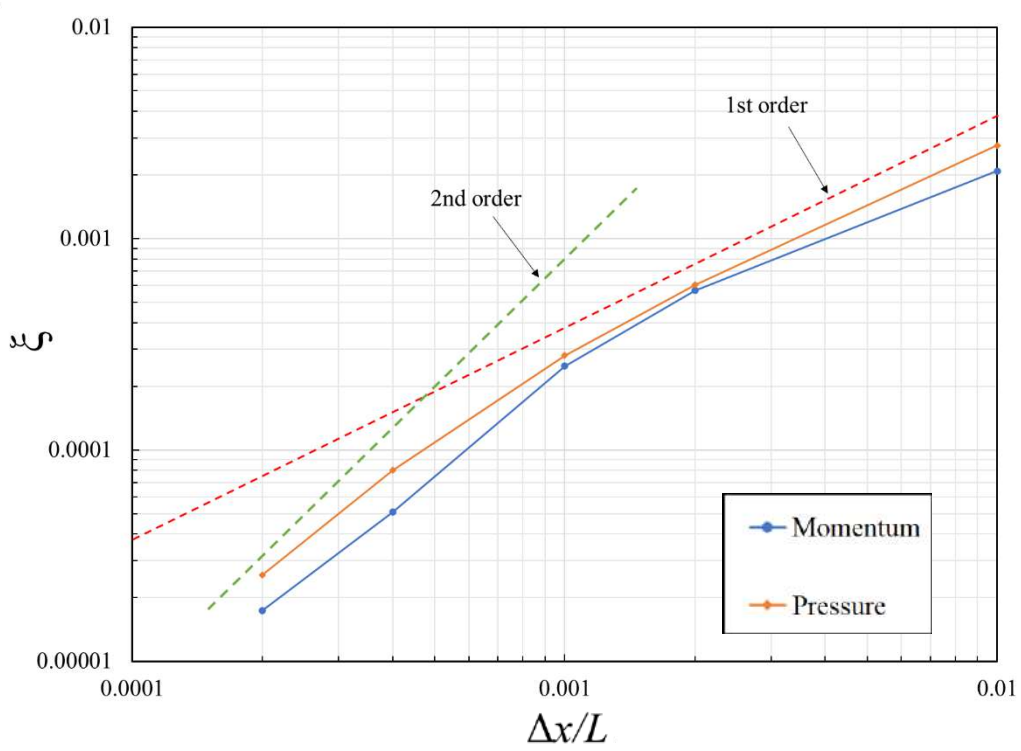

Figure 6.27: Accuracy analysis, 5E2P Roe scheme.

With the 5E2P model, the ModFORCE scheme has a different behavior, being first-order accurate. This seems to contradict the results obtained in the water faucet benchmark where the ModFORCE scheme shows the most accurate overall results, however, the scheme is sensitive to the balance selected between the Lax-Friedrich and Richtmyer schemes. This balance is controlled by a selected constant parameter that is also sensitive to mesh size and time step. The selection of 2% Lax-Friedrich solution rendered results with small oscillations that increased the overall errors. The Roe scheme, on the other hand, presented consistent behavior under first-order accuracy.

7 Piston Models

This chapter will discuss the models for simulating pigging and plunger lift operations, and the general scheme utilized to interface the piston with the pipe flow. Both operations deploy a piston through a pipe, the piston moves passively driven by the pressure differential across it, given that the piston creates a restriction in the flow.

It is challenging to obtain exact formulations for all the interactions of a pig or plunger. There are many effects to be considered and a wide diversity of models, with different shapes and functions, for both pigs and plungers. Therefore, deriving a general mathematical model for any of those applications is a complex task. There is also limited literature on the perspective of a comprehensive transient model that interfaces both the piston and pipe flow. For purposes of simplification, all models presented here will consider an idealized piston as a cylinder of diameter d_p, length L_p, and mass m_p. The piston models are primarily based on Newton's second law, obtaining the piston acceleration by the net force consequent from the forces acting on it,

$$\frac{d(m_p v_p)}{dt} = \sum F_p, \tag{7.1}$$

where v_p is the piston velocity and F_p represents the external forces acting on the piston. Continuity equations are also used to consider the fluids that pass through the piston gaps and holes.

The models presented here are as general as possible and should be perceived as an initial approximation for the quantities involved. To obtain more accurate approximations, it is primordial to employ studies on the specific plunger or pig geometries, then closure relations can be obtained and used to improve the results.

7.1 Pig Model

This section will present the formulation for the generalized pig model followed by subsections for the specific models utilized to simulate pigging operations in single and two-phase flow lines. For the formulation of the model, it is important to mention that the pipe is considered in mint condition, without major bumps, imperfections, or debris.

Bering in mind that the pig has constant mass, the formulation is given by Eq.(7.1) can be written as,

$$m_p \frac{dv_p}{dt} = \Delta p_p A_p - F_M - F_H - m_p g \sin\theta, \tag{7.2}$$

where Δp_p is the pressure difference across the pig, A_p is the cross-sectional area covered by the pig, F_M is the mechanical force coming from the friction between the pig and the pipe walls, F_H is the hydraulic force from the fluids passing through the pig, and the last term represents the pig weight. The hydraulic force is particular for each single and two-phase models, whereas for the mechanical friction force the modeling is considered the same.

To increase cleaning and sealing efficiency, pigs usually are inserted into the pipeline with interference, and under that condition, the cross-sectional covered by the pig is the same as the pipe cross-sectional area $A_p = A$. In practice, though, even with interference, there is always a narrow effective gap, δ, between the pig and the pipe walls originating from the imperfect contact between the surfaces, as reported by Patricio *et al.* (2020), and represented in Fig. 7.1.

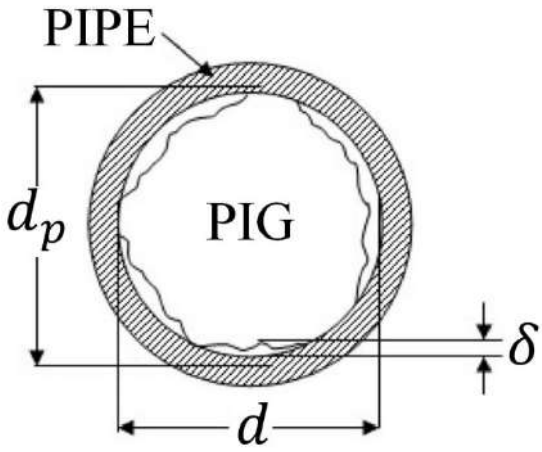

Figure 7.1: Schematic drawing of the fitting of a pig inside a pipeline (Patricio *et al.*, 2020).

This narrow gap induces hydraulic losses. A formulation for the value of this gap is a challenge, and not found in the literature. Azevedo *et al.* (1996) use an average value,

while Patricio *et al.* (2020), based on Schlumberger's OLGA software, sets this parameter as two times the roughness of the pipe.

Motivated by this imperfect contact, Campo (1998) defines a contact ratio between pig and pipe surfaces $\xi \in [0,1]$. If ξ=0, there is no contact, thus, no mechanical friction, and if ξ=1, there is full contact, thus, no gap or hydrodynamic losses between pipe and piston. The contact ratio can be defined as,

$$\xi \equiv \frac{A_M}{A_c}, \tag{7.3}$$

where A_c and A_M are respectively the total contact area and the mechanical contact area. The total contact area between the pig and the pipe inner wall can be expressed by the difference between the mechanical and hydrodynamic contact areas, given by,

$$A_c = \pi d_p L_c = A_M - A_H, \tag{7.4}$$

where L_c is the characteristic length of the pig to represent pigs that may not make full contact throughout its entire length L_p. Consequently, it can be inferred that,

$$A_M = \xi A_c, \tag{7.5}$$

$$A_H = (1 - \xi) A_c. \tag{7.6}$$

Patricio *et al.* (2020) derive the mechanical friction force through Coulomb's law of friction, which relates the normal forces between solid bodies. Neglecting deformations and using a first-order approximation, the mechanical friction force can be approximated to be directly proportional to the normal force N, between the surfaces. Then, the static and dynamic friction forces are,

$$F_M^s = \eta_s N, \tag{7.7}$$

$$F_M^d = \eta_d N, \tag{7.8}$$

with η_s and η_d being the static and dynamic friction forces respectively. There are three configurations for the value of the mechanical friction force: when the pig is stationary; when the pig is in motion; and when the pig is in the imminence of motion, which are given respectively in the following relation,

$$F_M = \begin{cases} \Delta p_p A_p - F_H - m_p g \sin\theta, & \text{if } v_p = 0 \text{ and } \dfrac{dv_p}{dt} = 0 \\ \operatorname{sgn}(v_p) F_M^d, & \text{if } v_p \neq 0 \\ \operatorname{sign}\left[\Delta p_p A_p - F_H - m_p g \sin\theta\right] F_M^s, & \text{if } v_p = 0 \text{ and } \dfrac{dv_p}{dt} \neq 0. \end{cases} \tag{7.9}$$

The normal force between the pig is determined by the contact pressure, p_c, between the surfaces times the mechanical contact area, written in terms of the total contact area of the pig is given by,

$$N = \xi A_c p_c. \tag{7.10}$$

To obtain the contact pressure the equation derived by Gomes (1994) by means of the infinitesimal theory of elasticity on a cylindrical pig proposed,

$$p_{cp} = \frac{1}{1-\upsilon}\left(\frac{E\Delta d}{d_p} + \upsilon \min(p_t, p_f)\right), \tag{7.11}$$

where υ and E are respectively the Poisson coefficient and Young's modulus of the pig material, Δd the pig and internal pipe diameter difference. The entities p_t and p_f are both the pressures at the pig tail and head (front) respectively.

Since pigs come in different sizes, shapes, and combinations of materials, it is difficult to determine the mechanical properties E and υ. To cover a general-purpose formulation, Patricio *et al.* (2020) proposes getting average values E^* and υ^*. The authors recommend obtaining those values through experimental testing, but also come up with a formulation based on a minimum critical pressure difference Δp_c. The critical pressure difference is the minimum value for Δp_p to set the pig into motion. When it takes place, the pig is considered to be in the imminence of motion and the forces applied to the pig are under

static equilibrium, $\sum F_p = 0$. The hydrodynamic friction force will come entirely from the pressure difference and the mechanical friction will be of static nature. Neglecting the gravitational effect there the authors derive that,

$$E^* = \frac{1 - \upsilon^*}{\eta_s \xi} \frac{d_p}{\Delta d} \left\{ \Delta p_c \left[\frac{D}{4L_c} + \frac{(1-\xi)\delta}{2L_c} \right] - \upsilon^* p_t \right\}. \tag{7.12}$$

A great portion of pigs have a relatively large empty space inside them, rather than a full solid cylindrical body, so the Poisson coefficient υ^* , in these cases, is less representative of the pig stiffness that the Young modulus E^*. Because of that, for those types of pigs, the authors assume that $\upsilon^* = 0$.

7.1.1 Pig Model Under Single-Phase Flow

To solve the hydraulic force acting on the pig under single-phase flow conditions, the consideration from Azevedo *et al.* (1996) of an effective gap being much smaller than the pipe inner diameter, $\delta \ll d$ is followed. From there, the solution for the flow through the pig gap can be approximated by a parallel plate problem known as the Couette flow, represented in Fig. 7.2.

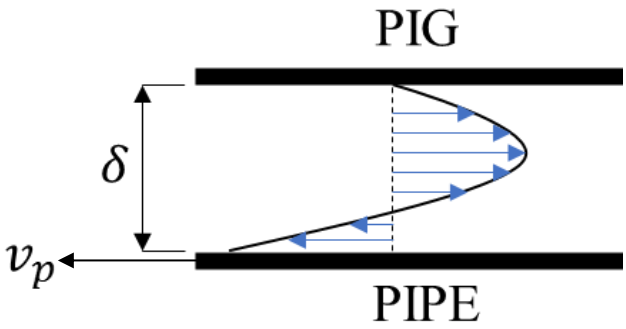

Figure 7.2: Velocity profile through the gap from the pig frame of reference.

The flow in the gap is considered fully developed, incompressible and steady, although the flow in the pipe is intrinsically unsteady, and the flow dynamics are dominated by three effects: the pressure differential across the pig; the pig motion; and the gravitational effect. Typically, the pressure differential is positive, pushing the fluid

from upstream to downstream of the pig gap, whereas for positive velocities, the pig drags the fluid that moves backward relative to the pig frame of reference. The gravitational effect is usually neglected for near-horizontal pipes, included here as means of completion. Combining these effects, the solution to the problem is straightforward, and the shear stress at the pig surface is obtained,

$$\tau_p = \frac{\Delta p_p}{2L_p} - \mu\frac{v_p}{\delta} - \frac{1}{2}\rho g \sin\theta. \tag{7.13}$$

The hydrodynamic friction force can be obtained by multiplying the shear stress Eq.(7.13) with the hydrodynamic contact surface area Eq.(7.6),

$$F_H = (1-\xi)A_c\left[\frac{1}{2}\left(\frac{\Delta p_p}{L_c} - \rho g \sin\theta\right) - \mu\frac{v_p}{\delta}\right]. \tag{7.14}$$

To solve the bypass flow, which is mass flow through the pig, a mass balance relation must be defined. Patricio *et al.* (2020) considered a control volume around the pig, and the pig as a singular surface, meaning that no fluid accumulates under the gap through time. With this simplification, a mathematical expression for continuity can be obtained through,

$$\int_{S_{p,f}} \rho_t(u_t - v_p)dS = \int_{S_{p,t}} \rho_f(u_f - v_p)dS. \tag{7.15}$$

The subscripts t and f denote the values of the flow parameters right at the pig's control volume surfaces, pig tail, and pig front respectively. Where $\rho_t = \rho_t(x = x_{p,t}, t)$, $\rho_f = \rho_f(x = x_{p,f}, f)$ and so forth, with x_p being the pig centroid position, Fig. 7.3.

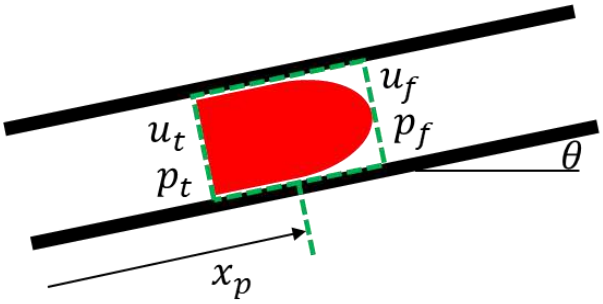

Figure 7.3: Schematic of the pig control volume.

The terms $S_{p,t}$ and $S_{p,f}$ are the control volume surface at the front and tail, which are the same as the pipe cross-sectional area, therefore,

$$\dot{m}_{bp} = \rho_t(u_t - v_p)A = \rho_f(u_f - v_p)A, \tag{7.16}$$

where $\dot{m}_{bp}$ is the total mass bypassed through the pig. There are three types of mass bypass for pigs, one is the already mentioned bypass through the gap between the piston and pipe, another one is through holes that some pigs, called bypass pigs, can have, and lastly, some pigs are made of porous materials that are permeable to the fluid. The flow rates by means of these types of bypasses are given respectively by Q_{gap}, Q_h, Q_p. Campo (1998) expresses the total mass flow rate through the bypass as a function of these flow rates by,

$$\dot{m}_{bp} = \bar{\rho}Q_{bp} = \bar{\rho}(K_1Q_{gap} + K_2Q_h + K_3Q_p), \tag{7.17}$$

with Q_{bp} being the total bypass flow rate. Depending on the type of pig that is being modeled, the parameters K_1, K_2, and K_3 are set as 0 or 1 to turn on or off the types of bypasses that the pig has. The averaged density $\bar{\rho}$ is a function that relates the fluid densities at the pig tail and front, defined by,

$$\bar{\rho} = \bar{\rho}(\rho_t, \rho_f) \equiv \frac{\rho_t + \rho_f}{2}. \tag{7.18}$$

To calculate the bypass flow through the gap Q_{gap}, Patricio *et al.* (2020) used the solution of the Couette flow represented by Fig. 7.2, and by multiplying the averaged velocity through the gap to the gap annulus area obtained,

$$Q_{gap} = \pi d\delta\left[\frac{\delta^2}{12\mu}\left(\frac{\Delta p_p}{L_c} - \rho g\sin\theta\right) - \frac{1}{2}v_p\right]. \tag{7.19}$$

Here, the gravitational component is inserted for completion.

To control the pig's velocity and pressures, holes can be made in the body of the device, connecting the pig's front to the tail. This type of pig can also be employed for safety reasons, in order to not let the upstream pressure rise uncontrollably, such as in Fig. 7.4 that is representing a sketch of a cup pig with bypass holes.

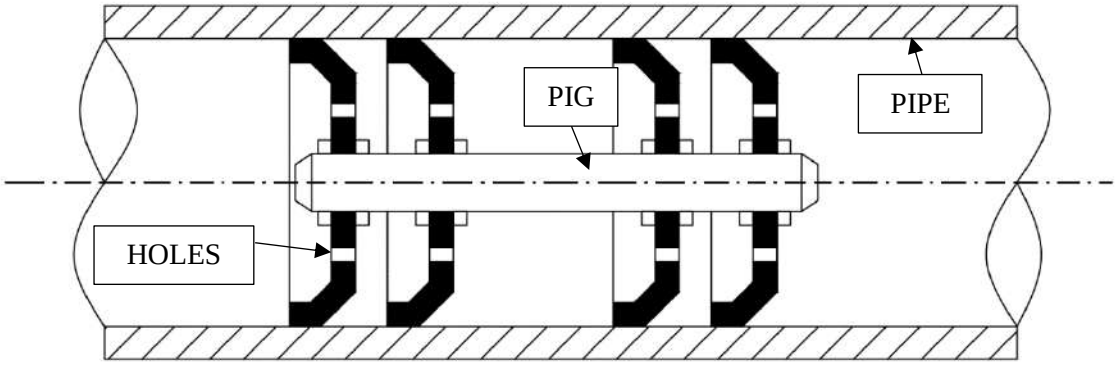

Figure 7.4: Cup pig with holes (Patricio, 2016).

Campo (1998) provided an expression for Q_h, where it is considered that the holes are longitudinal tubes with equal diameter and length parallel to the pig axis. Campo (1998) modeled the flow through each tube, and neglected the gravitational effect, obtaining the flow rate through the bypass holes as follows,

$$Q_h = \text{sgn}(\Delta p_p) n_h \frac{\pi d_h^2}{4} \sqrt{\frac{2\frac{|\Delta p_p|}{\bar{\rho}}}{k_h + \frac{f_h L_h}{d_h}}}, \tag{7.20}$$

where n_h, d_h, k_h, f_h, and L_h are respectively the number of bypass holes, the diameter of the holes, holes local loss coefficient, tubes friction factor, and the length of the holes.

The cases for permeable pigs will not be considered here. As a reference, a formulation of Q_p can be found in Azevedo *et al.* (1996).

Combining equations Eq.(7.2), Eq(7.16), and Eq.(7.17) the system of algebraic ordinary-differential equations that describes the pig motion is given by,

$$\begin{cases} m_p \dfrac{dv_p}{dt} = \Delta p_p A_p - F_M - F_H - m_p g \sin\theta \\ \dot{m}_{bp} = \rho_t (u_t - v_p) A \\ \dot{m}_{bp} = \rho_f (u_f - v_p) A, \end{cases} \tag{7.21}$$

with,

$$\begin{cases} p_t \equiv p(x = x_{p,t}, t) \text{ and } p_f \equiv p(x = x_{p,f}, t) \\ u_t \equiv u(x = x_{p,t}, t) \text{ and } u_f \equiv u(x = x_{p,f}, t) \\ \rho_t \equiv \rho(x = x_{p,t}, t) \text{ and } \rho_f \equiv \rho(x = x_{p,f}, t) \end{cases} \tag{7.22}$$

The pig's system of equations must be solved for each time step as an initial value problem. Since the system has three equations, three unknows are solved: v_p, u_f, and p_t. The other flow parameters u_t and p_f are determined from the solution of the flow upstream and downstream from the pig. The solution of the pig is used as a moving boundary condition for the flow upstream and downstream, and a strategy for coupling flow models with the piston models will be discussed in section 7.3.

7.1.2 Pig Model Under Two-Phase Flow

The dynamics of the pig under two-phase flow are different from the single-phase case. It will be considered here cases where the stratified flow takes place. The driving force responsible for the movement of the pig under these conditions is still the pressure differential across the pig body and the force balance in the pig, given by Eq. (7.2). In general, under these flow patterns and under specific operational conditions, as the pig moves inside the pipe it drags the liquid in front of it. When this happens in the case of bypass pigs, as the pig moves faster, the liquid accumulates at the pig front, creating a higher liquid film or even, in some cases, a liquid slug body, as represented in Fig. 7.5. This occurrence is dependable mainly on the altimetry conditions where the pipe is launched. Horizontal or upward inclinations typically induce the formation of a liquid body, whereas downward inclinations may not.

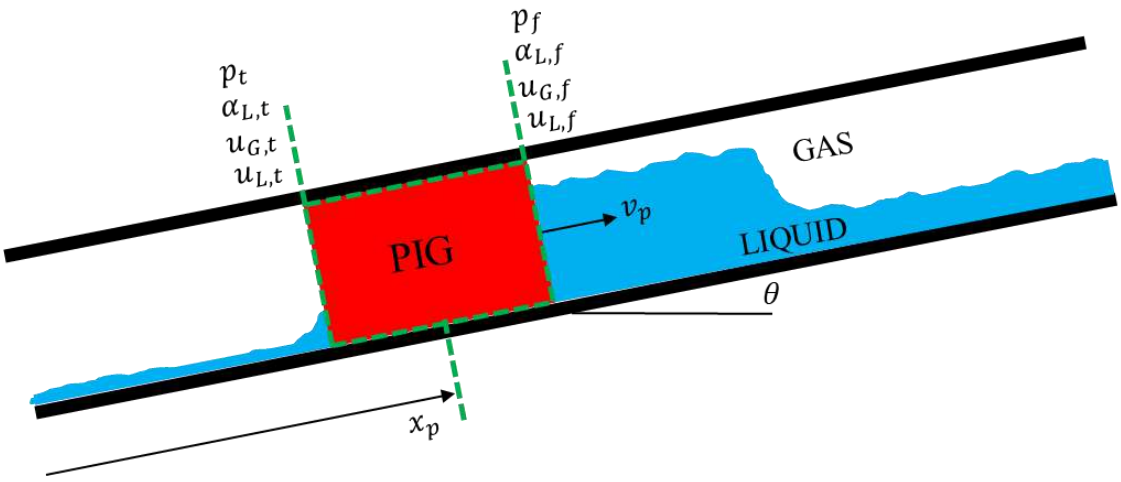

Figure 7.5: Sketch for a Two-phase flow bypass pig.

In this work, the most complete model for the two-phase pig found in the literature is implemented, which is the one presented by Patricio (2016). Expanding from the pig model presented in the previous section, it is straightforward to obtain the equations for the two-phase flow. For the mechanical friction force, the equations utilized are strictly the same as presented in section 7.1, whereas for the hydraulic force the presence of both fluids is incorporated,

$$F_H = (1-\xi)A_c\left\{\frac{1}{2}\left[\frac{\Delta p_p}{L_c} - (\bar{\alpha}_G\bar{\rho}_G + \bar{\alpha}_L\bar{\rho}_L)g\sin\theta\right] - \bar{\mu}\frac{v_p}{\delta}\right\}, \tag{7.23}$$

with $\bar{\alpha}_G$ and $\bar{\alpha}_L$, the averaged values for the volume fractions across the pig gap, and $\bar{\rho}_G$ and $\bar{\rho}_L$ the averaged densities, given by,

$$\bar{\alpha}_k = \frac{1}{2}\left(\alpha_{k,t} + \alpha_{k,f}\right), \tag{7.24}$$

$$\bar{\rho}_k = \frac{1}{2}\left(\alpha_{k,t}\rho_{k,t} + \alpha_{k,f}\rho_{k,f}\right). \tag{7.25}$$

The parameter $\bar{\mu}$ is the averaged dynamic viscosity for the mixture of the fluid phases, obtained through,

$$\bar{\mu} = \bar{\alpha}_G\mu_G + \bar{\alpha}_L\mu_L, \tag{7.26}$$

The mass balance across the pig for the two phases is obtained analogously from the single-phase case, with the inclusion of the phases' volume fractions,

$$\dot{m}_{k,bp} = \alpha_{k,t}\rho_{k,t}\left(u_{k,t} - v_p\right)A = \alpha_{k,f}\rho_{k,f}\left(u_{k,f} - v_p\right)A, \tag{7.27}$$

with $\dot{m}_{k,bp}$ being the mass bypass flow through the pig for each phase. To represent the mass flow rate of the phases through the bypass, the formulation given by Campo (1998) is expanded, considering the bypass flow rate through the gap, holes, and porous media as,

$$\dot{m}_{k,bp} = \bar{\rho}_k Q_{k,bp} = \bar{\rho}_k\left(K_1 Q_{k,gap} + K_2 Q_{k,h}\right). \tag{7.28}$$

Analogously to the bypass flow rates presented in single-phase flow, Eq. (7.19) and Eq. (7.20),

$$Q_{k,gap} = \pi d\delta\left[\frac{\delta^2}{12\mu_k}\left(\frac{\Delta p_{k,p}}{L_c} - \bar{\rho}_k g\sin\theta\right) - \frac{1}{2}v_p\right], \tag{7.29}$$

$$Q_{k,h} = \mathrm{sgn}\left(\Delta p_p\right) n_h \frac{\pi d_h^2}{4}\sqrt{\frac{2\frac{\left|\Delta p_{k,p}\right|}{\bar{\rho}_k}}{k_{k,h} + \frac{f_{k,h}L_h}{d_h}}}. \tag{7.30}$$

Again, the cases for permeable pigs in two-phase flow will not be considered here. As a reference, a formulation of $Q_{k,p}$ can be found in Patricio (2016).

Combining equations Eq. (7.2), Eq. (7.27), and Eq. (7.28), the system of algebraic ordinary-differential equations that describes the pig motion when travels through a two-phase flow pipeline is given by,

$$\begin{cases} m_p \dfrac{dv_p}{dt} = \Delta p_p A_p - F_M - F_H - m_p g \sin\theta \\ \alpha_{G,t}\rho_{G,t}\left(u_{G,t} - v_p\right)A = \alpha_{G,f}\rho_{G,f}\left(u_{G,f} - v_p\right)A \\ \alpha_{L,t}\rho_{L,t}\left(u_{L,t} - v_p\right)A = \alpha_{L,f}\rho_{L,f}\left(u_{L,f} - v_p\right)A \\ \dot{m}_{G,bp} = \bar{\rho}_G\left(K_1 Q_{G,gap} + K_2 Q_{G,h} + K_3 Q_{G,p}\right) \\ \dot{m}_{L,bp} = \bar{\rho}_L\left(K_1 Q_{L,gap} + K_2 Q_{L,h} + K_3 Q_{L,p}\right) \end{cases} \tag{7.31}$$

7.2 Plunger Upstroke Model

The plunger model presented in this section covers the upstroke stage of plunger lift operations. The model will be used for conventional plunger lift simulations, however, it can be expanded to continuous plunger cases with the correct fluid flow interface.

Some of the transient models in the literature, such as Lea (1982) and Gasbarri and Wiggins (2001), treat the plunger and the liquid column, or liquid slug, on its top as one control volume with a fixed length, where both plunger and liquid slug are moving with the same velocity, as detailed in Fig. 7.6 (a). Also, they do not take into account the effects of the liquid falling back from the control volume or the gas slipping in, meaning the total mass of the control volume, m_{CV}, is constant and equal to the sum of the plunger mass and liquid slug mass, $m_{CV} = m_p + m_{ls}$. In that configuration, the net force acting on the control volume is given by,

$$m_{CV} \frac{dv_{CV}}{dt} = \Delta p_{CV} A_p - F_{ls} - m_{CV} g \sin\theta, \tag{7.32}$$

with v_{CV} being the velocity of the entire control volume body, where $v_{CV} = v_p$. The pressure differential across the control volume Δp_{CV} is analogous to the pressure differential of the pig models, with $\Delta p_{CV} = p_{CV,t} - p_{CV,f}$. The friction force added by the presence of the liquid slug is given by F_{ls},

$$F_{ls} = \frac{1}{2}\pi d L_{ls} f_{ls} \rho_L v_{ls} |v_{ls}|, \tag{7.33}$$

where in this v_{ls} is the liquid slug body velocity, that for this specific case is equal to the control volume velocity $v_{ls} = v_{CV}$. For the friction factor f_{ls}, Moody's (1947) correlation can be used.

Since a large enough gap is required to drop the plungers from the lubricator at the top of the well to the bumper spring at the downhole, any mechanical friction force is neglected in plunger models, since they are not designed to be scraping the pipe walls as intensively as pigs do. However, some plunger, such as pads and brush type plungers will have contact with the pipe walls and mechanical friction may be considered.

Liquid loss through the gap, the liquid fallback, is an expected effect reported in the literature of Foss and Gaul (1965), Rosina (1983), Mower *et al.* (1985), Hernandez *et al.* (1993), Pan (2017), Zao *et al.* (2018) and Akhiiardinov (2020). This effect is important to evaluate the overall efficiency of the plunger in the deliquification of a well. Moreover, the gas slippage through the gaps is overlooked, especially in its physical relationship with the liquid fallback. Through experimental measurements and video observations, Akhiiardinov *et al.* (2020) verified that, for conventional operations, the liquid slug and plunger travel with different velocities during an upstroke. This happens because, with the gas slippage, there is an onset of a Taylor bubble (gas pocket) between the plunger and the liquid slug, Fig. 7.6 (b), being the major region occupied by the slipped gas. Based on their observations, there is also some gas entrained in the slug, but, since these effects were proved to be minor, the assumption of no gas entrainment in the liquid slug is also followed in the present work. Then, Taylor bubble pressure, rather than the pressure at the piston tail, drives the dynamics of the liquid slug, giving rise to separate force balance equations for the plunger and for the liquid slug. Expanding from the equations given by Akhiiardinov et al. (2020), and taking into account the transient effect of mass loss in the liquid slug through fallback, the force balance equations that govern the liquid slug and plunger dynamics are respectively given by,

$$\frac{d}{dt}(m_{ls}v_{ls}) = \Delta p_{ls}A - F_{ls} - m_{ls}g\sin\theta, \tag{7.34}$$

$$m_p\frac{dv_p}{dt} = \Delta p_p A_p - F_H - m_p g\sin\theta. \tag{7.35}$$

According to Akhiiardinov *et al.* (2020), the dynamics of the bubble region resemble the dynamics of Taylor bubbles in vertical slug flow. Following Sylvester (1987), the pressure in this region, p_{tb}, is assumed to be locally constant, in other terms, the friction in the gas pocket region is neglected. Then, the Taylor bubble pressure is equal to the

pressure in front of the plunger and the pressure at the liquid slug tail, $p_{tb} = p_{p,f} = p_{ls,t}$. With that, the pressure differentials across the liquid slug, Δp_{ls}, and across the plunger, Δp_p, are respectively given by,

$$\Delta p_{ls} = p_{ls,t} - p_{ls,f} = p_{tb} - p_{ls,f}, \tag{7.36}$$

$$\Delta p_p = p_{ls,t} - p_{ls,f} = p_{tb} - p_{ls,f}. \tag{7.37}$$

In Fig. 7.6 (a) and (b), a schematic of both the simplified version of the control volume model and the extended model proposed in this work can be seen. The dashed red region is the control volume region that encompasses the liquid slug, Taylor bubble, and plunger. Similar to the pig models, the control volume represents a lumped model where all effects are considered. However, differently in the pig models, the control volume can grow or shrink with the addition of the liquid fallback and the gas slippage. With that, the control volume front velocity, which is equal to the liquid slug front velocity, $v_{CV,f} = v_{ls,f}$, is different from the control volume tail velocity that is equal to the plunger velocity, $v_{CV,t} = v_p$. The mean velocities, v_{CV} and v_{ls}, are, respectively, the center of mass velocities of the control volume and the liquid slug. It is straightforward to correlate the velocities with the liquid slug length, L_{ls}, Taylor bubble length, L_{tb}, and control volume length, $L_{CV} = L_p + L_{tb} + L_{ls}$, through kinematic relations,

$$\frac{dL_{CV}}{dt} = v_{CV,f} - v_{CV,t} = v_{ls,f} - v_p, \tag{7.38}$$

$$\frac{dL_{tb}}{dt} = v_{ls,t} - v_p, \tag{7.39}$$

$$\frac{dL_{ls}}{dt} = v_{ls,f} - v_{ls,t}, \tag{7.40}$$

and the liquid slug center of mass velocity,

$$v_{ls} = v_{ls,f} - \frac{1}{2}\frac{dL_{ls}}{dt}. \tag{7.41}$$

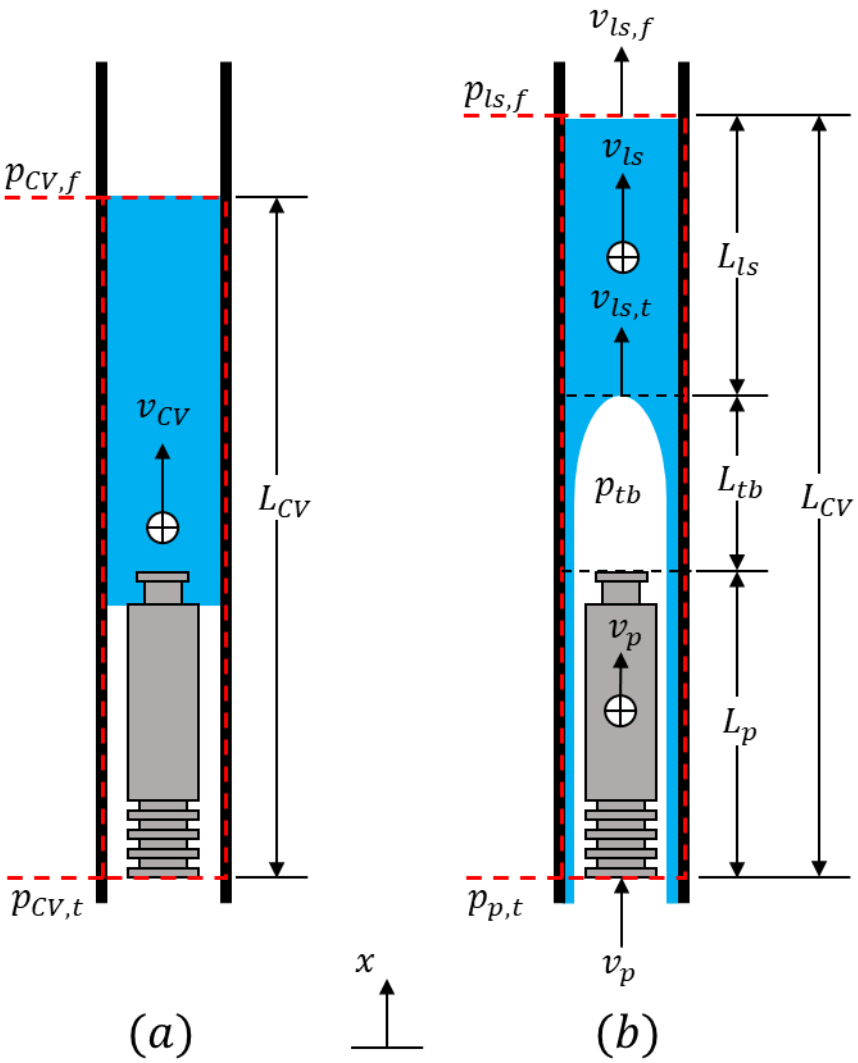

Figure 7.6: Plunger upstroke schematic. (a) Simplified version with no gas slippage or liquid fallback. (b) Extended version considering gas slippage, liquid fallback, and the onset of a Taylor bubble region.

Since the flow models used here assume the ideal gas law for state equations, the same is followed for the Taylor bubble. Therefore, if assumed that the Taylor bubble approximately occupies a cylindrical volume section of the pipe between the plunger and the liquid slug, then,

$$p_{tb}V_{tb} = p_{tb}AL_{tb} = m_{tb}RT. \tag{7.42}$$

Differentiating, it is possible to obtain that,

$$\frac{dp_{tb}}{dt} = \frac{1}{L_{tb}}\left[\frac{\dot{m}_{G,gap}RT}{A} - p_{tb}\left(\frac{dL_{tb}}{dt}\right)\right], \tag{7.43}$$

where $\dot{m}_{G,gap}$ is the gas mass flow rate through the gap between the plunger and the pipe, that has the same value as the rate at which the mass changes in the Taylor bubble, $\dot{m}_{G,gap} = \dot{m}_{tb}$.

Moreover, with the liquid being incompressible it can be written for the liquid flow through the gap that,

$$\dot{m}_{L,gap} = \rho_L A \frac{dL_{ls}}{dt}, \tag{7.44}$$

which is proportional to the rate of change of the liquid slug region length. Substituting the previous equation Eq. (7.44) into Eq. (7.34), an equation for the liquid slug acceleration is obtained as follows

$$\frac{dv_{ls}}{dt} = \frac{1}{\rho_L L_{ls} A}\left(\Delta p_{ls} A - F_{ls} - v_{ls}\rho_L A \frac{dL_{ls}}{dt}\right) - g\sin\theta. \tag{7.45}$$

Combining the herein equations, the following system of ordinary differential equations is obtained,

$$\begin{cases} \dfrac{dv_{ls}}{dt} = \dfrac{1}{\rho_L L_{ls} A}\left[\left(p_{tb} - p_{ls,f}\right)A - F_{ls} - v_{ls}\rho_L A \dfrac{dL_{ls}}{dt}\right] - g\sin\theta \\ \dfrac{dv_p}{dt} = \dfrac{1}{m_p}\left[\left(p_{p,t} - p_{tb}\right)A_p - F_H\right] - g\sin\theta \\ \dfrac{dL_{ls}}{dt} = \dfrac{\dot{m}_{L,gap}}{\rho_L A} \\ \dfrac{dL_{tb}}{dt} = v_{ls} - \dfrac{1}{2}\dfrac{dL_{ls}}{dt} - v_p \\ \dfrac{dp_{tb}}{dt} = \dfrac{1}{L_{tb}}\left[\dfrac{\dot{m}_{G,gap}RT}{A} - p_{tb}\left(\dfrac{dL_{tb}}{dt}\right)\right]. \end{cases} \tag{7.46}$$

The given system of equations comprises an initial value problem with five unknows v_{ls}, v_p, L_{ls}, L_{tb}, and p_{tb}. The other parameters come from the solution of the flow and

the respective closures. For instance, the gas velocity ahead of the control volume is given by,

$$u_{G,f} = v_{CV,f} = v_{ls,f}. \tag{7.47}$$

At the tail of the plunger, it is not as straightforward, since correlations are required to obtain $\dot{m}_{G,gap}$ and $\dot{m}_{L,gap}$. The following subsection discusses an analytical approximation for obtaining these parameters.

7.2.1 Liquid Discharge

The liquid discharge phase of the upstroke occurs when the liquid slug reaches the lubricator at the top. In this phase, the flow solution ahead of the liquid slug vanishes and, thus, the output boundary condition gets suppressed. To keep taking this boundary into account, it is set that,

$$p_{ls,f} = p_{flowline}. \tag{7.48}$$

Moreover, a few terms need to be added to the model. First, there is the additional friction of the liquid slug turning to the production flowline, as represented in Fig. 7.7.

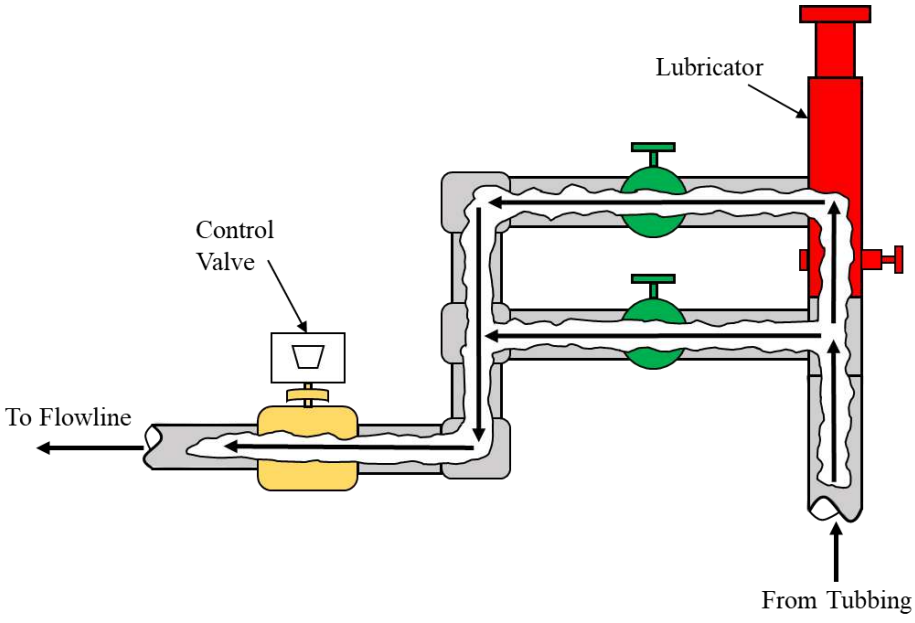

Figure 7.7: Fluid path through the wellhead.

Consequently, an extra friction force, F_{lb}, is added, taking into account the local pressure drop from the discharge at the wellhead.

$$F_D = \frac{1}{2} K_D A \rho_L v_{ls} |v_{ls}|, \tag{7.49}$$

where K_D is a local pressure drop coefficient. With the complex geometries, it becomes challenging to evaluate all the effects in the discharge section. Then, K_D is an approximation trying to lump all bends and restrictions of the wellhead section into one coefficient.

Also, with the turn from the vertical tubbing to the horizontal flowline, the weight relief from the liquid slug needs to be considered during the transient solution. However, the friction from the slug and the slug length stay unchanged after the turn, since the overall dynamics are still overcoming the inertia and the friction of the entire liquid slug even after the turn. Considering the length of the liquid that was discharged, transferred from the vertical tubbing to the flow line L_D that can explicitly be accessed from the transient solution, then the system of equations becomes,

$$\begin{cases} \frac{dv_{ls}}{dt} = \frac{1}{\rho_L L_{ls} A}\left[\left(p_{tb} - p_{ls,f}\right)A - F_D - F_{ls} - v_{ls}\rho_L A \frac{dL_{ls}}{dt}\right] - \frac{(L_{ls} - L_D)}{L_{ls}} g\sin\theta \\ \frac{dv_p}{dt} = \frac{1}{m_p}\left[\left(p_{p,t} - p_{tb}\right)A_p - F_H\right] - g\sin\theta \\ \frac{dL_{ls}}{dt} = \frac{\dot{m}_{L,gap}}{\rho_L A} \\ \frac{dL_{tb}}{dt} = v_{ls} - \frac{1}{2}\frac{dL_{ls}}{dt} - v_p \\ \frac{dp_{tb}}{dt} = \frac{1}{L_{tb}}\left[\frac{\dot{m}_{G,gap} RT}{A} - p_{tb}\left(\frac{dL_{tb}}{dt}\right)\right]. \end{cases} \tag{7.50}$$

Once the entire liquid slug is discharged, the local loss at the wellhead is suppressed again. In addition, there is no more liquid loss in the control volume at this point, thus, the L_{ls} stays constant with the last obtained value from the previous system and the system reduces from five to four equations,

$$\begin{cases} \dfrac{dv_{ls}}{dt} = \dfrac{1}{\rho_L L_{ls} A}\left[\left(p_{tb} - p_{ls,f}\right)A - F_D - F_{ls}\right] \\ \dfrac{dv_p}{dt} = \dfrac{1}{m_p}\left[\left(p_{p,t} - p_{tb}\right)A_p - F_H\right] - g\sin\theta \\ \dfrac{dL_{tb}}{dt} = v_{ls} - v_p \\ \dfrac{dp_{tb}}{dt} = \dfrac{1}{L_{tb}}\left[\dfrac{\dot{m}_{G,gap} RT}{A} - p_{tb}\left(\dfrac{dL_{tb}}{dt}\right)\right]. \end{cases} \tag{7.51}$$

7.2.2 A Plunger Gap Model

Similarly to the assumptions made for the gap in the pig model, an effective gap,

$$\delta = \frac{1}{2}\left(d - d_p\right), \tag{7.52}$$

is much smaller than the pipe's inner diameter, $\delta \ll d$, the flow under the gap is laminar and fully developed with no sudden change during a time step of the simulation, and the gas is incompressible through the gap with an averaged density, a model is proposed for the bypass through the plunger and the pipe walls, where an equilibrium solution between the phases exists. It is important to point out that these assumptions are less applicable to plungers, since the gaps are larger than with pigs, thus, the following model must be used more carefully. The model is written based on analytical formulations that represent the expected physics of the problem and can serve as a basis for formulating future empirical closures. Some simplification hypotheses are assumed for deriving the model that may lead to non-perfect results, however, it is expected that the model will capture the correct trends as well as obtain the wanted unknown entities related to the plunger upstroke stage in terms of the right order of magnitude.

A similar problem to the Couette flow is considered and the hypothesis of segregated flow is used with the liquid occupying the outer annulus region against the pipe walls, and the gas occupying the inner annulus against the piston walls, as in Fig. 7.8. From the perspective of the parallel plate's approximation, the liquid occupies a film region with a thickness δ_L. Following the y-axis from the tubing to the plunger, and the previous state hypothesis, a general formulation of the problem can be written as,

$$\frac{\partial^2 u_k}{\partial y^2} = -\frac{1}{\mu_k}\left(\frac{\Delta p_p}{L_c} - \rho_k g\right), \tag{7.53}$$

where bellow under the liquid film, $y < \delta_L$, the properties must account for the liquid phase and above, $y > \delta_L$, the gas phase.

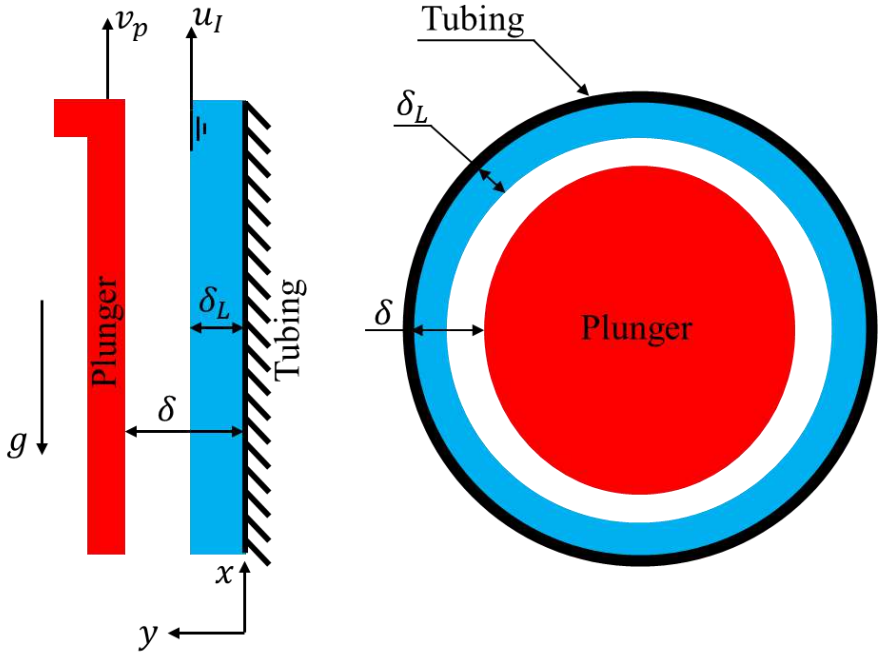

Figure 7.8: Schematic for plunger-tubing gap problem.

To conclude the formulation of the given problem, the boundary conditions are defined with the no-slip condition at the tubing wall, $u_L(0) = 0$, no slippage between the fluids, $u_L(\delta_L) = u_G(\delta_L) = u_I$, no-slip between the gas and the plunger surface, $u_G(\delta) = v_p$, and equal shear stress at the interface between fluids $\tau_L(\delta_L) = \tau_G(\delta_L)$, therefore,

$$\mu_L \frac{\partial u_L}{\partial y}\bigg|_{y=\delta_L} = \mu_G \frac{\partial u_G}{\partial y}\bigg|_{y=\delta_L}. \tag{7.54}$$

After setting the boundary conditions and integrating Eq.(7.53), the following solutions are obtained for the gas and liquid velocities profiles through the gap,

$$u_G(y) = \frac{1}{2\mu_G}\left(\frac{\Delta p_p}{L_c} - \rho_G g\right)(\delta - y)(\delta_L - y) + \frac{(\delta - y)}{(\delta - \delta_L)}u_I - v_p\frac{(\delta_L - y)}{(\delta - \delta_L)}, \tag{7.55}$$

$$u_L(y) = y\left[\frac{1}{\mu_L}\left(\frac{\Delta p_p}{L_c} - \rho_L g\right)\left(\frac{\delta_L}{2} - \frac{y}{2}\right) + \frac{u_I}{\delta_L}\right]. \tag{7.56}$$

Also, from the velocities $u_G(y)$ and $u_L(y)$ it is obtained that,

$$\mu_G \left.\frac{\partial u_G}{\partial y}\right|_{y=\delta_L} = \mu_G \frac{(v_p - u_I)}{(\delta - \delta_L)} + \frac{(\delta - \delta_L)}{2}\left(\frac{\Delta p_p}{L_c} - \rho_G g\right), \tag{7.57}$$

$$\mu_L \left.\frac{\partial u_L}{\partial y}\right|_{y=\delta_L} = \mu_L \frac{u_I}{\delta_L} - \frac{\delta_L}{2}\left(\frac{\Delta p_p}{L_c} - \rho_L g\right). \tag{7.58}$$

Combining Eq. (7.57) and Eq. (7.58) with the boundary condition given by Eq. (7.54) renders,

$$\mu_G \delta_L\left[v_p - u_I + \frac{(\delta - \delta_L)^2}{2}\left(\frac{\Delta p_p}{L_c} - \rho_G g\right)\right] = \mu_L(\delta - \delta_L)\left[u_L - \frac{{\delta_L}^2}{2}\left(\frac{\Delta p_p}{L_c} - \rho_L g\right)\right]. \tag{7.59}$$

Since the one-dimensional models are averaged and the objective is to determine the quantities for the entities $\dot{m}_{G,gap}$ and $\dot{m}_{L,gap}$, the averaged quantities for the velocities through the gap are given by,

$$\bar{u}_G = \frac{1}{\delta - \delta_l}\int_{\delta_l}^{\delta} u_G(y)\, dy = \frac{1}{2}(u_I + v_p) + \frac{(\delta - \delta_L)^2}{12\mu_G}\left[\frac{\Delta p_p}{L_c} - \rho_G g\right], \tag{7.60}$$

$$\bar{u}_L = \frac{1}{\delta_l}\int_0^{\delta_l} u_L(y)\, dy = \frac{u_I}{2} + \frac{{\delta_L}^2}{12\mu_L}\left[\frac{\Delta p_p}{L_c} - \rho_L g\right]. \tag{7.61}$$

For evaluating the interfacial velocity, Saurel and Abgrall's (1999) model is evoked again, Eq. (4.38), in the herein context will give that,

$$u_I = \frac{\bar{u}_G(\delta - \delta_L)\rho_G + \bar{u}_L\delta_L\rho_L}{(\delta - \delta_L)\rho_G + \delta_L\rho_L}. \tag{7.62}$$

Finally, by combining Eq. (7.60), Eq. (7.61), Eq. (7.59), and Eq. (7.62), the following system of algebraic equations is obtained,

$$\begin{cases} \bar{u}_G = \dfrac{1}{2}(u_I + v_p) + \dfrac{(\delta - \delta_L)^2}{12\mu_G}\left(\dfrac{\Delta p_p}{L_c} - \rho_G g\right) \\ \bar{u}_L = \dfrac{u_I}{2} + \dfrac{{\delta_L}^2}{12\mu_L}\left(\dfrac{\Delta p_p}{L_c} - \rho_L g\right) \\ \mu_G\delta_L\left[v_p - u_I + \dfrac{(\delta - \delta_L)^2}{2}\left(\dfrac{\Delta p_p}{L_c} - \rho_G g\right)\right] = \mu_L(\delta - \delta_L)\left[u_I - \dfrac{{\delta_L}^2}{2}\left(\dfrac{\Delta p_p}{L_c} - \rho_L g\right)\right] \\ u_I \equiv \dfrac{\bar{u}_G(\delta - \delta_L)\rho_G + \bar{u}_L\delta_L\rho_L}{(\delta - \delta_L)\rho_G + \delta_L\rho_L}, \end{cases} \tag{7.63}$$

with four equations and four unknows $\bar{u}_G$, $\bar{u}_L$, δ_L and u_I. It is important that since the gas phase is considered incompressible in this model, the gas density is obtained by averaging the density of the states at the plunger tail and front in with the same equation used in the pig model, Eq. (7.25), ρ_G=$\rho_G\left(p_{p,t}, p_{p,f}\right) = \rho_G\left(p_{p,t}, p_{tb}\right)$. Also, the values for Δp_p and v_p come from the coupled solution between piston and flow.

To give a perspective of the solution of the system given by Eq. (7.63) a case where the fluids are IsoparL and air are considered, detailed in Table 7.1, with a gap of δ=0.035in and L_c=482.6mm(19in), while the pressure difference across the plunger ranging from Δp_p=0Pa(0psi) to Δp_p=34474Pa(5psi), let $p_{p,t}$=184.062kPa(12psig) for several plunger velocities.

Table 7-1: Fluid Properties, IsoparL, and air for the gap problem example.

Parameter	Symbol	Value
Temperature	T	298 K²
Ideal gas constant	R	287 J/kg.K
Sound speed in gas	$c_G = \sqrt{RT}$	292 m/s
Reference gas density	$\rho_{0,G}$	0 kg/m^3
Liquid density	ρ_L	720 kgm^3
Dynamic viscosity gas	μ_G	1.9_x10^{-5} Pa.s
Dynamic viscosity liq.	μ_L	1.25_x10^{-3}Pa.s

Figure 7.9 presents the results for the phase fraction, δ_L/δ, against Δp_p obtained with the system of equations described in Eq. (7.63). The curves can present from two to four solutions depending on the value of Δp_p. When interpreting the results, there are, in general, three continuous curves. The lower one gives negative values for the phase fraction, $\delta_L/\delta < 0$, thus, this solution is non-physical and disregarded. The top curve gives two solutions, one always returns values of phase fraction greater than one, $\delta_L/\delta >1$, and this non-physical solution is also disregarded. The other one can give physical values, $0< \delta_L/\delta <1$, however, in most cases, also returns results with $\delta_L/\delta >1$. When this solution is in the physical interval, the values for δ_L/δ are near unity, and the correspondent velocities are near or under supercritical flow velocities, thus, this curve is also disregarded. The only curve that always seems to return physical values is the middle one, Fig. 7.10, where for lower pressure differences, when gravity is the flow driving force, there is a single solution with a high liquid film. Then, there is a transition when two or three solutions are available, and, finally, when the pressure difference is high enough, there is only one solution with a near-constant film, in this case $\delta_L/\delta \approx 0.18$.

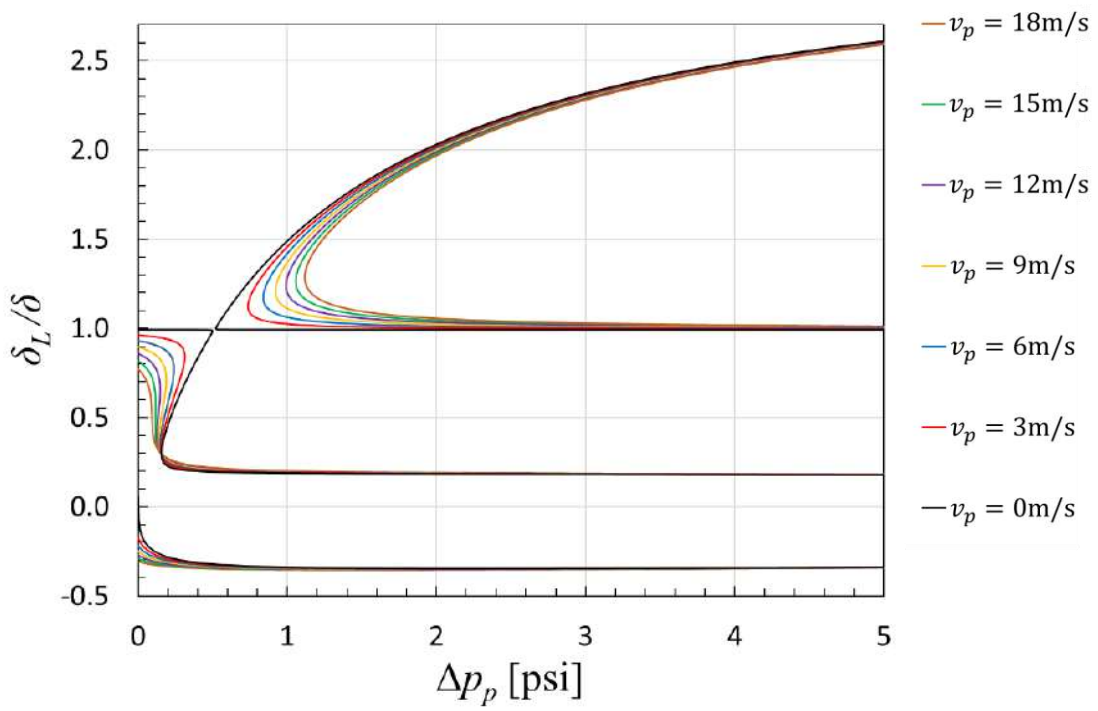

Figure 7.9: Example of a phase fraction solution for the plunger gap problem (1).

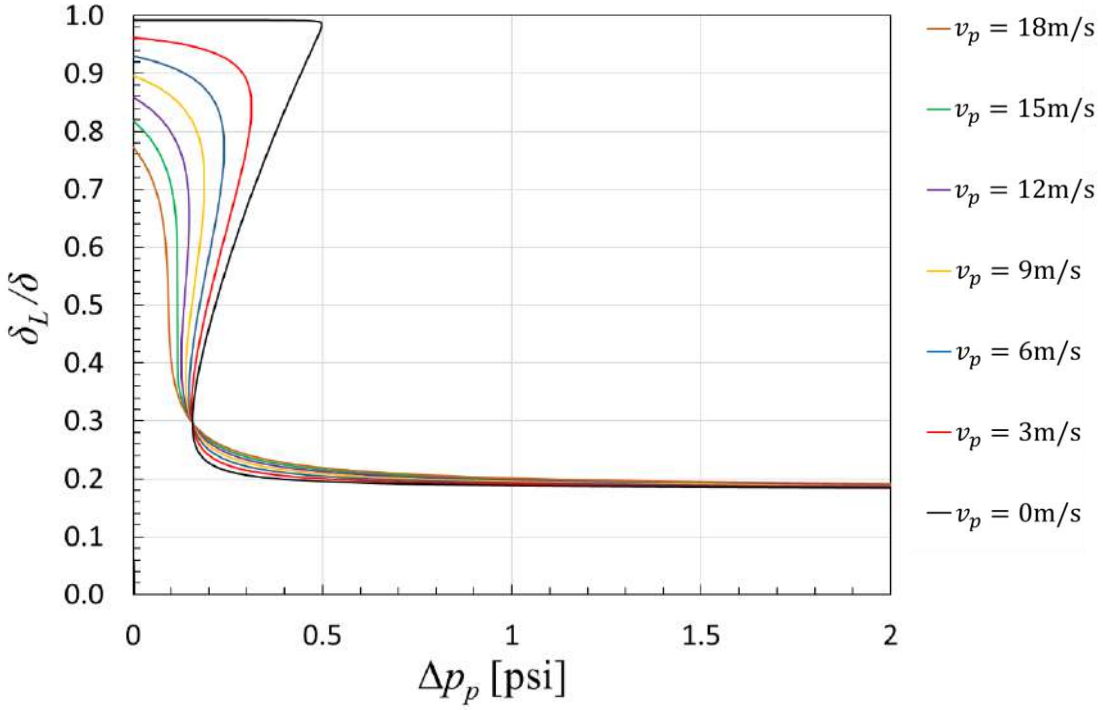

Figure 7.10: Example of a phase fraction solution for the plunger gap problem (2).

With this physically representative solution, the following graphs for the gas, liquid, and interfacial velocities are given respectively by Figs. 7.11, 7.12, and 7.13.

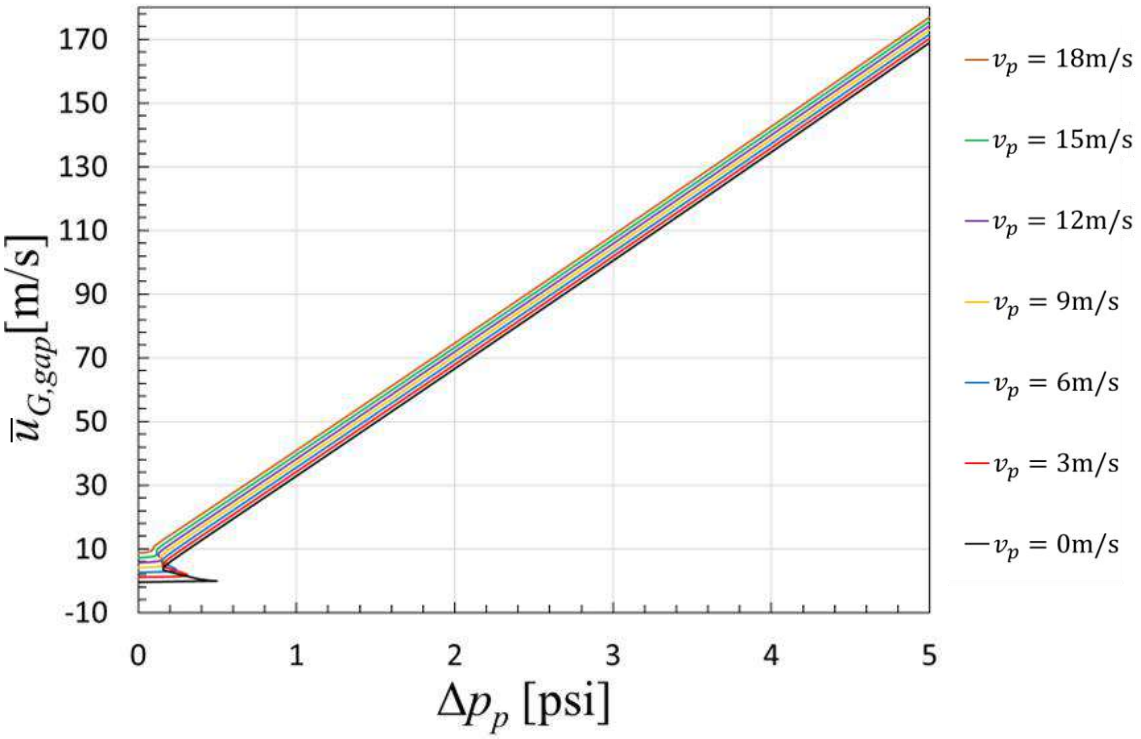

Figure 7.11: Example of a gas velocity solution for the plunger gap problem.

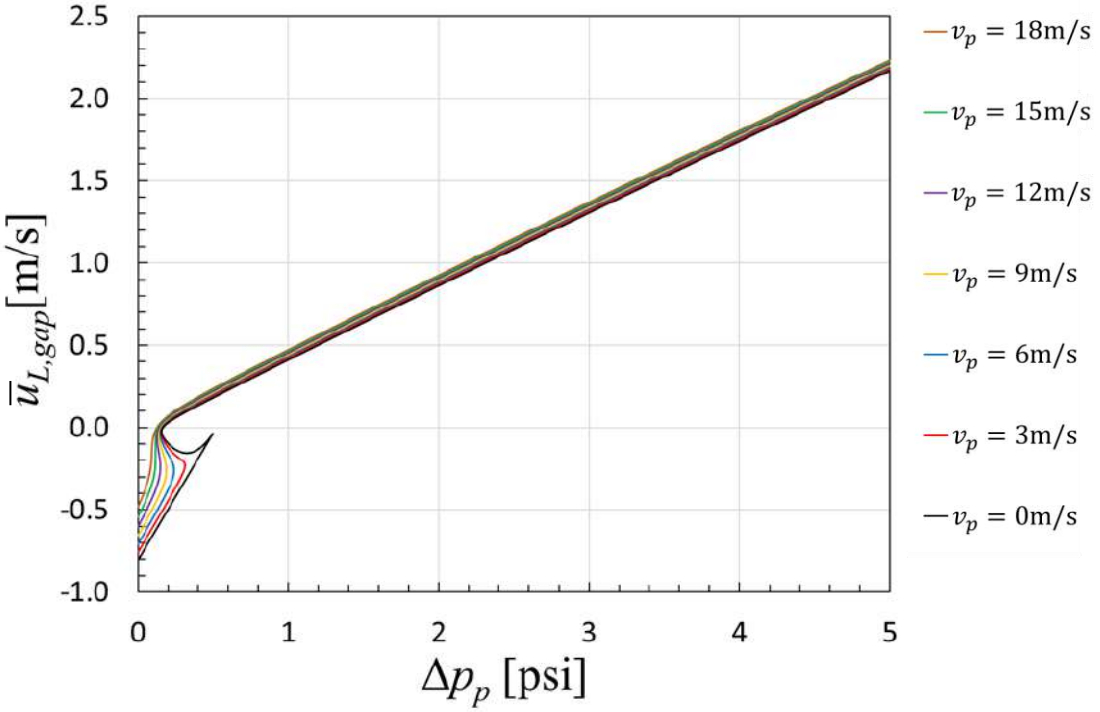

Figure 7.12 Example of a liquid velocity solution for the plunger gap problem.

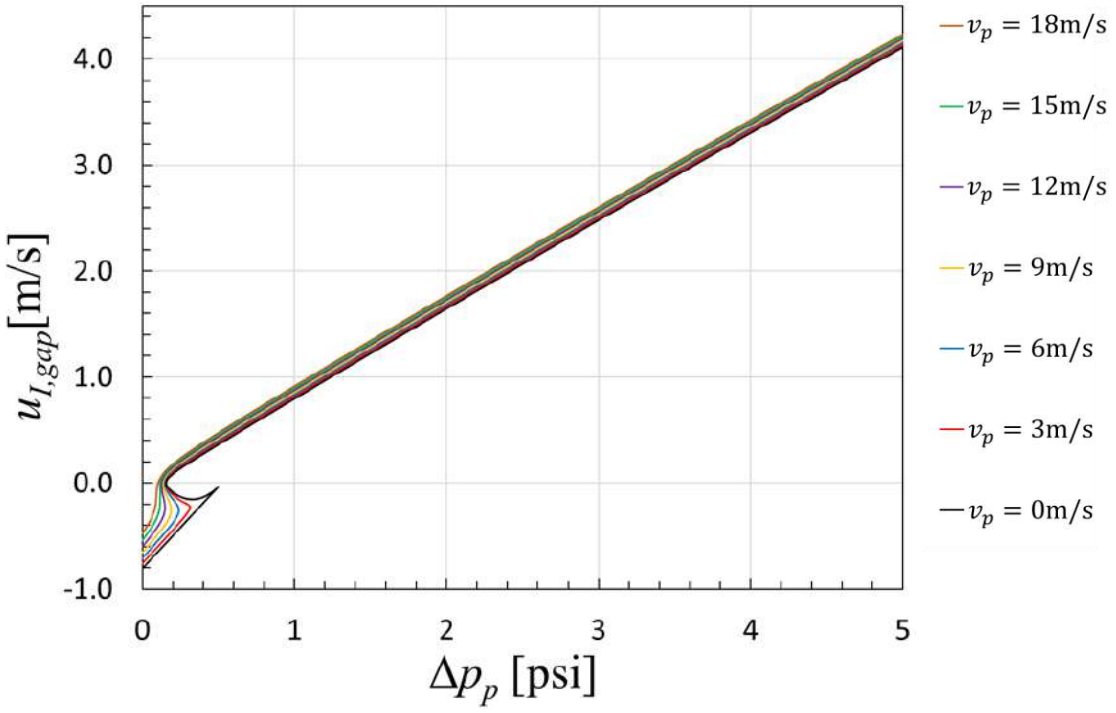

Figure 7.13: Example of interfacial velocity solution for the plunger gap problem.

The velocities, in general, show an approximately linear trend with little variation across the selected plunger velocities.

To obtain the mass flow rate through the gap the following calculations are performed,

$$\dot{m}_{G,gap} = \rho_G \bar{u}_G A_{G,gap} = \rho_G \bar{u}_G \pi \left[\frac{1}{4}\left(d^2 - d_p^2\right) - \delta_L (d - \delta_L)\right], \tag{7.64}$$

$$\dot{m}_{L,gap} = \rho_L \bar{u}_L A_{L,gap} = \rho_L \bar{u}_L \pi \delta_L (d - \delta_L). \tag{7.65}$$

With a tubbing diameter of d=50.8mm(2in), the trend for the mass flow rate is obtained according to Figs. 7.14 and 7.15.

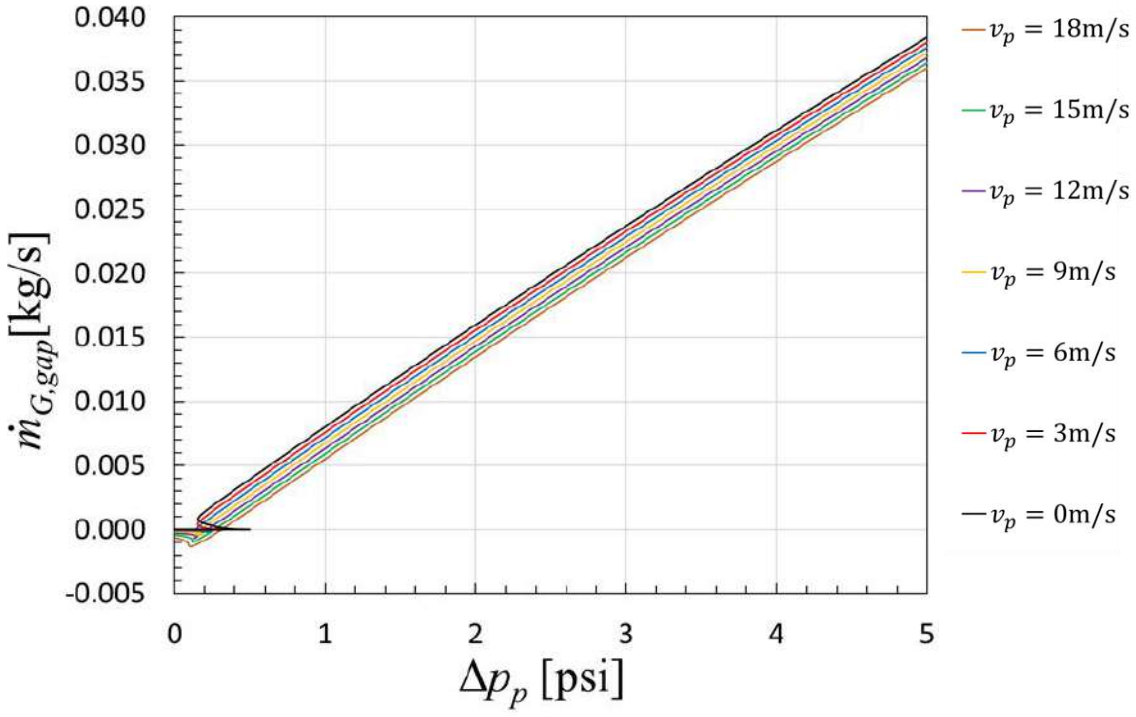

Figure 7.14: Example of gas mass flow rate solution for the plunger gap problem.

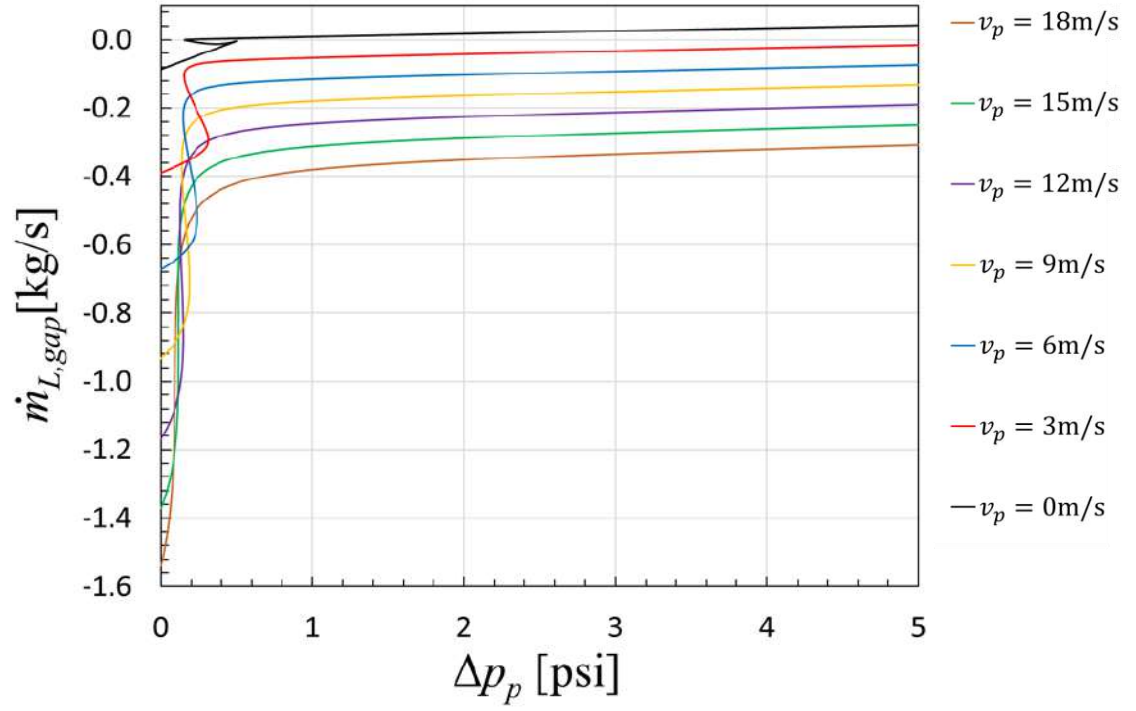

Figure 7.15: Example of liquid mass flow rate solution for the plunger gap problem.

The gas mass flow rate solution also shows an approximately linear trend with little variation across the selected plunger velocities, whereas the liquid mass flow rate shows a smooth variation with Δp_p, except for very small values of Δp_p. The model also satisfies

the expected behavior for the gas slipping from the plunger tail to the front, which causes the emergence of the Taylor bubble, and the liquid fallback, which reduces deliquification efficiency. The rate of change of the liquid mass flow is also quite linear with the plunger velocities, which corroborates with the finds of Akhiiardinov *et al.* (2020) and Mower *et al.* (1985).

Analyzing the solution represented in Figs. 7.10 to 7.15, the region with low-pressure differences brings more concern since within the perspective of an initial value problem the multiplicity of solutions can bring instability to a numerical solution. To exemplify, if in the overall transient solution of the plunger problem the pressure gradient across the plunger starts at $\Delta p_p = 0\text{Pa}$ and increases gradually, to keep robustness, a numerical solution will follow the continuous solution with a higher δ_L/δ, then a jump in the solution may appear, which may create oscillations or even failure in convergence. This attribute in the solution of the system comes from the approximations of fully developed flow and from not considering the transient terms within a time step of the simulation. These hypotheses give the plunger-gap model a pseudo-steady-state character that is unable to cover this transition stage.

7.3 Coupled Piston and Flow Motion Problem

The models previously presented are a separate system of equations that must interface with a flow model so that a full transient solution for each application can be obtained. In the next subsection, the methodology to couple the piston models with the transient flow model is detailed.

7.3.1 Piston Model Solution

Each of the piston models composes a different system of equations with each having its own particularities, however, none of the systems have available analytical solutions requiring a numerical methodology to obtain approximate solutions. An effort was made to select a single numerical solver for each of the systems, however, with the particularities of each system, different solvers needed to be selected. The IMSL® Fortran math library has a wide range of well-tested routines that used a single or a combination of numerical methods for solving systems of ordinary-differential equations or a system of algebraic ordinary-differential equations.

For the single-phase pig model, the IMSL® routine DAESL based on the methods of Petzold (1982) and Ascher and Petzold (1988), is used to solve the first order differential-algebraic system of equations. This routine uses multiple sub-steps to obtain the solution for implicit differential-algebraic systems with a differential index lower or equal to 1. The system differentiation index is the minimum number of differentiations required to reduce a system of algebraic ordinary differential equations into a system of ordinary differential equations. The routine uses backward differentiation formulas, BDF, of orders 1 to 5. A second option is to simply do a backward second-order differentiation on the ODE and solve the resulting algebraic system, where the particularly low time steps from the explicit differentiation of the flow are deemed enough. A third option is using a classic 5th order implicit Runge-Kuta method with 3 stages. For all cases tested there is no noticeable difference between the results using either of the three suggested approaches. The system is solved by using the initial values from the current time step, u_t, p_f, and returns the solution for v_p, p_t and u_f, the obtained solution is, then, used as boundary conditions for the flow model at the respective borders of the pig.

For the two-phase piston model, the IMSL® routine DAESL was not able to return a solution. The Runge-Kuta method also was not able to return a solution for that system. However, the second-order backward differentiation on the force balance equation was enough to obtain a stable and representative solution, then the routine NEQNF from IMSL® is used, solving the resulting system of nonlinear algebraic equations using a modified Powell hybrid algorithm and a finite-difference approximation to the Jacobian. Similarly to the single-phase model, the two-phase pig model uses $u_{G,t}$, $u_{L,t}$ p_f, as input and returns v_p, $\alpha_{G,f}$, $u_{G,f}$, $u_{L,f}$ p_t that are used as boundary conditions for the two-phase flow models at the borders of the pig.

Finally, for the plunger model, since the systems can be written entirely of ordinary-differential equations, the first try was to use a Runge-Kuta method. The IMSL® routine IVPRK, Hull *et al.* (1976), was employed for a 5th Runge-Kuta, but the system of equations proved to be quite stiff for that type of method. Then the IMSL® routine IVPAG was used, as an alternative, it solves a system of first-order ordinary differential using the Gear Stiff method BDF of 5th order. The model uses $p_{ls,f}$, $p_{p,t}$ as initial condition and solves v_{ls}, v_p, L_{ls}, L_{tb}, p_{tb}, that simultaneously with the gap model returns $\dot{m}_{L,gap}$ and $\dot{m}_{G,gap}$, then the values for v_{ls}, $\bar{u}_G$ and $\bar{u}_L$ are used as boundary conditions for the flow.

At the front of the liquid slug, the gas is assumed to be moving with the same velocity as the liquid slug front then,

$$u_{G,CV_f} \equiv v_{ls,f} = v_{ls} - \frac{1}{2}\frac{dL_{ls}}{dt}. \tag{7.66}$$

At the tail of the plunger, it can be written that,

$$u_{G,CV_t} \equiv \bar{u}_{G,gap}, \tag{7.67}$$

$$u_{L,CV_t} \equiv \bar{u}_{L,gap}. \tag{7.68}$$

To couple the plunger gap model, Eq. (7.63), with the plunger control volume models Eq. (7.46), Eq. (7.50), and Eq. (751), is not straightforward. The coupled models result in an algebraic ordinary-differential system that was too stiff to be solved with any of the previously stated methodologies. Also, at the start of the plunger lift simulation, the gap model passes through the transition where the gap flow goes from gravity-driven to pressure-driven, then, the numerical solution through that transition introduces discontinuities or even failure in convergence. Since that portion only covers a relatively small time of the plunger lift operation, an approximate approach is adopted here. For a given configuration, the liquid film height in the gap is nearly constant for reasonable values of plunger velocity and the pressure difference across the plunger after the transitional state. Then, an approximately constant value for the liquid film is estimated by solving the gap system, Eq. (7.63), a priori. With that, the values for the fluid velocities through the gap become functions of the pressure differential and the plunger velocity, $u_{I,gap} = u_{I,gap}(\Delta p_p, v_p)$, $\bar{u}_{G,gap} = \bar{u}_{G,gap}(\Delta p_p, v_p)$ and $\bar{u}_{L,gap} = \bar{u}_{L,gap}(\Delta p_p, v_p)$, that can be obtained analytically. Since the gas is considered incompressible through the gap, it can be also stated that $\dot{m}_{L,gap} = \dot{m}_{L,gap}(\Delta p_p, v_p)$, and $\dot{m}_{G,gap} = \dot{m}_{G,gap}(\Delta p_p, v_p)$, and the overall plunger model is reduced to a model of ordinary-differential equations. The interfacial velocity equation is taken out of the system and the interfacial velocity through the gap is obtained by manipulating the shear stress equation at the interface,

$$u_{I,gap}(\Delta p_p, v_p) = \frac{\mu_G \delta_L \left[v_p - \frac{\kappa_G}{2}(\delta - \delta_L)^2 \right] - \mu_L (\delta - \delta_L) \frac{\kappa_L}{2} {\delta_L}^2}{\mu_G \delta_L + \mu_L (\delta - \delta_L)}, \tag{7.69}$$

with,

$$\kappa_G = -\frac{1}{\mu_G}\left(\frac{\Delta p_p}{L_c} - \rho_{G,gap} g\right), \qquad \kappa_L = -\frac{1}{\mu_L}\left(\frac{\Delta p_p}{L_c} - \rho_L g\right). \tag{7.70}$$

Then the velocities $\bar{u}_{G,gap}$ and $\bar{u}_{L,gap}$ are directly obtained through Eq.(7.60) and Eq.(7.61).

7.3.2 Mesh Reconstruction

A scheme proposed by Patricio *et al.* (2020) simulates the piston as a singular surface, with no length, moving within a fixed mesh, with a constant number of cells. Here this approach is modified, where the piston is a moving control volume within a mesh that is reconstructed at each time step. The piston sets two boundaries and the domain is divided into two separate meshes, the upstream mesh 1 and the downstream mesh 2. The upstream mesh has a total length of L_1 and cell size of Δx_1, and the downstream mesh has a length of L_2 and cell size of Δx_2, since in the herein methodology, the piston occupies a volume within the mesh, $L = L_1 + L_{CV} + L_2$, as represented in Fig. 7.16.

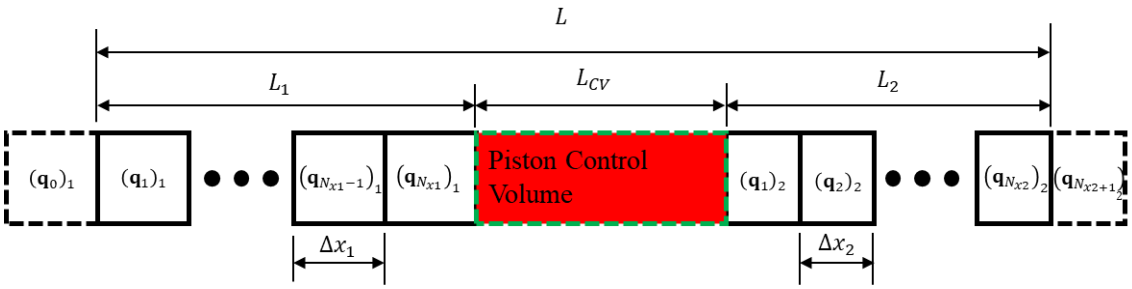

Figure 7.16: Sketch of upstream and downstream meshes with the piston control volume.

The sizes for Δx_1 and Δx_2 are initially determined based on the original single mesh domain selected from the initial condition, Eq.(5.1), where the size $\Delta x \equiv \Delta x_{max}$ is defined here as the maximum value that Δx_1 and Δx_2 can have so that the overall

resolution of the original mesh is not decreased. A minimum value is also needed since the CFL condition, Eq. (5.5), always needs to be satisfied, if the values for the mesh sizes are too small the time step of the simulation must follow. To keep reasonable time steps for the herein work the minimum value of $\Delta x_{min} = 0.75\Delta x$ is set and a fixed time step is obtained using this minimum value through Eq. (5.5). The mesh sizes upstream and downstream are defined respectively by,

$$N_{x1} = \lceil L_1 \Delta x \rceil, \qquad N_{x2} = \lceil L_2 \Delta x \rceil, \tag{7.71}$$

and the cell sizes are obtained using Eq. (5.1), $\Delta x_1 = L_1/N_{x1}$, $\Delta x_2 = L_2/N_{x2}$. Since the sealing function is used, it is guaranteed that $\Delta x_1 \leq \Delta x_{max}$, $\Delta x_2 \leq \Delta x_{max}$, thus the resolution is not decreased. The minimum value though needs to be verified if $\Delta x_1 \leq \Delta x_{min}$, for example, then N_{x1} is reduced by one cell. This also applies for Δx_2 and N_{x2}, if it still does not meet the criteria a new minimum value must be set. The values for the conservative variables downstream $(\mathbf{q}_i)_1$ and upstream $(\mathbf{q}_i)_2$ are obtained through linear interpolation, based on their position in the domain,

$$(\mathbf{q}_i)_1 = \mathbf{q}_j + \frac{\mathbf{q}_{j+1} - \mathbf{q}_j}{\Delta x}\left[(x_i)_1 - x_j\right], \text{ if } x_j < (x_i)_1 < x_{j+1} \tag{7.72}$$

$$(\mathbf{q}_i)_2 = \mathbf{q}_j + \frac{\mathbf{q}_{j+1} - \mathbf{q}_j}{\Delta x}\left[(x_i)_2 - x_j\right], \text{ if } x_j < (x_i)_2 < x_{j+1}. \tag{7.73}$$

After one time step, with the movement of the piston, new upstream and downstream meshes have to be generated, and the upstream mesh changes in size as,

$$L_1^{n+1} = L_1^n + v_{CV,t}\Delta t, \tag{7.74}$$

whereas downstream as,

$$L_1^{n+1} = L_1^n - v_{CV,t}\Delta t. \tag{7.75}$$

With the new mesh lengths, the same procedure is followed to obtain $\Delta x_1^{n+1} \in [\Delta x_{min}, \Delta x_{max}]$, and $\Delta x_2^{n+1} \in [\Delta x_{min}, \Delta x_{max}]$, by using Eq. (7.71) for each side. And the

values for the conservative variables are linearly interpolated for each time step, considering that $(x_j)_1^n < (x_i)_1^n < (x_{j+1})_1^n$ and $(x_j)_2^n < (x_i)_2^n < (x_{j+1})_2^n$,

$$(\mathbf{q}_i)_1^{n+1} = (\mathbf{q}_j)_1^n + \frac{(\mathbf{q}_{j+1})_1^n - (\mathbf{q}_j)_1^n}{\Delta x_1^n}\left[(x_i)_1^{n+1} - (x_j)_1^n\right], \tag{7.76}$$

$$(\mathbf{q}_i)_2^{n+1} = (\mathbf{q}_j)_2^n + \frac{(\mathbf{q}_{j+1})_2^n - (\mathbf{q}_j)_2^n}{\Delta x_2^n}\left[(x_i)_2^{n+1} - (x_j)_2^n\right]. \tag{7.77}$$

Not that the methodology implemented through Eqs. (7.76) and (7.77) evolve the downstream grids from the time step n to the time step $n+1$, however, the solution of primitive variables does not evolve through time during this scheme, with the obtained grids representing the same time fields of primitive variables but through dislocated meshes. In a finite volume perspective, the linear interpolation done to obtain the conservative variables at the new reconstructed cells can be seen as new values weighted by the volume of the previous mesh cells.

The general idea of coupling the models is to use the results of the piston models as moving boundary conditions for the flows upstream and downstream. Since the models for flow and piston are solved separately, the movement of the piston control volume through the pipe still needs to be incorporated into the flow solution to respect the conservation principles, even after the reconstruction of the meshes downstream and upstream. For simplicity, first, consider the cases where the piston control volume is constant, $L_{CV} = L_p$. In this case, the mesh reconstruction presented previously is based on the distance Δx_p covered by the piston between a time step Δt of the simulation. The reconstruction procedure only covers the transient solution of the flow through a fixed pipe length as it does not incorporate the transport of the fluid through and with the movement of the piston control volume boundaries. Therefore, the reconstructed mesh still represents the solution of the flow as if the piston was stationary and the upstream and downstream sections fixed. Thus, a correction to cells adjacent to the boundary interface is required to fully couple the piston and flow dynamics. Following the mesh reconstruction, the new mesh boundaries have overtaken the non-updated piston position, according to Fig. 7.17.

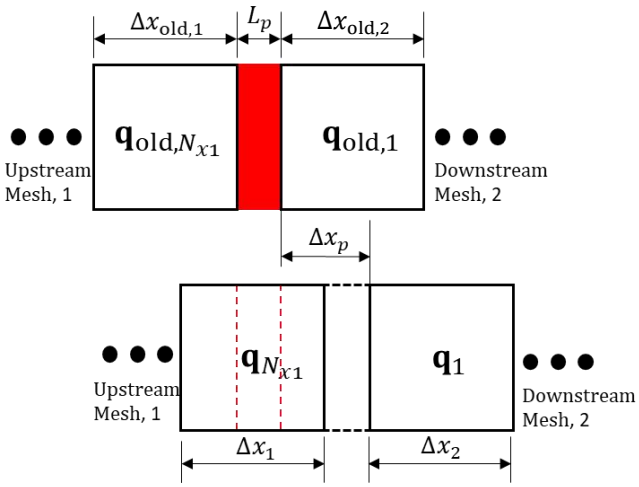

Figure 7.17: Mesh composition after mesh reconstruction procedure, note that the piston position is highlighted in red.

Since piston movement is not yet integrated into the solution, the newly reconstructed meshes need to be representative of the old meshes, prior to the reconstruction. Then, to fully reestablish a new mesh, the last cell in the upstream section needs to be shrunk by Δx_p, whereas the first cell downstream to grown also by Δx_p, as in Fig. 7.18. Then,

$$\Delta x_{T,1} = \Delta x_1 - \Delta x_p, \tag{7.78}$$

$$\Delta x_{T,2} = \Delta x_2 + \Delta x_p, \tag{7.79}$$

where $\Delta x_{T,1}$ is the new length for the last cell, N_{x1}, of the upstream mesh and $\Delta x_{T,2}$ the new length for the first cell of the downstream mesh.

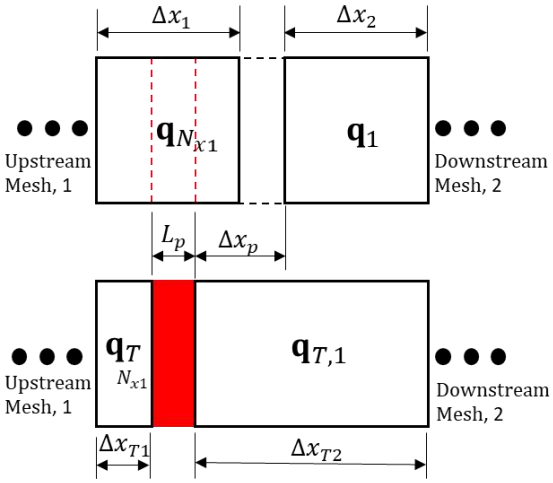

Figure 7.18: Mesh composition after readjusting the last cell of the upstream mesh, and the first cell of the downstream mesh.

In a control volume framework, the new conservative variables' value $\left(\mathbf{q}_{T,N_{x1}}\right)_1$ at the upstream mesh and the new $\left(\mathbf{q}_{T,1}\right)_2$ at the downstream mesh needs to be estimated, for that, they are defined by a volume-weighted average,

$$\left(\mathbf{q}_{T,N_{x1}}\right)_1 \equiv \frac{\Delta x_1\left(\mathbf{q}_{N_{x1}}\right)_1 - \Delta x_p\left(\mathbf{q}_{\text{old},N_{x1}}\right)_1}{\Delta x_{T,1}}, \tag{7.80}$$

$$\left(\mathbf{q}_{T,1}\right)_2 \equiv \frac{\Delta x_2(\mathbf{q}_1)_2 + \Delta x_p\left(\mathbf{q}_{\text{old},1}\right)_2}{\Delta x_{T,2}}. \tag{7.81}$$

8 Experimental Facility

This chapter describes the experimental facility used to gather data to compare with the results obtained from the plunger lift simulations, the experimental procedure, the experimental matrix, and the data treatment. The facility is the same used by Akiiartdinov *et al.* (2020), equipped to handle real plungers utilized in the field. The facility has three main sections that are connected into a loop, the casing section, the tubbing section, and the separator section or return section.

8.1 Experimental Facility Description

The casing section, made of polycarbonate tubes, is directly connected to the compressor that feeds air into the system, thus serving as a pressure tank to provide energy to raise the plunger. This section is divided into two connected tubes, one of 152.4mm(6-in) internal diameter and 7m(23ft) in length, and the second of the same internal diameter and 2.74m(9ft) long. The casing pressure can be remotely controlled by a control valve connected to the compressor flowline and a pressure transmitter. For safety and to respect the integrity of the facility, there is a rupture disk and a safety valve with a burst pressure of 308.17kPa(30psig) also connect to the casing.

Directly connected to the casing is the tubbing section where the testing section and most of the instrumentation are present. The tubbing of 50.8mm(2-in) internal diameter and length of 10.67m(35ft) is also made from transparent polycarbonate to allow visualization of the plunger transients. At its bottom, there is a check valve bumper spring assembly, that ensures there is no backflow into the casing, and the bumper spring is used to dampen the impact of a falling plunger. Right at the base of the bumper spring, there is a line that feeds liquid to the facility. The liquid is transported through a pump from a storage tank and the liquid flow is controlled by a control valve connected to the liquid feed line. Along the tubbing length, there are six high-speed pressure sensors, HSP, nine inducive proximity sensors, PS, and six optical sensors, OS, all recording data at a sampling frequency of 1000 HZ. These sensors are used to analyse the dynamics of the plunger, liquid slug, and Taylor bubble. Their position in relation to the base of the bumper spring, the initial siting position of the plunger, is given in Table 8.1. A chamber is mounted in the middle of the facility to house a high-speed camera, installed at the position of 5.27m(17.3ft) in relation to the base of the bumper spring. The camera can be

used to record videos at 2000 frames per second, which was deemed adequate to visually capture the main effects occurring during the experimental data acquisition. At the very top of the facility, lies the lubricator, which is equipped with a pneumatic catcher. The catcher has the purpose of holding the plunger once it hits the top of the lubricator. There are two exits connected to the lubricator leading to the flowline since, after an upstroke, the plunger is caught and sits at the lubricator obstructing the top connection, and requiring the bottom one to keep the flow going. Between the base of the tubing and the top, there is also a differential pressure transducer mainly used to measure the liquid loading in the facility at each experimental point.

Between the tubbing section and the separator section, there is a connection line where the main control valve sits. This valve is the one that opens the tubbing to the separator pressure allowing the plunger to go up. The gravity-type separator feeds the liquid-gas mixture into an acrylic tube of 152.4mm(6-in) internal diameter and 9.14m(30ft) in length. Once the mixture comes, the liquid settles in the bottom where a return line is connected to the liquid storage tank, and the gas is dumped into the atmosphere from the top of the separator. The separator was dimensioned so as to not greatly influence the outlet pressure of the tubbing through buildup backpressure. For a schematic of the entire facility see Fig. 8.1 provided by Akiiartdinov *et al.* (2020).

Table 8-1: Instrument position in the tubbing, from the base of the bumper spring.

Position	Prox. sensor	HS pressure	Opt. sensor
1.280m (4.2ft)	PS-1	HSP-1	OS-1
1.737m (5.7ft)	PS-1A	-	-
2.195m (7.2ft)	PS-2	HSP-2	OS-2
2.652m (8.7ft)	PS-2A	-	-
3.109m (10.2ft)	PS-3	HSP-3	OS-3
3.566m (11.7ft)	PS-3A	-	-
4.023m (13.2ft)	PS-4	HSP-4	OS-4
4.511m (14.8ft)	-	HSP-5	-
4.938m (16.2ft)	PS-5	-	OS-5
8.138m (26.7ft)	-	HSP-6	-

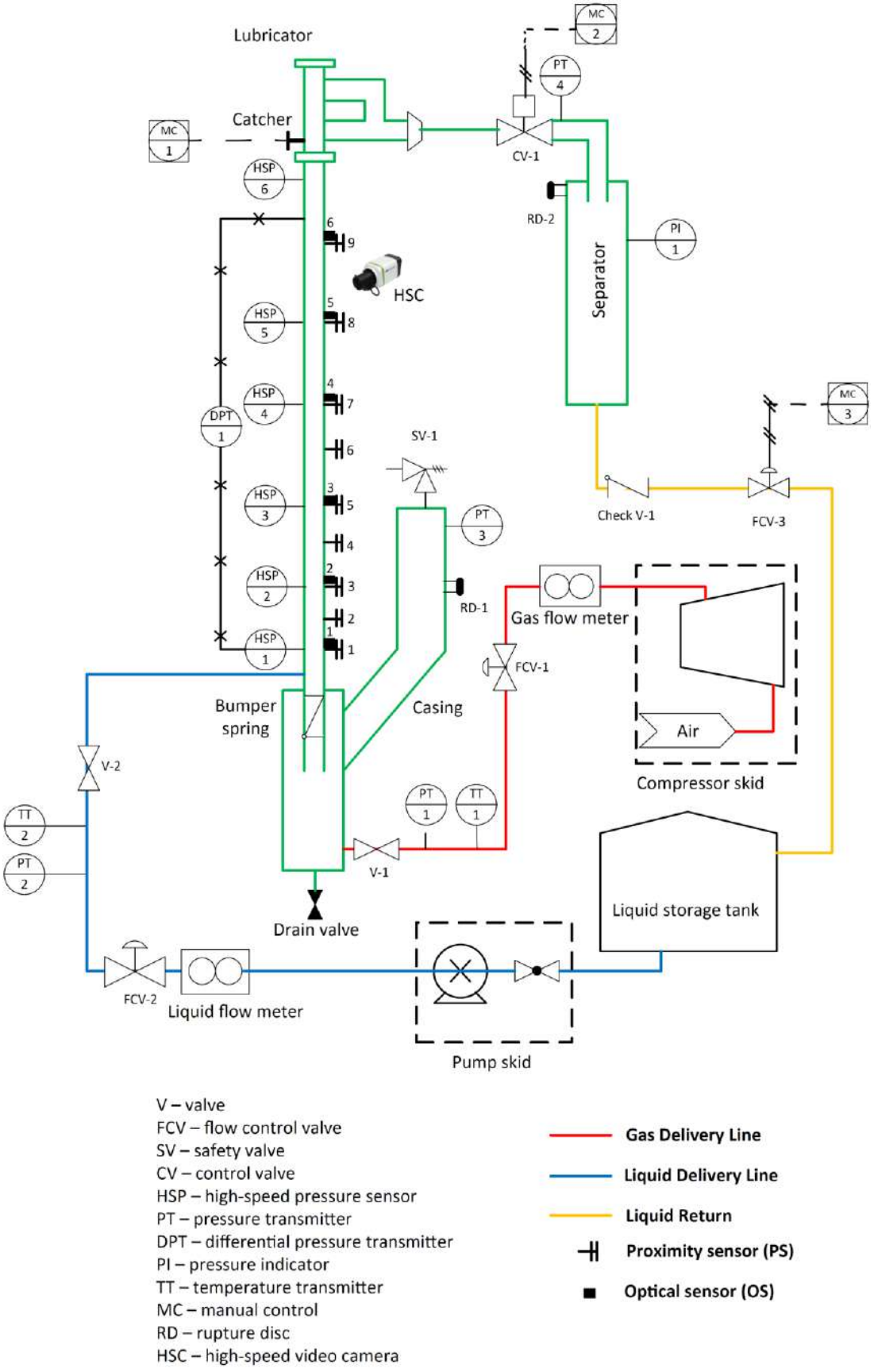

Figure 8.1: Experimental facility schematic (Akiiartdinov *et al.*, 2020).

8.2 Experimental Procedure

The experimental runs made on the facility were focused on conventional plunger lift operations on a vertical tubbing section, as to gather data on the dynamics of the plunger during this transient stage for different initial casing pressures.

Since the facility launches a metal piston at high velocities it is extremely important to inspect the condition of all equipment. First identifying the position of the piston before the start is critical, since the risk of launching a piston in dry conditions may damage the equipment and create risks to the operator and close-by personnel. If the plunger is on top of it for safety reasons it should never be dropped without a liquid load on the bottom. If the plunger is on the bottom of the facility, it should also not be pressurized without loading it with liquid. To check the integrity of the pipping, with the plunger stuck on top, the amount of liquid inside, and CV-1 closed the facility is pressurized to 239.22kPa (20psig) and the internal pressure is monitored over time to ensure there is no leakage.

With the facility empty and the control valve CV-1 open, empty data is recorded to generate a calibration file of all sensors and to verify their recording conditions. Especially the HSP sensors are very sensitive to offsetting and need to be corrected based on the empty file. The offsetting of the sensor may occur quite often so, for good practice, empty data is recorded every other three runs. If the empty data between the recorded data drifts in a considerable way, the data may be disregarded and the experimental runs are repeated.

To set up the experiment, first, ensure CV-1 is open and the plunger is on the bottom. Then load the tubbing with the desired liquid load, liquid slug length L_{ls}. The liquid load can be determined by the measurement from DPT-1 and double-checked visually through the surveillance cameras installed in the facility. After setting the liquid load CV-1 is closed and the facility is pressurized to the desired condition. For safety reasons, pressures must be kept below 225.43kPa(18psig). After the pressure is settled, data starts being recorded, CV-1 is opened again and the plunger rises with the liquid column.

8.3 Experimental Matrix

For the experiments performed, the test fluids are air and IsoparL. The mineral oil IsoparL was selected mainly to avoid corrosion of the metal parts of the facility and due to having similar rheology properties to water, as detailed in Table 8.2.

Table 8-2: IsoparL properties.

Property	Value
Density -	720 kgm^3
Dynamic viscosity- μ_L (25°C)	1.25_x10^{-3}Pa.s
Dynamic viscosity- μ_L (40°C)	0.99_x10^{-3}Pa
Surface tension -σ_L	0.024 N.m

For the experimental matrix, a relatively light titanium alloy plunger was selected as described in Table 8.3.

Table 8-3: Titanium alloy Plunger properties.

Parameter	Symbol	Value
Plunger mass	M_p	1.615 kg
Plunger length	L_p	355.6 mm (14in)
Plunger diameter	d_p	49.22 mm (1.93in)

The experiments were run a liquid loading of 1.17m(45in) with four distinct casing pressures, 184.062kPa(12psig), 197.852kPa(14psig), 211.641kPa(16psig), and 225.431kPa(18psig).

8.4 Experimental Data Treatment

The facility record data at two different samples, the high-speed sensors (PS, HSP, and OS) that record data at 1000 Hz, since they measure the fast-transient effects of plunger lift. The other instruments, DPT, PT, TT, and CV state, record data at 4Hz. Then, the first procedure is to synchronize the data obtained from both frequencies. A

synchronization by determining the start of the upstroke based on the status of CV-1 would be ideal, however, since the frequency of this data is too low in relation to the high-speed data, the errors are too high. Then, it is more accurate to determine the initial time stamp of the upstroke by using HSP-6 data, when a decrease in pressure is detected by the sensor. By setting this initial time, the data from both the low and highspeed sides are synchronized through their time stamp.

The data from the proximity sensors are processed to determine the plunger position over time. The proximity sensor records a base signal of 5V with low noise when a metal object passes through the voltage drops to about 1V. It is straightforward to set a threshold in the data to detect the drop in the voltage. When this drop is detected, it records the time of the passage of the plunger front at the position of the sensor. It was expected that the data would go back to 5V after the tail of the plunger passed through the sensors, however, the data revealed that there is an inconsistent delay after the passage of the plunger tail. This delay made it unfeasible to estimate the velocities based on the position of the plunger front and tail in a single sensor through time. However, there is great consistency in detecting the plunger front, then the velocities are estimated using the recommended procedure detailed by Akiiartdinov *et al.* (2020) that estimates the velocity using the adjacent sensor,

$$v_{p,i} = \frac{x_{p,i+1} - x_{p,i}}{t(x_{p,i+1}) - t(x_{p,i})}, \tag{8.1}$$

$$t_{v_p,i} = \frac{t(x_{p,i+1}) - t(x_{p,i})}{2}, \tag{8.2}$$

where $v_{p,i}$ is the plunger velocity local to the sensor at the $x_{p,i}$ position, and $t_{v_p,i}$ is the time of the recorded velocity that is estimated by the averaged time between the measurements of the sensors. To process the data from the optical sensors, the same Eqs. (8.1) and (8.2) should be used. However, the data from the sensor are noisier and require filtering to properly be processed.

The high-speed sensors used have a measurement range from 101.353kPa(14.7psia) to 344.738kPa(50psia) and also record the pressure at a sample of 1000 Hz. To process the HSP data, calibration is done with the use of the empty files recorded.

$$p_{HSP,i} = c_{1,i}E_p - c_{2,i} - p_{offset}^{atm}, \quad (8.3)$$

where E_p is the recorded voltage, p_{offset}^{atm} the averaged pressure measurement with no flow conditions, and the coefficients $c_{1,i}$ and $c_{2,i}$ given in Table 8.4.

Table 8-4: High-speed pressure sensors calibration coefficients.

HSP sensor	$c_{1,i}$ [1/V]	$c_{2,i}$ [psi]
HSP-1	12.397	5.859
HSP-2	12.397	5.859
HSP-3	12.397	5.959
HSP-4	12.396	5.650
HSP-5	12.397	5.735
HSP-6	12.397	5.983

After the calibration, the data is converted from voltage to pressure units. A Fourier Transform was done to try to estimate the noise from the frequencies, however, the noise perceived in the data is not correlated to any specific frequency within the spectrum of the sampling frequency. This indicates that the noise occurs at random frequencies, then a moving average with 30 samples was done to smooth the data. This size was chosen by trial and error and the resulting plots represent well the original unfiltered one with enough sharpness.

9 Pigging Results and Discussion

This chapter presents and discusses the results obtained herein using the proposed methodology for simulating transient pigging operations. The first study corresponds to an idealized case of a pig with no bypass flow through it under a single-phase gas flow. The second and third cases are dedicated to pigging under single-phase flow considering the bypass. These cases are based on the ones presented by Patricio *et al.* (2020), which are constructed based on Gomes *et al.* (1995) using typical parameters of gas and liquid lines found in the oil and gas industries. These cases are chosen here to validate the current methodology, and the software OLGA is also used for comparison. In addition, in these single-phase cases, the influence of bypass holes in the pig model is tested. For these simulations, the previously presented model for single-phase flow coupled with the single-phase pig model is used. Note that for all the single-phase flow simulations herein presented, there were only minor differences between the selected numerical method utilized to render the results. Then, for simplicity and to keep the single-phase studies more focused on the physical representation of the problems, only the results with the Roe scheme are presented.

Finally, a pigging operation case under two-phase flow is tested using all the method-model combinations previously presented, with the two-phase pig model.

9.1 Single Phase Ideal Pig

First, to test the basics of the methodology of the general piston model an idealized problem of a pig with no bypass flow running in a single-phase gas line is set. In this case, only the force balance equation, Eq. (7.2), is considered in the modeling of the pig dynamics, since there is no mass flowing through the pig and consequently no hydrodynamic friction. Consider the following pipeline given in Table 9.1, where a steady-state flow condition is generated using the boundary conditions given in Table 9.2 and the fluid properties detailed in Table 9.3, in a mesh of 2500 cells and CFL=0.9 with the Roe scheme.

Table 9-1: Pipe properties, single-phase pigging cases.

Parameter	Symbol	Value
Pipe length	L	20 km
Pipe diameter	d	0.3032m (12in)
Roughness	ε	4.572_x10^{-5} m

Table 9-2: Inlet and outlet boundary conditions for the ideal pig case.

Flow Variable	Value
p at outlet ($x=L$)	10 MPa
u_G at inlet ($x=0$)	5.0 m/s

Table 9-3: Gas properties for the ideal pig case.

Parameter	Symbol	Value
Temperature	T	293 K²
Gas constant	R	287 J/kg.K
Sound speed in the gas	$c_G = \sqrt{RT}$	290 m/s
Reference gas density	ρ_0	0 kg/m³
Dynamic viscosity	μ_G	1.9_x10^{-5} Pa.s

After establishing a steady-state flow, the pig described in Table 9.4 is launched into the line at the position of $x_p(t_0)$=2000m. Since no bypass is considered in this case, the velocity of the gas at the pig tail and front is considered to be the same as the pig velocity, thus, the pig velocity sets the moving boundaries of the problem. With the velocities as boundaries at the pig tail and front, the pressure at the inlet, estimated during the establishment of the steady-state condition, is considered a new boundary at the inlet, and the velocity at the inlet is an open boundary during the passage of the pig.

Table 9-4: Pig properties for the single-phase pigging cases.

Parameter	Value
Pig mass M_p	50 kg
Pig characteristic length -L_c	0.5 m
Pig diameter -d_p	0.3036m
Static friction coefficient -η_s	0.45 (-)
Dynamic friction coefficient -η_d	0.40 (-)

Observe that the pig has a diameter greater than the pipe internal diameter, entering the pipe with interference. With that, through Eq. (7.2), the critical pressure difference is estimated to be around Δp_c=15kPa, that with Eq. (7.12) produces E^*=4.23MPa, with the value of υ^*=0. These values are selected to obtain a pressure driving force around the magnitude of $\Delta p_p A$=1kN, according to Patricio *et al.* (2020). The resulting mechanical friction force acting on the pig when it is moving is equal to F_M=964.6N.

At the beginning of the simulation, the pig is stationary and, since it has no bypass, it completely clogs the line. With this blockage, the pressure at the front of the pig will drop, whereas the pressure at the tail will increase, accelerating the piston. The transient effects on the pressure are quite fast, with a bit of an overshoot that afterward is dumped into a near-constant equilibrium pressure difference Δp_p=13.36kPa, as detailed in Fig. 9.1. This overshoot then creates a fast-transient region where the acceleration of the pig is quite high, afterwards there is a second acceleration region where the pig accelerates locally with the gas while the waves travel through the pipe, Fig. 9.2. Once this second acceleration is finished, a quasi-steady state is reached, where the pig travels with the same local gas velocity that increases from upstream to downstream, Fig. 9.3 and Fig. 9.4.

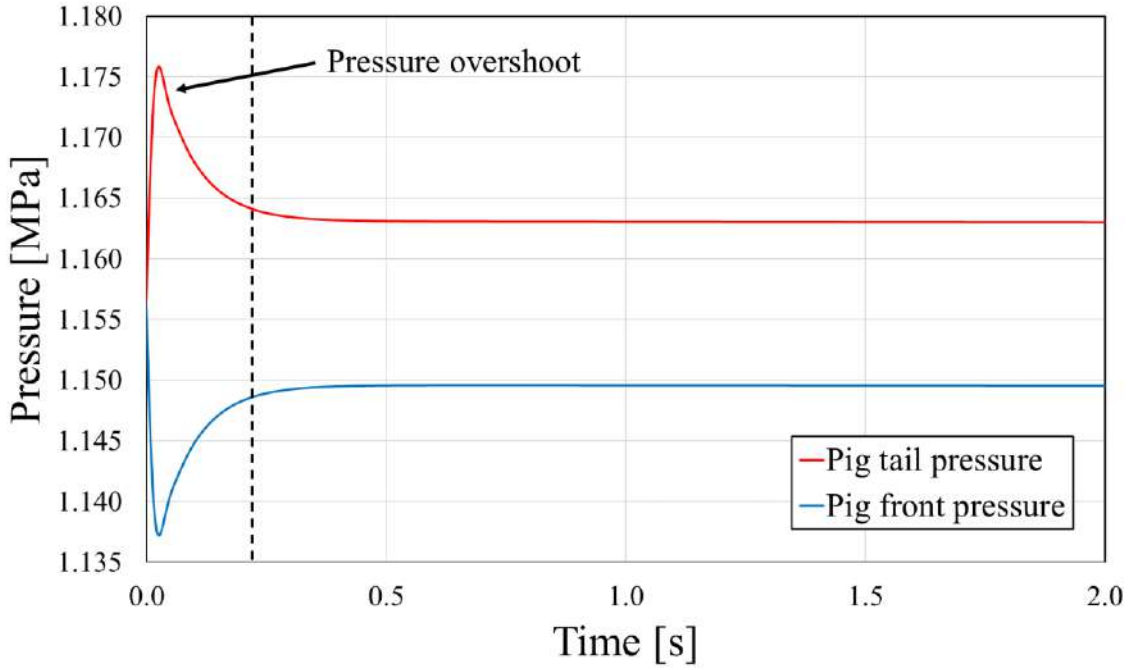

Figure 9.1: Pressure at pig front and tail during the first seconds of the simulation.

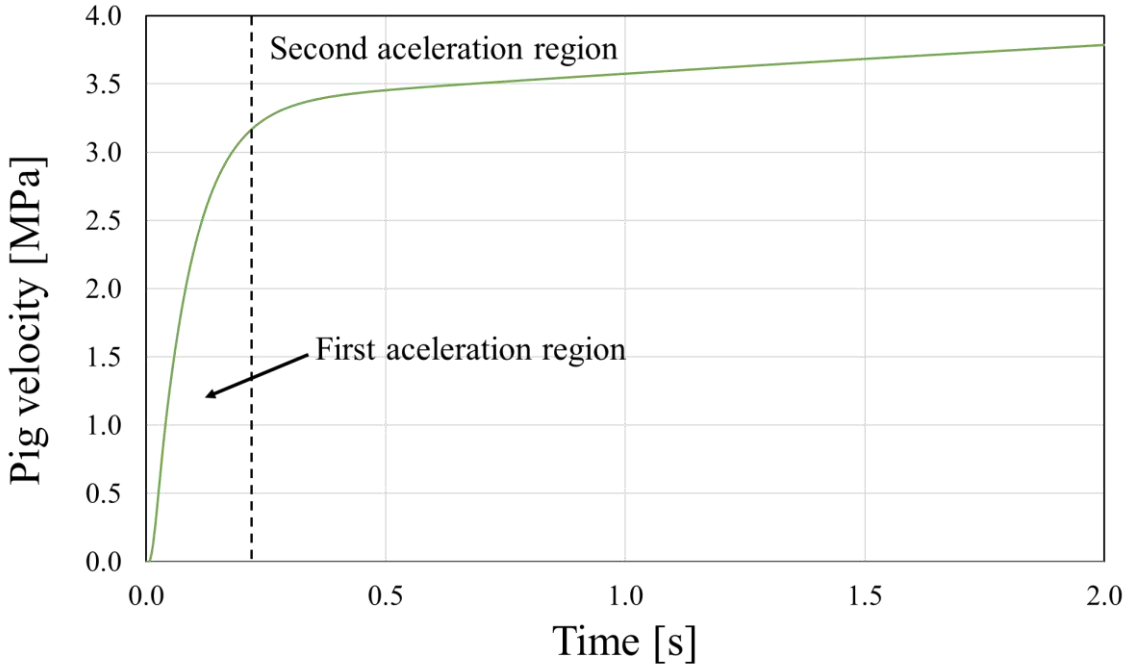

Figure 9.2: Pig velocity during the first seconds of the simulation.

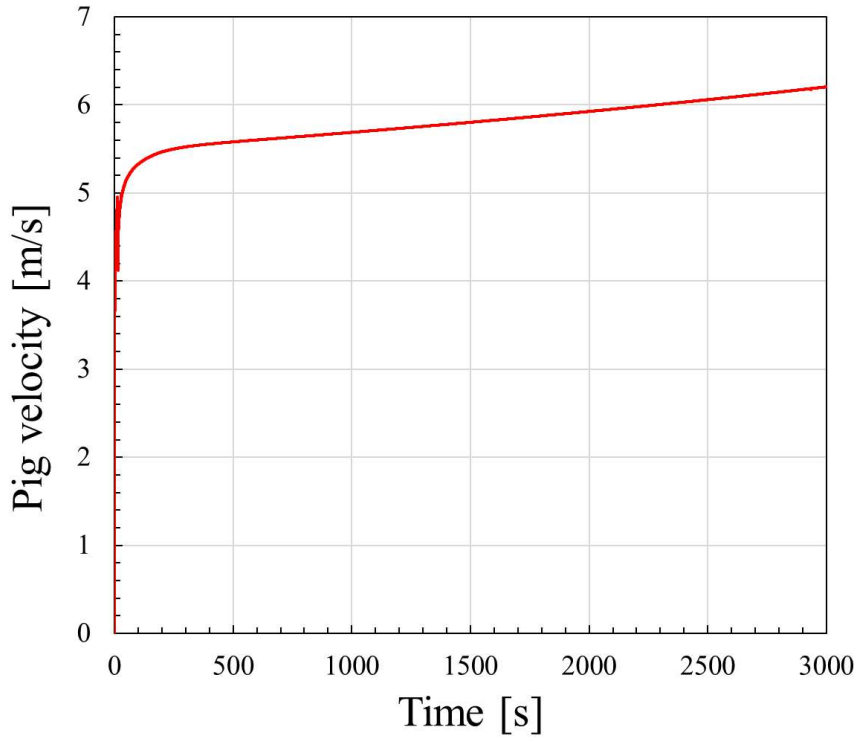

Figure 9.3: Pig velocity through time for the single-phase ideal pig case.

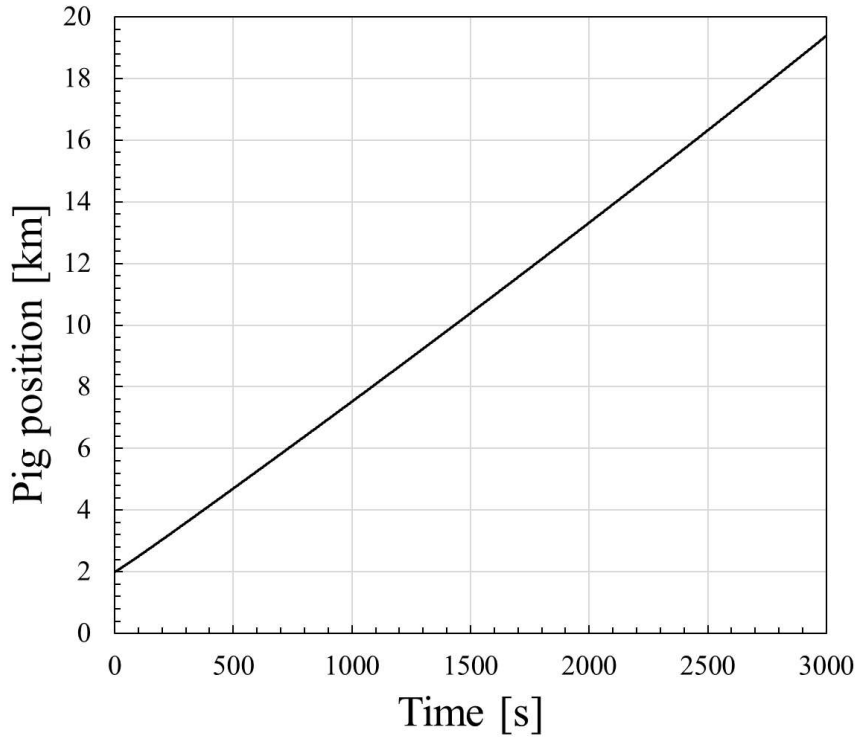

Figure 9.4: Pig position through time for the single-phase ideal pig case.

The pig travels driven by the pressure gradient created by its restriction to the flow. Then, through the pressure plots along the line at different snapshots in time, the pig position can be tracked by the pressure discontinuity present at each snapshot, Fig. 9.5. Note that the steady-state condition is represented by the dashed curve.

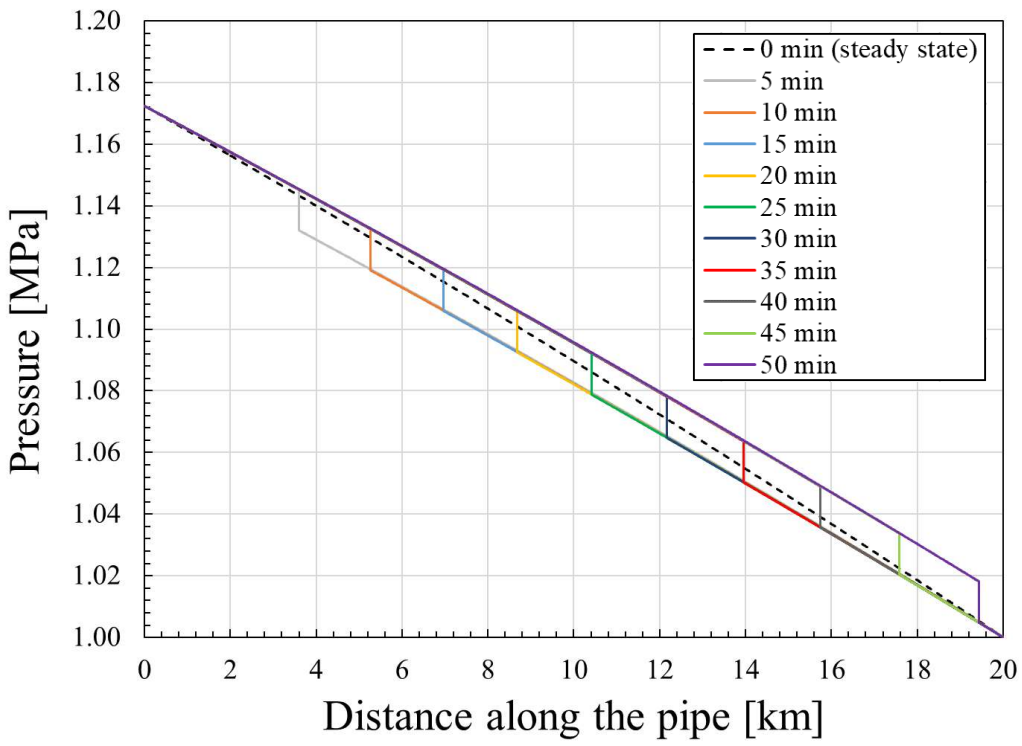

Figure 9.5: Pressure along the line for the single-phase ideal pig case.

This preliminary study is important to verify that the expected physics can be captured by the proposed methodology in the simplest scenario. The physics on different time scales are captured and the dynamics of the problem are well represented.

The following sections will approach the problem using the more complex modeling where the bypass is taken into account, then the pig model estimates the pressure difference in its body, using that information and the bypass flow rates to provide the moving boundary conditions.

9.2 Pigging in Single-Phase Liquid Flow

The next simulation studies the case of a pig traveling in a single-phase liquid line, given by Patricio *et al.* (2020). Analogously to the previous case, a steady-state is

generated prior to launching the pig in the simulation, the fluid properties and flow conditions to generate the steady-state are given in Table 9.5 and Table 9.6, with the same pipeline as the previous case, given by Table 9.1. The pig is also the same used in the previous case, given in Table 9.4, but now with a gap of δ=10^{-3}m. Note that for simulating the transient liquid flow using the single-phase flow model, Eqs. (3.2) and (3.3), the fluid is assumed compressible by means of the equation of state Eq. (4.6). With that, a reference liquid density can provide enough stiffness to the liquid so it can be deemed to be close to incompressible. Again, the Roe scheme is used with *CFL*=0.9 and N_x=2500 cells.

Table 9-5: Liquid properties for the pigging in liquid flow case.

Parameter	Symbol	Value
Temperature	T	293 K
Sound speed in the gas	c_L	290 m/s
Reference liquid density	ρ_0	997.98 kg/m³
Dynamic viscosity	μ_L	1.00114_x10^{-3} Pa.s

Table 9-6: Inlet and outlet boundary conditions for the pigging in liquid flow case.

Flow Variable	Value
p at outlet (x=L)	10^6 Pa
u_L at inlet (x=0)	2.0 m/s

The critical pressure difference for this case is estimated to be around Δp_c=139.8kPa, which produces E^*=36.11Mpa, with the value of υ^*=0. These values are selected to obtain a pressure driving force around the magnitude of $\Delta p_p A$=10kN, again following the example of Patricio *et al.* (2020). The resulting mechanical friction force acting on the pig when it is moving is equal to F_M=8984.7N. Also, it was verified that the hydrodynamic force, in this case, reached a near-constant value of F_H=0.55N, showing that this term has negligible effects on the pig dynamics since it is four orders of magnitude lower than the other forces.

Here again, the pig is launched from a stationary condition, but at the starting position of $x_p(t_0)$=100m. The initial dynamics of the pig are similar to the previous case, hence it is not detailed again. However, since the liquid is far stiffer, it is interesting to point out

that the first and second transients verified in the previous case are even faster here. The next plot, Fig. 9.6, shows the pressure distribution along the line. Note again that the steady-state is marked by the black dashed curve with the pressure decreasing to the downstream direction due to the friction of the fluid with the pipe walls. In that plot, the pressure jumps mark the position of the pig in the current snapshot in time with the pressure difference across the pig being almost constant, Δp_p=124.43kPa, representing again a quasi-steady state. Figure 9.7 show the liquid velocity distribution along the line for multiple snapshots. At the steady-state condition note that the liquid velocity is near-constant since the liquid is practically incompressible and continuity must be preserved. Jumps can be seen at the pig boundaries for the velocity plot as well again where the jumps mark the pig position, with the bypass the fluid flows through the gap between the pig and the pipe and expands a little, justifying the tiny jumps seen in the velocity.

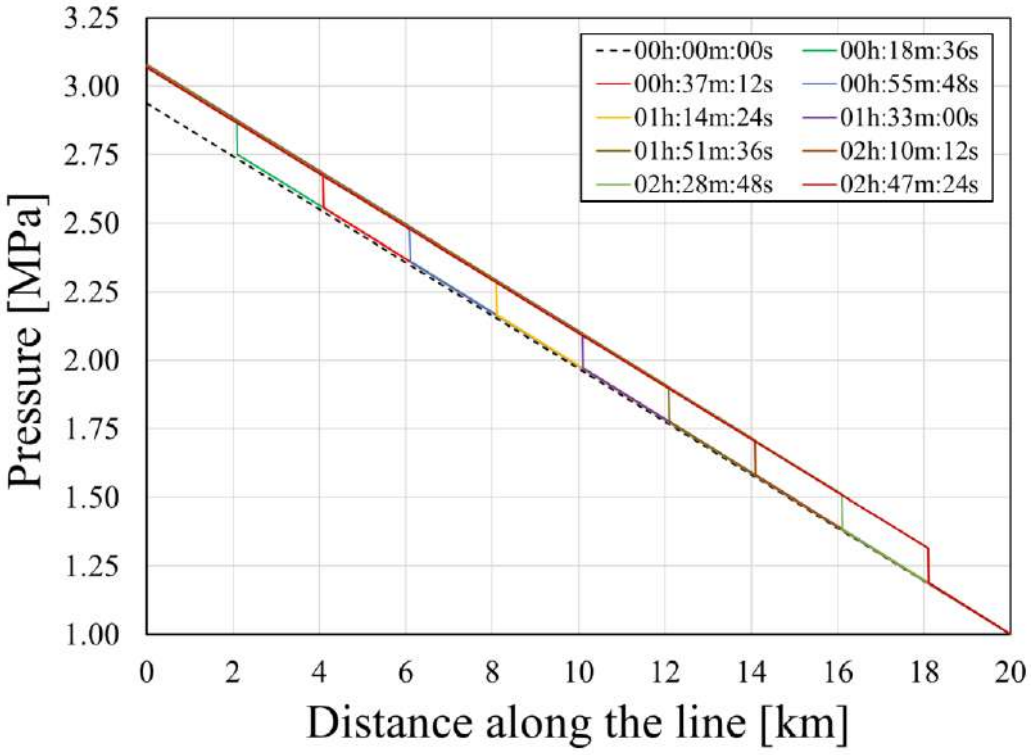

Figure 9.6: Pressure along the line for the pigging in liquid flow case.

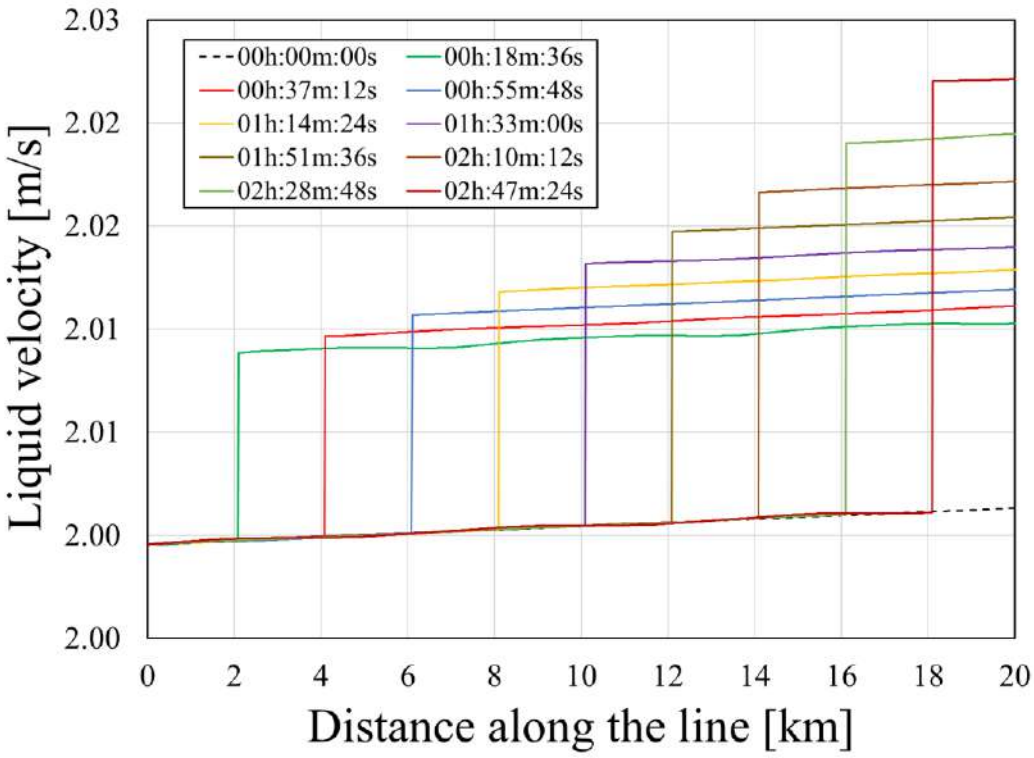

Figure 9.7: Liquid velocity along the line for the pigging in liquid flow case.

The next figures show the comparison between the simulation with OLGA and Patricio *et al.* (2020). Figure 9.8 shows the pressure distribution when the pig reaches the position of x_p=10km, whereas Fig. 9.9 shows the plot for the velocity distribution at the same pig position. For the pig here simulated, all the pig's physical characteristics are estimated based on physical models, similarly to Patricio *et al.* (2020). For the OLGA simulations, is important to mention that these parameters are provided differently: the friction force, the effective bypass clearance, and the static and dynamic forces between the pig and pipe wall must be provided directly a priori as input for the simulation. The friction parameters are chosen for the OLGA simulation based on the ones found in the current model, however, the bypass parameter in OLGA is trickier to set up. The selection of this parameter was done here to closely match the bypass flow rate through the pig in the current results, around 10% of the mass flow rate at the inlet mas flow of 5kg/s.

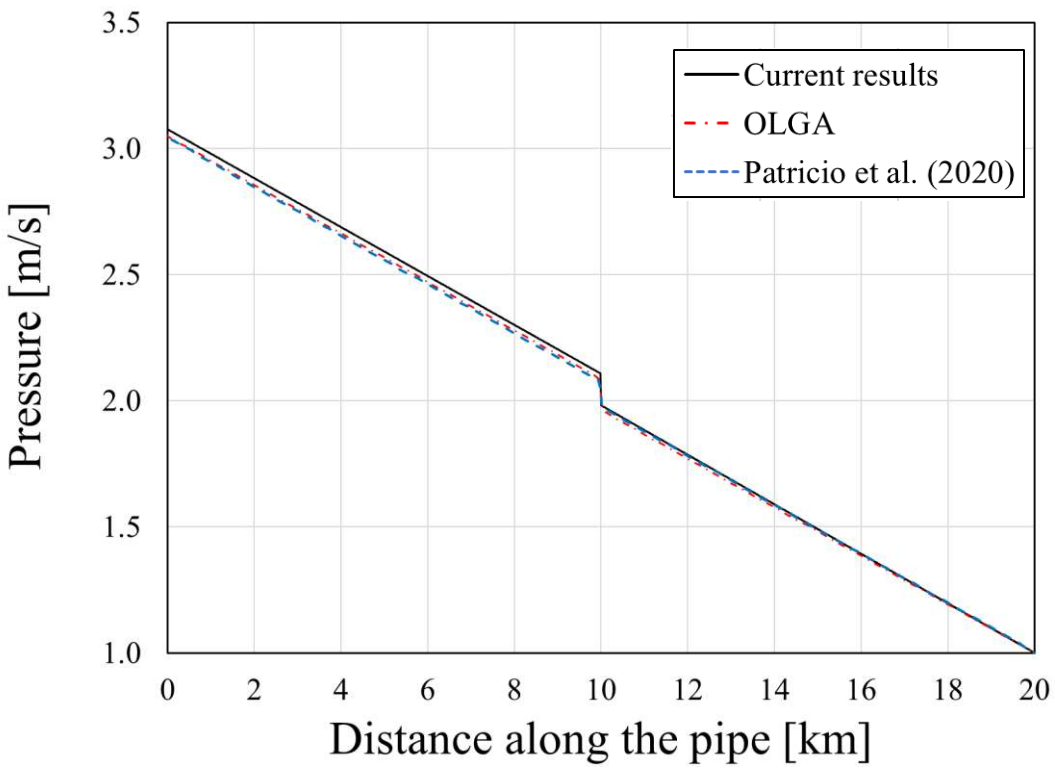

Figure 9.8: Pressure profile comparison for the pigging in liquid flow case.

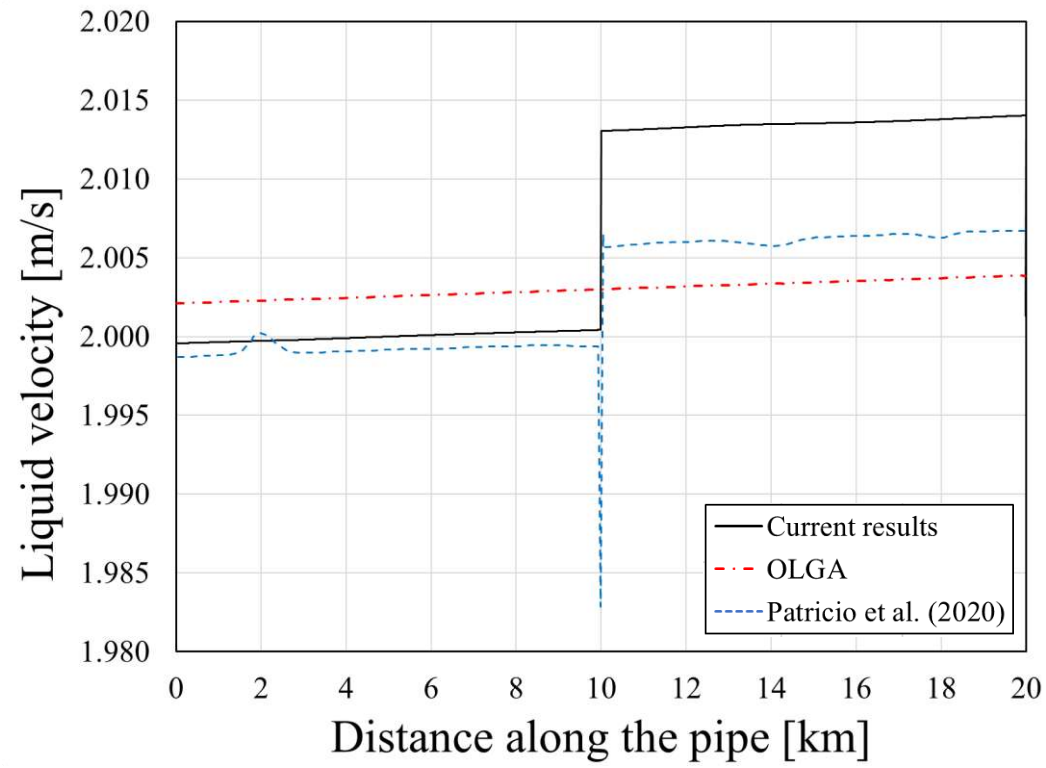

Figure 9.9: Liquid velocity comparison for the pigging in liquid flow case.

From the pressure plot, it can be inferred that the models have great agreement with each other presenting similar values for the pressure jump. However, a few differences can be inferred from the velocity plots from Patricio *et al.* (2020). Similar behavior is presented with the velocity increasing a little ahead of the pig. In their results, there is also another jump near the pig discontinuity and some oscillations that are believed to come from their pig-flow coupling scheme. In their work, the pig is assumed to be a singular surface moving in a fixed grid, here the grid is divided into two sections that are updated at each time step through the mesh reconstruction scheme previously presented. This new scheme seems to eliminate oscillations that would come from the pig moving from one cell to the other. Also, this behavior contradicts the claim of Li et al. (2021) that points out that an interpolating scheme would be susceptible to oscillations. The pig velocity for this case is near-constant throughout all the simulation time. This is expected since the liquid velocity is also near-constant, thus the local parameters shared by the pig and flow models have negligible variation, Δp_p, $u_{L,t}$ and $u_{L,f}$. The equilibrium pig velocities can be found in Table 9.7 where the results show good agreement.

Table 9-7: Pig velocities comparison for the pigging in liquid flow case.

Methodology	Pig velocity
Current model	1.79 m/s
Patricio *et al.* (2020)	1.85 m/s
OLGA	1.83 m/s

9.2.1 Influence of Bypass Holes

Some pigs have holes through their bodies to control the velocities they travel through the pipeline ensuring the efficiency of their cleaning or monitoring operations. Here, two options are tested for a pig with one single hole of 25mm diameter and a 50mm diameter and compared against the previous no-hole case presented, as well as the results obtained by Patricio *et al.* (2020). Figure 9.10 shows the plots for the pig velocity in each case with the reference plots, and Table 9.8 shows the values obtained for each result with the bypass percentage in reference to the inlet mass flow.

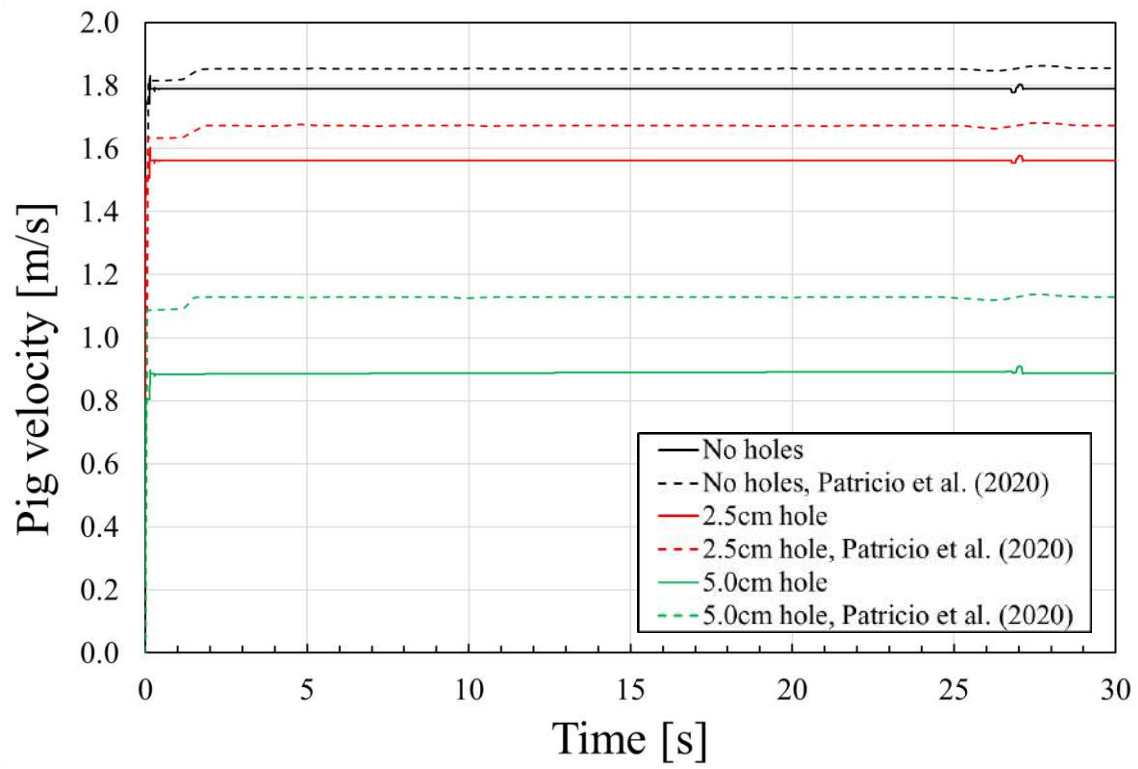

Figure 9.10: Influence of bypass holes for the pigging in liquid flow case.

Table 9-8: Influence of holes on traveling time and bypass flow rate for the single-phase liquid case.

Hole diameter	No holes	25 mm	50 mm
Traveling time	3.08h	3.56h	6.17h
Traveling time reference	2.83h	3.23h	4.68h
Velocity	1.79m/s	1.56m/s	0.89m/s
Velocity reference	1.85m/s	1.68m/s	1.12m/s
Bypass	14.8kg/s	31.6kg/s	80.2kg/s
Bypass reference	9.54kg/s	22.6kg/s	61.8kg/s
Bypass percentage	10.3%	21.9%	55.7%
Bypass percentage reference	6.6%	15.7%	42.2%

The behavior from adding the holes matches the different approaches since the magnitude of the estimated velocities and bypass flow rate are a bit different from the current results estimating higher bypass flow rates and, consequently, lower velocities. It is interesting to notice the little wiggle on the pig velocity trend at around 25 seconds,

which is present for both the reference and the herein results. This effect comes from the pressure waves traveling from the pig discontinuity that gets reflected at the pipe ends.

9.3 Pigging in Single-Phase Gas Flow

Like the pigging in the single-phase liquid flow case, the settings are taken from Patricio et al. (2020), the same pipeline conditions are used (Table 9.1), the fluid properties are given in Table 9.9, and the pipeline boundary conditions are given in Table 9.10.

Again, a steady-state is generated, and the pig is launched. The critical pressure difference is the same as the ideal pig case, Δp_c=15.0kPa, which produces E^*=4.23MPa. The resulting mechanical friction force acting on the pig when it is moving is equal to F_M=964.6N. The hydrodynamic force is in this case reached a negligible value around F_H=0.06N.

The pressure distribution for the different snapshots can be found in Fig. 9.11, with a pressure differential given by, Δp_p=13.35kPa. The velocity in this case becomes difficult to plot with different snapshots since the disturbance in the velocity is too small compared to the velocity change along the pipeline. A snapshot of a velocity profile is presented in Fig. 9.13 and Fig 9.14 when comparing the results with the references.

Table 9-9: Gas properties for the pigging in gas flow case.

Parameter	Symbol	Value
Temperature	T	293 K²
Gas constant	R	287 J/kg.K
Sound speed in the gas	$c_G = \sqrt{RT}$	290 m/s
Reference gas density	ρ_0	0 kg/m³
Dynamic viscosity	μ_G	1.9_x10^{-5} Pa.s

Table 9-10: Inlet and outlet boundary conditions for the pigging in gas flow case.

Flow Variable	Value
p at outlet (x=L)	10^6 Pa
u_G at inlet (x=0)	4.96 m/s

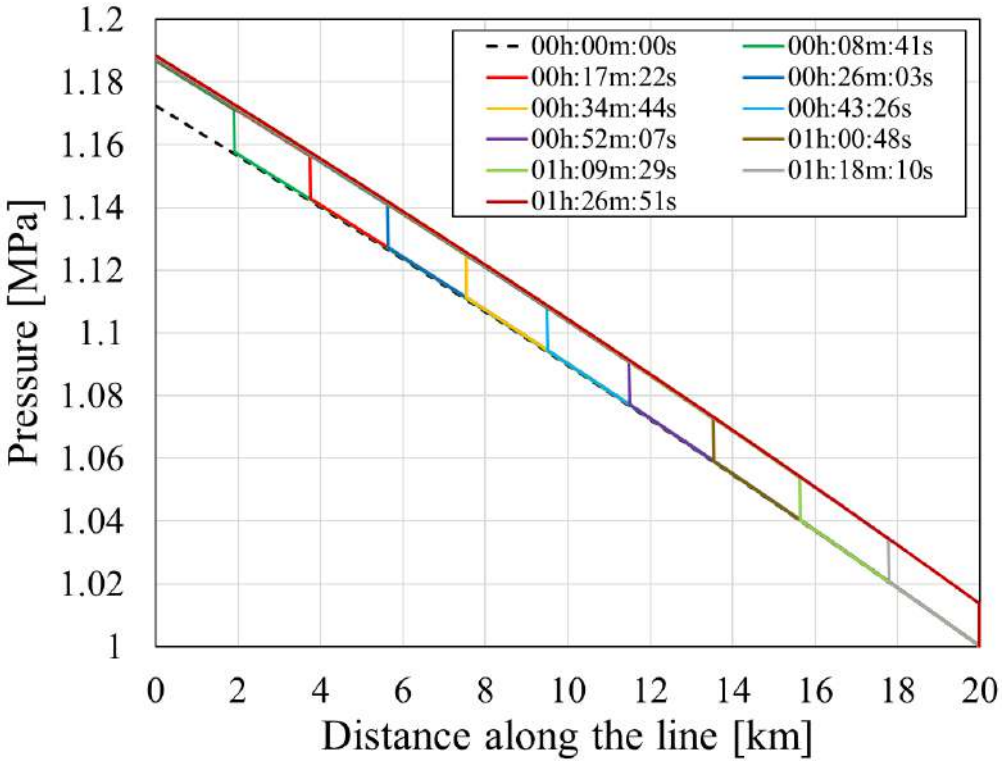

Figure 9.11: Pressure along the line for the pigging in gas flow case.

The obtained results again represent well the expected physics of the problem, with the pig creating a discontinuity in the pressure that moves it through the pipeline. The following plot shows the comparison of the pressure distribution against the reference results when the pig is at the position of 10km. Figure 9.12 shows the pressure distribution, where the herein results have a good match against the references. Figure 9.13 shows the gas velocity distribution, and Fig. 9.14 the same plot focused on the discontinuity position. In the velocity plots, the oscillations presented in Patricio *et al.* (2020) results can be noticed. In addition, their results show a slight decrease in the gas velocity ahead of the piston which is not expected with the expansion of the gas ahead of the pig. The current results, along with OLGA, show an increase in the velocity that is expected from the problem.

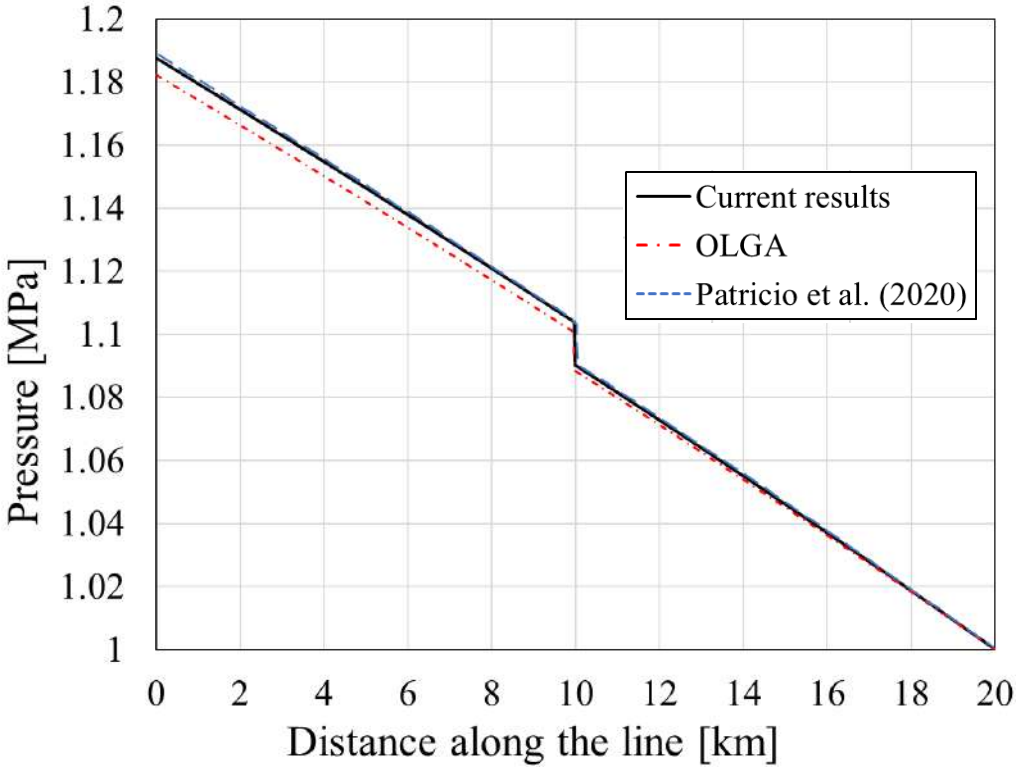

Figure 9.12: Pressure profile comparison for the pigging in gas flow case.

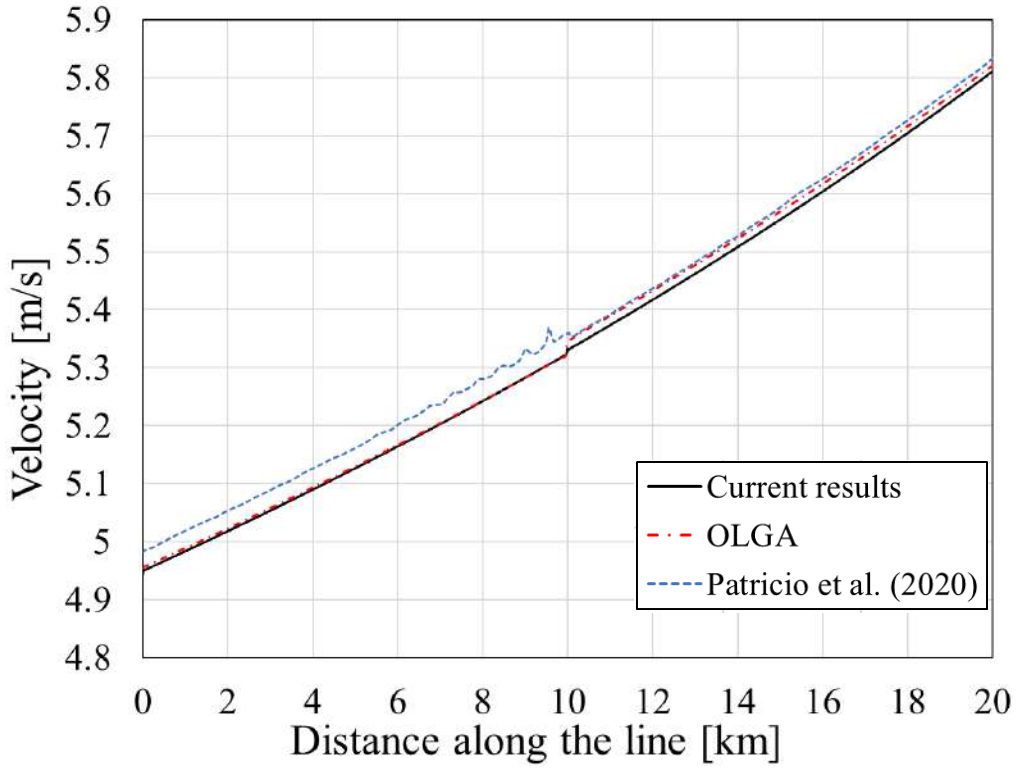

Figure 9.13: Gas velocity comparison for the pigging in gas flow case (1).

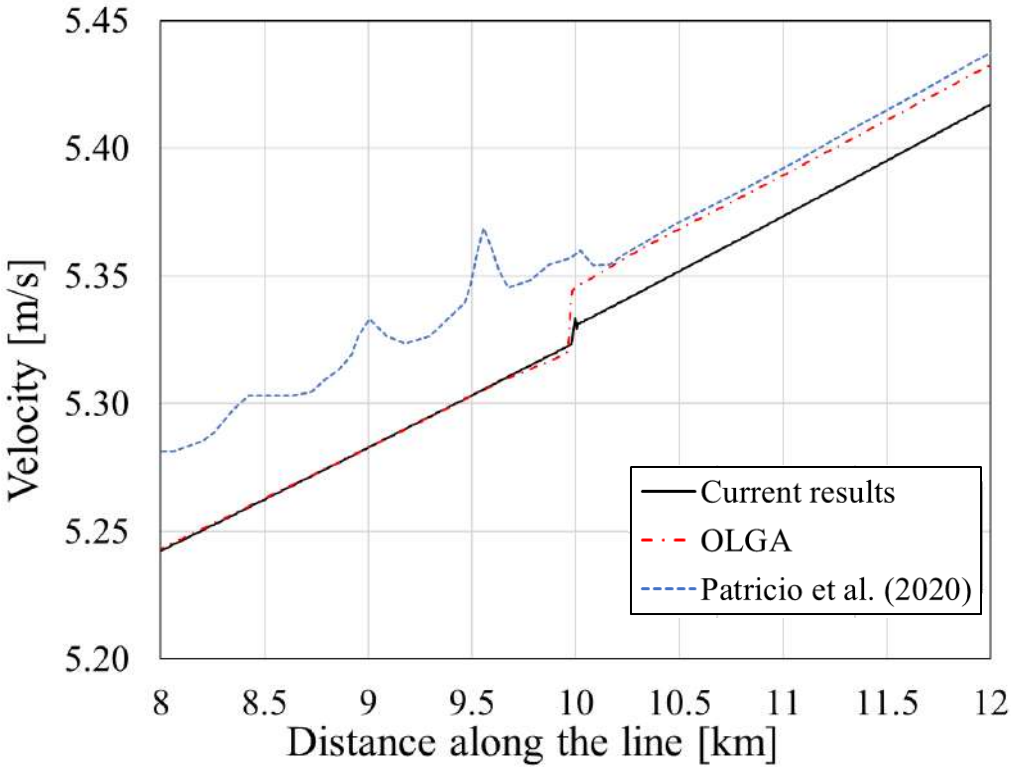

Figure 9.14: Gas velocity comparison for the pigging in gas flow case (2).

The plot given in Fig. 9.15 shows the velocity of the pig varying with time. Differently from the liquid flow case the gas velocity changes along the line, and the parameters shared by the pig and flow models change, affecting the solution of the pig velocity. The herein simulation provides greater velocity values than both references. Initially, it seems that it would match better with OLGA, however, as time progresses it shows to have a similar slope to Patricio *et al.* (2020). This may be an artifact of the gas properties calculation, which is different in OLGA, that estimates local state properties of the gas through a PVT table.

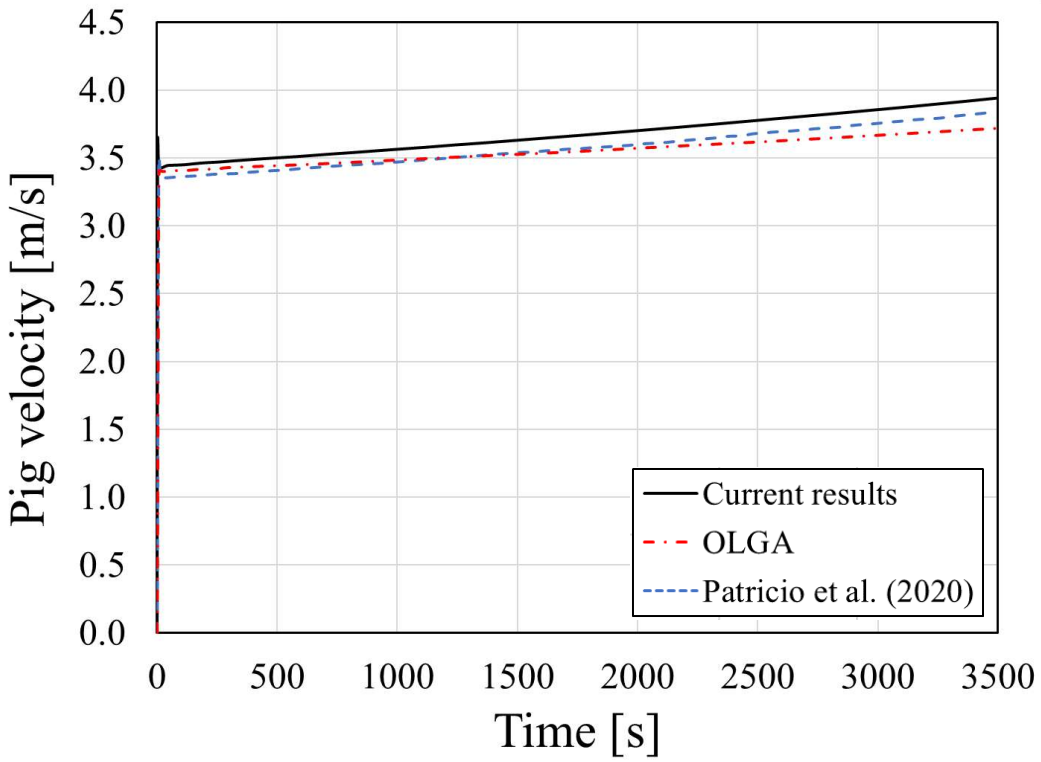

Figure 9.15: Pig velocity comparison for the single-phase gas flow case.

9.3.1 Influence of Bypass Holes

To conclude the single-phase pig results, the influence of the bypass holes is tested in the gas phase as well. The same hole diameters are used from the previous test 25mm and 50mm. Figure 9.16 shows the influence of the holes in the pig velocity and Table 9.11 shows the traveling times, the approximate velocity at the time of 30 seconds, and the bypass flow rate for each configuration.

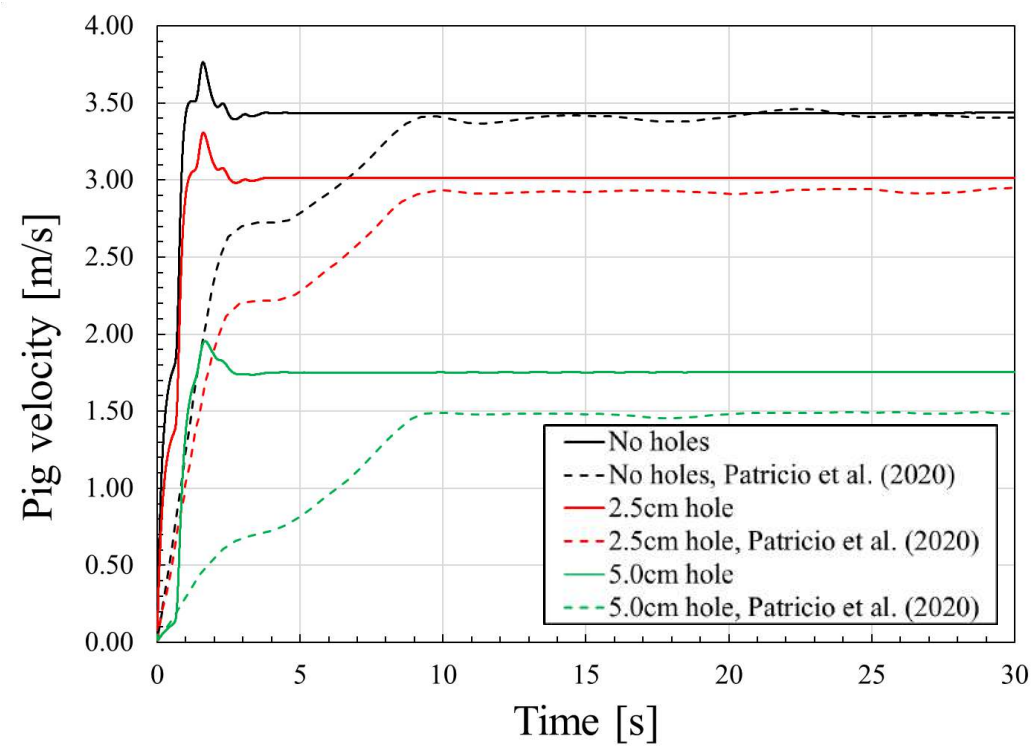

Figure 9.16: Single-phase pig gas pressure along the line.

Table 9-11: Influence of holes on traveling time and bypass flow rate for the single-phase gas case.

Hole diameter	No holes	25 mm	50 mm
Traveling time	1.45h	1.64h	2.68h
Traveling time reference	1.41h	1.62h	3.01h
Velocity	3.44m/s	3.01m/s	1.75m/s
Velocity reference	3.40m/s	2.94m/s	1.48m/s
Bypass	1.15 kg/s	1.96kg/s	3.24kg/s
Bypass reference	0.69 kg/s	1.16kg/s	2.64kg/s
Bypass percentage	22.9%	39.1%	64.5%
Bypass percentage reference	12.8%	25.2%	49.2%

The two methodologies presented similar results in terms of pig velocities with slightly higher velocities for the current results. The estimated bypass values are higher as well contradicting the higher velocity values. It is difficult to point out exactly why this is, one plausible reason is the inlet gas velocity, that the reference results show a

higher value than what it is supposed to be set, indicating that it may have a jump to higher values on the inlet boundary. Moreover, an unexpected jump is seen at the pig position for the gas velocity, Figs. 9.13 and 9.14. The current solution, on the other hand, does not present these unexpected jumps, with the only jump present between the pig tail and front that happens due to the expansion of the gas at the front.

9.4 Two-Phase Pigging

The two-phase pigging case was taken from Patricio (2016), in which the pipeline properties are given in Table 9.12, and the fluid properties in Table 9.13. Similar to the single-phase simulations, the steady-state flow is generated with the initial and boundary conditions given in Table 9.14, which reproduces stratified flow conditions. The steady-state condition is generated with a mesh of 2500 cells, with the different models and methods presented in chapters 4 and 5.

Table 9-12: Pipe properties for the two-phase pigging case.

Parameter	Symbol	Value
Pipe length	L	45 km
Pipe diameter	d	0.3032 m
Inclination Angle	θ	0
Roughness	ε	4.572_x10^{-5} m

Table 9-13: Fluid Properties for the two-phase pigging case.

Parameter	Symbol	Value
Temperature	T	293 K
Ideal gas constant	R	392.50 J/kg.K
Sound speed in gas	$c_G = \sqrt{RT}$	339.12 m/s
Sound speed in liquid	c_L	900 m/s
Reference gas density	$\rho_{0,G}$	0 kg/m^3
Reference liquid density	$\rho_{0,L}$	777.2 kg/m^3
Dynamic viscosity gas	μ_G	1.2847_x10^{-5} Pa.s
Dynamic viscosity liq.	μ_L	8.580_x10^{-4} Pa.s

Table 9-14: Inlet and outlet boundary conditions for the two-phase pigging case.

Flow Variable	Value
α_L at inlet ($x=0$)	0.008
u_G at inlet ($x=0$)	5.25 m/s
u_L at inlet ($x=0$)	0.98 m/s
p at outlet ($x=L$)	6 MPa

The steady-state flow is used as the initial condition for the pig problem. The pig properties are given in Table 9.15, and the pig is launched from the initial position of 100m. The effect of the bypass through the gap between the pig and the pipe is considered.

Table 9-15: Pig properties for the two-phase pigging case.

Parameter	Value
Pig mass M_p	50 kg
Pig characteristic length -L_c	0.5 m
Pig diameter -d_p	0.3036m
Static friction coefficient -η_s	0.45 (-)
Dynamic friction coefficient -η_d	0.40 (-)

To simulate this case, the 4E1P two-fluid model is used, and the different methods are tested to analyze how they affect the solution of the problem.

9.4.1 4E1P Results

The following plots report the results for the 4E1P solution of the primitive variables along the pipe with different snapshots in time. Figures 9.17 to 9.20 give the pressure distributions obtained with the Roe scheme, AUSMV, ModFORCE, and FCT methods, respectively. For the Roe scheme, a *CFL*=0.9 is used, whereas for the other schemes, *CFL*=0.45 is employed. It is worth mentioning that the AUSMDV method presented spurious oscillations, and failed to converge.

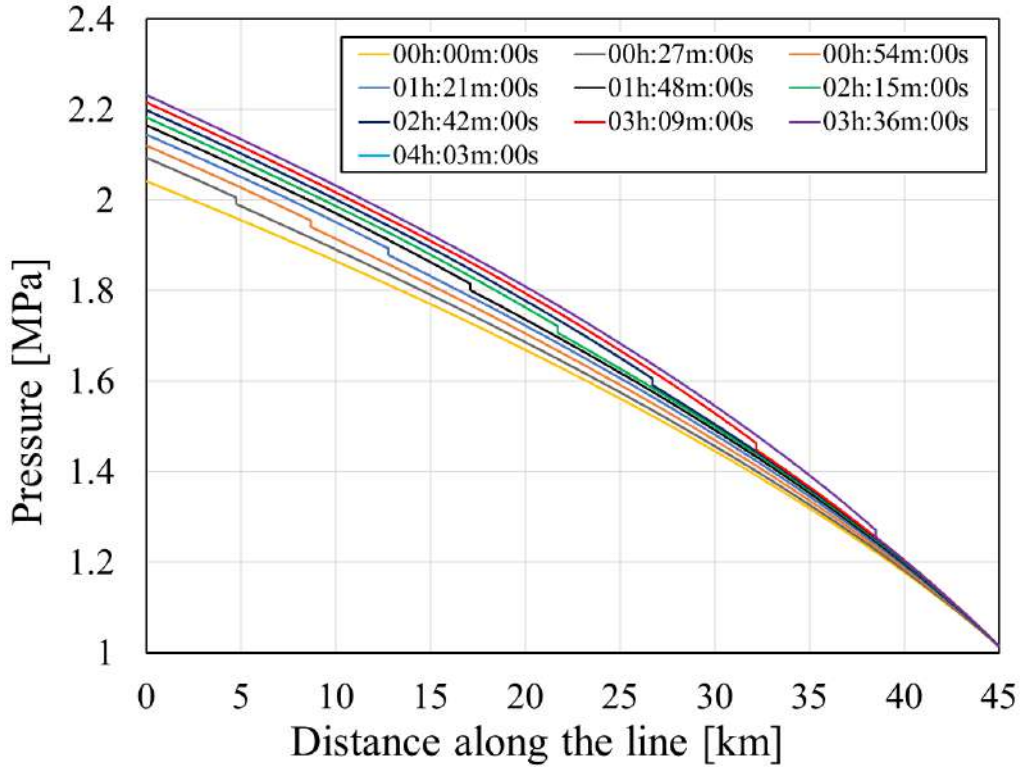

Figure 9.17: Pressure profile with Roe scheme and 4E1P, two-phase pigging.

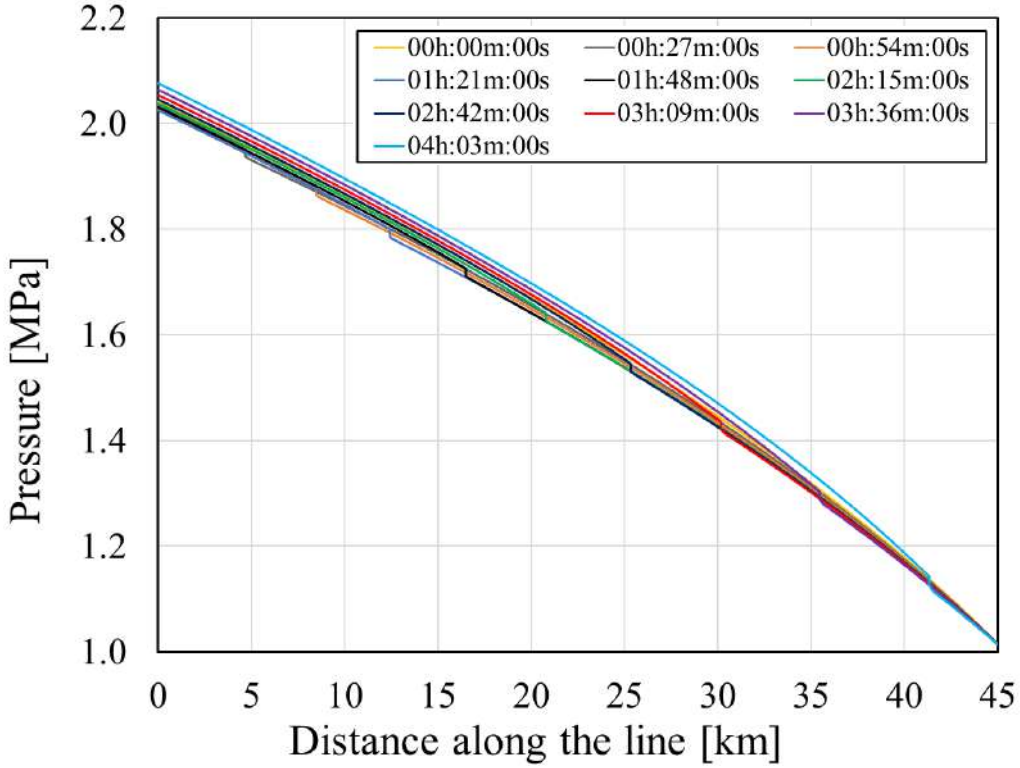

Figure 9.18: Pressure profile with AUSMV method and 4E1P, two-phase pigging.

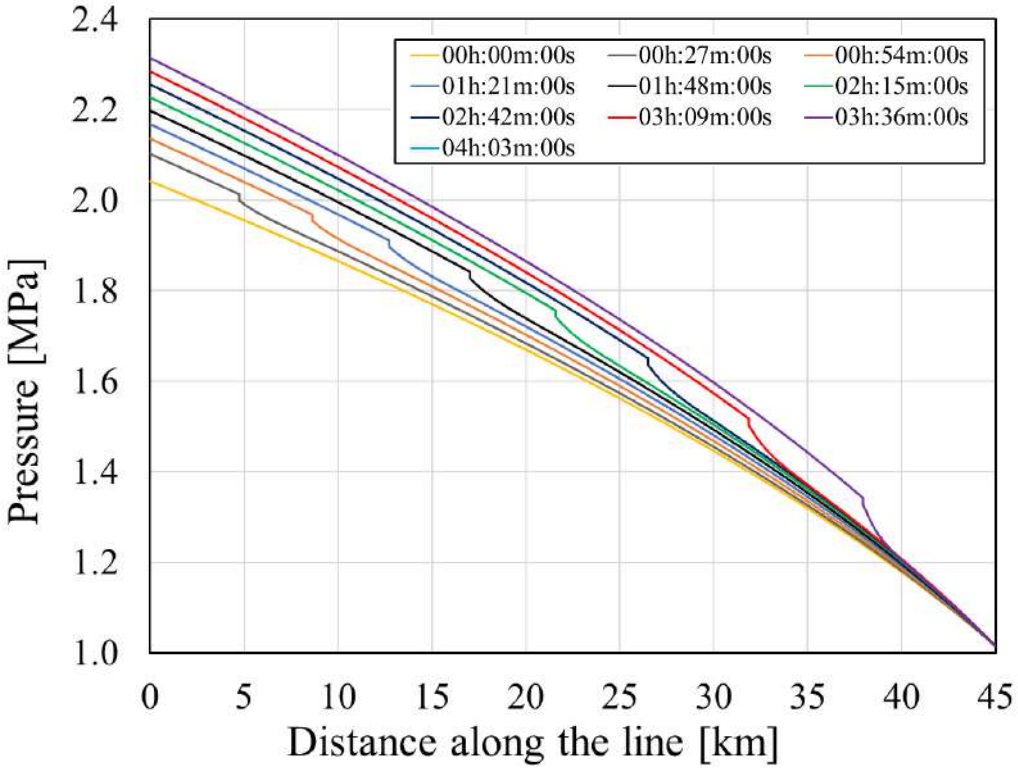

Figure 9.19: Pressure profile with ModFORCE method and 4E1P, two-phase pigging.

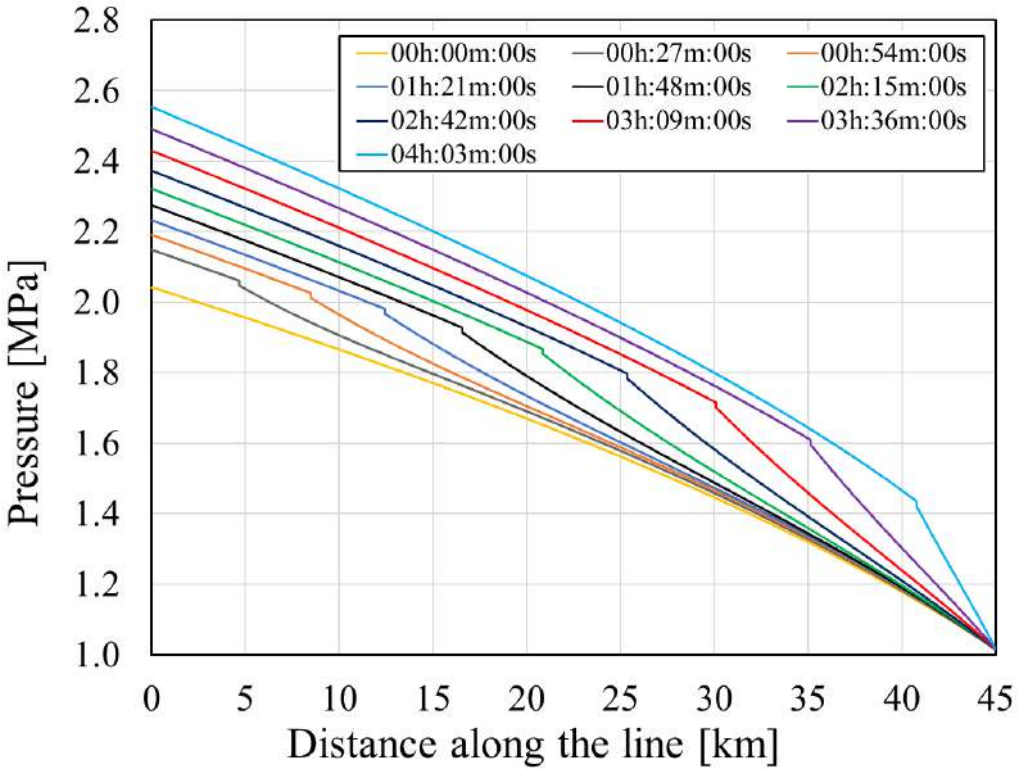

Figure 9.20: Pressure profile with FCT method and 4E1P, two-phase pigging.

Note that for all the pressure solutions reported, the expected effect of the pig disturbing the flow and generating a pressure difference across its body, which entails its movement, was captured. The obtained results also report some differences between the methodologies. The Roe scheme results show more sharp discontinuities resembling the discontinuities that are obtained in the benchmark cases. the AUSMV presented, a priori, a decrease in pressure at the pig front rather than the increase in pressure at the tail that the other methods and the single-phase simulations predict. However, later in the transient, an increase relative in the tail pressure can be seen. In the following result, ModFORCE shows a larger pressure increase behind the plunger than the Roe and AUSM-type solutions, and the FCT an even higher one. Note that for these results, the pressure discontinuity reported by the pig model is very sharp due to the near-vertical discontinuity at the pig position and, after that, another pressure gradient was detected represented by the ramp in front of the discontinuity. This ramp indicates that both the FCT and ModFORCE schemes capture a liquid accumulation at the front of the pig, generated with the liquid displacement by the movement of the pig, as reported by Minami and Shoham (1995).

This liquid accumulation should be present in the holdup distribution, as well as a liquid fraction reduction at the tail from the pig scraping the pipe. Then, Figs. 9.21 to 9.24 report the holdup distribution along the line for different snapshots in time, in the same order as the pressure curves, the Roe scheme, AUSMV, ModFORCE, and FCT methods, respectively.

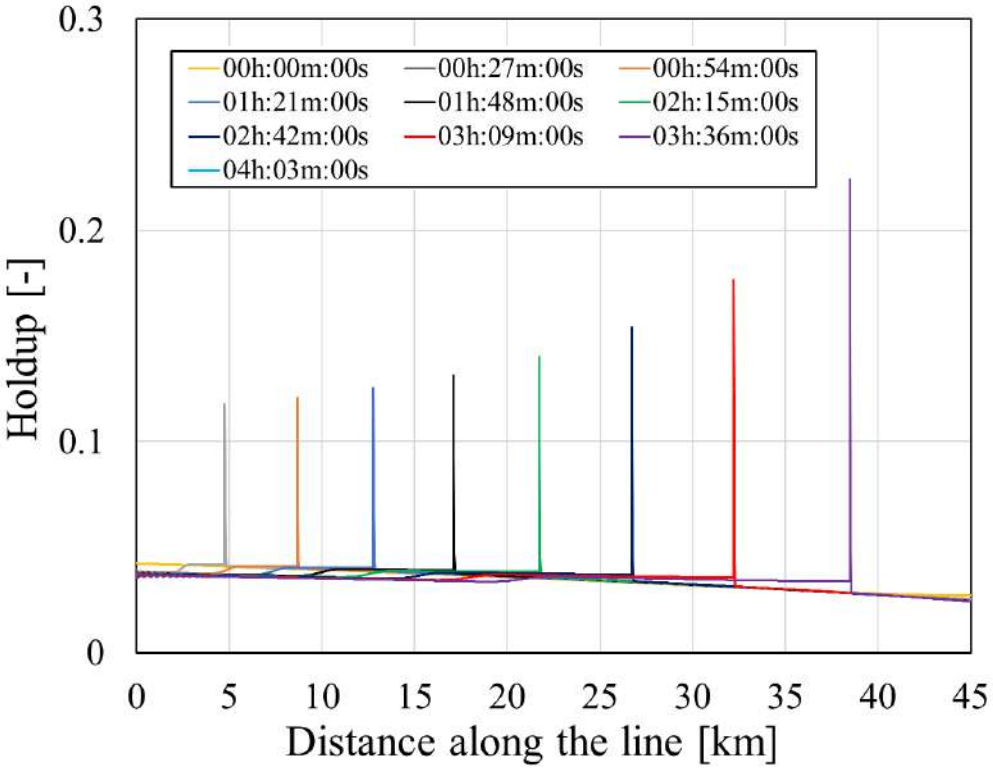

Figure 9.21: Holdup profile with Roe scheme and 4E1P, two-phase pigging.

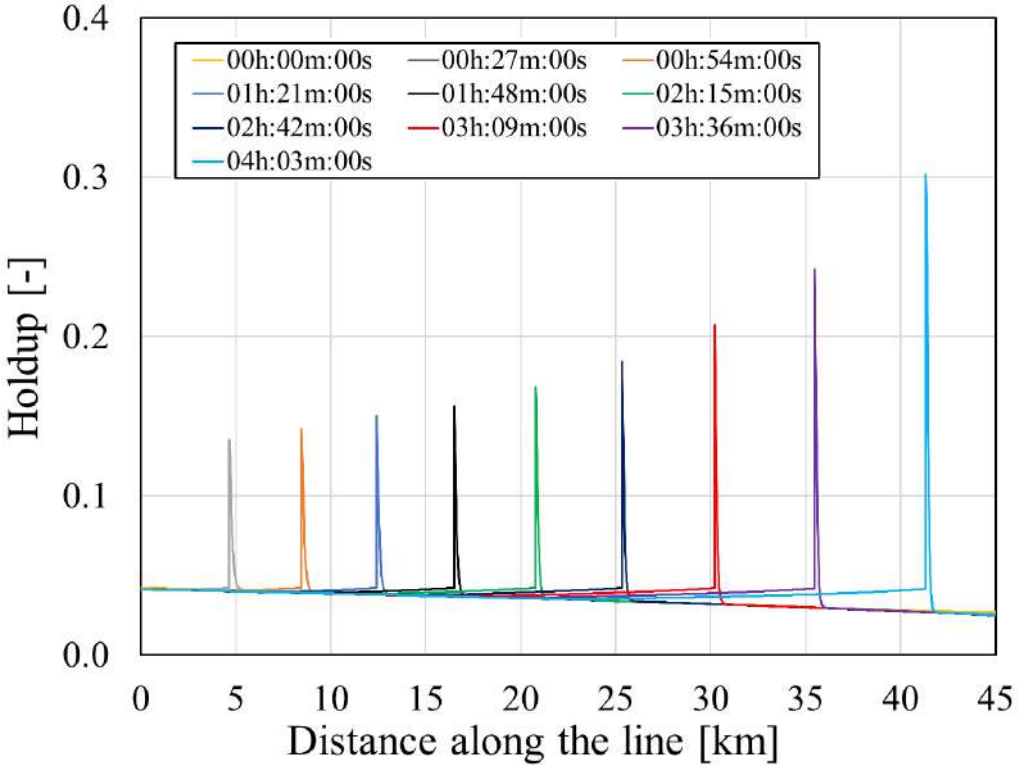

Figure 9.22: Holdup profile with AUSMV method and 4E1P, two-phase pigging.

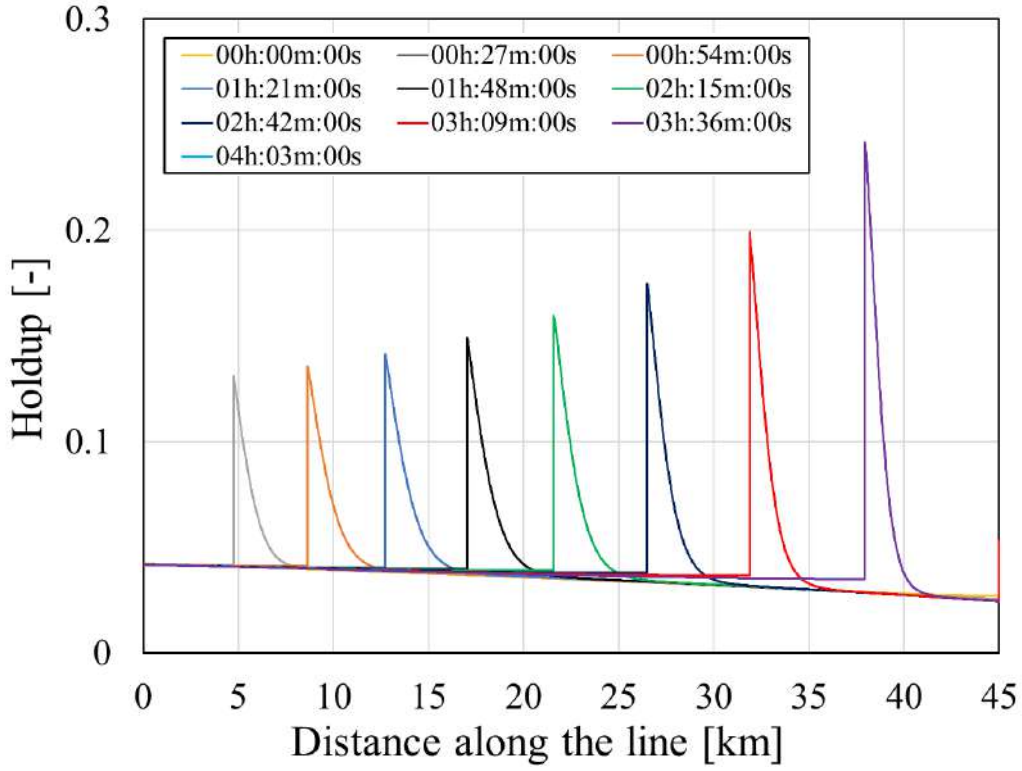

Figure 9.23: Holdup profile with ModFORCE method and 4E1P, two-phase pigging.

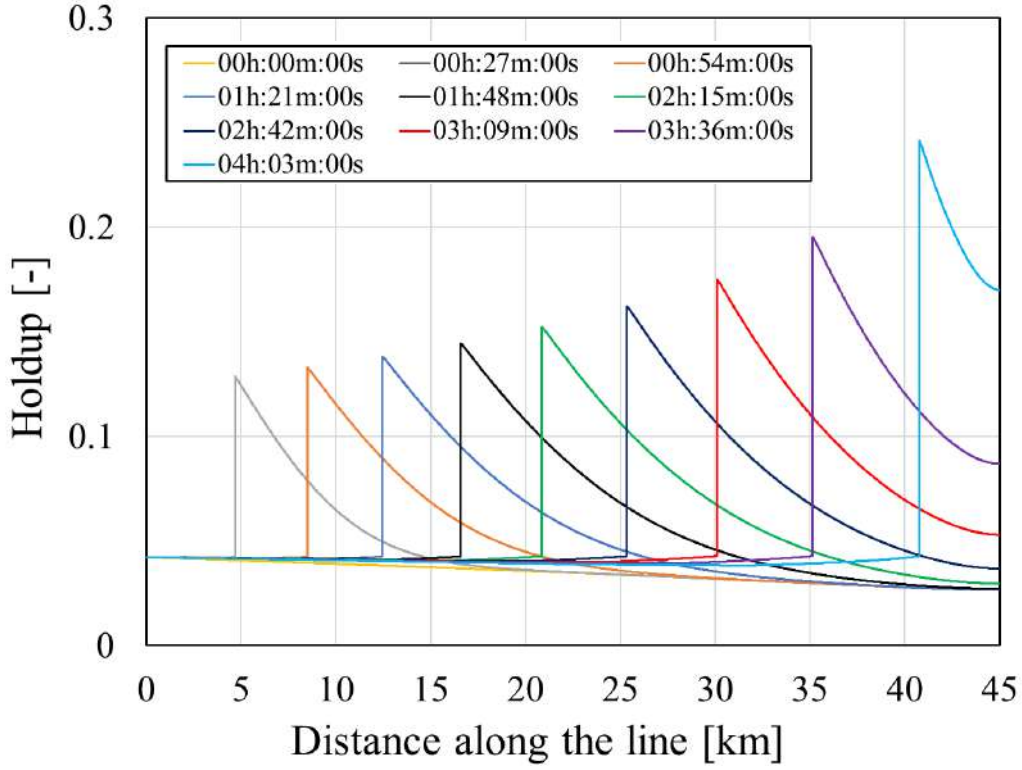

Figure 9.24: Holdup profile with FCT method and 4E1P, two-phase pigging.

From the holdup distributions, the Roe scheme shows very sharp discontinuities at the pig front. This discontinuity shows some of the liquid accumulation at the front of the pig that increases in time with the increase of the holdup peak in each of the snapshots. There is also a small reduction of the holdup at the upstream section of the pipe, however, this reduction was not caused by the pig interaction with the flow, it seems to be a jump from the inlet boundary conditions to the inlet section of the pipe created by the changes in the upstream section. The AUSM-type methods show more liquid displacement than the Roe scheme in both peak values and axial displacement. Also, more liquid displacement in the axial direction is seen in the ModFORCE, and more so in the FCT method results. Although the ModFORCE and FCT represent the expected physical behavior of the problem with more liquid being accumulated, it is expected that this effect is being caused artificially by the numerical solution by the introduction of diffusive errors that make the discontinuities diffuse. Through the analysis done in chapter 6, it was verified that the FCT method presented more diffusive errors than the other ones reinforcing the previous statement.

Another expected behavior was the liquid holdup displaced at the pig tail, with the pig scrapping the pipe it is expected to see a decrease in the holdup at the pig tail. Unfortunately, with the current methodology, this effect was not verified with any of the methods utilized.

The following Figs. 9.21 to 9.28 report the gas velocity along the line for different snapshots in time, respectively with the Roe scheme, AUSMV, ModFORCE, and FCT methods. In the same fashion, Figs. 9.29 to 9.32 report the liquid velocity along the line.

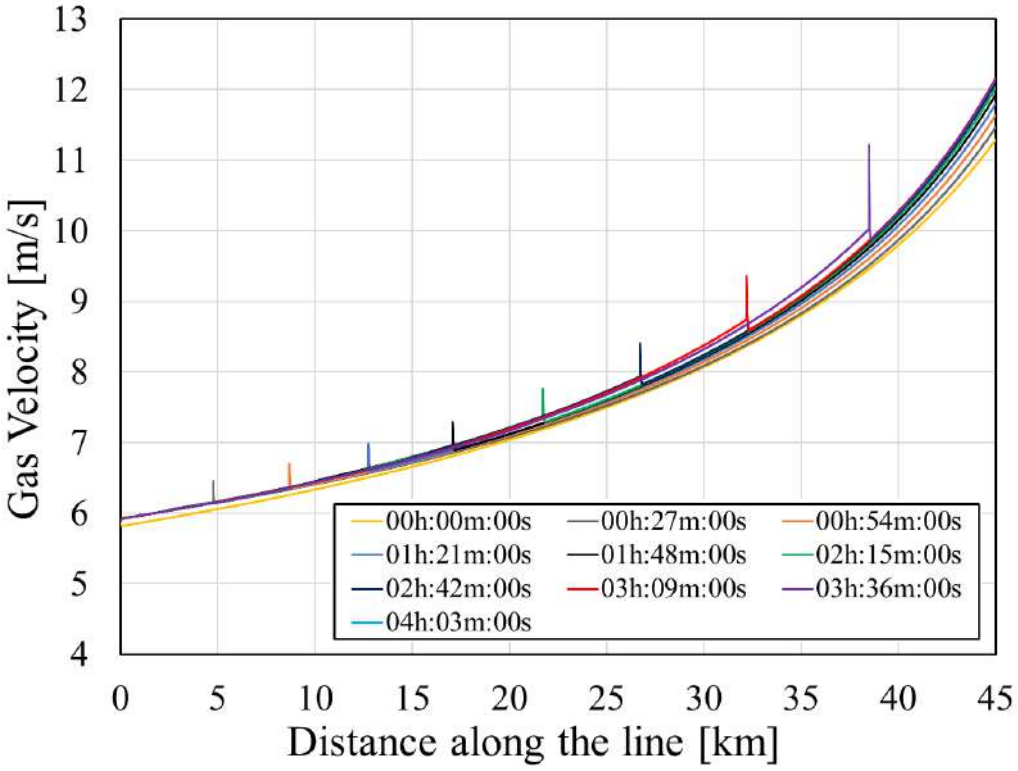

Figure 9.25: Gas velocity profile with Roe scheme and 4E1P, two-phase pigging.

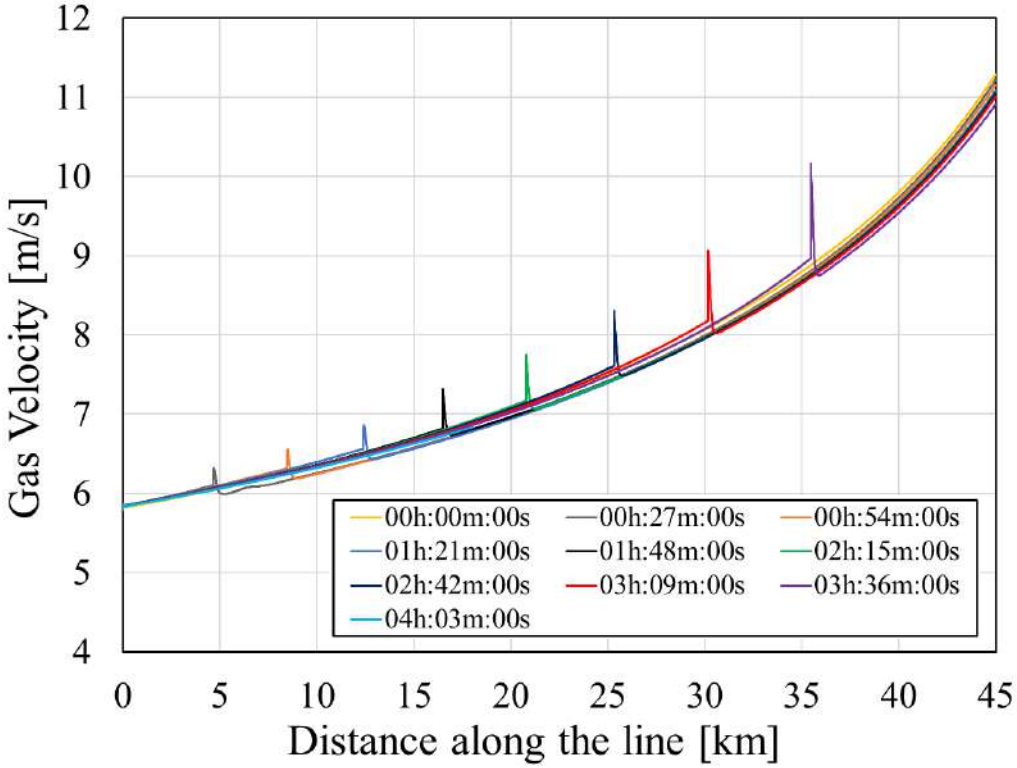

Figure 9.26: Gas velocity profile with AUSMV method and 4E1P, two-phase pigging.

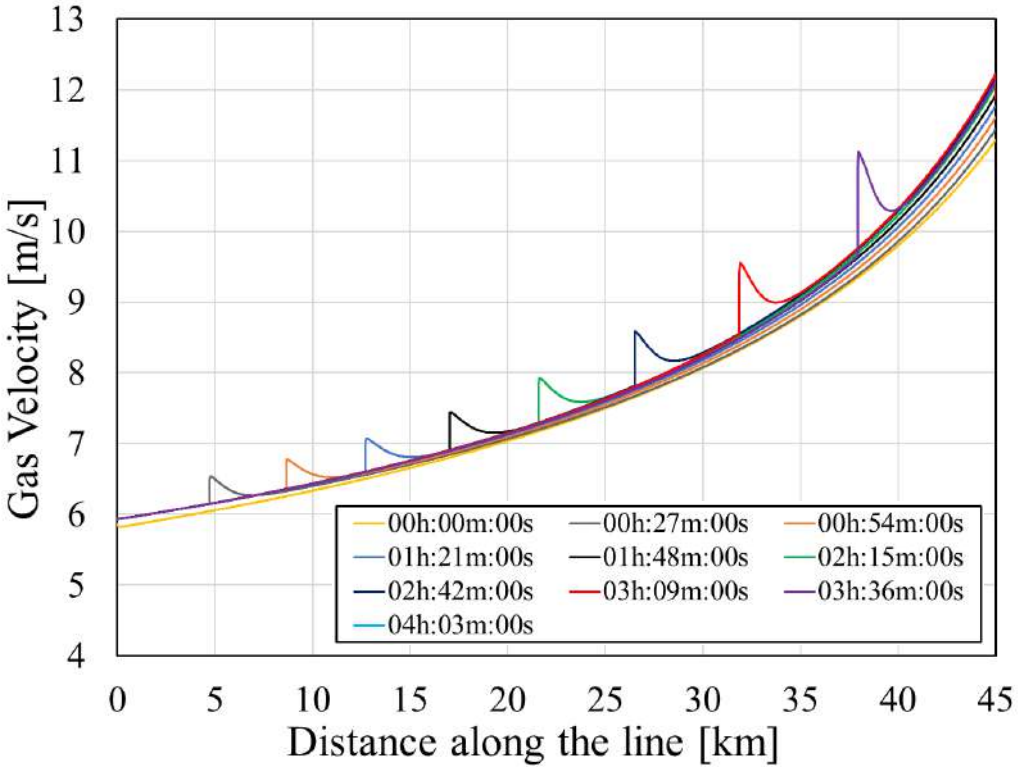

Figure 9.27: Gas velocity profile with ModFORCE method and 4E1P, two-phase pigging.

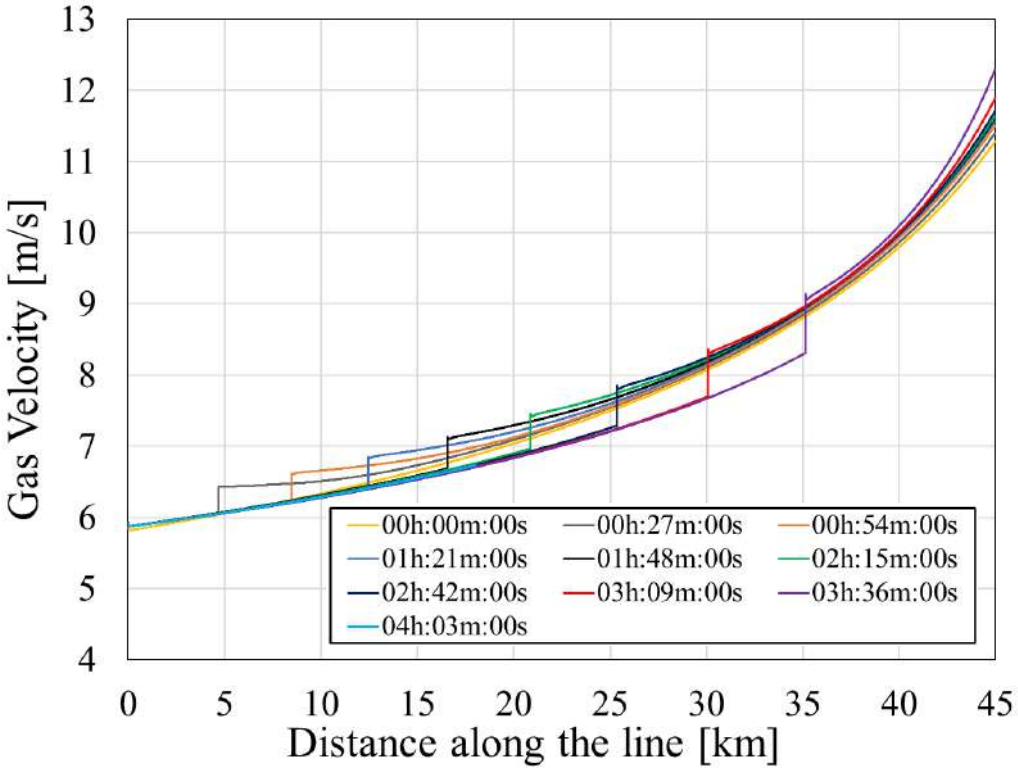

Figure 9.28: Gas velocity profile with FCT method and 4E1P, two-phase pigging.

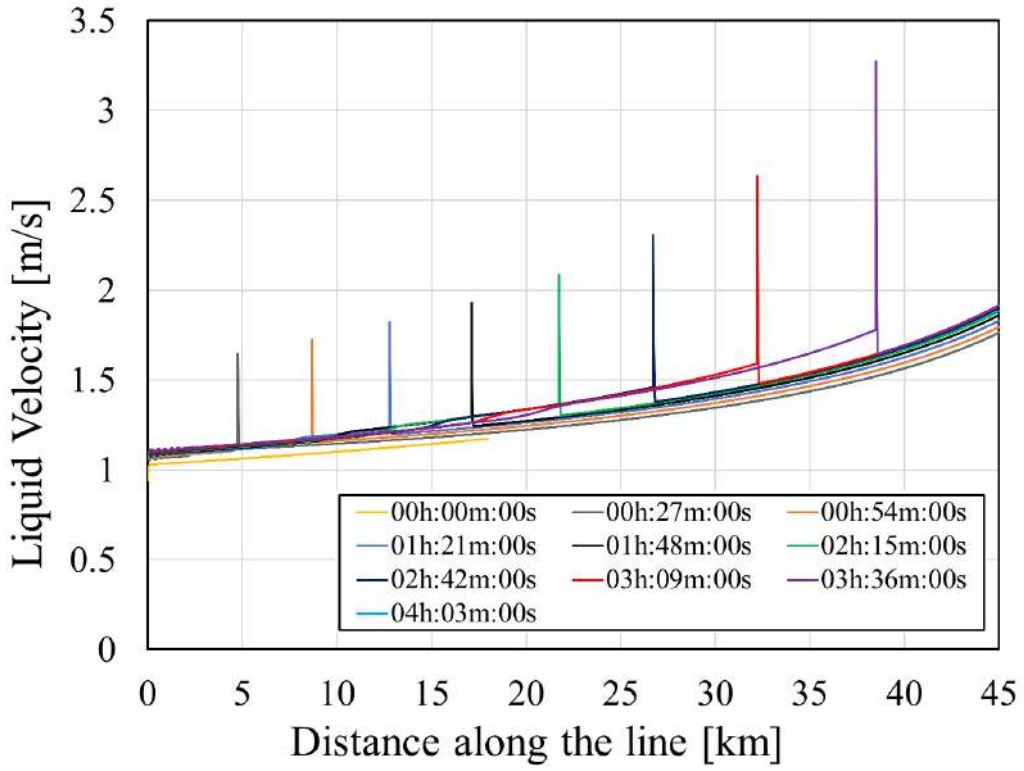

Figure 9.29: Liquid velocity profile with Roe scheme and 4E1P, two-phase pigging.

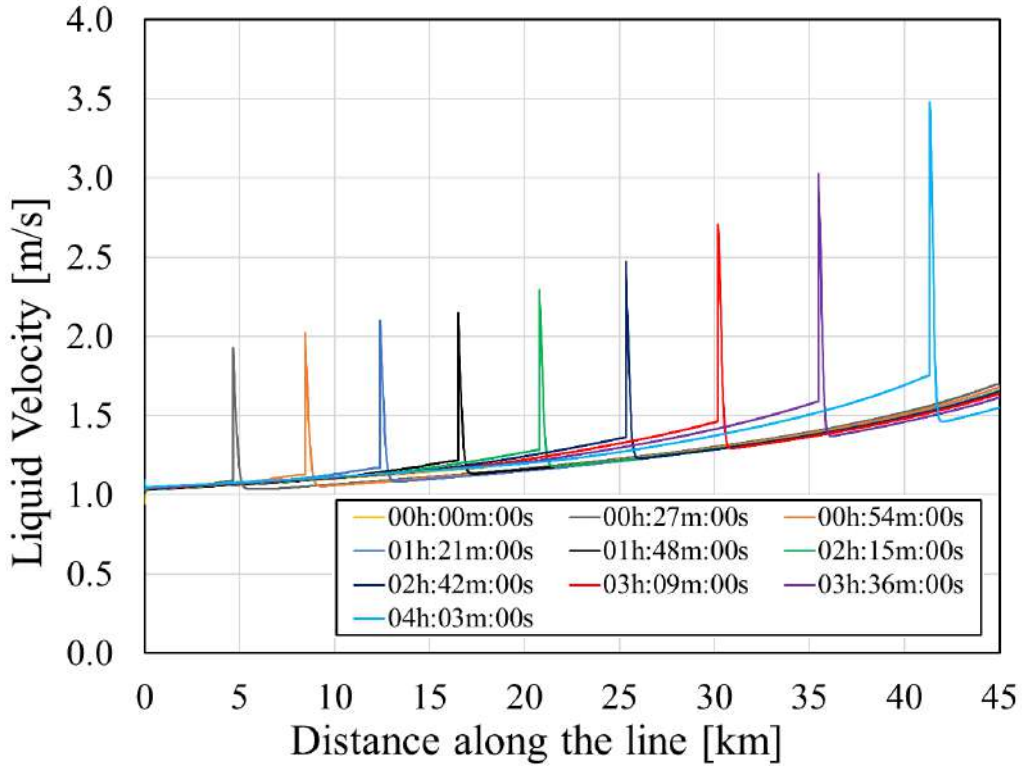

Figure 9.30: Liquid velocity profile with AUSMV method and 4E1P, two-phase pigging.

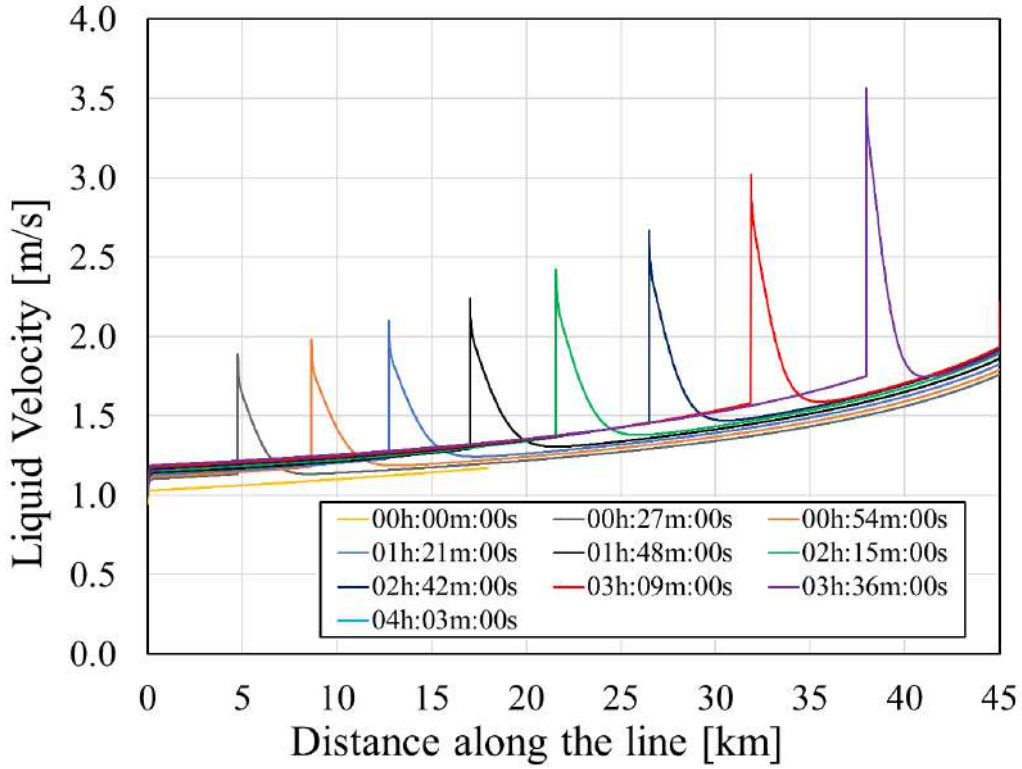

Figure 9.31: Liquid velocity profile with ModFORCE method and 4E1P, two-phase pigging.

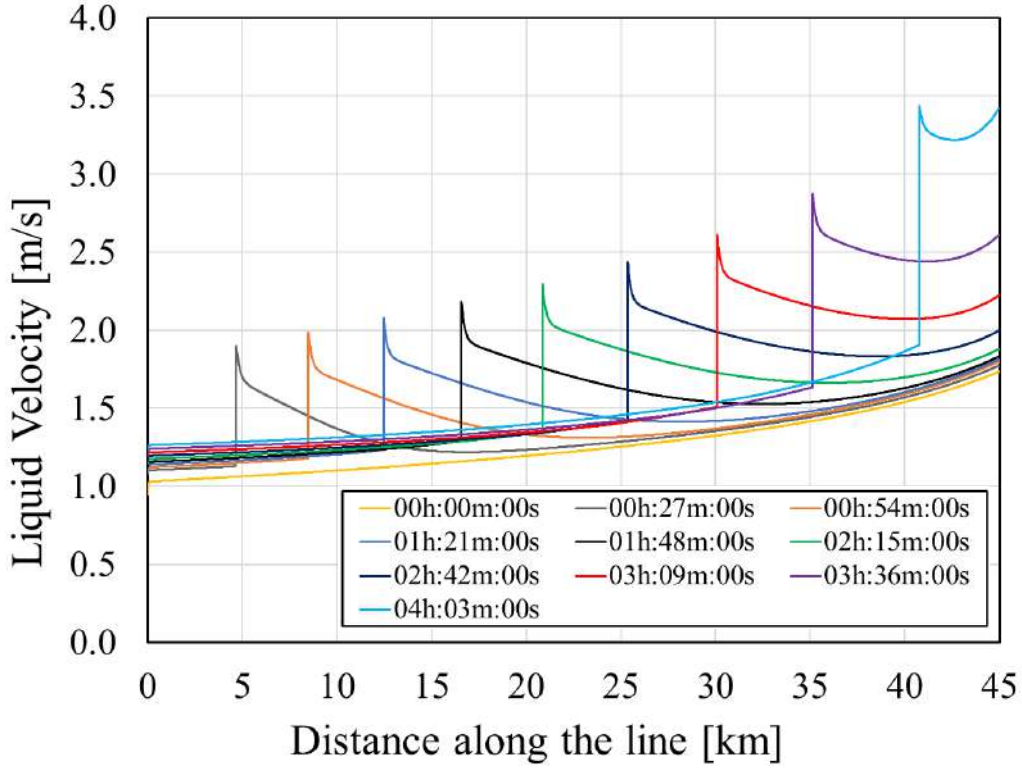

Figure 9.32: Liquid velocity profile with FCT method and 4E1P, two-phase pigging.

From the gas velocities, all the results obtained show that the gas velocity increases in the region right after the gas leaves the pig through the bypass since the gas is chocked by the increased holdup at the liquid front and its sudden expansion. After it passes through that region, the gas returns to velocity values near the steady-state condition. This effect is amplified in the methodologies that reproduce higher holdup accumulation levels, for instance, in the FCT method the gas velocity keeps its increase in the downstream section since the holdup level is kept at higher levels for this entire domain section.

The liquid velocity at the front boundary in the downstream section shares values near the pig velocity values, showing that the pig model was able to capture the interaction of the pig dragging the liquid in its front. The differences shown in each numerical method reflect the already discussed results for the other flow parameters.

To evaluate how the pig dynamics is reproduced by each of the schemes, Fig. 9.33 shows the pig velocity against time for each model-method combination.

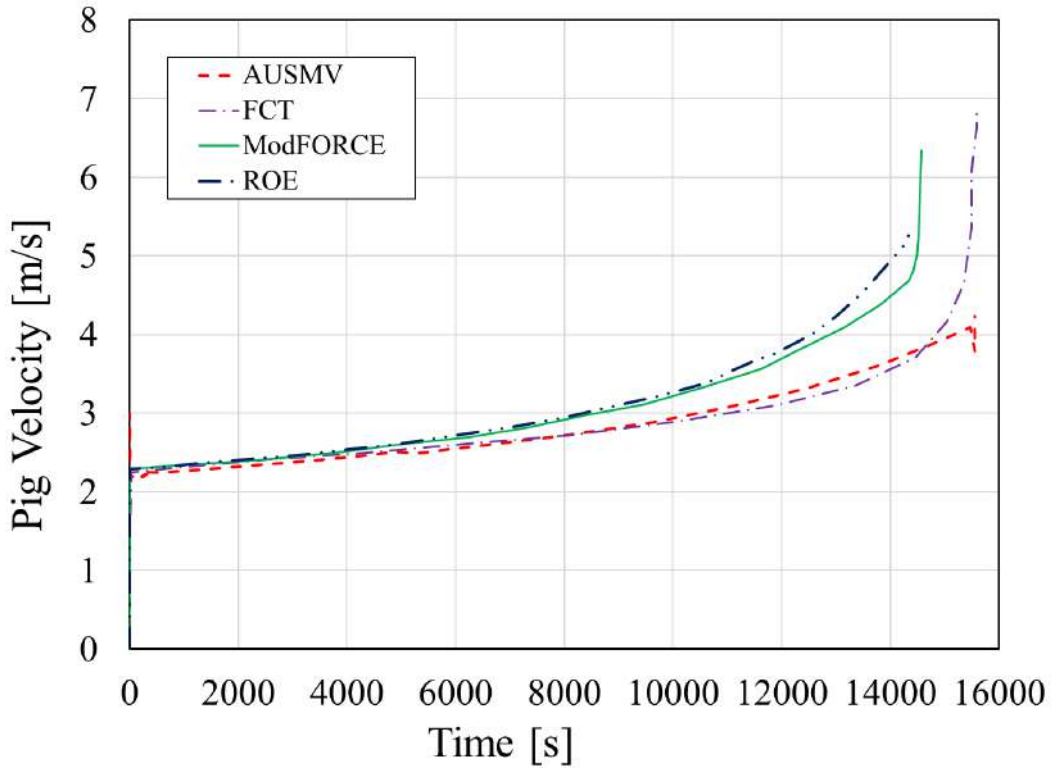

Figure 9.33: Pig velocities with time for the 4E1P model, two-phase pigging case.

It can be seen that every methodology was able to capture similar pig dynamics. The pig dynamics in the two-phase case are highly affected by the liquid accumulation at the pig front. With the increase of holdup at the front, the wet perimeter in this region increases, increasing the liquid friction and, consequently, the resistance that the pig needs to overcome by displacing the liquid body. The method that reproduced less liquid accumulation, the Roe scheme, should have less resistance acting on the pig, explaining why in this methodology the pig arrives earlier. Following this idea, the methodology that represents the next faster pig is the AUSMV followed by the ModFORCE and FCT methods. Also, in the pig dynamics at the end, there is a second acceleration region when the pig starts delivering the accumulated liquid body at its front to the outlet. This sudden increase in the velocity slope, in the acceleration, comes from the less resistance that the pig and the flow must overcome the liquid body region gets dumped at the outlet.

9.4.2 5E2P Results

To further study the methodology, the study performed in the previous section is also simulated with the 5E2P model. The following plots report the solution of primitive variables along the pipe with different snapshots in time. Both the AUSMV and AUSMDV with the 5E1P methods presented results that are nearly identical, hence why only the AUSMV was reported here. Figures 9.34 to 9.37 gives the pressure distributions obtained with the Roe scheme, AUSMV, ModFORCE, and FCT methods, respectively.

Some remarks about the 5E2P cases need to be reported first. The Roe scheme showed a lot of numerical spurious oscillations with CFL=0.9 and CFL=0.45, therefore, to maintain the simulation stable the use of CFL=0.1 was necessary. Unfortunately, this breaks the advantage found in the benchmark tests with the 5E2P and Roe scheme being faster than its 4E1P counterpart since it has direct analytical expressions for its eigenstructure entities. The same behavior was seen for the FCT method, and CFL=0.1 was also used to keep the oscillations under control. For the AUSMV and ModFORCE methods, the CFL=0.45 is employed.

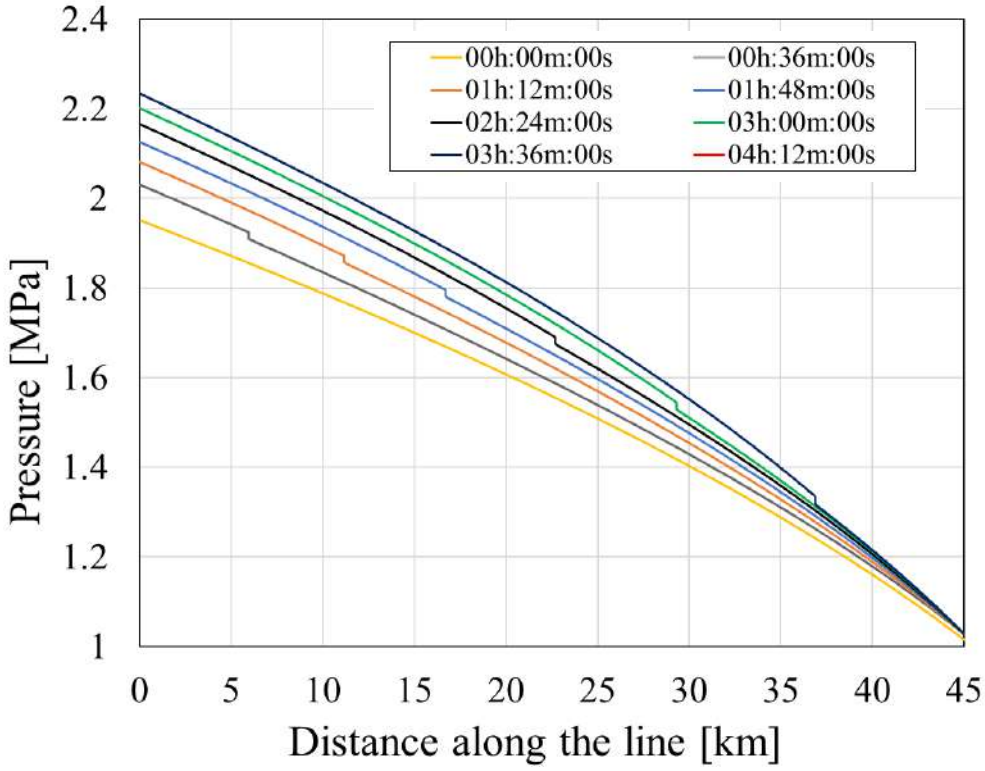

Figure 9.34: Pressure profile with Roe scheme and 5E2P, two-phase pigging.

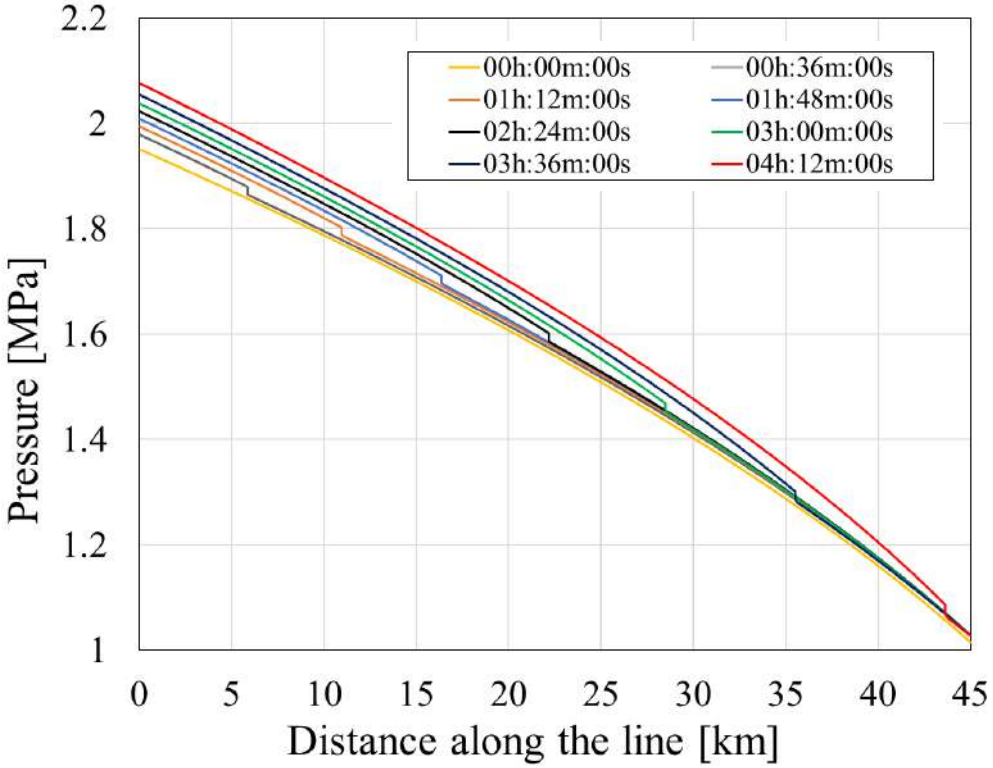

Figure 9.35: Pressure profile with AUSMV method and 5E2P, two-phase pigging.

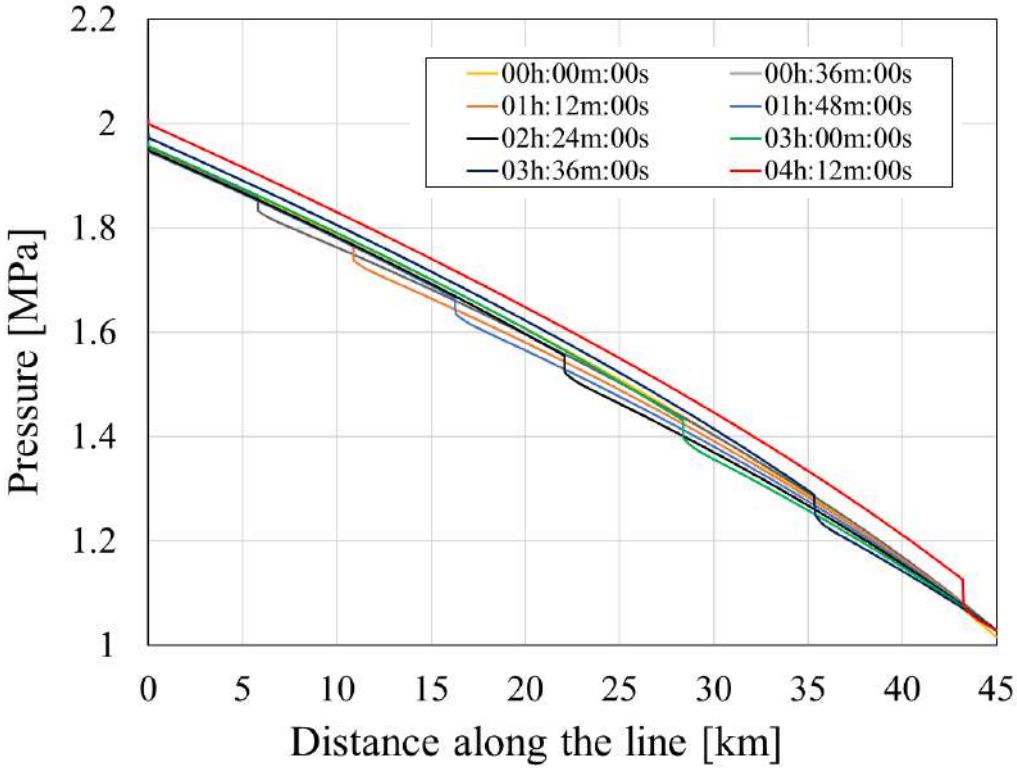

Figure 9.36: Pressure profile with ModFORCE method and 5E2P, two-phase pigging.

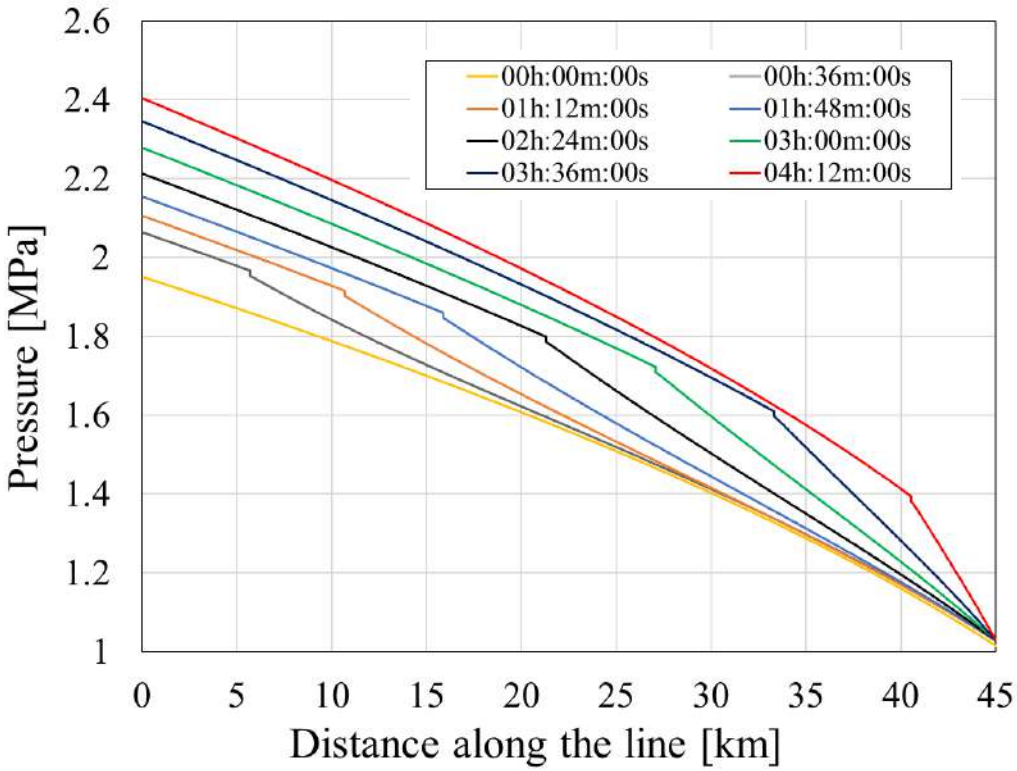

Figure 9.37: Pressure profile with FCT method and 5E2P, two-phase pigging.

It is important to observe that the initial condition, given by the steady-state flow simulated, presented some differences from the results with the 4E1P model like the ones observed and detailed in section 6.3. The pressure solutions reported by the 5E2P model with the different methods also captured the expected effect of the pig disturbing the flow and generating a pressure difference across its body, which entails its movement. The Roe scheme showed similar results to the ones obtained with the 4E1P method. The AUSMV, differently than the run with the 4E1P, showed the pressure increases at the tail before decreasing at the front, showing similar results to the Roe scheme. The ModFORCE method here showed the pressure decreasing at the front before, then, increasing at the tail, with similar behavior to the 4E1P with the AUSM type methods. The FCT method shows similar behavior to the results found with the 4E1P method and the pressure increase with time at the upstream section again indicating that this method predicts more liquid accumulation than the other ones.

Figures 9.38 to 9.41 report the holdup distribution along the line for different snapshots in time, in the same order as the pressure curves, the Roe scheme, AUSMV, ModFORCE, and FCT methods, respectively.

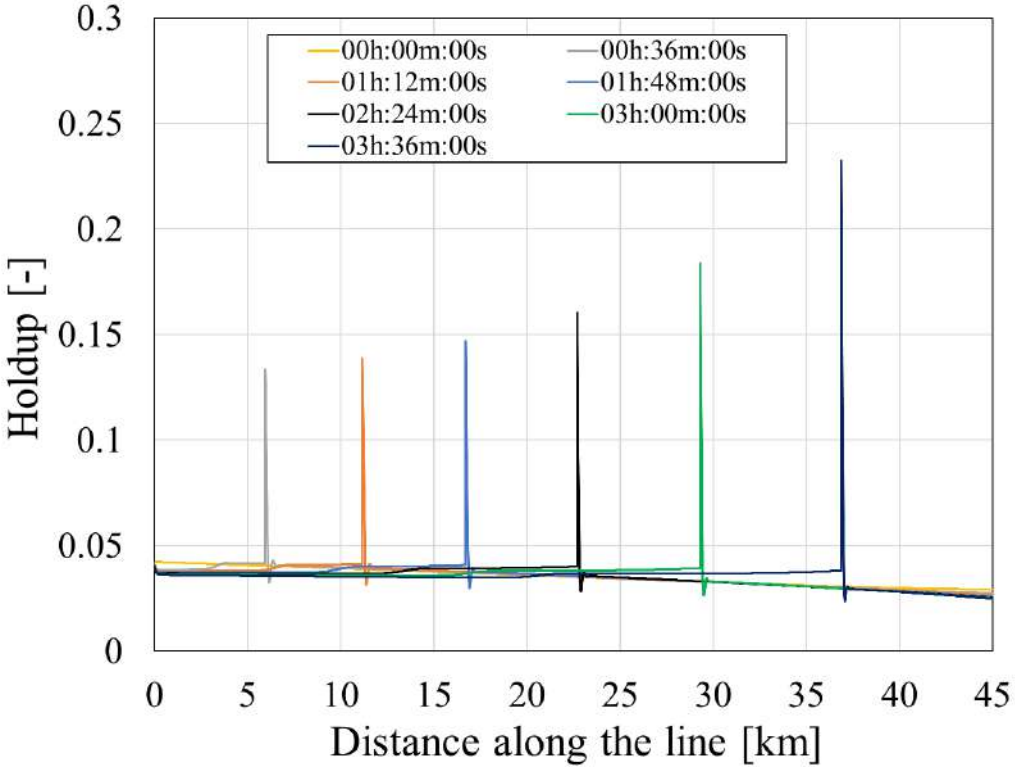

Figure 9.38: Holdup profile with Roe scheme and 5E2P, two-phase pigging.

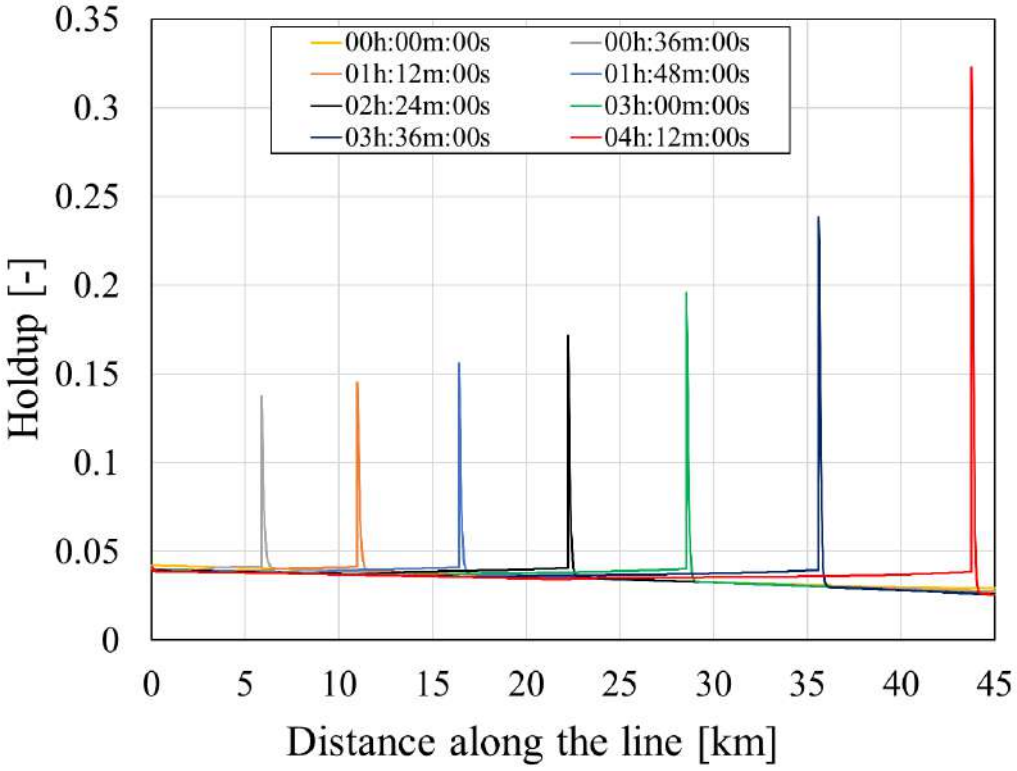

Figure 9.39: Holdup profile with AUSMV method and 5E2P, two-phase pigging.

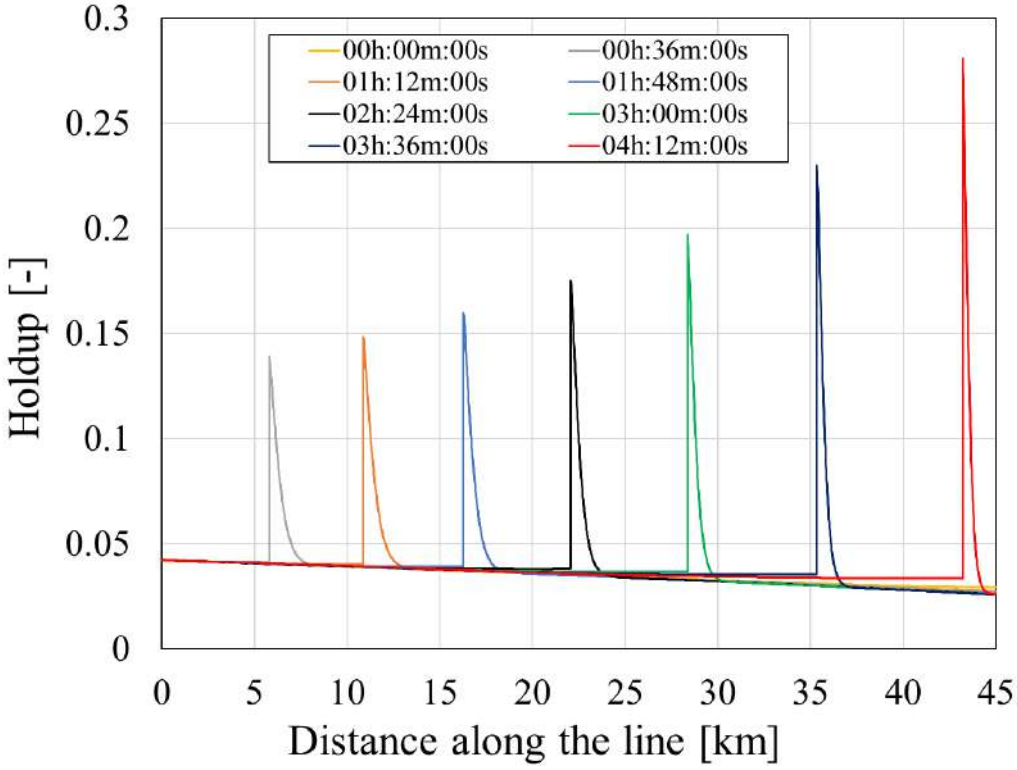

Figure 9.40: Holdup profile with ModFORCE method and 5E2P, two-phase pigging.

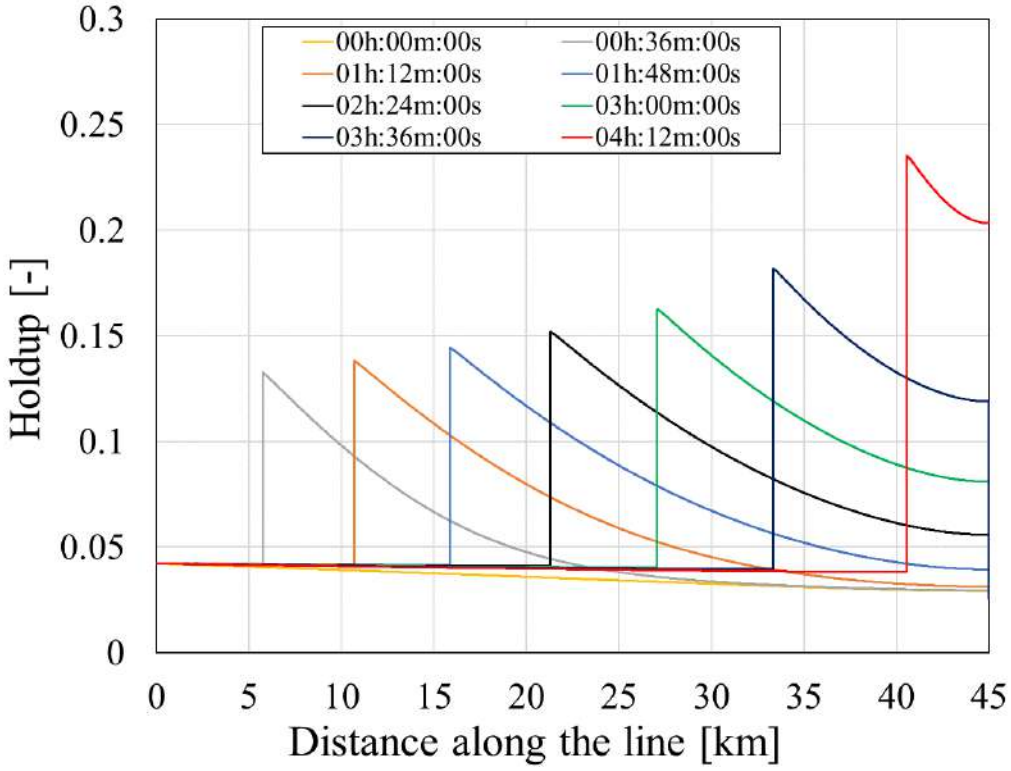

Figure 9.41: Holdup profile with FCT method and 5E2P, two-phase pigging.

Similar to the 4E1P method, the Roe scheme predicts very sharp results for the holdup accumulated at the front of the pig. In this plot, some numerical oscillations can be seen with the undershot of the holdup at the front of the holdup discontinuity. This spurious oscillation is dependent on the *CFL*, increasing with larger *CFL* number values, the increase in this oscillation can render holdup values lower than 0, breaking the physical representatives of the numerical solution that fails to converge. The other methods presented holdup distributions very similar to the ones with the 4E1P model. The AUSMV shows a very sharp peak at the liquid accumulation region in the pig front, and the ModFORCE and FCT show some axial accumulation that also seems to come from diffusive errors in the numerical solution. The ModFORCE seems to perform better here than in the 4E1P solution, with sharper gradients, corroborating with the results found in the benchmark results where the 5E2P model performs better with the ModFORCE scheme. The FCT method with 5E2P shows even more diffusion than in the 4E1P scheme.

The next presented results are for the gas velocity along the line, in Figs. 9.42 to 9.45, and for the liquid velocities, in Figs. 9.46 to 9.49, in the same order for the methods, Roe scheme, AUSMV, ModFORCE, and FCT.

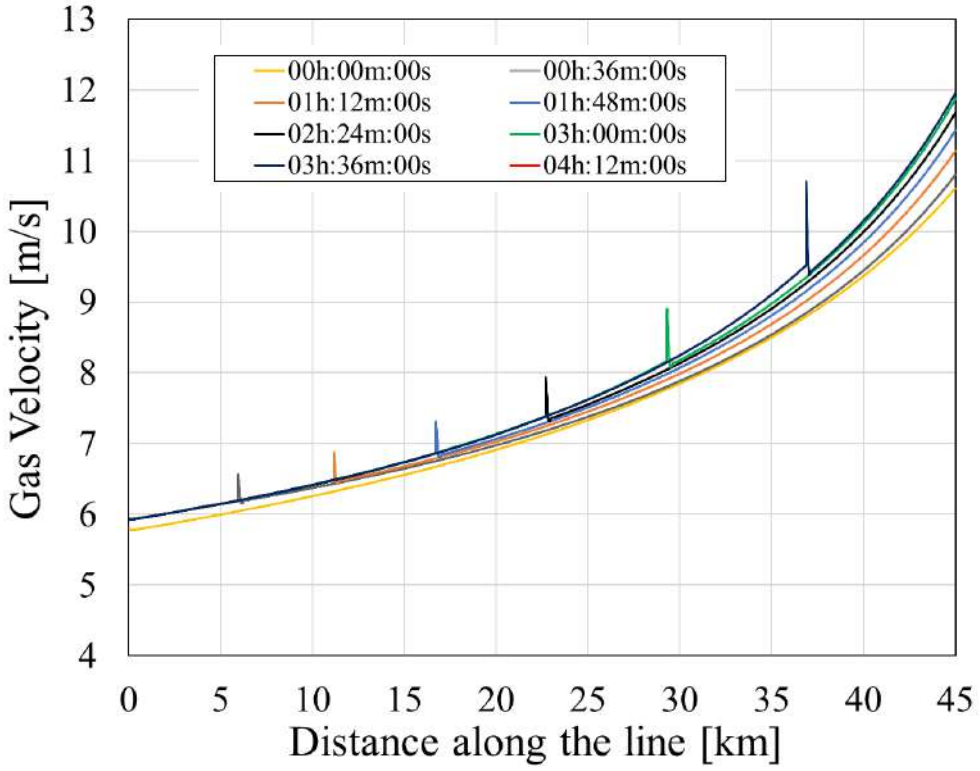

Figure 9.42: Gas velocity profile with Roe scheme and 5E2P, two-phase pigging.

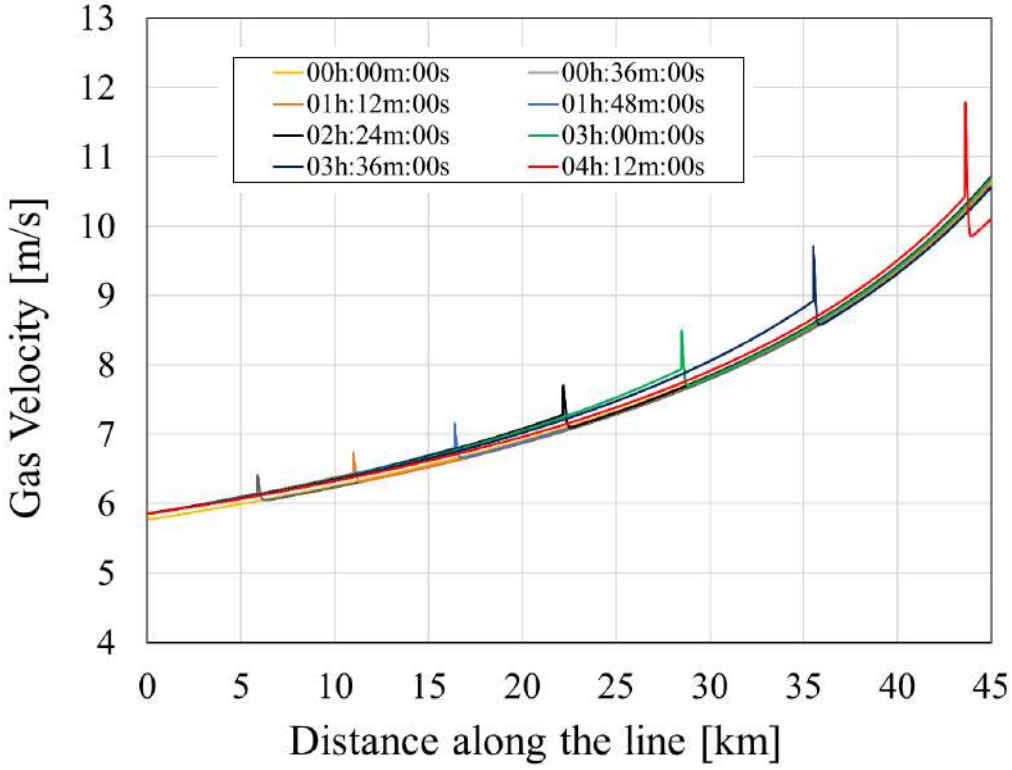

Figure 9.43: Gas velocity profile with AUSMV method and 5E2P, two-phase pigging.

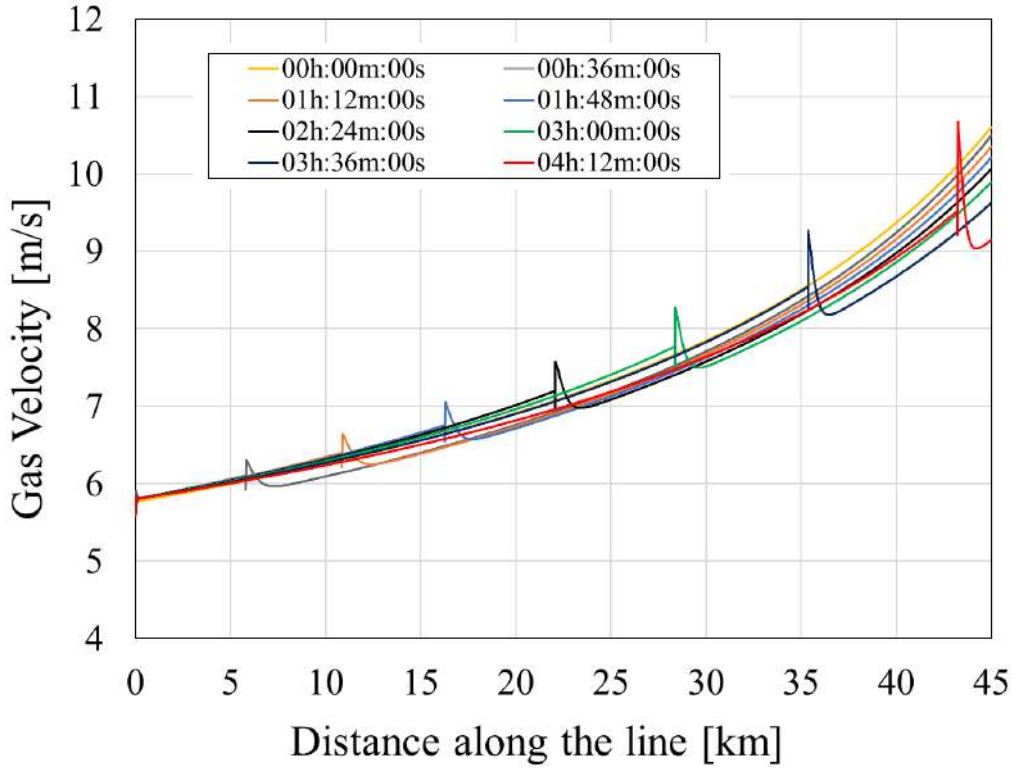

Figure 9.44: Gas velocity profile with ModFORCE method and 5E2P, two-phase pigging.

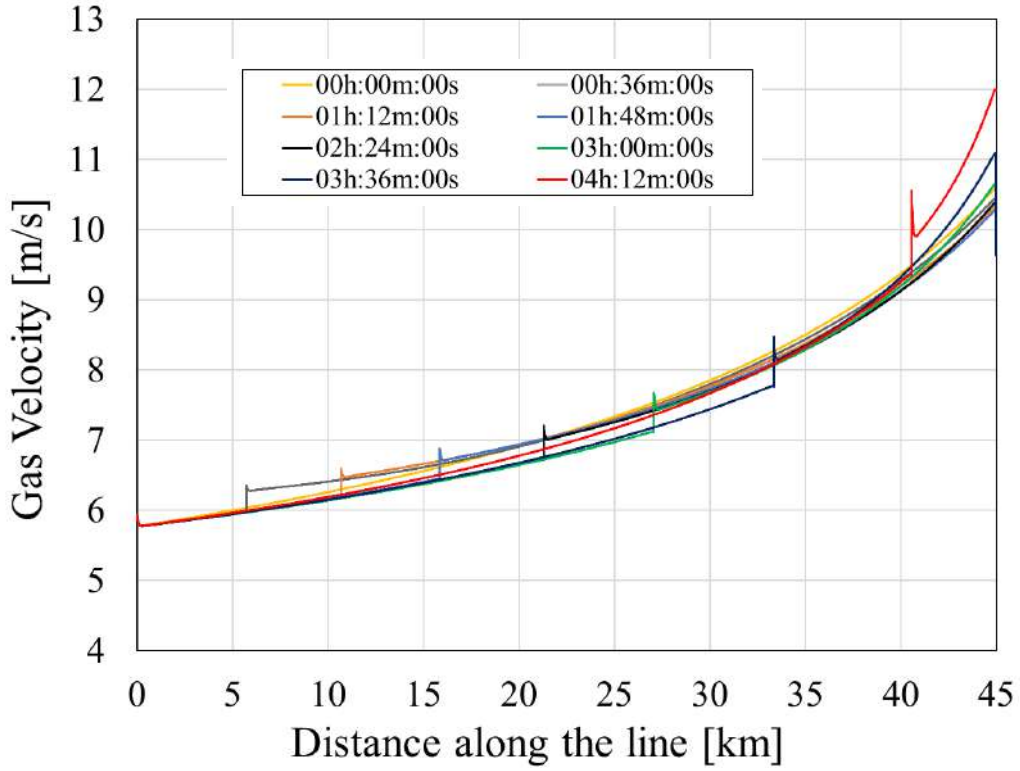

Figure 9.45: Gas velocity profile with FCT method and 5E2P, two-phase pigging.

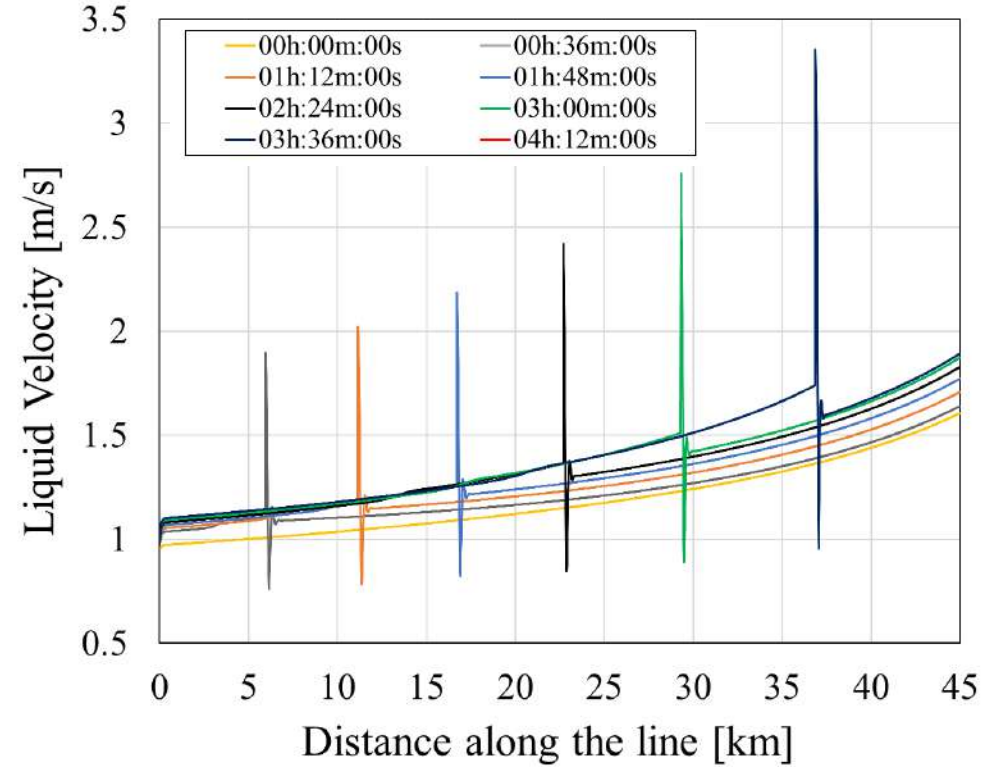

Figure 9.46: Liquid velocity profile with Roe scheme and 5E2P, two-phase pigging.

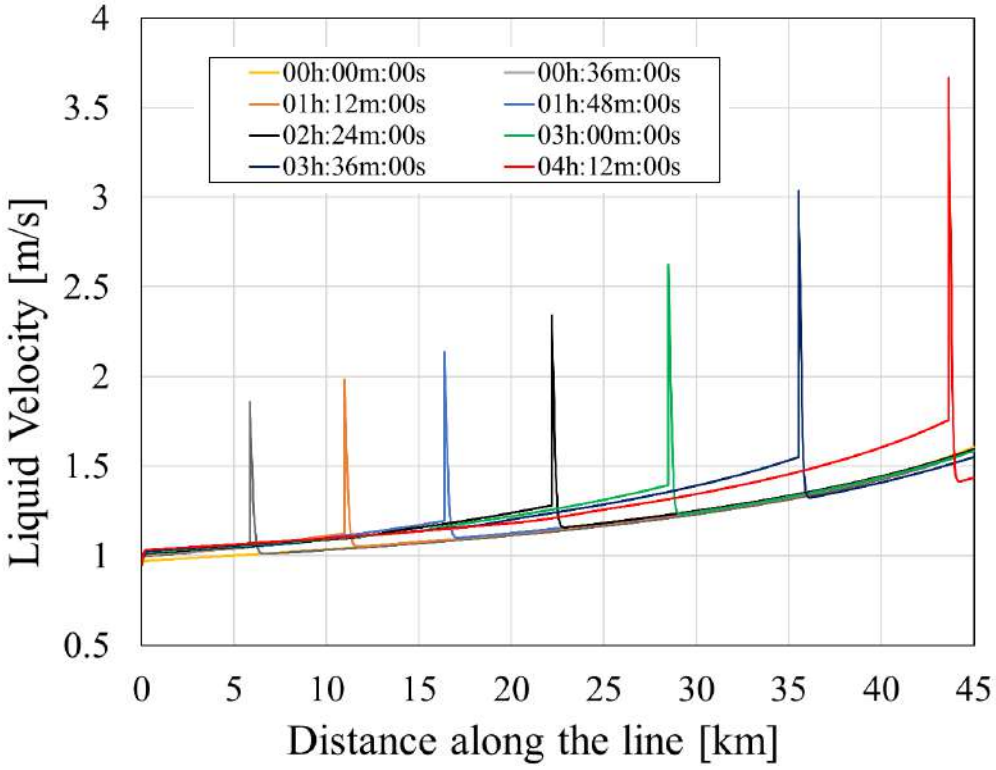

Figure 9.47: Liquid velocity profile with AUSMV method and 5E2P, two-phase pigging.

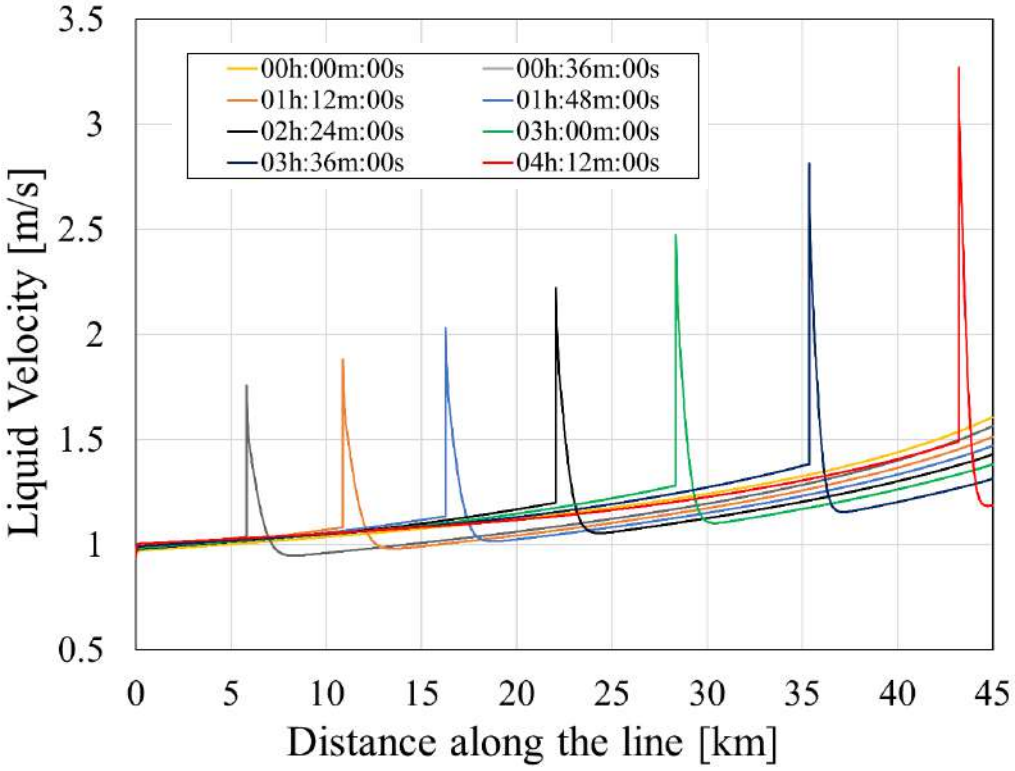

Figure 9.48: Liquid velocity profile with ModFORCE method and 5E2P, two-phase pigging.

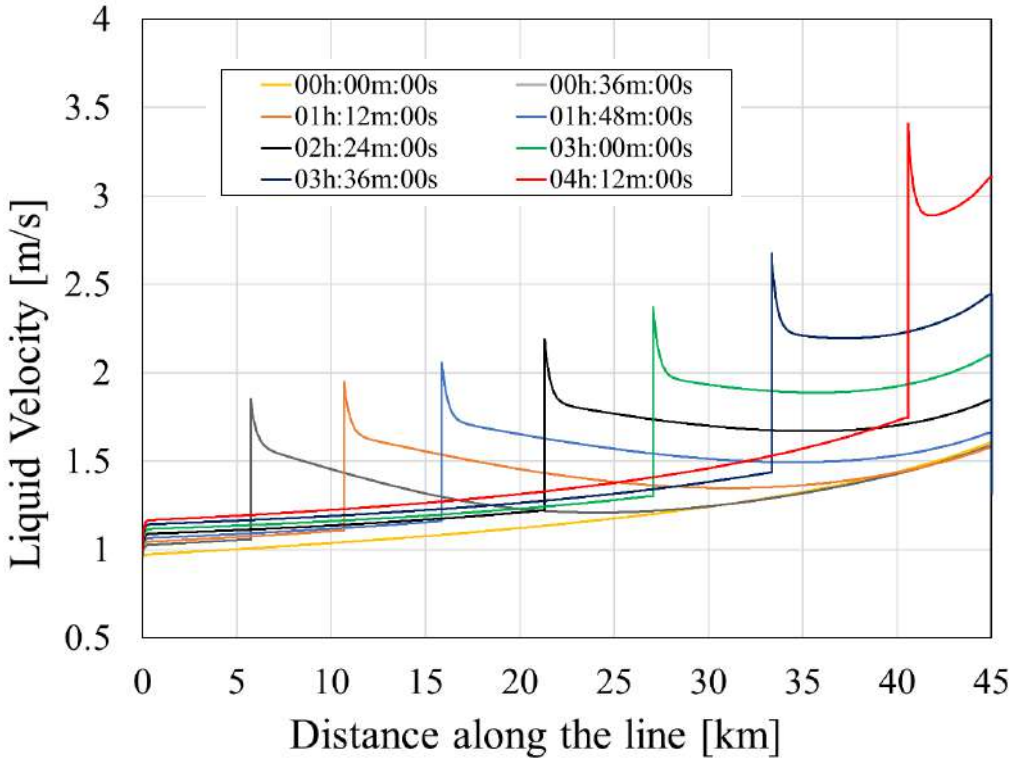

Figure 9.49: Liquid velocity profile with FCT method and 5E2P, two-phase pigging.

In the gas velocity, the same behavior found in the 4E1P method was found with the velocity increasing in the region right after the gas leaves the pig through the bypass and returning to values near the steady-state solution past this region. Again, this effect is amplified in the methodologies that reproduce higher holdup accumulation levels, such as the FCT method.

With the 5E2P, the liquid velocity shows at the front boundary of the downstream section velocities near the pig velocity for all methods, showing that the pig model was able again to capture the interaction of the pig dragging the liquid in its front. Note again that the results with the Roe scheme reproduce spurious oscillations near sharp gradients that in the liquid velocity produce swings that are in the same order of magnitude as the liquid flow velocities.

To complete the analysis the pig velocities with the 5E2P model are shown in Fig. 9.50.

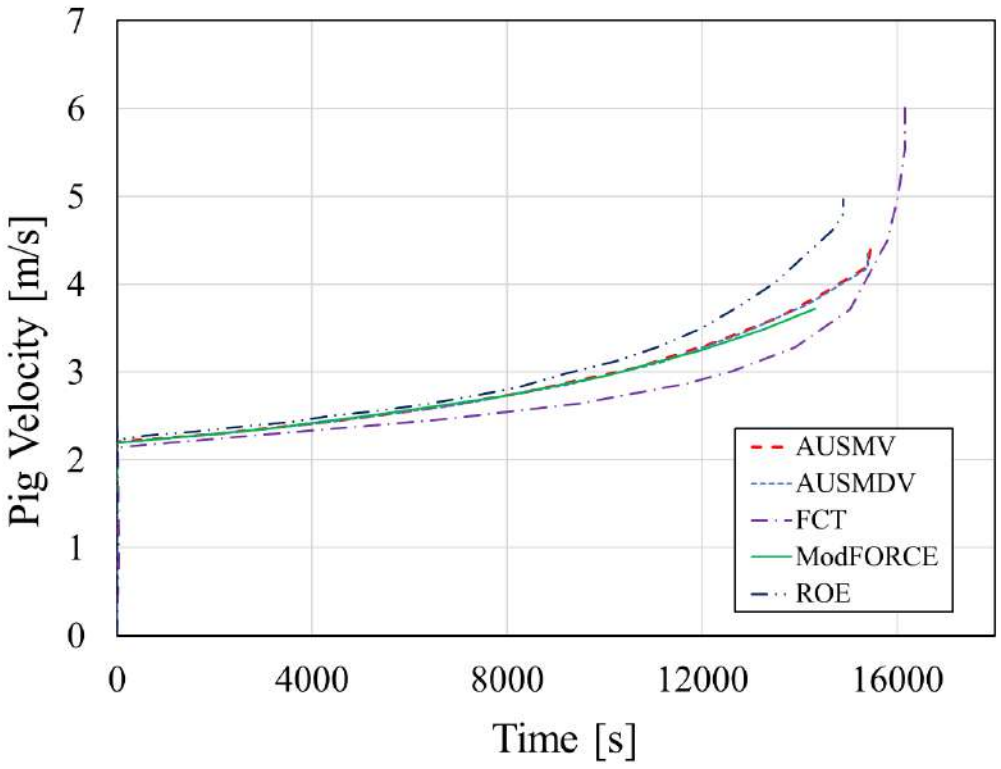

Figure 9.50: Pig velocities with time for the 5E2P model, two-phase pigging case.

The results share pretty much the same conclusions as the results obtained with the 4E1P model. The models that predict more overall liquid accumulation provide lower velocities with an increase in the velocity slope at the end due to liquid discharge to the outlet.

9.4.3 Comparison with References

The same case is now compared with the results obtained by Patricio (2016), and the commercial software OLGA. To have a direct comparison between the pig-flow coupling schemes, one of the results shown in Figs. 9.51 to 9.55 is the solution with the 4E1P model with the FCT method since it is the same model-method combination used by Patricio (2016). In his work, Patricio (2016) considers the pig as a singular surface moving within a fixed mesh, that differs from the current work that considers the dimensions of the pig, and two separate upstream and downstream meshes that are updated at each time step. The second result obtained in the herein work that is selected to compare with the references is the 4E1P model with the Roe scheme, since it shows the best results in the benchmark comparisons, as well as the sharpest gradients in the pigging results. Figures 9.51 to 9.54 show the current results for the pressure, holdup, gas velocity, and liquid velocity along the pipe, respectively, comparing the obtained results with the references. In all of these figures, the pig position is the same with the pig at 14.2km from the pipeline inlet.

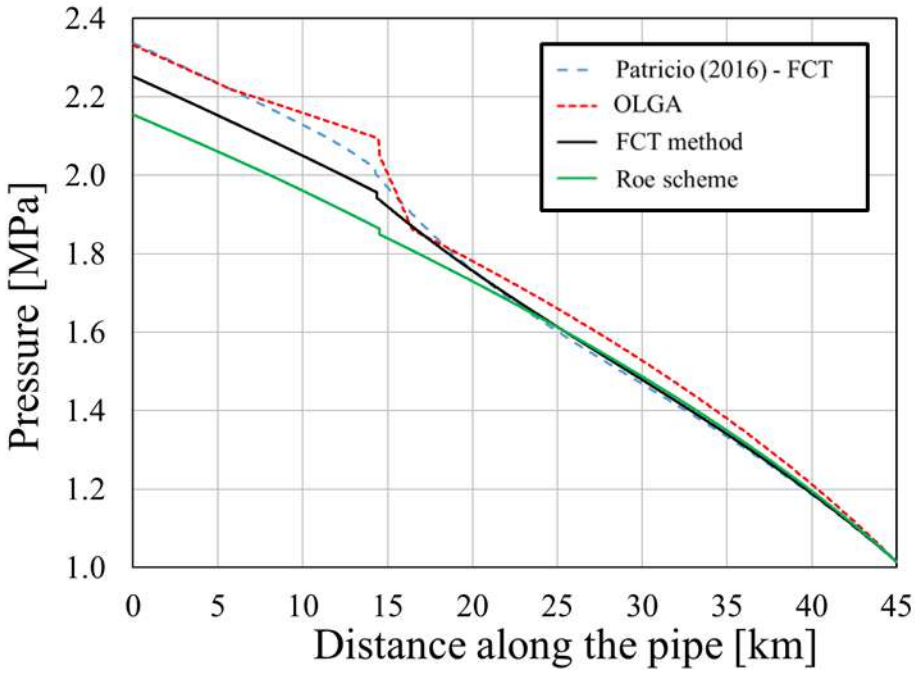

Figure 9.51: Pressure profile 4E1P, two-phase pigging, comparison with references.

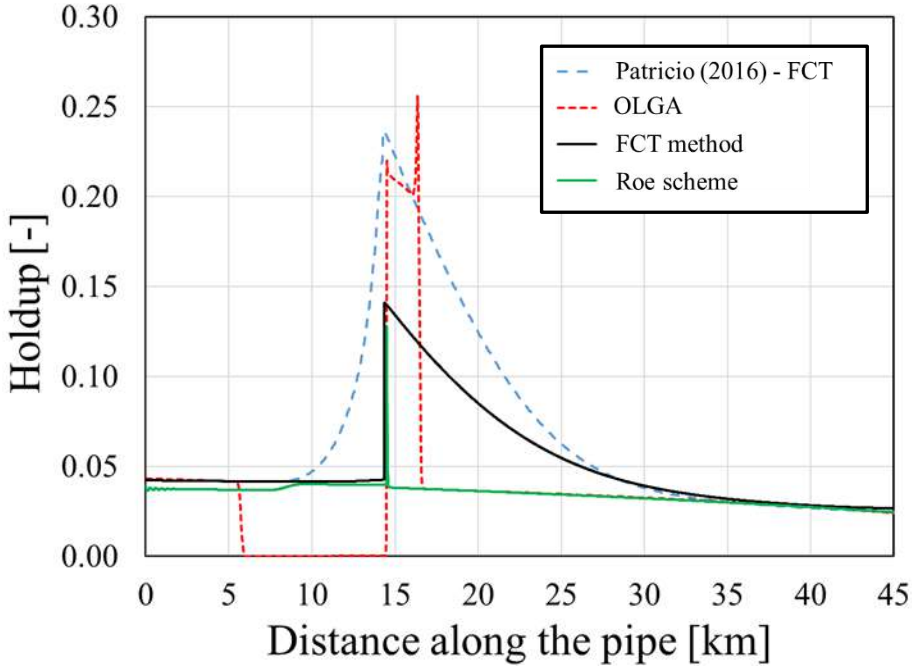

Figure 9.52: Holdup profile 4E1P, two-phase pigging, comparison with references.

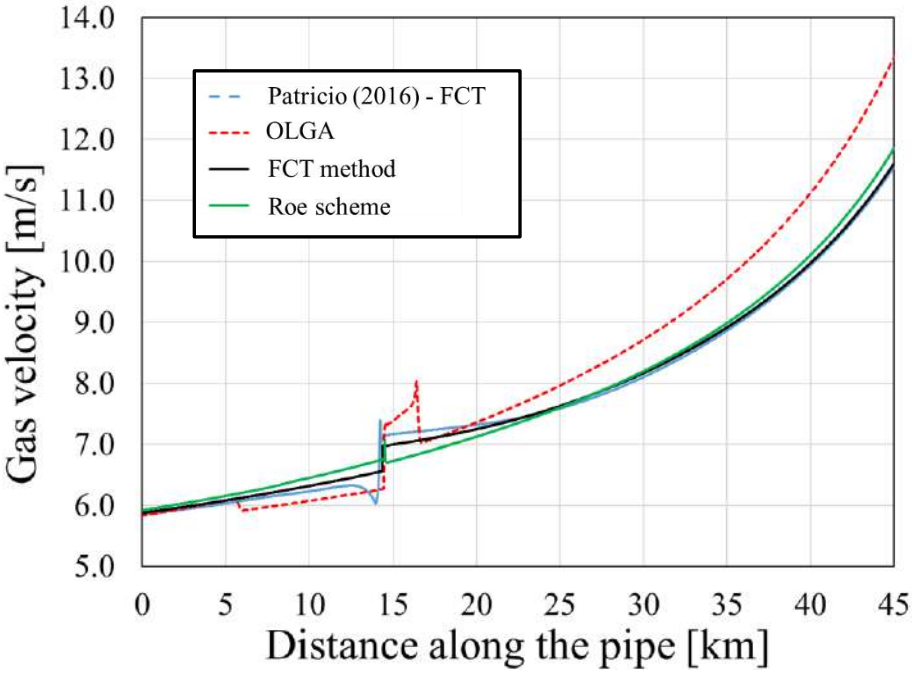

Figure 9.53: Gas velocity profile 4E1P, two-phase pigging, comparison with references.

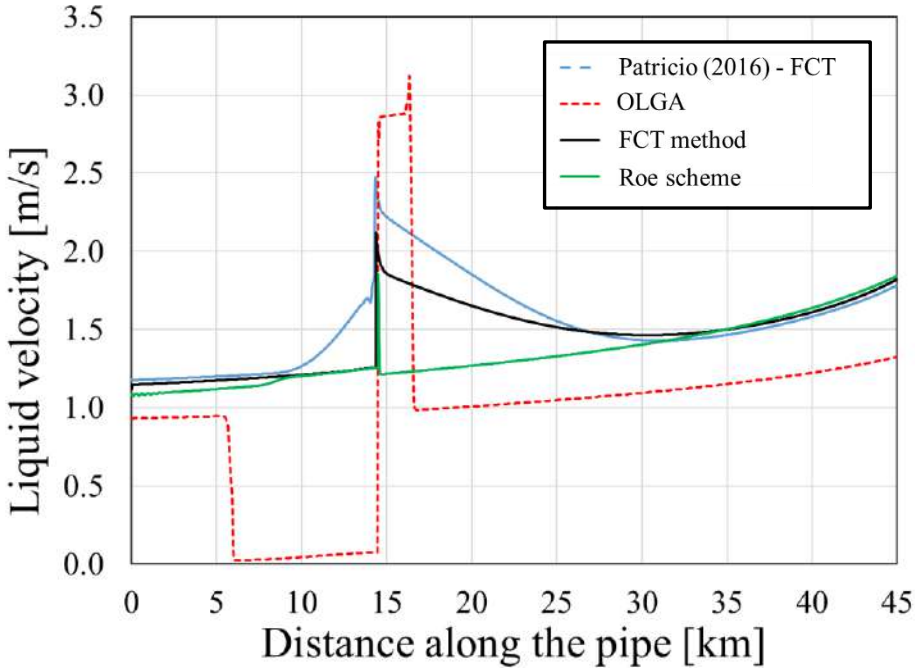

Figure 9.54: Liquid velocity profile 4E1P, two-phase pigging, comparison with references.

In the pressure distribution, the same behavior was captured by all methodologies, in which there is a jump in pressure through the pig that induces its movement. For both results presented by the simulations of the current work, the pressure values at the pig tail and front are lower than in the reference results, however the pressure differential across the pig is in the same order of magnitude. In the holdup, when comparing Patricio (2016) and the FCT results herein provided, both have a liquid accumulated region at the pig front, however this accumulation seems to be an artifact of the numerical diffusion that the FCT method provides when used in combination with the two-fluid models. The Roe scheme, on the other hand, shows the sharp gradients as reported in the previous sections. Patricio (2016) results also show an offset on the holdup difference across the pig, with some numerical diffusion behind the pig. None of the simulations herein provided show this non-physical effect, showing an improvement with the proposed methodology. Differently, the OLGA simulation shows a liquid accumulation region ahead of the pig as well as a low liquid region behind it, although none of the other results predict that. As for the gas and liquid velocities, their behavior is intertwined with the pressure and holdup distributions respecting continuity and momentum conservations, thus the comparison analysis reflects the same insights previously stated.

Figure 9.55 shows the pig velocity against time for the current work results as for the references

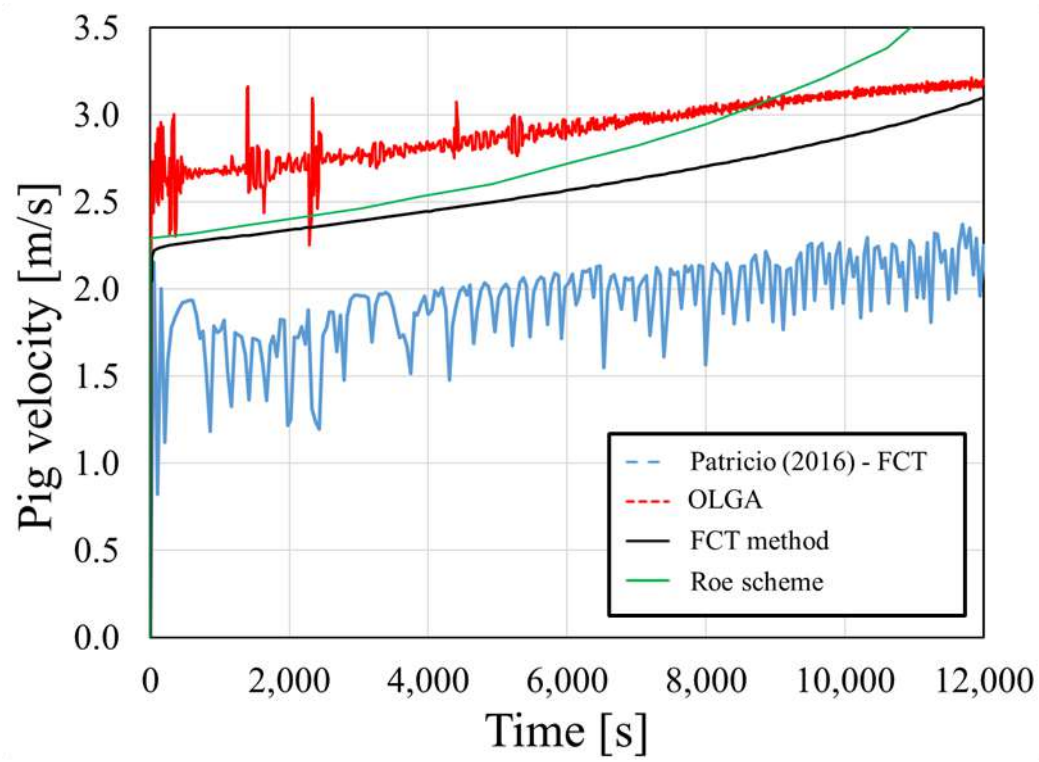

Figure 9.55: Pig velocities with time for the 4E1P model, comparison with references.

From the pig velocity results, the same behavior was captured by all methodologies, with a first region, right after the launch, where a higher pig acceleration is reported and then a second region where the pig velocity slightly increases with time. The current methodologies improve from the other ones as it estimates pig velocities without the oscillations seen for both OLGA's and Patricio's (2016) simulations. The reason for these oscillations is not clear for the OLGA simulation, since a full comprehensive material for how the modeling is done is not provided. Whereas for Patricio (2016), the oscillations can be consequence of his proposed scheme for pig-flow coupling, since the author considers a fixed mesh that may induce jumps in the flow parameters as the pig crosses from one cell to the other.

To summarize, this study provided results for pigging operation in a two-phase pipeline under stratified flow, and the upstream and downstream flow sections of the simulations are done using full Eulerian transient modeling. Even though some of the expected behavior for this example was not captured, the results are promising, since they represent some of the expected physics of the problem. The methodology was not able to

capture the liquid bodies dragged by the pig in the same order of magnitude as the ones that are shown in the commercial software OLGA, or the liquid holdup decreased at the pig tail, indicating that there may be gaps to be filed in the methodology. This might come from the pig-flow coupling methodology elaborated here. The pig-flow coupling methodology herein presented was formulated to enhance the methodology proposed by Patricio (2016) and Patricio *et al.* (2020), some oscillations present in their results are corrected here, however, the given results still do not capture all expected effects in the case of two-phase pigging. A reason for that might be the decoupled evolution of the pig position and the transient solution of the flow, where the pig position is updated between time steps of the simulation rather than incorporated through the transient solution.

10 Plunger Upstroke Results and Discussion

In this chapter, the plunger upstroke model is tested for conventional plunger operations. The first section is dedicated to the experimental data acquired in this work comparing the plunger dynamics obtained with the numerical code herein proposed. The next section compares the numerical results, in another configuration, with the experimental data acquired by Akiiartdinov *et al*. (2020) that used a logging piston.

10.1 Comparison Against Experimental Data

The two following studies compare two different cases carried out with the experimental facility detailed in chapter 8. For modeling this case, the flow is assumed to be a single-phase flow both ahead and in front of the plunger control volume. This assumption is based on the observation that the amount of liquid falling back from the plunger is negligible from the perspective of determining the pressure drop and velocities of the flow. However, the amount of liquid fallback flowing is still estimated by the plunger model affecting the liquid height of the plunger ahead of the slug, thus changing the overall mass displaced by the plunger entailing in the overall dynamics of the upstroke. For the following numerical simulations presented here the Roe scheme previously presented is used to solve the fluid flow sections upstream and downstream of the plunger.

The boundary conditions at the pipe inlet are the bottom hole pressure at the inlet, just past the bumper spring assembly, and the outlet boundary is the separator pressure. The experimental facility has a big enough casing to store enough gas for a plunger upstroke, where during the upstroke there is no gas influx into the casing. Then to determine the inlet pressure, and bottom hole pressure, a simple model is implemented given as follows,

$$\left.\frac{dp}{dt}\right|_{casing} = \frac{\dot{m}_{casing}}{V_{casing}} RT = \frac{\rho(x_0,t)u(x_0,t)}{V_{casing}} ART. \tag{10.1}$$

Using a second-order backward difference,

$$p_{casing}^{n} = \frac{4}{3}p_{casing}^{n-1} - \frac{1}{3}p_{casing}^{n-2} + \frac{2}{3}\Delta t \frac{A\rho^{n}(x_0)u^{n}(x_0)}{V_{casing}} ART, \quad (10.2)$$

where p_{casing}^{n} is the casing pressure at the current time step. For determining the pressure at the inlet, the local pressure drop across the bumper spring assembly can be included through a local pressure drop coefficient K_{inlet}, then it can be written as

$$p^{n}(x_0) = p_{casing}^{n} - K_{inlet}\frac{\rho^{n}(x_0)[u^{n}(x_0)]^2}{2} \quad (10.3)$$

For simplicity, the loss at the bumper spring assembly is neglected. The pressure at the outlet is kept constant in the simulations and equal to the separator pressure, that have an approximate value of 115.115 kPa(2psig) in the experiments herein performed.

For both experimental cases, the present one and Akiiartdinov *et al*. (2020), the test fluids are air and IsoparL, and their properties are presented in Table 10.1. The temperature of each experiment was averaged in the simulations to be around 298K since the experimental facility is external and multiple experiments were done with different temperatures ranging from 291K to 308K.

Table 10-1: Fluid properties, experimental plunger cases.

Parameter	Symbol	Value
Temperature	T	298 K²
Ideal gas constant	R	287 J/kg.K
Sound speed in gas	$c_G = \sqrt{RT}$	292 m/s
Reference gas density	$\rho_{0,G}$	0 kg/m^3
Liquid density	ρ_L	720 kgm^3
Dynamic viscosity gas	μ_G	1.9_x10^{-5} Pa.s
Dynamic viscosity liq.	μ_L	1.25_x10^{-3}Pa.s

10.1.1 Titanium Plunger Case

For this case, the focus is on comparing the simulations with the data acquired for the proximity sensors as well as the data for the high-speed pressure sensors (HSP). The

experiments were run a liquid loading of 1.17m(45in) with four distinct initial casing pressures, 184.062kPa (12psig), 197.852kPa(14psig), 211.641kPa(16psig), and 225.431kPa(18psig), that are replied in the experimental runs. The plunger used is detailed in Table 10.2.

Table 10-2: Titanium Alloy plunger properties.

Parameter	Symbol	Value
Plunger mass	M_p	1.615 kg
Plunger length	L_p	355.6 mm (14in)
Plunger diameter	d_p	49.22 mm (1.93in)

As an initial condition, all the experimental facility may be considered pressurized, in which a uniform pressure equal to the casing pressure is set behind the plunger, at the bottom. At the top, ahead of the liquid column, the pressure due to the difference between the casing pressure and the sum of the weight of the plunger divided by the cross-section area of the tubbing and the hydrostatic pressure of the liquid column,

$$p_{bottom} = p_{casing}(t_o) \tag{10.4}$$

$$p_{top} = p_{casing}(t_o) - Ag\left[M_p + M_{ls}(t_o)\right] \tag{10.5}$$

Basically, this initial condition creates a shock-tube type problem where a rarefaction wave travels from the outlet to the inlet in the direction of the liquid slug top. Figure 10.1 shows the numerical result for the wave coming into the tubbing and starting to reflect at the liquid slug top, where the direction of the black arrow indicates the direction that the wave is traveling. Notice the wave starting to reflect at the top of the liquid slug during the time snapshot of *t*=22.5ms. Unfortunately, this effect cannot be seen in the experimental results, because the HSP does not produce sharp enough data to reproduce this wave. After the rarefaction comes in, the waves bounce back from the liquid slug into the separator where it dissipates. To eliminate residual waves bouncing back and forth in the numerical solution another initial condition is reproduced with,

$$p_{bottom} = p_{casing}(t_o) \tag{10.6}$$

$$p_{top} = p_{separator} \tag{10.7}$$

However, to make the numerical results compatible with the experimental data, the time for this initial wave cycle must be added to the final numerical solution. The time that the first wave takes to completely travel from the inlet to the liquid slug top is estimated from the sound speed in the gas media, which is around 29.9ms corroborating the numerical results.

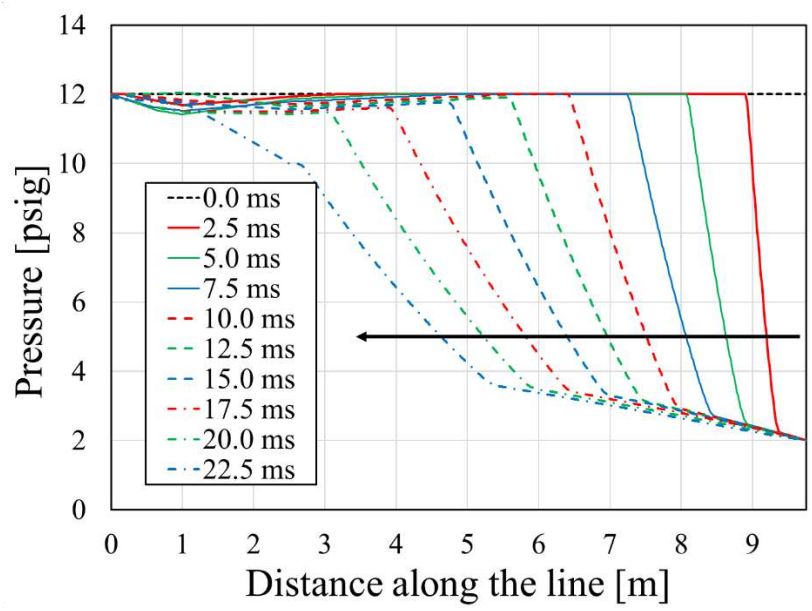

Figure 10.1: Rarefaction wave entering the tubbing.

With this setup, the numerical results for the position of the plunger against the time during the upstroke are obtained and compared to the experimental data from the proximity sensors (PS) processed as described in chapter 8, and the results are presented in Fig. 10.2. In that plot, the numerical data seems to corroborate well with the experimental points of the PS for all initial casing pressures, with the acceleration of the plunger during the upstroke. The experimental data shows the plunger reaching the first PS positions earlier than the numerical results, however, both results reach the higher points in the facility at almost the same time. This difference indicates that there is a switch between the experimental and numerical velocity solutions, where the

experimental solution has higher velocities at the beginning and the numerical lower, and later the numerical solution switch to higher velocities than the experimental.

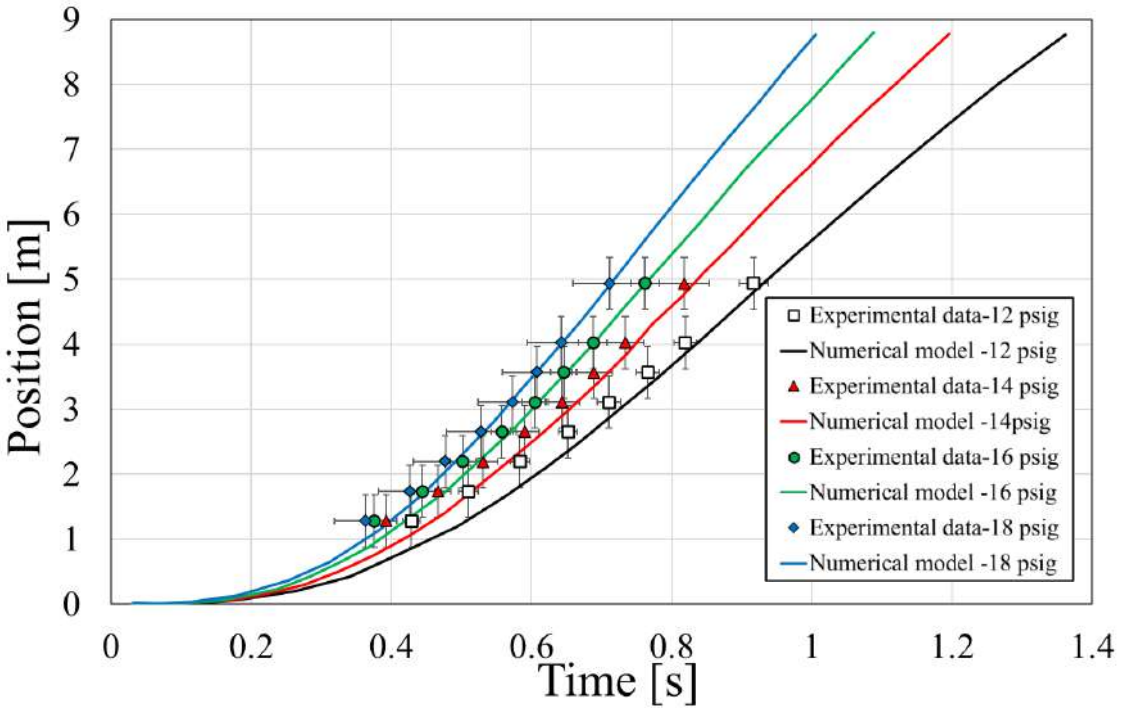

Figure 10.2: Plunger position against time, titanium plunger case.

Figure 10.3 shows the processed velocity experimental data against time plotted with the numerical solution. As the results show, the model presents excellent overall agreement with the experimental data. It was expected that, in general, the velocities would be higher in the numerical solution than in the experimental one since the numerical solution neglects any mechanical friction. However, the main difference in the results might come from the gap model herein proposed, because the model simplifies the dynamics of the flow in the plunger gap in a way that there is always gas and liquid flowing through it. It was not possible to verify the dynamics of the plunger during the beginning of the ascend with the high-speed camera at this position of the facility. However, speculation is that at the beginning of the experiment, the plunger is entirely surrounded by liquid, the liquid would then create a better seal during the first milliseconds with no loss through the gap by gas slippage, explaining why in this initial period the plunger goes faster than in reality than the numerical model. The model predicts gas slippage and liquid fallback right at the beginning of the simulation, thus, not capturing this effect. Although, if this phenomenon occurs, it would be in a time scale

that is not relevant to the overall problem of the plunger upstroke, hence not bringing a concern to the validity of the plunger model. Also, numerical data shows a change in the slope of the velocity indicating when the liquid slug hits the lubricator at the top of the facility and starts decelerating the plunger, unfortunately, the proximity sensors do not cover enough distance to capture that effect.

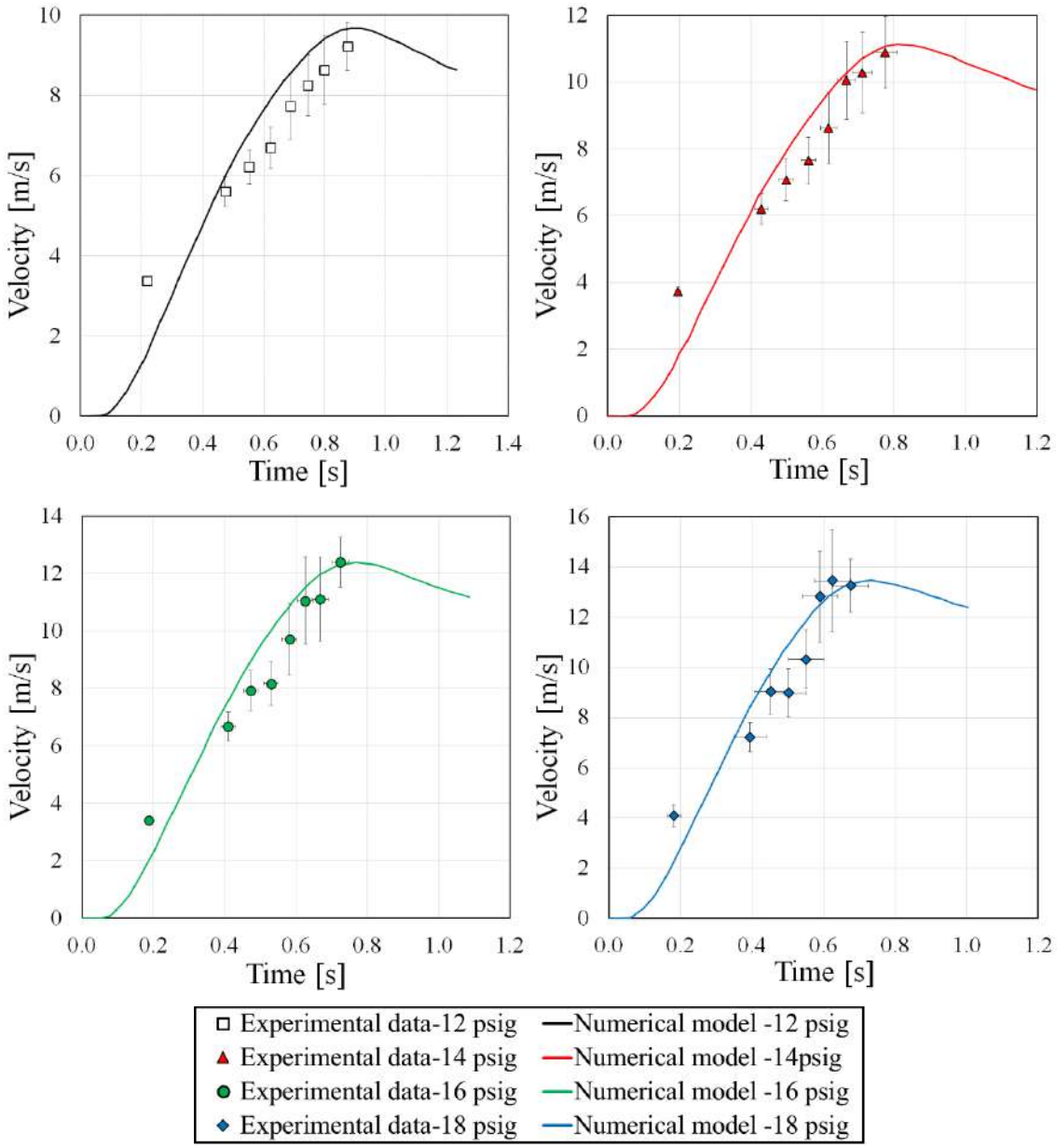

Figure 10.3: Plunger velocities against time, titanium plunger case.

Figures 10.4 to 10.7 show the different pressures at each HSP of the facility, continuous curves, with the PS data, vertical lines, and the dashed curves the simulated

bottom hole pressure, Taylor bubble pressure, and the set boundary condition at the outlet of the tubbing, approximately the separator section pressure.

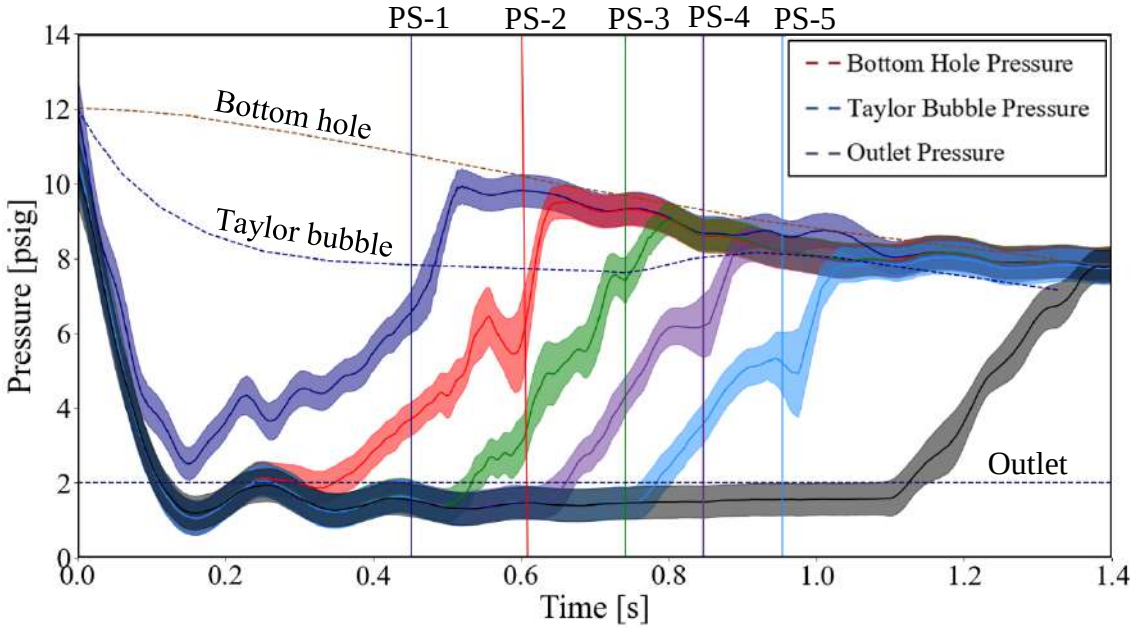

Figure 10.4: Pressure against time (12psig), titanium plunger case.

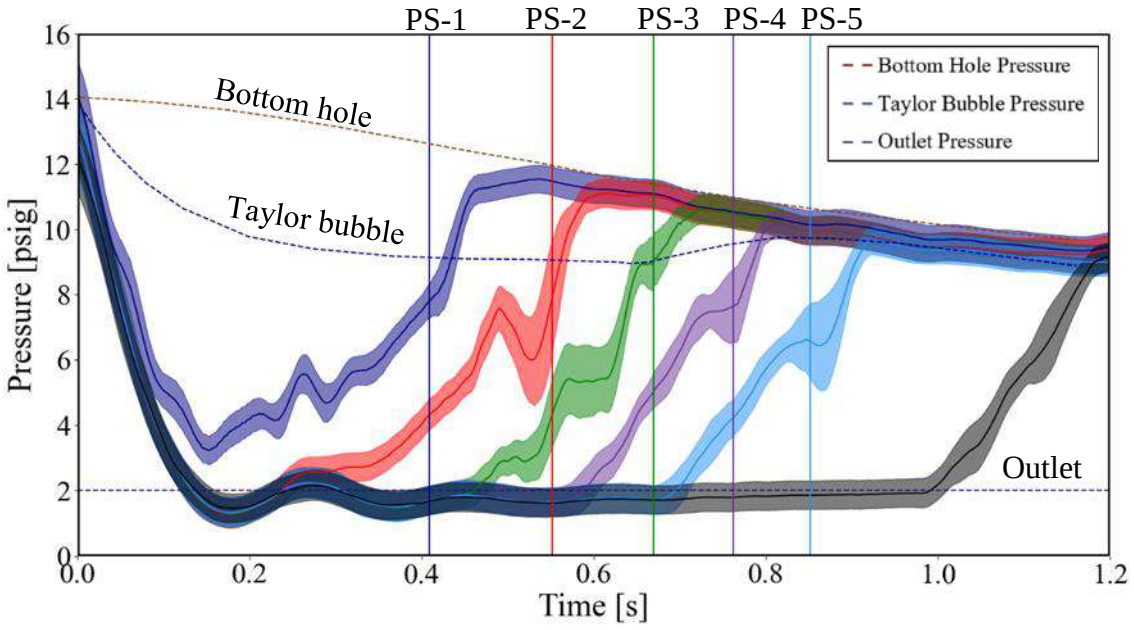

Figure 10.5: Pressure against time (14psig), titanium plunger case.

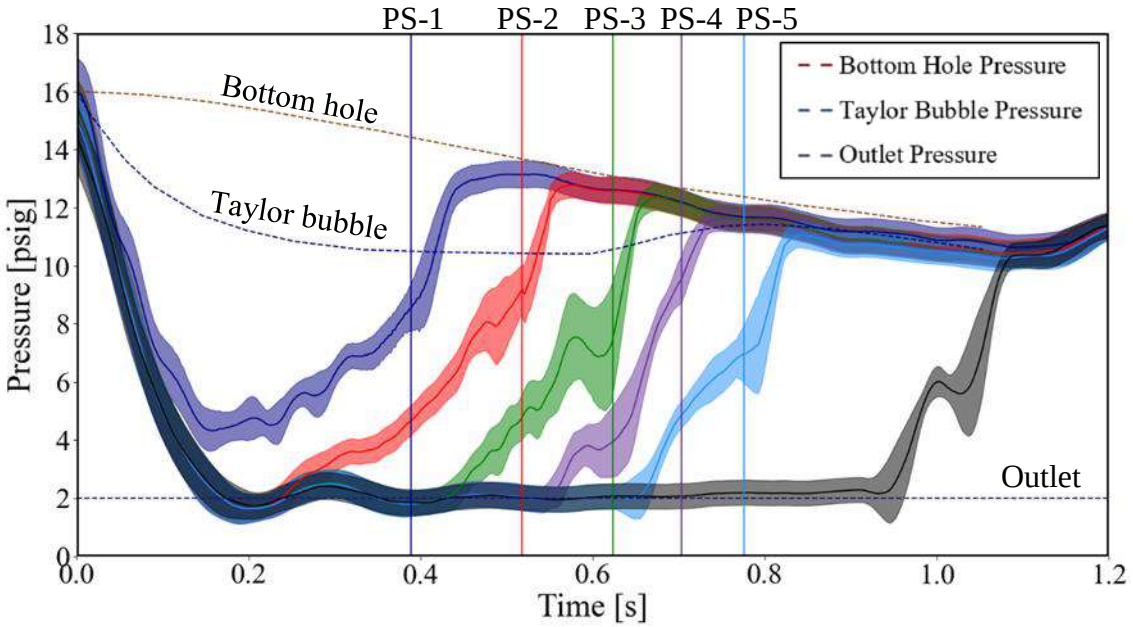

Figure 10.6: Pressure against time (16psig), titanium plunger case.

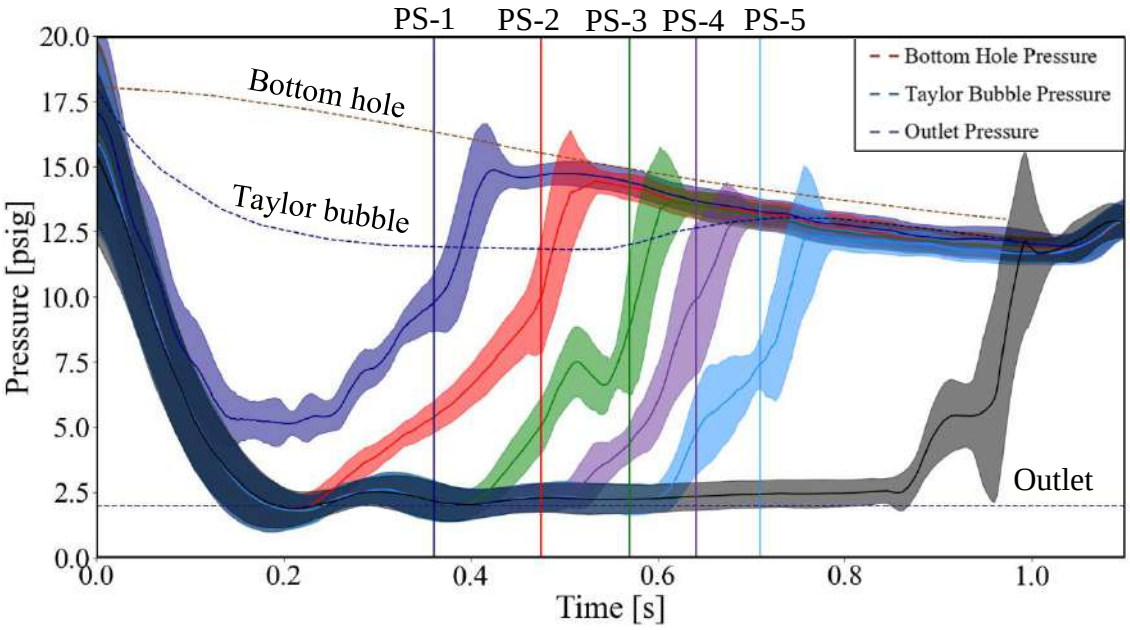

Figure 10.7: Pressure against time (18psig), titanium plunger case.

The PS lines share the same color as the HSP in the same position, with PS-1 and HSP-1 in dark blue, PS-2 and HSP-2 in red, PS-3 and HSP-3 in green, PS-4 and HSP-4 in purple, PS-5 and HSP-5 in light blue. Following the HSP curve, initially, the pressure marks the pressure when the facility is pressurized. With the opening of control valve CV-1, the pressure drops to mark the point when the numerical data, and the high-speed and low-speed experimental data are synchronized. This pressure drop is seen in all HSP almost simultaneously, and after that, the pressure reaches a plateau that represents the pressure at the outlet of the tubbing, the inlet section of the connection between the tubing and the separator, with an approximate value of 115.115 kPa(2psig) for all the different initial casing pressures. For the simulation, this pressure is assumed constant, represented by the dashed purple line. Continue following the HSP curve, when the liquid slug top passes through the sensor, the pressure rises, and after that, the plunger front passes through PS at the same position capturing the plunger front, given by the vertical line. Afterward, when the plunger tail passes through the pressure will reach the high pressure behind the plunger. The high-pressure values behind the plunger are almost identical for all HSP since the flow has a high void fraction and the facility is not long enough to produce large pressure drops, which is also represented by the numerical data, where the pressures behind the slug and ahead of the liquid slug front are almost constant along with the tubbing. The dashed brown line reproduces the bottom hole pressure estimated by the numerical simulation. This pressure curve matches well the pressure behind the plunger given by the HSP curves. The last presented curve in the plots is the numerical Taylor bubble pressure given by the dashed blue curve, unfortunately, there are no features found in the HSP curves that correlate with this pressure plot. The sensor HSP-6 does not have a PS sharing the same position, near the lubricator at 8.138m, but its data can give a general perspective on the plunger position with the jump seen in the plots. The bottom hole and Taylor bubble pressures end when the numerical plunger reaches the end of the tubbing, then the simulated upstrokes end before the experimental ones.

10.1.2 Logging Plunger Case

Akiiartdinov *et al*. (2020) gathered experimental data with a logging plunger, also called a smart plunger, that has a built-in accelerometer and pressure sensors at the tail and front of the piston. Their data is extremely useful for comparing with the herein proposed model since the position, velocity, and acceleration of the piston together with

the pressure at the tail and front, are recorded through all the upstroke experiments at a frequency of 100 Hz. Their data is expected to fill some of the gaps from the previous study, with a fuller position, velocity, and acceleration profiled through time being experimentally reported, as well as the front pressure of the piston that is comparable to the Taylor bubble pressure of the numerical simulation, and the tail pressure that should be close to the bottom hole pressure. The plunger used in this experimental setup is reported in Table 10.3. The experiments were run a liquid loading of 1.65m(65in) with three distinct initial casing pressures, 197.852kPa(14psig), 211.641kPa(16psig), and 225.431kPa(18psig).

Table 10-3: Logging Plunger properties

Parameter	Symbol	Value
Plunger mass	M_p	3.393kg(7.48lbs)
Plunger length	L_p	482.6mm(19in)
Plunger diameter	d_p	49.53mm(1.95in)

Figures 10.8, 10.9, 10.10, and 10.11 respectively show the position of the plunger, the velocity of the plunger, and the pressure at the plunger tail and Taylor bubble against time, for both the numerical results and the reference. The position plot and the velocity plot show that the numerical results produce, in general, higher velocities than the experimental one. This can be explained by the pressure plot in Figs. 10.10 to 10.12 show that, for this case, the bottom hole pressure is over-predicted by the numerical simulation, especially at the very beginning, where in the numerical data there is a sudden drop in the pressure. This drop is believed to come from the losses in the bumper spring assembly at the entrance of the tubbing and the slushing oil at the bottom that may have been amplified with the higher liquid load. Also, the numerical model predicts higher Taylor bubble pressures, affecting the overall dynamics of the plunger. Note that at the end of the experiment, the Taylor bubble pressure equals the plunger tail pressure that happens smoothly in reality, whereas in the experimental setup the different.

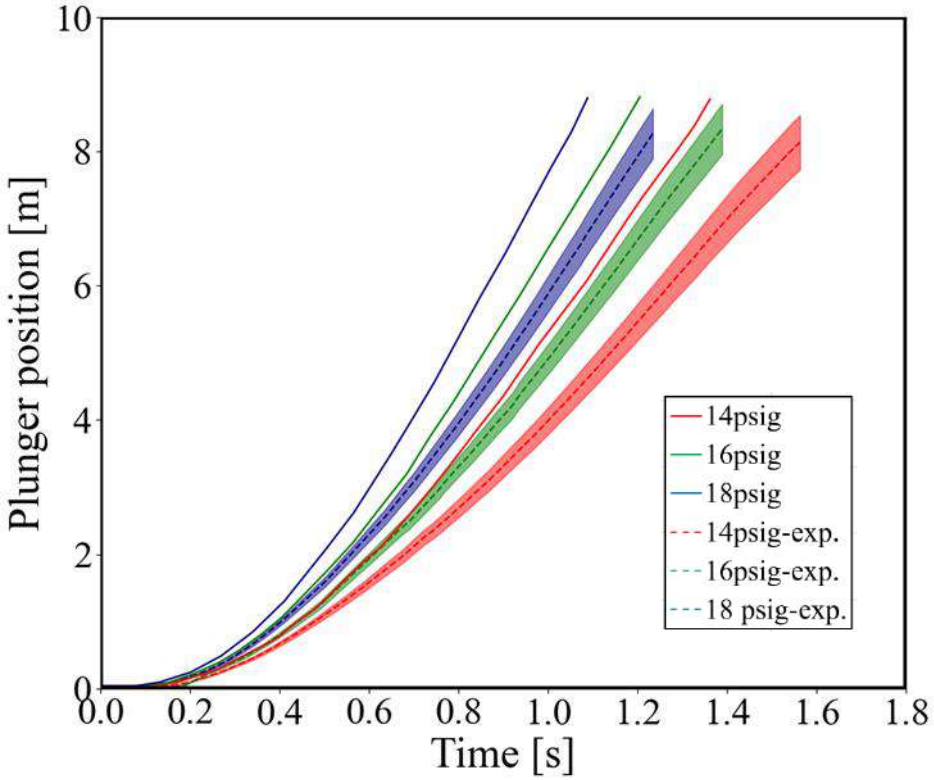

Figure 10.8: Plunger position against time, logging plunger case.

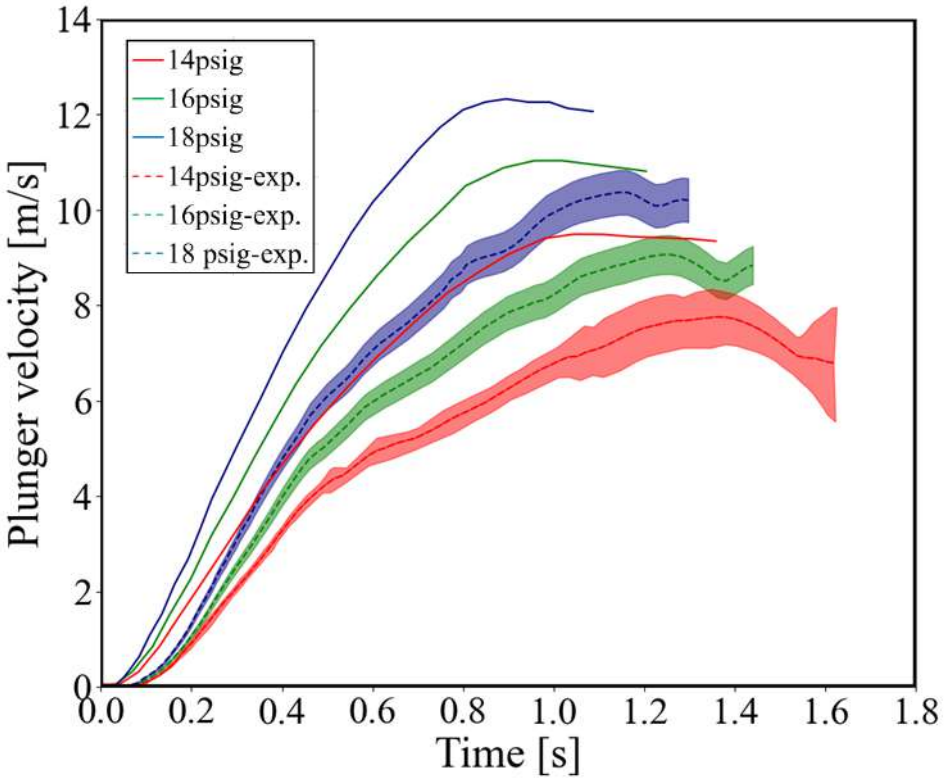

Figure 10.9: Plunger velocity against time, logging plunger case.

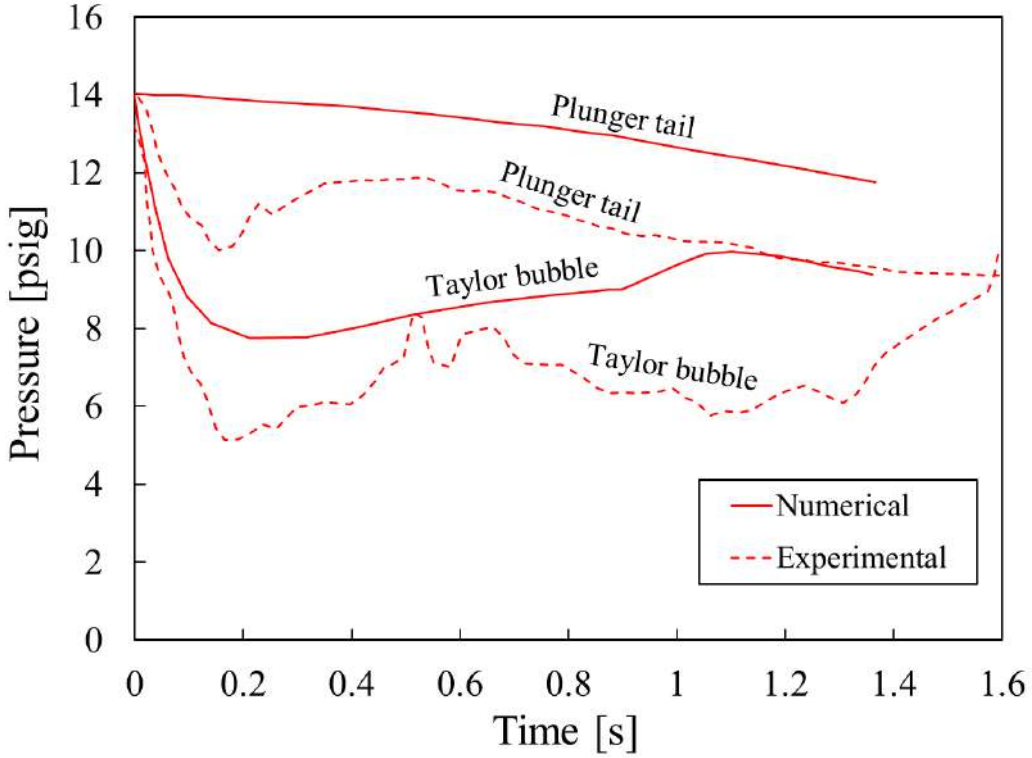

Figure 10.10: Pressure against time (14psig), logging plunger case.

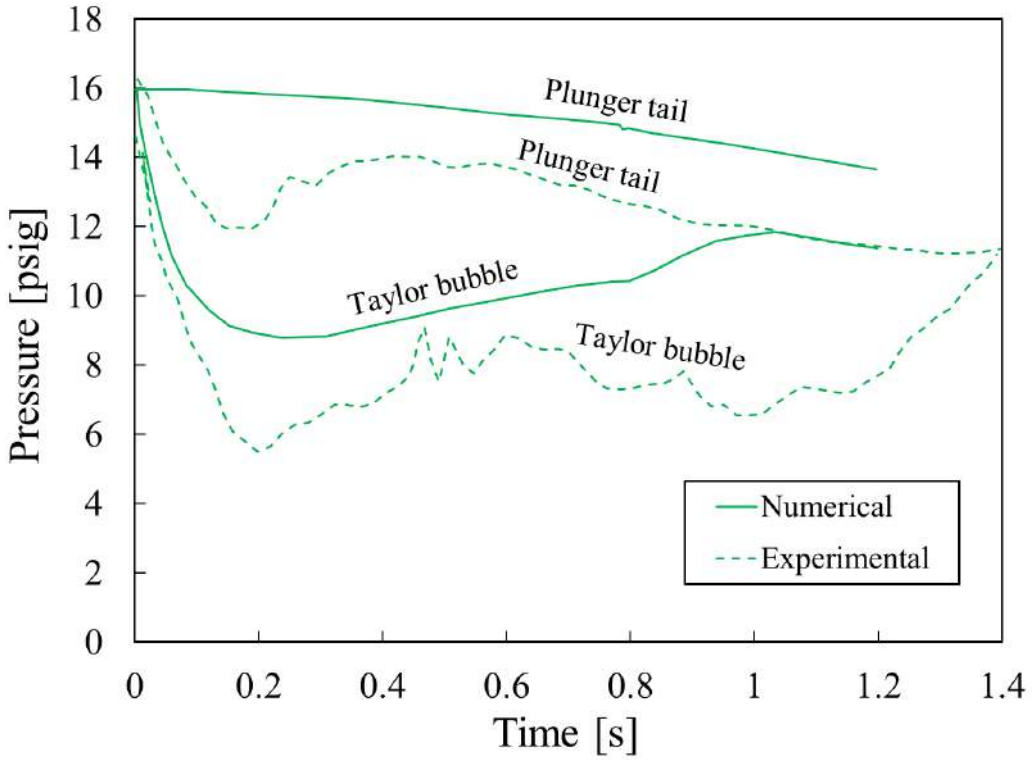

Figure 10.11: Pressure against time (16psig), logging plunger case.

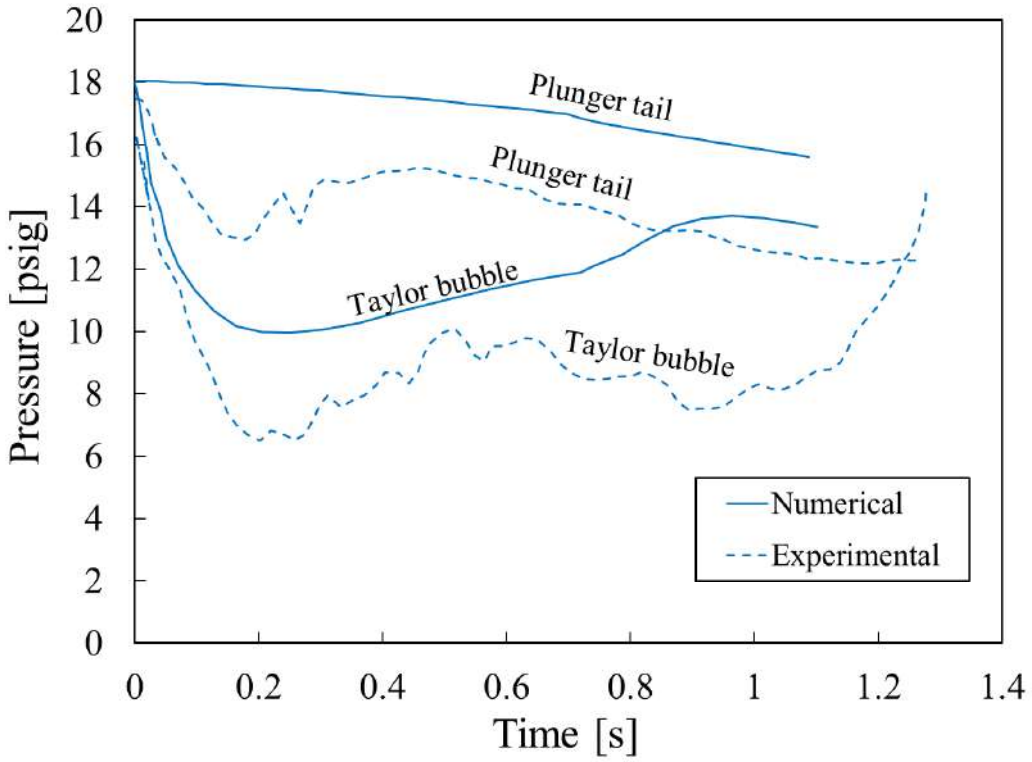

Figure 10.12: Pressure against time (18psig), logging plunger case.

Although for this case the dynamics do not match as well as in the previous one, some additional information points to the right representation of the problem, with the expected trends in the position and the velocity plots. The Taylor bubble pressure behavior also gives encouraging results where a drop in the pressure is seen at the beginning, similar to the experimental data. Comparing the figures with the ones from the previous simulation case, the higher liquid load with the higher plunger weight reduced the velocities in all simulations as expected.

10.1.3 Adjusted Bottom Hole Pressure

To further test the model against the data, the casing and inlet dynamics obtained from the numerical solution are taken out in this next test and are substituted by a polynomial fitting of the plunger tail pressure experimental data. Since the facility is short, the plunger tail pressure is close to the bottom hole pressure, therefore, the bottom hole pressure can be approximated by the plunger tail pressure. For that, the experimental data is fitted into six order polynomials for each of the initial casing pressures with,

$$p(x_0, t) = P_A t^6 + P_B t^5 + P_C t^4 + P_D t^3 + P_E t^2 + P_F t^1 + P_G, \quad (10.8)$$

Where the polynomial coefficients are reported in Table 10.4 for each of the respective initial casing pressures.

Table 10-4: Polynomial parameters for bottom hole pressure adjustment.

Polynomial Parameter	14psig	16psig	18psig
P_A [psig/s^6]	44.859	*86.510*	108.00
P_B [psig/s^5]	-243.63	-430.39	-515.87
P_C [psig/s^4]	512.35	833.57	969.51
P_D [psig/s^3]	-518.53	-781.29	-881.83
P_E [psig/s^2]	252.00	353.52	390.23
P_F [psig/s]	-50.955	-66.646	-72.627
P_G [psig]	14.095	16.696	18.176

Again here Figs. 10.13 to 10.17 respectively show the position of the plunger, the velocity of the plunger, and the pressure at the plunger tail and Taylor bubble against time, for both the numerical results and the reference. In this new numerical test, there is a better match with the experimental results for both the velocities and the position of the plunger during time with the different initial casing pressures. This confirms what was expected from the previous experiment, that the over-prediction of the bottom hole pressure affected the was the major influence in the discrepancy between the results.

Figures 10.15 to 10.17 show the plunger tail and Taylor bubble pressures for both experimental and numerical results after the bottom hole pressure adjustment. The numerical solution of the plunger tail matches the bottom hole pressure estimated by the polynomial, hence a separate plot for the numerical bottom hole pressure is not necessary, also this is consistent with the idea of adjusting the numerical bottom hole pressure with the experimental plunger tail pressure. After the adjustment, the numerical prediction for the Taylor bubble pressure shows great agreement with the experimental data showing that for this configuration setup, the plunger upstroke model matches the expected physics of the problem.

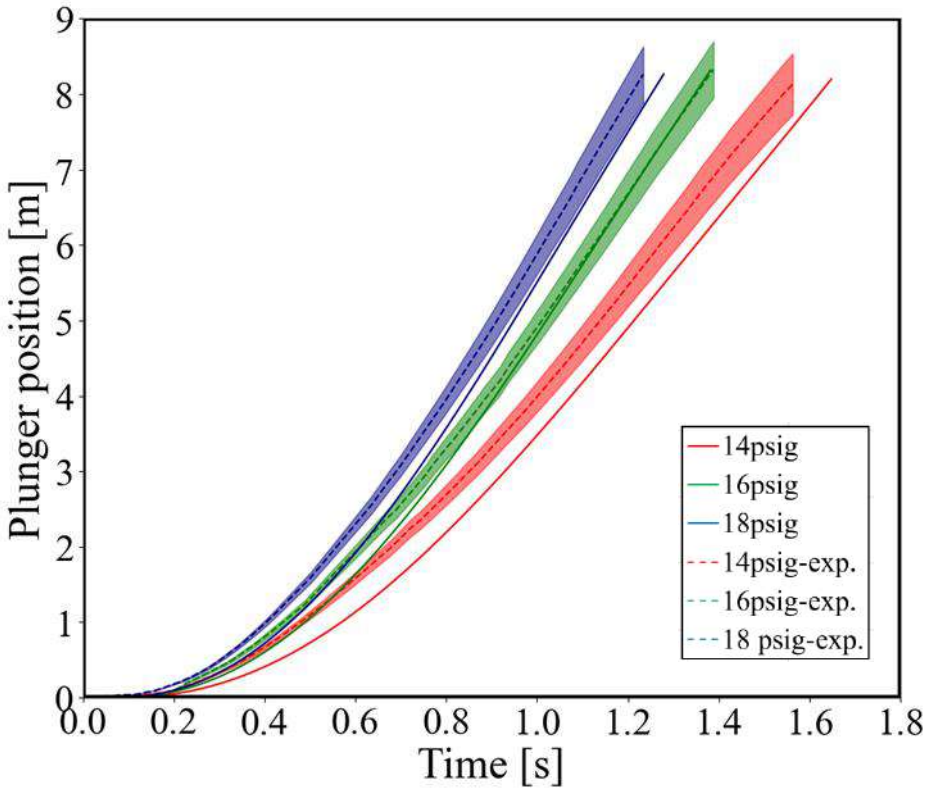

Figure 10.13: Plunger position against time, logging plunger case, after pressure adjustment.

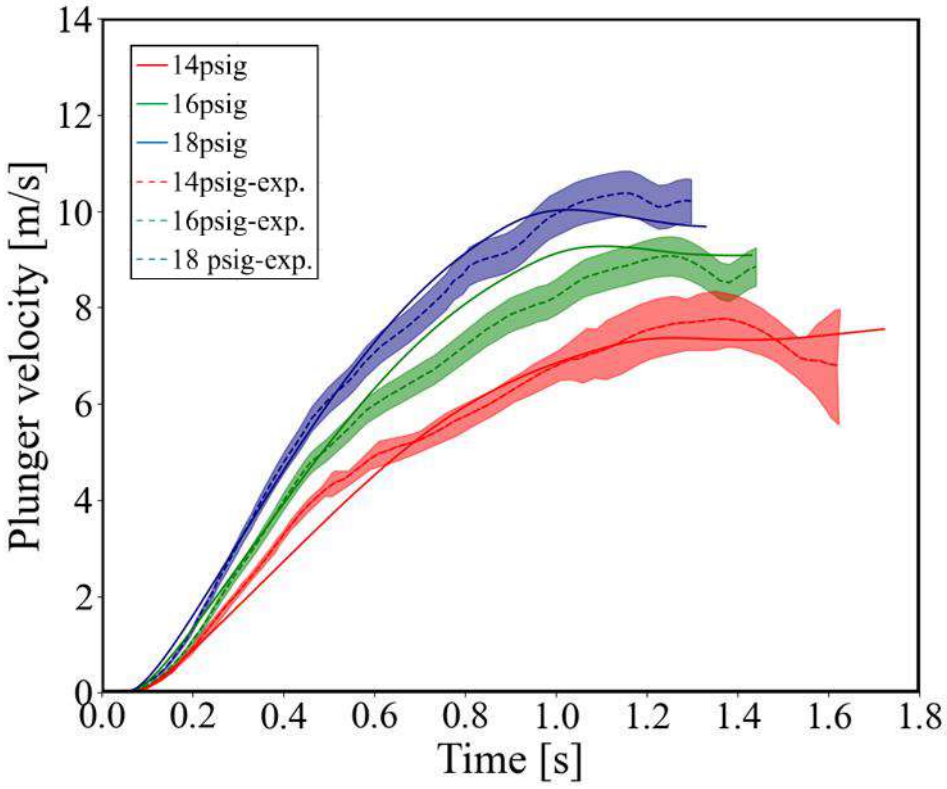

Figure 10.14: Plunger velocity against time, logging plunger case, after pressure adjustment.

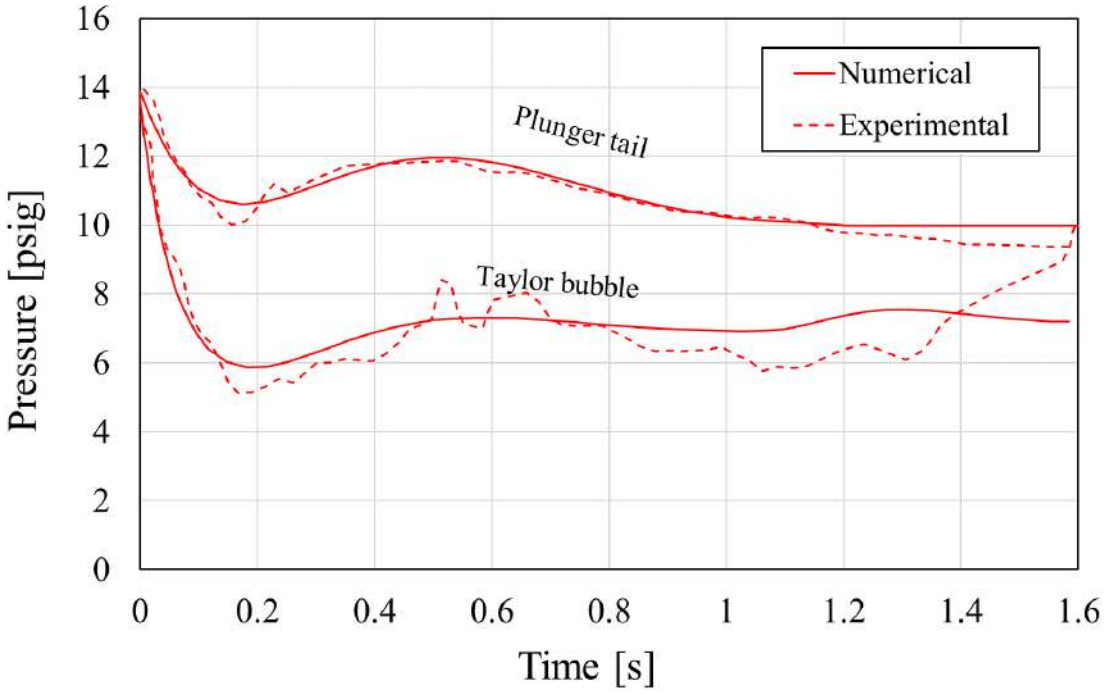

Figure 10.15: Pressure against time (14psig), logging plunger case, after pressure adjustment.

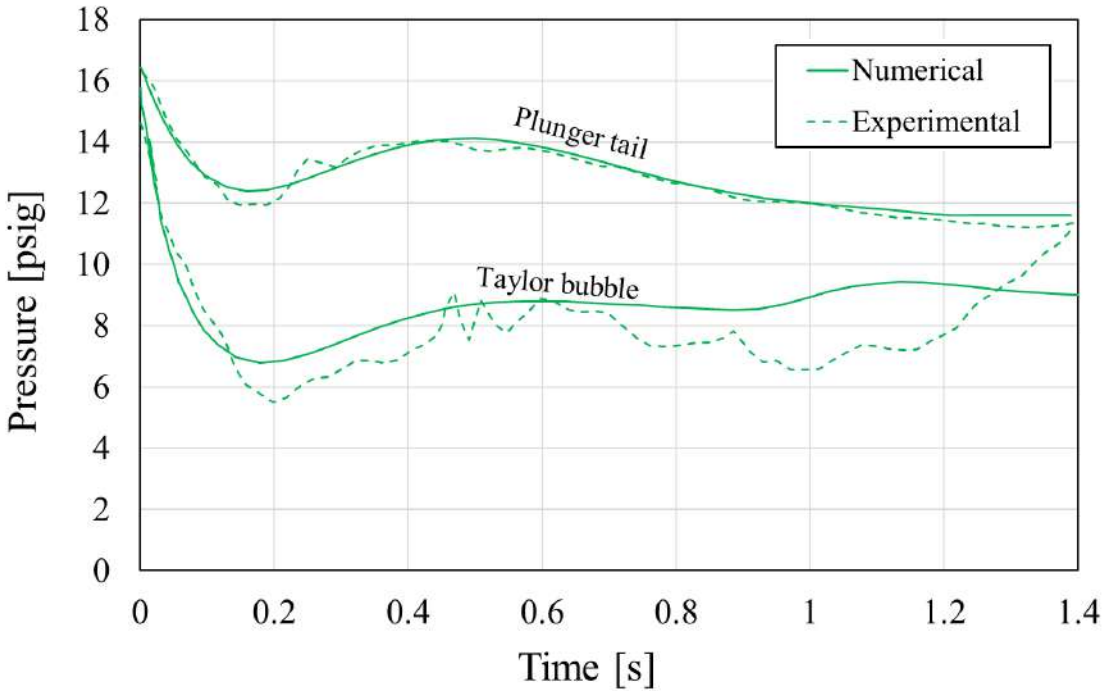

Figure 10.16: Pressure against time (16psig), logging plunger case, after pressure adjustment.

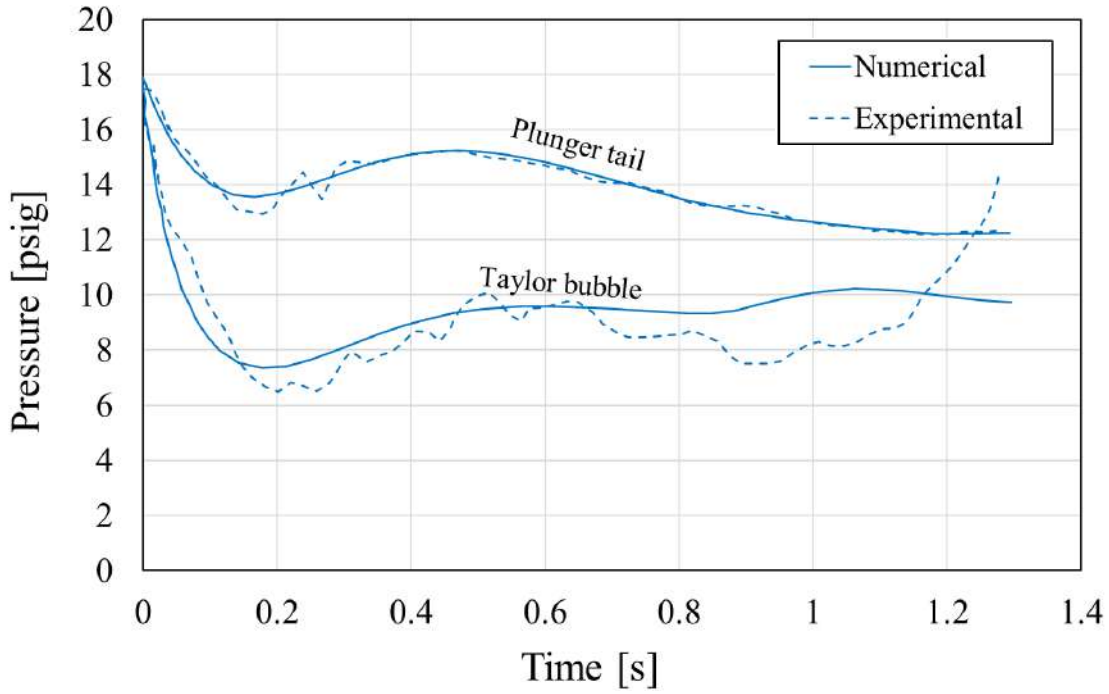

Figure 10.17: Pressure against time (18psig), logging plunger case, after pressure adjustment.

More plots are presented to further analyze the plunger model. The plunger acceleration, given in Fig. 10.18, shows that the experimental results are not as smooth as the numerical ones, however, a general trend is comparable between the results. Right after the plunger lives the static condition, the plunger acceleration increases very sharply. After that, the plunger acceleration starts decreasing until it reaches negative values, decelerating the plunger for a moment, and this can be verified in the velocity trends at the instant the velocity slope changes. Afterward, the plunger reaches low acceleration values in the simulation with the plunger moving at a near-constant speed, this moment is not seen in the experimental results that reflect a decrease and slight increase in velocity right at the end that is reflected in the acceleration results through the swings between positive and negative acceleration at the end. In the numerical results, there are two effects that can be seen in detail that are not reflected in the experimental data. First, is the sudden change in the slope of the acceleration, marking the point when the liquid slug hits the lubricator at the top of the facility, this happens due to de deflection of the liquid in the lubricator, which is numerically represented by switching the system of Eqs. (7.46) with the system given by Eq. (7.50) that has the additional term for the local pressure loss at the lubricator. With the decrease in the amount of weight of the liquid slug by the

change in direction of the liquid from vertical to horizontal flow, the plunger starts accelerating again for a moment.

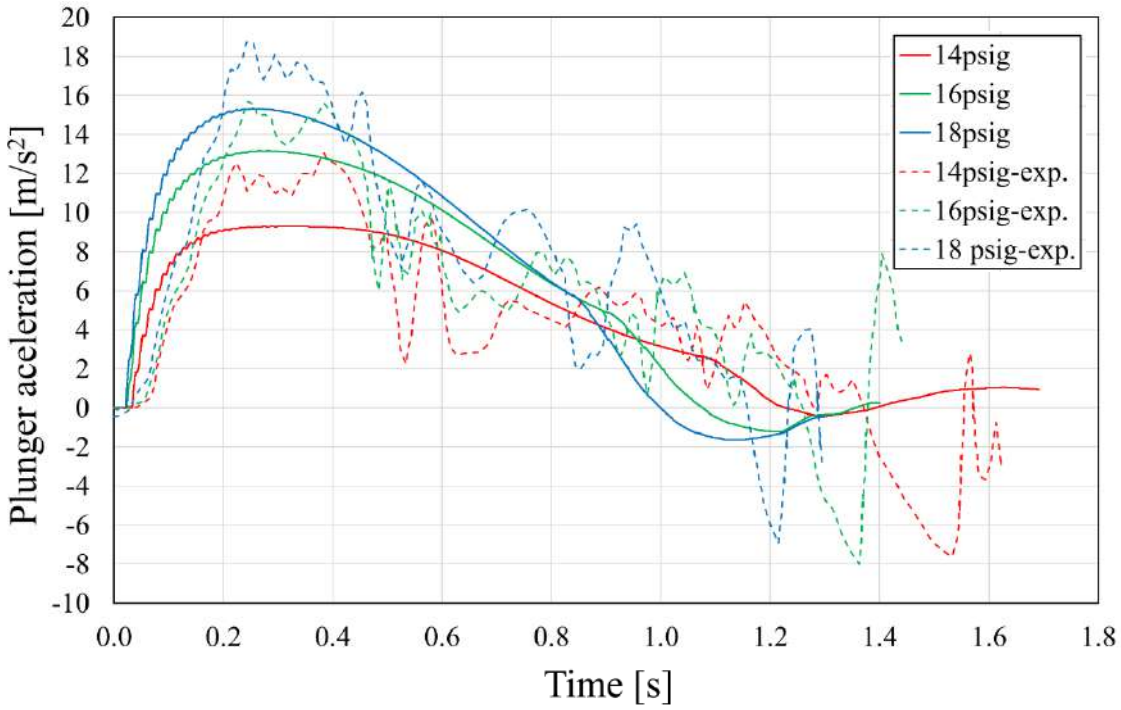

Figure 10.18: Plunger acceleration against time, logging plunger case, after pressure adjustment.

Another additional plot that is presented is the pressure difference across the plunger against time, given in Fig. 10.19. The behavior of the pressure difference across the plunger reflects the same behavior captured by the plunger acceleration, confirming that the dynamics of the plunger are mostly dominated by this pressure difference. The differences between the numerical and experimental results are like the ones seen in the acceleration, however, other remarks are shown in this plot. At the very end of the upstroke, the pressures at the plunger tail and front converge to the same value, which can be seen in Figs. 10.15, 10.16, and 10.17, hence the pressure differential across the plunger is zero for all initial casing pressures in the experiment. The simulation assumes constant pressure at the outlet of the tubbing, between the lubricator and the separator, and this is not reflected in reality, since this section is still composed of pipe sections and the separator pressure can be slightly affected by the inflow of the upstroke, justifying the differences between the numerical and experimental data in this stage.

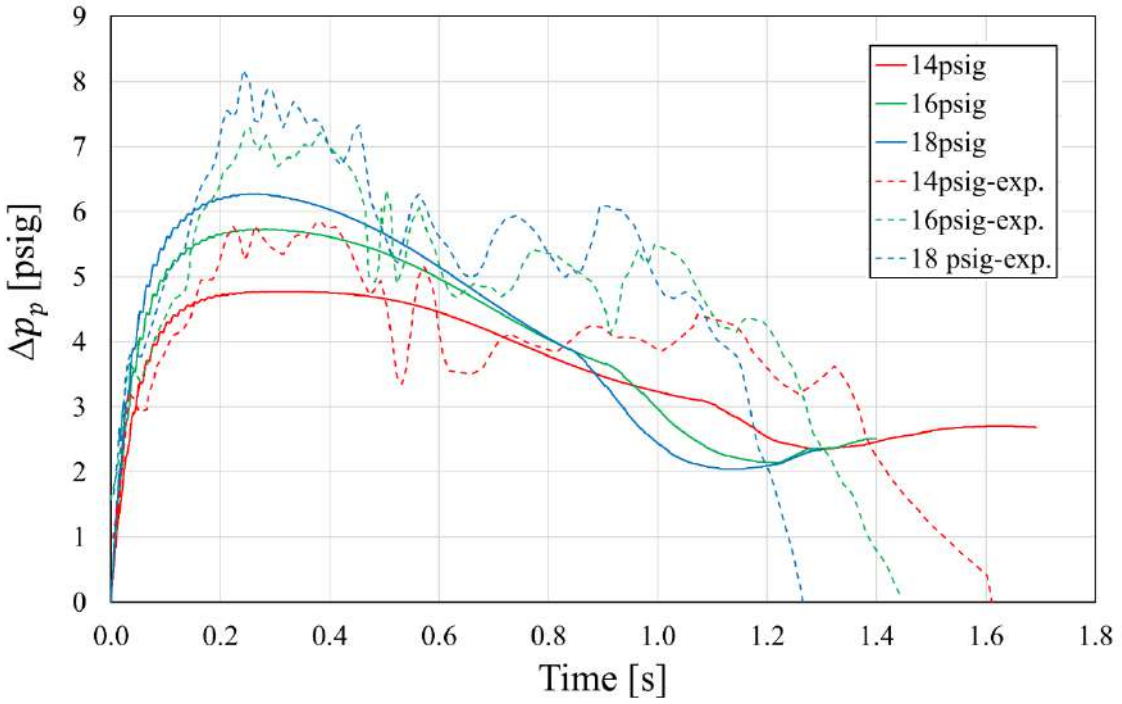

Figure 10.19: Pressure difference across the plunger against time, logging plunger case, after pressure adjustment.

To finalize, Akiiartdinov *et al*. (2020) also gathered data from the optical sensors. This data is in the local reference of the sensors present in the pipe and captures the dynamics of the slug front during the upstroke. A comparison between the obtained numerical results with their data is reported in Fig. 10.20. The results show two different behaviors between the experimental data and the numerical prediction, especially during the initial stages of the upstroke. In the simulation, the inflow of gas to the Taylor bubble occurs as soon as there is pressure discontinuity between the initial Taylor bubble pressure, that is the hydrostatic pressure of the liquid slug column and the plunger tail pressure. Therefore, the liquid slug is lifted immediately after the rarefaction wave hits the liquid slug top, as presented in Fig. 10.1. The experimental data reflects a different dynamic with the liquid slug front moving with velocities very close to the plunger velocity at the beginning stages and afterward the slug front moves faster, pointing to the onset of the Taylor bubble. The behavior of the experimental data can be justified by the hypothesis previously stated, that during the beginning of the upstroke, the plunger is completely surrounded by liquid, thus the plunger sealing with the pipe is more efficient. This hypothesis would reflect complexity in the model that is unjustified since in real case scenarios this stage only covers a small portion of the upstroke transient.

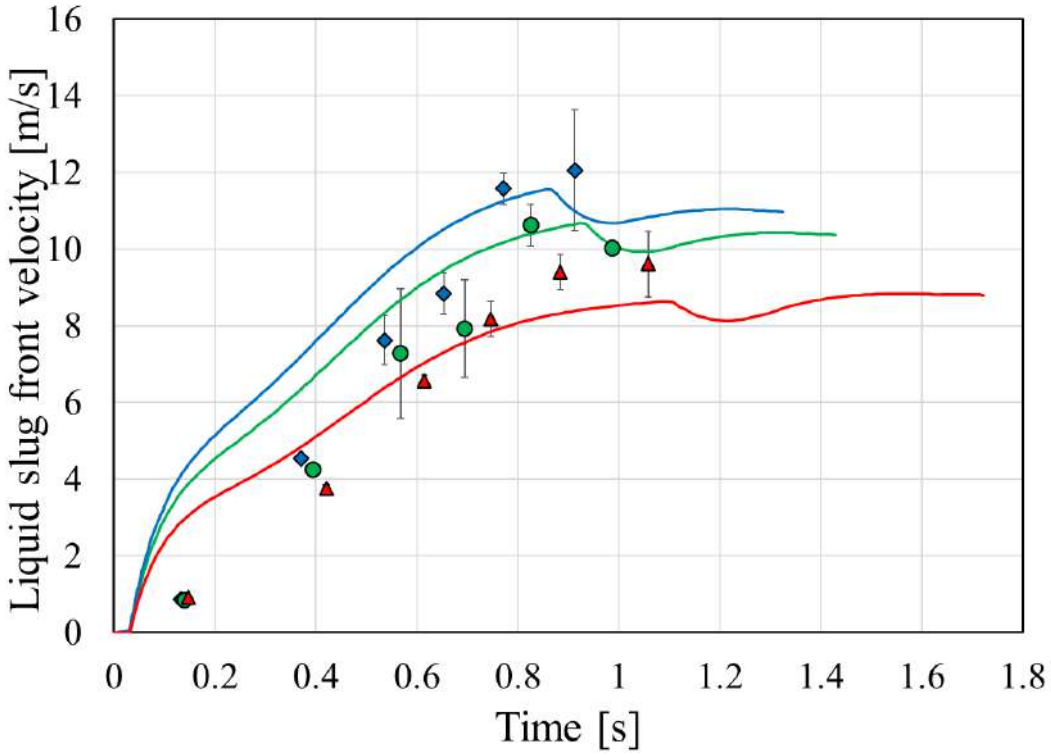

Figure 10.20: Liquid slug front velocity against time, logging plunger case, after pressure adjustment.

The model proposed here was then able to capture the main effects seen by the experimental data, showing promising results. However, further testing is required to completely validate it to use it in full-scale scenarios. Unfortunately, the facility used to gather the experimental data is limited to laboratory sizes, in the scale of meters, whereas real wells have a scale of a few kilometers.

11 Final Considerations

This chapter summarizes all the studies performed in the herein work with final comments, discussions, and analyses.

11.1 Conclusions

The first part of this work introduces the concept of solving transient fluid flow equations that are averaged into a one-dimensional approach for simulating single-phase flow in pipelines. The set of hyperbolic partial differential equations, the isothermal Euler equations for single-phase flow, are presented. A hyperbolicity analysis of the equations is performed to introduce the concept of this type of analysis and to obtain the entities that compose the eigenstructure of the model that is essential to many of the numerical methods used.

Extending from the concepts presented in the first part, a pair of one-dimensional transient two-fluid models aimed at solving two-phase flow in pipes is presented. The first one is a single pressure four equation model, 4E1P, and the second is the two pressure five equation model, 5E2P. The models are composed of a set of governing equations of continuity and momentum, in which each equation solves the conservation principles separately for each phase. The 5E2P model differs from the 4E1P by having an additional equation for the transport of the volume fraction, and by considering two different pressures, one for each phase, as well as treating the liquid phase as compressible. A hyperbolicity analysis is carried out for both models, concluding the conditional hyperbolicity of the 4E1P model, and the extra numerical difficulty this model presents by not having all eigenstructure entities analytically available. The analysis for the 5E2P model, on the order hand, provided simple analytical expression for the eigenvalues and their respective eigenvectors. An evaluation of these entities demonstrates that the model is hyperbolic under the applicable subcritical conditions that the model is proposed to physically represent the flow. The concept of relaxation procedures is introduced, and a pressure relaxation procedure is reported to make the 5E2P more physically representative and compatible with the 4E1P. To represent segregated two-phase flows with a well-defined smooth interface proper closures are also reported.

Since the models selected to perform the simulations in this work are composed of hyperbolic partial differential equations, a group of proper numerical schemes is selected.

The numerical schemes are based on an Eulerian finite volume framework, and the equations are solved explicitly requiring the *CFL* condition to be satisfied through all the time and space domains. The schemes chosen for solving the models are the FCT, ModFORCE, two AUSM type schemes, and a method based on the approximate Riemann solver of Roe. The combinations of a two-fluid model with a method, numerical models, are tested for different grid sizes with two benchmark problems. The first benchmark is the classical water faucet problem, and the evaluation of the obtained results concluded that all model-method combinations can represent the physics of the problem. However, some differences are reported, the 4E1P with the Roe scheme is exceptional in representing the void fraction and liquid velocity analytical curves if compared with any model-method combination. For the 5E2P model, all the methods behave more alike, with in this study the ModFORCE showing more accurate results. Another benchmark tested is the relatively large velocity problem, here the 4E1P with the Roe scheme was also remarkable in representing the reference solution even on the coarser grid used, besides that there is not much difference between the different model-method combinations, especially on finer grids. To conclude the evaluation of the numerical models, a study for a steady-state stratified flow case is performed and showed that all numerical models represent the expected physics with results comparable to the references of Figueredo *et al.* (2017) and the commercial software OLGA. Also, in this study, the evaluation of the behavior of relative errors with the grid refinement, the accuracy check, is performed for the 4E1P with the AUSM type methods, ModFORCE and Roe scheme, and the 5E2P with the ModFORCE and Roe scheme.

Lagrangian models for representing the passage of a piston through a pipe are presented in the sequence, with Newton's second law serving as an initial starting point for each model. The first two models focus on the pigging applications, with a model for pigging in single-phase flow and the extended version for two-phase flow. The pigging models presented can estimate the friction forces between the pig and the pipe wall, as well as the hydrodynamic friction. Also, the models consider the bypass effects through the gap between the pig and the pipe and through holes in the pig body. The bypass flows are incorporated in the modeling using the mass balance across the pig control volume.

For the plunger upstroke case, a model is proposed accounting for the separate movement between the plunger and the liquid slug it is carrying. The model is also based on Newton's second law, however separate momentum equations for the liquid slug and plunger are used. The control volume encompasses the liquid slug, plunger, and the

Taylor bubble that arise between them. The onset of the Taylor bubble happens with the gas slippage through the gap between the plunger and the pipe. Also, the loss of liquid falling through the gap is considered in the model. To lump all those effects, kinematic equations derived for the control volume, together with an equation for the pressure in the Taylor bubble, allow the control volume of the proposed model to increase in size due to the inflow of gas and decrease due to liquid loss. To estimate the gas and liquid mas flow rate through the gaps a closure model is proposed. The complete plunger model is a Lagrangian control volume that lumps all the effects predicted during an upstroke, different than the pig model the control volume can change in size with its mass exchange with the flow.

A scheme is proposed for coupling the piston models with the flow models. In this scheme the dimensions of the piston control volume are considered, dividing the domain into three sections, the piston control volume, the upstream flow, and the downstream flow. The sections share boundary conditions with each other, closing the global initial value boundary problem. The conditions of the flow during a given time at the piston boundaries are used as initial input conditions to the given piston model, and the outputs of the piston model then are used as boundary conditions for solving the flow at the upstream and downstream sections. In order to keep the numerical solution stable, a scheme for updating the upstream and downstream grids is proposed, by changing the position of the grid cells in a time step through the use of linear interpolation, without changing the slope of the flow field in the same time step.

To evaluate the scheme for coupling the models, first, a simple case for a pig with no bypass running in single-phase gas flow is tested. The result showed encouraging results representing the disturbance caused by the pig to the flow entailing in a pressure difference across the pig body. With this pressure difference, the dynamics of the piston are captured and analyzed, when the pig starts its motion there is a fast transient with a higher acceleration caused by the first jump in pressure, flowed by a second acceleration transient. After these two transients, the pig enters a quasi-steady state motion where it keeps accelerating with the gas.

The other studies for single-phase pigging are the ones based on the simulations of Patricio *et al* (2020). In these simulations only the bypass through the pig gaps with the pipe is considered at first, then the effects of a bypass through holes in the pigs are considered. The simulations are done for both gas and liquid flows, and the results obtained with the herein methodology compare well with the reference, obtaining similar

dynamics and bypass flow rates. Also, comparisons with the commercial software OLGA are performed with also good agreement. In conclusion, the numerical model for the pig motion in single-phase flow within a pipe simulates accurately this type of flow that occurs frequently in the oil and gas industry.

The next case studied was a two-phase pigging case, based on the case studied by Patricio (2016). Here the pig is launched in a two-phase stratified flow pipeline. The methodology was able to capture the effect of the growing pressure on the pig tail, as well as the dynamics of the pig. However, some of the effects reported by the numerical solution are not as expected, the methodology was unable to capture the expected sweep of the pig lowering the holdup at its tail. Some liquid accumulation at the front of the pig was predicted by some method-model combinations, however, most of it seems to come from numerical diffusion rather than the flow dynamics, since the most accurate numerical model, the 4E1P with the Roe scheme, only shows a sharp peak at the pig front. There were also some differences presented in the different schemes and methods used that should be considered for a future methodology. Some methods, especially the FCT method, seem to render too much diffusion to the solution, being unable to properly represent the necessary sharpness of a moving discontinuity caused by the pig-flow interaction. The numerical model analyzed in this work for a two-phase pigging flow is able to predict the main features of the flow, but still requires improvement in order to account more accurately for the liquid accumulation ahead of the pig, which, eventually, leads to the formation of a slug pattern in the pipe.

The first plunger simulations are based on the experimental campaign carried out at the University of Tulsa TUFFP/TUHWALP facilities. For that, a real plunger was used to simulate an upstroke with four different initial casing pressures. Experimental data was gathered from the high-speed proximity and pressure sensors spread out through the facility. The data obtained were processed, and the results capture some of the dynamics of the upstroke such as the position of the plunger with time, the velocity, and the local pressures in the facility. Numerical runs were performed to represent experimental ones, and the dynamics of the plunger were compared showing encouraging results. The pressure data also showed very good agreement. To further test the numerical methodology the experimental cases reported by Akhiiartdinov *et al.* (2020) were also reproduced numerically. Their experimental data set is extremely interesting for this case since they used a logging plunger with a build-in accelerometer and pressure sensors, that can capture almost continuously the dynamics of the plunger and the pressures at its front,

Taylor bubble, and tail. For the first runs, the model presented the right trends, but some discrepancy occurred that, overpredicted both velocities and pressures. After an adjustment to the bottom hole pressure, the results presented very good agreement. Through the optical sensor data, the liquid slug front velocity is also evaluated for this case, showing good agreement on the magnitudes at the end of the upstroke, although there are still some differences in the velocity trends at the begging of the upstroke. During the initial stages, there are some complex dynamics that the model fails to capture, however, this stage would be negligible in a real case scenario, not causing much of a concern. It is also important to mention that the facility dimensions, in terms of pipe length, are not representative of real wells found on the field, so to fully evaluate the applicability of the model, field data would be necessary. In summary, the unprecedent numerical plunger model proposed in this work presents excellent agreement with the two sets of experimental data used for comparison, especially if one considers that a one-dimensional model is used to predict a fully three-dimensional flow. Therefore, this model can be used by as a good estimate of the flow characteristics that occur in real-life engineering applications.

11.2 Recommendations for Future Work

As a first recommendation for future work, a comparison of two-fluid models against experimental results in stratified flow pattern is desirable. A first approach would be a numerical-experimental comparison between different steady-state configurations. Then extend the study to evaluate the capability of the numerical models in simulating transients. In this second approach, the flow conditions can go from one steady-state to another, for instance keeping one of the phases flow rate constant and varying the other one with a ramp-up or ramp-down function.

Similarly to the previous suggestion, an experimental campaign for pigging is desirable in both single and two-phase flow conditions. For that, a setup similar to the experimental plunger facility presented in the herein work can be designed, where the position of the pig and local pressure of the flow can be recorded. For the two-phase case, cameras may be mounted in the text section, and through image processing the transient changes in holdup may be estimated.

An extension of the two-phase pigging model with a control volume encompassing the liquid accumulated at the pig front would be interesting for comparison with the

current modeling work. Also, an extended region in the control volume behind the pig to try to consider the holdup decrease, as predicted by the OLGA model, would be interesting.

For the plunger model, an extension of the modeling work can be performed for the case of continuous flow plunger. In this new model, the fluids exchange at the front of the liquid slug should be considered.

Finally, in general, for all of the pig and plunger cases it would be of great contribution to have actual field data available to compare the models with real case scenarios.

References

Akhiiartdinov, A., 2020, “Experimental and theoretical study of conventional plunger lift in horizontal wells”, D.Sc. dissertation, The University of Tulsa, Tulsa, OK, USA.

Akhiiartdinov, A., Pereyra, E., Sarica, C., 2020, “Experimental and theoretical analysis of a pressure-driven logging piston during the liquid displacement process”, Experimental Thermal and Fluid Science, v. 115, pp.110090.

Andreussi, P., Persen, L.N., 1987, “Stratified gas-liquid flow in downwardly inclined pipes”, International Journal of Multiphase Flow, v. 13, n. 4, pp. 565-575.

Ansari, M., Daramizadeh, A.,2012, “Slug type hydrodynamic instability analysis using a five equations hyperbolic two-pressure, two-fluid model”, Ocean Engineering, v. 52, pp. 1–12.

Ansari, M., Shokri, V., 2011, “Numerical modeling of slug flow initiation in a horizontal channel using a two-fluid model”, International Journal of Heat and Fluid Flow, v. 32, pp. 145–155.

Ascher, U.M., Petzold, L.R., 1988, Computer Methods for Ordinary Differential Equations and Differential-Algebraic Equations, SIAM Classics Series.

Azevedo, L. F. A., Braga, A.M.B, Nieckele, A.O., Naccache, M. F, 1996, “Simple hydrodinamic models for the prediction of pig motions in pipelines”, Offshore Technology Conference, OTC 8232.

Baer, M.R. and Nunziato, J.W., 1986, “A two-phase mixture theory for the deflagration-to-detonation transition (DDT) in reactive granular materials”, Int. J. Multiphase flow, v.12, n. 6, pp. 861-889.

Bendiksen, K.M., Malnes, D., Moe, R., Nuland, S., 1991, “The dynamic two-fluid model OLGA: theory and application”, SPE production engineering, pp. 171-180.

Bestion, D., 1990, “The physical closure laws in the CATHARE code”, Nuclear Engineering and Design, v.124, pp. 229–245.

Boris, J., Book, D. L., 1973, “Flux correct transport I - SHASTA - A fluid transport algorithm that works”, Journal of Computational Physics, v. 11, pp. 38–69.

Book, D.L., Boris. J.P., Hain, K., 1975, “Flux-Corrected Transport II. Generalizations of the Method”, Journal of Computational Physics, v. 18, pp. 248–283.

Boris, J., Book, D. L., 1976, “Solution of continuity equation by the method of Flux-Corrected Transport”, Journal of Computational Physics, v. 16, pp. 85–129.

Bueno, D., 2013, “Modelagem numérica do escoamento bifásico em gasodutos com padrão estratificado”. In portuguese, M.Sc. Dissertation, COPPE/UFRJ, Rio de Janeiro, RJ, Brazil.

Bueno, D.E.G.P., Figueiredo, A.B., Baptista, R.M., Rachid, F.B.F., Bodstein, G.C.R., 2012, “Numerical simulation of stratified two-phase flow in a nearly horizontal gas-liquid pipeline with a leak”. In: Proceedings of the 10th International Pipeline Conference, IPC, Calgary, Alberta, Canada.

Campo, E. V., 1998, “Modelagem do movimento de PIGS em regime transiente”, In portuguese, M.Sc. Dissertation, PGMEC/UFF, Niterói, RJ, Brasil.

Chen, J., He S.H., L., Luo, X., Zhang, H., Li, X., Liu, H., He, S., Lu, L., 2020, “Characterization of bypass pig velocity in gas pipeline: An experimental and analytical study”, Journal of Natural Gas Science and Engineering, v. 73, pp. 103059.

Chen, S., Zhang, Y., Wang, X., Teng, K., Gong, Y., Qu, Y., 2022, “Numerical simulation and experiment of the gas-liquid two-phase flow in the pigging process based on bypass state”, Ocean Engineering, v. 252, pp. 111184.

Coquel, F., El Amine, K., Godlewski, E., Perthame, B., Rascle, P., 1997, “A numerical method using upwind schemes for the resolution of two-phase flows”, Journal of Computational Physics, v. 136, pp. 272-288.

Cortez, J., Debussche, A. and Toumi, I., 1998, “A density perturbation method to study the eigenstructure of two-phase flow equation systems”, Journal of Computational Physics, v. 147, no.2, pp 463-383.

Dieck, R.H., 2007, Measurement Uncertainty: Methods and Applications. ISA.

Drew, D.A. and Passman, S.L., 1999, Theory of Multicomponent Fluids. Springer.

Esmaeilzadeh, F., Mowla, D., Asemani, M., Shiraz U., 2006, “Modeling of PIG operations in natural gas and liquid pipeline”, SPE International, SPE 102049.

Esmaeilzadeh, F., Mowla, D., Asemani, M., 2009, “Mathematical Modeling and Simulation of PIGging Operation in Gas and Liquid Pipelines”, Journal of Petroleum Science and Engineering v.69, pp. 100-106.

Essama, C., 2004, “Numerical modelling of transient gas-liquid flows (Application to Stratified & Slug Flow Regimes)”, D.Sc. thesis, School of Engineering Applied Mathematics and Computing Group, Cranfield University, Bedford, United Kingdom.

Evje, S., Flätten, T., 2003, “Hybrid flux-splitting schemes for a common two-fluid model”, Journal of Computational Physics, v.192, pp. 175–210.

Ferrari, M., Bonzanini, A., Poesio, P., 2017, “A 5-equation, transient, hyperbolic, 1-dimensional model for slug capturing in pipes”, International Journal of Numerical Methods in Fluids, v. 85, pp. 327–362.

Figueiredo, A.B., 2010, “Validação teórica de uma modelagem para escoamentos bifásicos em gasodutos com duas equações de conservação para cada fase”. In portuguese, M.Sc. Dissertation, COPPE/UFRJ, Rio de Janeiro, RJ, Brazil.

Figueiredo, A.B., Bueno, D.E.G.P., Baptista, R.M., Rachid, F.B.F., Bodstein, G.C.R., 2012, “Accuracy sudy of the Flux-Corrected Transport numerical method applied to transient two-Phase flow simulations in gas pipelines”, In: Proceedings of the 9th International Pipeline Conference, IPC, Calgary, Alberta, Canada.

Figueiredo, A.B., Baptista, R.M., Rachid, F.B.F. and Bodstein, G.C.R., 2017, “Numerical simulation of stratified-pattern two-phase flow in gas pipelines using a two-fluid model”, International Journal of Multiphase Flow, v. 88, pp. 30 – 49.

Fletcher, C., 1988, Computational Techniques for Fluid Dynamics: Specific techniques for Flow Categories, v. 2. New York, Springer-Verlag.

Foss, D.L., Gaul, R.B., 1965. “Plunger-life performance criteria with operating Experience-Ventura Avenue field”, Presented at the Drilling and Production Practice, American Petroleum Institute.

Freitas, R.V.N., 2017, “Estudo de modelos de dois fluidos acoplados ao método FCT em escoamentos bifásicos”, In Portuguese, M.Sc. Dissertation, COPPE/UFRJ, Rio de Janeiro, Brazil.

Furfaro, D., Saurel, R., 2015, “A simple HLLC-type Riemann solver for compressible non-equilibrium two-phase flows”, Computer & Fluids, v. 111, pp. 159–178.

Gasbarri, S., Wiggins, M.L., 2001, “A Dynamic plunger lift model for gas wells”, SPE Prod. Facil., v.16, pp. 89–96.

Gomes, M. G. F. M., 1994, “The analysis cup pigs by the finite element method”, in Portuguese, M.Sc. Dissertation, UFRJ, Rio de Janeiro, Brazil.

Gomes, M. G. F. M., Pereira, F., Lino, A. C., 1995, Manual of Pig Utilization, Internal report, in Portuguese, Research and Development Center (CENPES), Petrobras, Rio de Janeiro, Brazil.

Hernandez, A., Maracano, L., Caicedo, S., Cabunaru, R., 1993, “Liquid fall-back measurements in intermittent gas lift with plunger”, Presented at the SPE Annual Technical Conference and Exhibition, Society of Petroleum Engineers.

Hirsch, C., 1990, Numerical Computation of Internal and External Flows: Fundamentals of numerical discretization, v. 2., John Wiley & Sons.

Hosseinalipour, S. M., Khalili, A. Z., Salimi, A., 2007 (a), “Numerical simulation of PIG motion through gas pipelines”, 16th Australasian Fluid Mechanics Conference.

Hosseinalipour, S. M., Khalili, A. Z., Salimi, A., 2007 (b), “Transient flow and PIGging operation in gas-liquid two phase pipelines”, 16th Australasian Fluid Mechanics Conference, pp. 976-979.

Hu, J., Tao, T., 2022, “Numerical investigation of ice pigging isothermal flow in water-supply pipelines cleaning”, Chemical Engineering Research and Design, v. 182, pp 428-437.

Hull, T. E., Enright, W. H., Jackson, K. R, 1976, User's guide for DVERK - A subroutine for solving non-stiff ODEs, Department of Computer Science Technical Report 100, University of Toronto.

Ishii M., 1975, Thermo-Fluid Dynamic Theory of Two-Phase Flow, Eyrolles, Paris.

Ishii, M., Hibiki, T., 2003, “One-dimensional drift-flux model and constitutive equations for relative motion between phases in various two-phase flow regimes”, International Journal of Heat and Mass Transfer, v. 46, pp. 4935-4948.

Ishii, M., Hibiki, T., 2006, Thermo-Fluid Dynamics of Two-Phase Flow, 1st ed. New York, Springer Science.

Ishii, M., Mishima, K., “Two-fluid model and hydrodynamic constitutive relations”, Nuclear Engineering and Design, v. 82, pp. 107–126, 1984.

Issa, R., Kempf, M., 2003, “Simulation of slug flow in horizontal and nearly horizontal pipes with the two-fluid model”, International Journal of Multiphase Flow, v. 29, pp. 69-95.

Jamshidi, B., Sarkari, M., 2016, “Simulation of pigging dynamics in gas-liquid two-phase flow pipelines”, Journal of Natural Gas Science and Engineering, v. 32, pp. 407-414.

Jeffrey, A., 1976, Quasilinear Hyperbolic Systems and Waves, London, Pitman Publishing.

Kitamura, K., Liou, M.-S., 2012, “Comparative study of AUSM-family schemes in compressible multiphase flow simulations”, Seventh International Conference on Computational Fluid Dynamics, Big Island, Hawaii.

Lea, J.F., 1982, “Dynamic analysis of plunger lift operations”, J. Pet. Technol. 34, v.11, pp. 2617-2629.

LeVeque, R., 2004, Finite-volume methods for hyperbolic problems, Cambridge University Press, U.K.

Lezeau, P., Thompson, C. P., 1998, “Numerical simulation of multi-phase flow: speed, error control & robustness”, Cranfield University Technical Report.

Li, X., He, L., Luo, X., Liu, H., He, S., Li, Q., 2021, “Numerical simulation and experimental study of bypass pigging slippage”, Ocean Engineering, v. 230, pp. 109023.

Lima, P. C. R., Yeung, H., 1999, “Modeling of PIGging operations”, SPE International, SPE 56586.

Liou, M-S., Steffen, C. J., 1993, “A new flux splitting scheme”, Journal of Computational Physics, v.107, pp. 23-39.

Marcano, L., Chacin, J., 1994, “Mechanistic design of conventional plunger lift installations”, SPE Adv. Technol. Ser. 2, v.1, pp. 15–24.

Minami, K., Shoham, O., 1995, “PIGging dynamics in two-phase flow pipelines: Experiment and Modeling”, SPE International.

Mirshamsi, M., Rafeeyan, M., 2015, “Dynamic analysis and simulation of long pig in gas pipeline”, Journal of Natural Gas Science and Engineering, v.23, pp. 294-303.

Moody, L.F., 1947, “An approximate formula for pipe friction factors”, Transactions of ASME, v. 69, pp.1005.

Mower, L.N., Lea, J.F., Beauregard, E., Ferguson, P.L., 1985, “Defining the characteristics and performance of gas-lift plungers”, Presented at the SPE Annual Technical Conference and Exhibition, Society of Petroleum Engineers.

Munkejord, S., 2005, “Analysis of the two-fluid model and the drift-flux model for numerical calculation of two-phase flow”, Ph.D. Thesis, NTNU Norwegian University of Science and Technology, Trondheim, Norway.

Munkejord, S.T., 2006, “Partially-reflecting boundary conditions for transient two-phase flow”, Communications in Numerical Methods in Engineering, v. 22 pp. 781-795.

Munkejord, S.T., 2007, “Comparison of Roe-type methods for solving the two-fluid model with and without pressure relaxation”, Computer & Fluids, v. 36, pp. 1061-1080.

Munkejord, S.T., 2010, “A numerical study of two-fluid models with pressure and velocity relaxation”, Advances in Applied Mathematics and Mechanics, v. 2, pp. 131-159.

Munkejord, S.T., Evje, S., Flatten, T., 2009, “A MUSTA scheme for a non-conservative two-fluid model”, SIAM Journal on Scientific Computing, v. 31, pp. 2587-2622.

Nguyen, T. T., Kim, S. B., Yoo, H. R., Rho, Y. W., 2001(a), “Modeling and simulation for PIG flow control in Natural Gas Pipeline”, KSME International Journal, v. 15, No. 8, pp. 1165-1173.

Nguyen, T. T., Kim, S. B., Yoo, H. R., Rho, Y. W., 2001(b), “Modeling and simulation for PIG with bypass flow control in Natural Gas Pipeline”, KSME International Journal, v. 15, No. 9, pp. 1302-1310.

Nieckele, A.O., Braga, A.M.B, Azevedo, L. F. A., 2001, “Transient PIG motion through gas and liquid pipelines”, Journal of Energy Resources Technology, DOI: 10.1115/1.1413466.

Pan, D., 2017. “Investigation of plunger rise velocity and liquid fallback in plunger lift of vertical gas wells”, M.Sc. Thesis, The University of Tulsa, Tulsa, OK.

Patricio, R.A.C., 2016, “Simulação de escoamento bifásico em gasodutos na presença de um pig utilizando o método numérico FCT”. In portuguese, M.Sc. Dissertation, COPPE/UFRJ, Rio de Janeiro, RJ, Brazil.

Patricio, R.A., Sondermann, C.N., Figueiredo, A.B., Baptista, R.M., Rachid, F.B.F., Bodstein, G.C.R., 2016 (a), “Numerical simulation of pig motion in gas-flow pipelines using the Flux-Corrected Transport method”, 16th Brazilian Congress of Thermal Science and Engineering (ENCIT), Vitória, ES, Brazil.

Patricio, R.A., Sondermann, C.N., Figueiredo, A.B., Baptista, R.M., Rachid, F.B.F., Bodstein, G.C.R., 2016 (b), In Portuguese: “Simulação numérica de escoamento monofásico de líquido em dutos na presença de pig utilizando o método Flux-Corrected Transport”, Congresso Nacional de Engenharia Mecânica (CONEM), Fortaleza, Ceará, Brazil.

Patricio, R.A.C., Sondermann, C.N., Figueiredo, A.B., Viggiano, R., Bodstein, G.C.R., Rachid, F.B.F., Baptista, R.M., 2018, “Numerical simulation of pig motion in two-phase flow pipelines in the presence of a leak”, Proceedings of the 12th International Pipeline Conference, v. 3, Alberta, Canada. ,doi: 10.1115/IPC2018-78093.

Patricio, R.A., Baptista, R.M., Rachid, F.B.F., Bodstein, G.C.R., 2020, “Numerical simulation of pig motion in gas and liquid pipelines using the Flux-Corrected Transport method”, Journal of Petroleum Science and Engineering, v. 189, pp. 106970.

Petzold, L.R., 1982, “A Description of DASSL: A differential-algebraic system solver”, In Proceedings of the IMACS World Congress, Montreal, Canada.

Ramshaw, J. D., Trapp, J. A., 1978, “A numerical technique for low-speed homogeneous two-phase flow with sharp interfaces”, Journal of Computational Physics, v.21, pp. 48-453.

Ransom, V.H., 1987, “Numerical benchmark test no. 2.1: faucet flow”, Multiphase Science and Technology, v. 3, pp. 465-467.

Ransom, V. H., Hicks, D. L., 1984, “Hyperbolic two-pressure models for two-phase flow”, Journal of Computational Physics, v. 53, pp. 124-151.

Roe, P. L., 1981, “Approximate Riemann solvers, parameter vectors, and difference schemes”, Journal of Computational Physics, v. 43, pp. 357-372.

Romenski, E., Drikakis, D., Toro, E., 2010, “Conservative models and numerical methods for compressible two-phase flow”, J. Sci. Comput., v. 42, pp. 68–95.

Rosina, L., 1983, “A Study of Plunger Lift Dynamics”, M.Sc. Thesis, The University of Tulsa, Tulsa, OK.

Santim, C.G.S., Rosa, E.S., 2015, “Roe-type Riemann solver for gas–liquid flows using drift-flux model with an approximate form of the Jacobian matrix”, International Journal for Numerical Methods in Fluids, v. 80, pp. 536–568.

Saurel, R., Abgrall, R., 1999, “A multiphase Godunov method for compressible multifluid and multiphase flows”, Journal of Computational Physics, v. 150, pp. 425–467.

Shoham, O., 2006, Mechanistic Modeling of Gas-Liquid Two-Phase Flow in Pipes, Society of Petroleum Engineers.

Sondermann, C.N., 2016, “Simulação de escoamento bifásico em gasodutos com uma equação da energia para a mistura utilizando o método numérico FCT”, In portuguese, M.Sc. Dissertation, Universidade Federal do Rio de Janeiro, Rio de Janeiro, Brazil.

Sondermann,C.N., 2021, “Numerical prediction of intermittent two-phase flow in horizontal and inclined pipelines and comparison with experiments”, D.Sc. Thesis, Universidade Federal do Rio de Janeiro, Rio de Janeiro, Brazil

Sondermann, C.N., Baptista, R.M., Rachid, F.B.F. and Bodstein, G.C.R., 2019, “Numerical simulation of non-isothermal two-phase flow in pipelines using a two-fluid model”, Journal of Petroleum Science and Engineering, v. 173, pp. 298-314.

Sondermann, C.N., Viggiano, R., Rachid, F.B.F. and Bodstein, G.C.R., 2021, “A suitability analysis of transient one-dimensional two-fluid numerical models for simulating two-phase gas-liquid flows based on benchmark problems”, Computer & Fluids, v. 229, pp. 105070.

Stewart, H., Wendroff, B., 1984, “Two-phase flow: models and methods”, Journal of Computational Physics, v. 56, pp. 363-409.

Sylvester, N.D., 1987, “A mechanistic model for two-phase vertical slug flow in pipes”, J. Energy Resour. Technol., v.109, pp. 206–213.

Taitel, Y., Dukler, A. E.,1976, “A model for predicting flow regime transitions in horizontal and near-horizontal gas-liquid flow”. AIChE Journal, v. 22, n. 1, pp. 47-55, January.

Tolmasquin, S. T., Nieckele, A. O., 2008, “Design and control of PIG operations through pipelines, Journal of Petroleum Science and Engineering”, v. 62, pp. 102-110.

Toro, E. F., 1999, Riemann Solvers and Numerical Methods for Fluid Dynamics. Springer.

Toro, E., Titarev, V., 2006, “Musta fluxes for systems of conservative laws”, Journal of Computational Physics, v. 216, pp. 403–429.

Wada, Y., Liou, M-S., 1997, “An accurate and robust flux splitting scheme for shock and contact discontinuities”, Society for Industrial and Applies Mathematics, v. 18, n. 3, pp. 633-657.

van Leer, B., 1974, “Towards the ultimate conservative difference scheme II. Monotonicity and conservation combined in a second-order scheme”, Journal of Computational Physics, v. 14, pp. 361-370.

Van Leer, B., 1977, “Towards the ultimate conservation difference scheme IV, new approach to numerical convection”, J. Computational Physics, v. 23, pp. 276-299, 1977.

Xiao-Xuan Xu, Gong, J., 2005, “Pigging simulation for horizontal gas-condensate pipelines with low-liquid loading”, Journal of Petroleum Science and Engineering, v. 48, pp. 272-280.

Xiao, J. J., Shoham, O., 1991, “Evaluation of Interfacial Friction Factor Prediction Methods for Gas/Liquid Stratified Flow”, SPE 22765 66th Annual Technical Conference and Exhibition, Dallas, Texas, U.S.A.

Zalesak, S. T., 1979, “Fully multidimensional Flux-Corrected Transport algorithms for fluids”, Journal of Computational Physics, v. 31, pp. 335–362.

Zhao, K., Bai, B., 2018, “Transient liquid leakage during plunger lifting process in gas wells”, J. Nat. Gas Sci. Eng., v.59, pp. 250–261.

Zou, L., Zahao, H., Zhang, H., 2016, “New analytical solutions to the two-phase water faucet problem”, Progress in Nuclear Energy, v. 91, pp. 389-398.

Appendix A – Matrices for AUSM-type Methods

According to Evje and Flätten (2003), the inter-cell flux is calculated as a contribution of a convective flux and a pressure flux, such as

$$\mathbf{f}^{\mathrm{AUSM}}_{\mathrm{i}+\frac{1}{2}} = \mathbf{f}^{c}_{\mathrm{i}+\frac{1}{2}} + \mathbf{f}^{p}_{\mathrm{i}+\frac{1}{2}}. \tag{A.1}$$

These terms can be written for the 4E1P as,

$$\mathbf{f}^{c} = \begin{bmatrix} \rho_G \alpha_G u_G \\ \rho_L \alpha_L u_L \\ \rho_G \alpha_G u_G^2 \\ \rho_L \alpha_L u_L^2 \end{bmatrix}, \mathbf{f}^{p} = \begin{bmatrix} 0 \\ 0 \\ \alpha_G \Delta p_{IG} \\ \alpha_L \Delta p_{IL} \end{bmatrix}, \tag{A.2}$$

and for the 5E2P, as

$$\mathbf{f}^{c} = \begin{bmatrix} 0 \\ \rho_G \alpha_G u_G \\ \rho_L \alpha_L u_L \\ \rho_G \alpha_G u_G^2 \\ \rho_L \alpha_L u_L^2 \end{bmatrix}, \mathbf{f}^{p} = \begin{bmatrix} 0 \\ 0 \\ 0 \\ \alpha_G \Delta p_{IG} \\ \alpha_L \Delta p_{IL} \end{bmatrix}. \tag{A.3}$$

A.1-AUSMV Fluxes

The inter-cell flux for the AUSMV method is calculated as

- For the 4E1P model

$$\mathbf{f}^{c}_{\mathrm{i}+\frac{1}{2}} = \begin{bmatrix} \mathbf{Q}_{1,i}\tilde{V}^{+}\left((u_G)_i, c_{i+\frac{1}{2}}, \chi_G^L\right) + \mathbf{Q}_{1,i+1}\tilde{V}^{-}\left((u_G)_{i+1}, c_{i+\frac{1}{2}}, \chi_G^R\right) \\ \mathbf{Q}_{2,i}\tilde{V}^{+}\left((u_L)_i, c_{i+\frac{1}{2}}, \chi_L^L\right) + \mathbf{Q}_{2,i+1}\tilde{V}^{-}\left((u_L)_{i+1}, c_{i+\frac{1}{2}}, \chi_L^R\right) \\ \mathbf{Q}_{3,i}\tilde{V}^{+}\left((u_G)_i, c_{i+\frac{1}{2}}, \chi_G^L\right) + \mathbf{Q}_{3,i+1}\tilde{V}^{-}\left((u_G)_{i+1}, c_{i+\frac{1}{2}}, \chi_G^R\right) \\ \mathbf{Q}_{4,i}\tilde{V}^{+}\left((u_L)_i, c_{i+\frac{1}{2}}, \chi_L^L\right) + \mathbf{Q}_{4,i+1}\tilde{V}^{-}\left((u_L)_{i+1}, c_{i+\frac{1}{2}}, \chi_L^R\right) \end{bmatrix} \tag{A.4}$$

$$\mathbf{f}^{p}_{\mathrm{i}+\frac{1}{2}} = \begin{bmatrix} 0 \\ 0 \\ P^{+}\left(u_G, c_{i+1/2}\right)(\alpha_G \Delta p_{IG})_i + P^{-}\left(u_G, c_{i+1/2}\right)(\alpha_G \Delta p_{IG})_{i+1} \\ P^{+}\left(u_L, c_{i+1/2}\right)(\alpha_L \Delta p_{IL})_i + P^{-}\left(u_L, c_{i+1/2}\right)(\alpha_L \Delta p_{IL})_{i+1} \end{bmatrix}. \tag{A.5}$$

- For the 5E2P model

$$\mathbf{f}^{c}_{\mathrm{i}+\frac{1}{2}} = \begin{bmatrix} 0 \\ \mathbf{Q}_{2,i}\tilde{V}^{+}\left((u_G)_i, c_{i+\frac{1}{2}}, \chi^{L}_{G}\right) + \mathbf{Q}_{2,i+1}\tilde{V}^{-}\left((u_G)_{i+1}, c_{i+\frac{1}{2}}, \chi^{R}_{G}\right) \\ \mathbf{Q}_{3,i}\tilde{V}^{+}\left((u_L)_i, c_{i+\frac{1}{2}}, \chi^{L}_{L}\right) + \mathbf{Q}_{3,i+1}\tilde{V}^{-}\left((u_L)_{i+1}, c_{i+\frac{1}{2}}, \chi^{R}_{L}\right) \\ \mathbf{Q}_{4,i}\tilde{V}^{+}\left((u_G)_i, c_{i+\frac{1}{2}}, \chi^{L}_{G}\right) + \mathbf{Q}_{4,i+1}\tilde{V}^{-}\left((u_G)_{i+1}, c_{i+\frac{1}{2}}, \chi^{R}_{G}\right) \\ \mathbf{Q}_{5,i}\tilde{V}^{+}\left((u_L)_i, c_{i+\frac{1}{2}}, \chi^{L}_{L}\right) + \mathbf{Q}_{5,i+1}\tilde{V}^{-}\left((u_L)_{i+1}, c_{i+\frac{1}{2}}, \chi^{R}_{L}\right) \end{bmatrix}. \tag{A.6}$$

$$\mathbf{f}^{p}_{\mathrm{i}+\frac{1}{2}} = \begin{bmatrix} 0 \\ 0 \\ 0 \\ P^{+}\left(u_G, c_{i+1/2}\right)(\alpha_G \Delta p_{IG})_i + P^{-}\left(u_G, c_{i+1/2}\right)(\alpha_G \Delta p_{IG})_{i+1} \\ P^{+}\left(u_L, c_{i+1/2}\right)(\alpha_L \Delta p_{IL})_i + P^{-}\left(u_L, c_{i+1/2}\right)(\alpha_L \Delta p_{IL})_{i+1} \end{bmatrix}. \tag{A.7}$$

A.2-AUSMD Fluxes

Similarly, for the AUSMD method:

- 4E1P model

$$\mathbf{f}^{c}_{\mathrm{i}+\frac{1}{2}} = \begin{bmatrix} \mathbf{Q}_{1,i}\tilde{V}^{+}\left((u_G)_i, c_{i+\frac{1}{2}}, \chi^{L}_{G}\right) + \mathbf{Q}_{1,i+1}\tilde{V}^{-}\left((u_G)_{i+1}, c_{i+\frac{1}{2}}, \chi^{R}_{G}\right) \\ \mathbf{Q}_{2,i}\tilde{V}^{+}\left((u_L)_i, c_{i+\frac{1}{2}}, \chi^{L}_{L}\right) + \mathbf{Q}_{2,i+1}\tilde{V}^{-}\left((u_L)_{i+1}, c_{i+\frac{1}{2}}, \chi^{R}_{L}\right) \\ 0.5\left\{\left(\mathbf{f}^{c}_{\mathrm{i}+1/2}\right)_1[(u_G)_i + (u_G)_{i+1}] - \left|\left(\mathbf{f}^{c}_{\mathrm{i}+1/2}\right)_1\right|[(u_G)_{i+1} - (u_G)_i]\right\} \\ 0.5\left\{\left(\mathbf{f}^{c}_{\mathrm{i}+1/2}\right)_2[(u_L)_i + (u_L)_{i+1}] - \left|\left(\mathbf{f}^{c}_{\mathrm{i}+1/2}\right)_2\right|[(u_L)_{i+1} - (u_L)_i]\right\} \end{bmatrix}. \tag{A.8}$$

$$\mathbf{f}^{p}_{\mathrm{i}+\frac{1}{2}} = \begin{bmatrix} 0 \\ 0 \\ P^{+}\left(u_G, c_{i+1/2}\right)(\alpha_G \Delta p_{IG})_i + P^{-}\left(u_G, c_{i+1/2}\right)(\alpha_G \Delta p_{IG})_{i+1} \\ P^{+}\left(u_L, c_{i+1/2}\right)(\alpha_L \Delta p_{IL})_i + P^{-}\left(u_L, c_{i+1/2}\right)(\alpha_L \Delta p_{IL})_{i+1} \end{bmatrix}. \tag{A.9}$$

- 5E2P model

$$\mathbf{f}^{c}_{\mathrm{i}+\frac{1}{2}} = \begin{bmatrix} 0 \\ \mathbf{Q}_{2,i}\tilde{V}^{+}\left((u_G)_i, c_{i+\frac{1}{2}}, \chi_G^L\right) + \mathbf{Q}_{2,i+1}\tilde{V}^{-}\left((u_G)_{i+1}, c_{i+\frac{1}{2}}, \chi_G^R\right) \\ \mathbf{Q}_{3,i}\tilde{V}^{+}\left((u_L)_i, c_{i+\frac{1}{2}}, \chi_L^L\right) + \mathbf{Q}_{3,i+1}\tilde{V}^{-}\left((u_L)_{i+1}, c_{i+\frac{1}{2}}, \chi_L^R\right) \\ 0.5\left\{\left(\mathbf{f}^{c}_{\mathrm{i}+1/2}\right)_2[(u_G)_i + (u_G)_{i+1}] - \left|\left(\mathbf{f}^{c}_{\mathrm{i}+1/2}\right)_2\right|[(u_G)_{i+1} - (u_G)_i]\right\} \\ 0.5\left\{\left(\mathbf{f}^{c}_{\mathrm{i}+1/2}\right)_3[(u_L)_i + (u_L)_{i+1}] - \left|\left(\mathbf{f}^{c}_{\mathrm{i}+1/2}\right)_3\right|[(u_L)_{i+1} - (u_L)_i]\right\} \end{bmatrix}. \quad \text{(A.10)}$$

$$\mathbf{f}^{p}_{\mathrm{i}+\frac{1}{2}} = \begin{bmatrix} 0 \\ 0 \\ 0 \\ P^{+}\left(u_G, c_{i+1/2}\right)(\alpha_G \Delta p_{IG})_i + P^{-}\left(u_G, c_{i+1/2}\right)(\alpha_G \Delta p_{IG})_{i+1} \\ P^{+}\left(u_L, c_{i+1/2}\right)(\alpha_L \Delta p_{IL})_i + P^{-}\left(u_L, c_{i+1/2}\right)(\alpha_L \Delta p_{IL})_{i+1} \end{bmatrix}. \quad \text{(A.11)}$$

Appendix B –Averaged States for Roe Linearization

B.1-Single-phase model

A definition of the Roe averaged velocity can be found in Toro (1999) for a one-dimensional single-phase isothermal model, given by,

$$\hat{u} \equiv \frac{u_i\sqrt{\rho_i} + u_{i+1}\sqrt{\rho_{i+1}}}{\sqrt{\rho_i} + \sqrt{\rho_{i+1}}}, \tag{B.1}$$

B.2-Two-Fluid models

Evje and Flaten (2003), and Munkejord (2005) define an average state for the two-fluid models where the previously stated conditions are satisfied. The primitive variables are averaged as follows,

$$\hat{u}_k \equiv \frac{u_{k_i}\sqrt{(\alpha_k\rho_k)_i} + u_{k_{i+1}}\sqrt{(\alpha_k\rho_k)_{i+1}}}{\sqrt{(\alpha_k\rho_k)_i} + \sqrt{(\alpha_k\rho_k)_{i+1}}}, \tag{B.2}$$

$$\hat{\alpha}_k \equiv \frac{1}{2}\left(\alpha_{k_i} + \alpha_{k_{i+1}}\right), \tag{B.3}$$

$$\hat{\rho}_k \equiv \frac{1}{2}\left(\rho_{k_i} + \rho_{k_{i+1}}\right), \tag{B.4}$$

$$\Delta\hat{p}_k \equiv \frac{1}{2}\left(\Delta p_{k_i} + \Delta p_{k_{i+1}}\right), \tag{B.5}$$

$$\hat{u}_I \equiv \frac{1}{2}\left(u_{I_i} + u_{I_{i+1}}\right). \tag{B.6}$$

Appendix C – Uncertainty Analysis

To observe, understand and quantify a physical phenomenon an experimental setup can be constructed, and an analysis of the measurements performed. However, errors are intrinsic to experimental measurements, as the instruments and the measured parameters may be affected by multiple sources. An uncertainty analysis is then paramount as it provides the reliability of the results through error intervals.

Two types of error may be encountered: the systematic and the random errors. Systematic errors are the same for all experimental conditions, being generated due to calibration errors, and data acquisition errors, for instance. Random errors are generated due to the variation in the experimental data, that inherently changes with the repetition of the tests. Both uncertainties are estimated according to Dieck (2007), as follows:

- Systematic Uncertainty

The systematic errors for different instruments are estimated according to Tables C.1.

Table C. 2: Systematic uncertainty of instruments for the plunger lift facility.

Instrument	Measured Variable	Systematic Uncertainty
Promass 83F	Gas Mass Flow Rate	$\pm$0.35% of operational range
Promass 83F	Liquid Mass Flow Rate	$\pm$0.05% of operational range
Rosemount 3051S2	Differential Pressure	$\pm$0.15% of 150 psi span
Rosemount 3051S2	Pressure Low-speed	$\pm$0.15% of 150 psi span
Kavlico P265-50A-E4C	Pressure High-speed	$\pm$2.00% of 36 psi span
Rosemount 3144P	Temperature	$\pm$0.25°F

- Random Uncertainty

Considering N the number of data points, X_i the value of the i^{th} measurement and $\bar{X}$ is the average value of all data points, the standard deviation of the average can be obtained as follows

$$S_X = \sqrt{\frac{\sum_{i=1}^{N}(X_i - \bar{X})^2}{N-1}}. \quad \text{(C.1)}$$

The standard deviation of the average is given by

$$S_{\bar{X}} = \frac{S_X}{\sqrt{N_p}}. \tag{C.2}$$

- Combination of random and systematic uncertainty

Random and systematic uncertainty are combined according to

$$U_{95} = \pm t_{95}[(b_R)^2 + (S_{\bar{X}})^2]^{1/2}, \tag{C.3}$$

where U_{95} is the overall uncertainty, t_{95} is the student-t coefficient of 95% confidence.

- Uncertainty Propagation

The uncertainty propagation is calculated when a parameter is a function of two or multiple quantities that are obtained from the instruments. It is calculated, as follows, based on Taylor's series

$$U(f(x_1, x_2, \dots, x_m)) = \sqrt{\sum_{i=1}^{m} \left(\frac{\partial f}{\partial x_i} U(x_i)\right)^2}, \tag{C.4}$$

where x_i are the independent quantities obtained from the instruments, and U is the propagated uncertainty.